# Grafted polymers on spherical nanoparticles in solution and in polymer melts

**Gepfropfte Polymere auf sphärischen Nanopartikeln in Lösung und in Polymerschmelzen**
Vom Fachbereich Physik der Technischen Universität Darmstadt
zur Erlangung des Grades eines Doktors der Naturwissenschaften (Dr. rer. nat.)
genehmigte Dissertation von M.Sc. Chang Jong Kim aus Seoul (Korea)
April 2014 — Darmstadt — D 17

TECHNISCHE UNIVERSITÄT DARMSTADT

Fachbereich Physik
Institut für Festkörperphysik

Grafted polymers on spherical nanoparticles in solution and in polymer melts
Gepfropfte Polymere auf sphärischen Nanopartikeln in Lösung und in Polymerschmelzen

Genehmigte Dissertation von M.Sc. Chang Jong Kim aus Seoul (Korea)

1. Gutachten: Prof. Dr. B. Stühn
2. Gutachten: Prof. Dr. R. Feile

Tag der Einreichung: 12.02.2014
Tag der Prüfung: 14.04.2014

Darmstadt — D 17

# Grafted Polymers on spherical nanoparticles in solution and in polymer melts

Gepfropfte Polymere auf sphärischen Nanopartikeln in Lösung und in Polymerschmelzen

Vom Fachbereich Physik der Technischen Universität Darmstadt
zur Erlangung des Grades eines Doktors der Naturwissenschaften (Dr. rer. nat.)
genehmigte Dissertation von M. Sc. Chang Jong Kim aus Seoul (Korea)

1. Gutachter: Prof. Dr. B. Stühn
2. Gutachter: Prof. Dr. R. Feile
Datum der Einreichung: 12.02.2014
Datum der Prüfung: 14.04.2014

Darmstadt 2014
D 17

# Erklärung zur Dissertation

Hiermit versichere ich, die vorliegende Dissertation ohne Hilfe Dritter nur mit den angegebenen Quellen und Hilfsmitteln angefertigt zu haben. Alle Stellen, die aus Quellen entnommen wurden, sind als solche kenntlich gemacht. Diese Arbeit hat in gleicher oder ähnlicher Form noch keiner Prüfungsbehörde vorgelegen.

Darmstadt, den 30. April 2014

_____

(Chang Jong Kim)

# Inhaltsverzeichnis


**1. Introduction** **6**

**2. Experimental Methods** **11**
2.1. Basics of X-ray and neutron scattering . . . 11
2.1.1. Elastic scattering . . . 11
2.1.2. Differential cross section . . . 12
2.1.3. Scattering by a single atom . . . 13
2.1.4. Atomic form factor (scattering of x-ray) . . . 13
2.1.5. Nuclear scattering length (scattering of neutrons) . . . 14
2.1.6. Neutron and x-ray source . . . 16
2.2. Small angle scattering . . . 17
2.2.1. Absolute intensities for SANS . . . 17
2.2.2. Experimental techniques, SAXS and SANS . . . 19
2.3. Dynamic light scattering (DLS) . . . 21
2.3.1. Theoretical background of DLS . . . 21
2.3.2. Experimental technique, DLS . . . 27

**3. Polymer brush** **30**
3.1. Polymer basics . . . 30
3.2. Polymer brush . . . 33
3.2.1. Polymer brush in a good solvent . . . 34
3.2.2. Grafted polymer in a melt . . . 40
3.2.3. Conclusion . . . 44

**4. Form factors for the various density profiles** **46**
4.1. Intensity calculation of small angle scattering curves . . . 46
4.2. Model independent analysis of small angle scattering spectra . . . 49
4.3. Form factor calculation for the polymer coated nanoparticle . . . 51
4.3.1. Core-shell-chain model . . . 51
4.3.2. Core-shell model added with chain form factor . . . 57
4.4. Conclusion . . . 60

**5. Polymer grafted nanoparticles in a good solvent** **62**
5.1. PS grafted silica in a good solvent . . . 62
5.1.1. Synthesis . . . 62
5.1.2. Experimental methods . . . 63
5.1.3. Results and discussion . . . 63
5.1.4. Conclusion . . . 74
5.2. PS grafted d-PS in a good solvent: “ATRP grafting from” method . . . 76
5.2.1. Synthesis . . . 76
5.2.2. SANS data fitting . . . 77
5.2.3. Results and Discussion . . . 77
5.2.4. Determination of the conformation of PS chains . . . 84
5.2.5. Conclusion . . . 87

5.3. PS grafted d-PS in a good solvent: “NMRP grafting from” method . . . . . 89
5.3.1. Synthesis . . . . . 89
5.3.2. Results and discussion . . . . . 89
5.3.3. Conclusion . . . . . 93
5.4. Conclusion . . . . . 94

**6. Polymer grafted nanoparticle in the same polymer matrix 96**
6.1. Sample preparation . . . . . 97
6.2. Description of experimental data . . . . . 99
6.3. Results and discussion . . . . . 101
6.3.1. Results of PS grafted silica and small d-PS particles in d-PS matrices . . . . . 101
6.3.2. Results of PS grafted, large d-PS particles in d-PS matrices . . . . . 107
6.4. Comparison of the results from different PNC systems . . . . . 114
6.5. Conclusion . . . . . 118

**7. Summary 119**

**8. Acknowledgement 123**

**A. Hansen solubility parameter 124**

**B. Analytical calculations of core-linear and core-exponential form factor 125**

# Abstract

The main focus of this work is the experimental observation of the static structure of the grafted chain conformation in a good solvent or in a melt. Therefore, the structural properties of the grafted chains in given conditions were investigated by small angle neutron scattering (SANS), small angle x-ray scattering (SAXS), and dynamic light scattering (DLS) to get insight into the conformation feature of the grafted chains on the spherical substrate, which is expected to be clearly discernible from that of the bulk chains in the same conditions. Polystyrene (PS) was grafted from the surface of silica nanoparticles (diameter 50 nm) and deuterated polystyrene (d-PS) nanoparticles (diameter 40 and 60 nm) using different synthesis methods. The particles had variation in grafting densities and molecular weights of grafted PS, which was expected to influence the conformation of the grafted chains either in a good solvent or in a polymeric matrix. First, the grafted particles were dispersed in good solvents for the experiments, and the results demonstrated that the grafted PS layer on the silica and d-PS particle with a small core size retained the slightly stretched conformation compared to that in the bulk state. For the d-PS particles with a large core, moreover, the grafted chains retained more highly stretched conformation compared to the silica and small d-PS. Second, the conformation of the grafted chains in a melt was investigated by SANS and SAXS. Variation in the molecular weights of the matrix polymer of d-PS allowed for the direct observation of change in the conformation of the grafted PS by means of SANS. The conformation change of the grafted PS was observed for the silica and d-PS particles with a large core and was related to the chain autophobicity driven by wetting or dewetting of the matrix chains. The critical value of the ratio of the molecular weight of the matrix to the grafted PS, where the wetting-dewetting occurs, was found to be small for the d-PS of a large core and large for the silica, which may originate from the difference in grafting densities of the two particle systems.

# Zusammenfassung

Schwerpunkt dieser Arbeit ist die experimentelle Beobachtung der statischen Struktur der gepfropften Polystyrol-Kettenkonformationen in einem guten Lösungsmittel oder in einer Schmelze. Die Struktureigenschaften der gepfropften Ketten wurden mit SANS, SAXS, DLS und TEM untersucht. Dabei zeigte sich ein klarer Unterschied zwischen der Konformation der Ketten im Volumen und der Konformationseigenschaften von Ketten, die auf sphärische Substrate gepfropft wurden. Durch unterschiedliche Syntheseverfahren wurden Polystyrol (PS) auf Silika- Nanopartikel (Durchmesser 50nm) und deuterierte PS Nanopartikel (d-PS, Durchmesser 40 und 60nm) aufgepfropft. Bei den hergestellten Teilchen variierten die Pfropfdichten und die Molekulargewichte der Ketten auf den Kernen. Es ist zu erwarten, dass diese Variation die Konformation der gepfropften Ketten in einem guten Lösungsmittel oder in einer Polymerenmatrix beeinflusst.
Zunächst wurden für die Experimente die gepfropften Teilchen in einem guten Lösungsmittel dispergiert und die Ergebnisse zeigten, dass die gepfropfte PS-Schicht auf den Silikapartikeln und auf den kleineren d-PS-Teilchen eine leicht gestreckte Konformation im Vergleich zu der Bulk-Konformation einnehmen. Bei den größeren d-PS-Teilchen zeigte sich eine noch gestrecktere Konformation. Ausserdem wurde die Konformation der gepfropften Kette in einer Schmelze mittels SANS untersucht. Eine Variation der Molekulargewichte der d-PS Polymermatrix ließ eine direkte Beobachtung von der Änderung der gepfropften PS Kettenkonformationen bei den Silikapartikeln und den großen d-PS zu. Die Änderung der gepfropften PS Kettenkonformation zeigt sich durch Be- und Entnetzung (wetting, dewetting) angetrieben durch die Matrixketten. Das kritische Verhältnis von Molekulargewichten zwischen den Matrixpolymerketten und den gepfropften Ketten, bei dem dewetting einsetzt, is klein für größere d-PS Systeme und groß für Silikapartikel. Dies könnte an dem Unterschied der Pfropfdichten der beiden Systeme liegen.

# 1 Introduction [1, 2, 3, 4]

Polymers at interfaces may show different conformation features compared to those in the bulk state. The conformation perturbation of polymer chains at an interface may occur if the polymers are attached at high coverage onto the substrate surface. Along with the advent and development of the synthesis of the polymer chains on the solid substrate, a theoretically expected highly stretched conformation of the polymer chains on the substrate surface, a polymer brush, has been realized recently by numerous experiments and simulations. A polymer brush is an array of polymer chains with a highly stretched conformation which is formed when the polymer chains are covalently attached by one end at high coverage to the substrate.

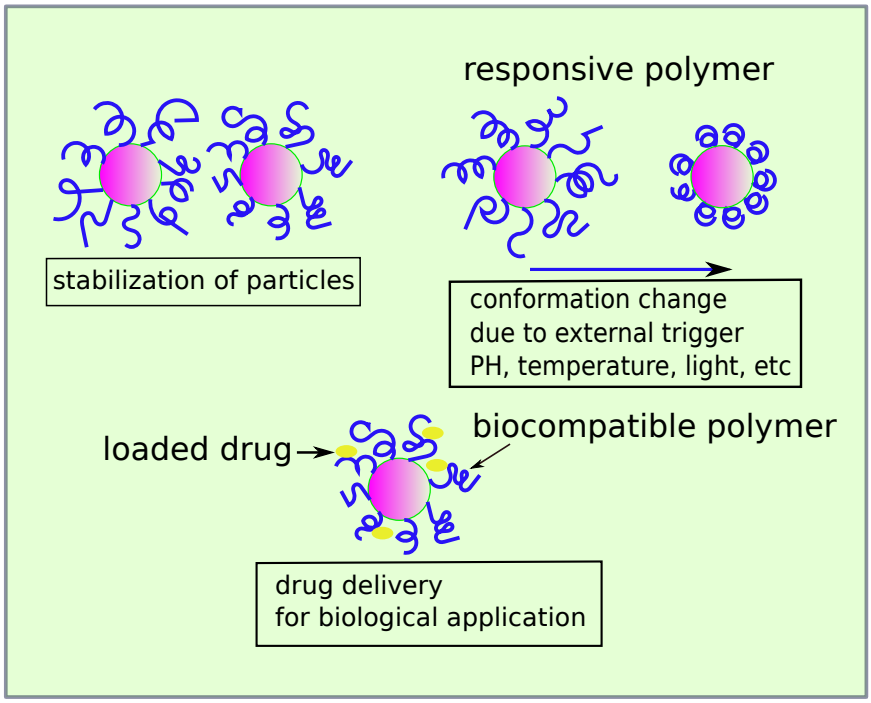


**Figure 1.1.:** Schemes of potential applications making use of polymer grafted nanoparticles

For several years now, research in the field of the polymer brush has no longer been confined to the realm of pure polymer science but has begun to be expanded to that of engineering and material science. The increasing interest in the polymer brush arose from the potential use of various kinds of substrate materials as well as those of the polymer brush. The aim is to enable the fabrication of the new functional materials to combine the physical properties of a polymer and a substrate. One of the basic applications would be steric stabilization achieved by a polymer brush when the polymer brush is formed on colloidal particles in suspension. The increased osmotic pressure between particles due to the polymer brush would be responsible for the steric stabilization, and this could be utilized for various applications, such as lubrication, painting, and drug delivery for biological applications. Another promising application will be related to the use of a responsive polymer for the polymer brush material. The polymer brush inherently tends to form a well defined architecture on a solid substrate and can be considered a soft building block capable of changing its conformation due to external stimulation in a well controlled manner. These changes tend to correspond to changes in the physical properties of the polymers on the surface of the substrate as well. Figure 1.1 demonstrates the variation in the functionality of the polymer

brush for potential applications depending on the tunablity of the conformations of the polymer brush by external stimulations such as temperature, solvent, electric and magnetic field, light and so forth. Correspondingly soft building blocks of polymer brush materials may find a use in sensing and optical applications for medical or engineering purposes. For example, poly(N-isopropylacrylamide) (PNIPAM) brushes respond with a large conformation change to temperature. Polyelectrolyte brushes change their conformation with respect to a change in PH or ionic strength. Therefore, deeper understanding of the conformation feature of the polymer chains is required to advance toward the potential applications.

Covalent anchoring of the polymer chains onto the surface of the substrate has been performed by the "grafting" method. In essence, there are two methods to tether polymer chains onto the substrate: "grafting to" and "grafting from". The "grafting to" method utilizes the preformed and functionalized polymer to attach the chains onto the substrate surface. It is advantageous to make use of this method in that "grafting density", the density of the grafted sites, can be precisely determined. However, the grafting density using this method tends to be low due to the sterical hindrance of incoming with preformed polymer, leading to low grafitng density. Therefore, this method is not a preferred choice to tether the polymer. "Grafting from", on the other hand, has become a preferred choice due to its ability to yield dense grafted polymer in a well-controlled manner. Grafted polymers are synthesized "in situ" onto the substrate, which is functionalized with a polymerization initiator. Various methods are already in use, including nitroxide-mediated polymerization (NMP), atom transfer radical polymerization (ATRP), and reversible addition fragmentation chain transfer polymerization (RAFT).

Under good solvent conditions, the parameters known to affect the chain conformation are the grafting density, the length of the grafted chains, and the geometry of the substrate on which the polymers are grafted. Planar, cylindrical, and spherical geometry can be employed to provide the substrate. A planar substrate is prototypical and most frequently used due to the relatively easy access to graft polymers on such a substrate. The surface-attached chains adopt the conformation features as a consequence of the balance of the entropy gain due to repulsive interaction between neighbouring chains and entropy loss due to chain stretching. Many experimental and simulational works have been reported recently concerning spherical nanoparticles grafted with various polymers, although many works have also contributed to planar and cylindrical geometry.

In addition to the nano-scaled issue or the microscopic structure on the polymer tethered to the substrate, another class of materials, composed of polymers and nano-objects, usually nanoparticles, generally identified as polymer nanoparticle composites (PNC), exhibits diverse functional properties ranging from mechanical and biomedical to electronical and optical properties. The properties of PNC depend not only on the chemical composition of the polymer and nanoparticles but also on the geometry and size of the nano-objects and the spatial distribution of the materials. In particular, the spatial correlations between nanoparticles can be controlled by the morphology of the particles, namely by grafting methods. Mechanical properties can be, for instance, controlled by the spatial distribution of the nanoparticles and by optimization of the strength and range of the interaction between the particles [5]. Therefore, in order to control the spatial distribution of the nanoparticles, a deeper understanding of the microscopic structure of the grafted chains within a polymer matrix is required. As previously stated, with solvent present, the structure of the grafted chains are affected by the grafting density and the length of the grafted chains, as well as the geometry of the substrate. For melt conditions, the particles embedded in a polymer matrix, the interaction between the free matrix and the grafted chains will additionally contribute to the structure of the grafted chains and result in a phase transition, namely the wetting-dewetting transition. The length ratio of the free and grafted chains will be a parameter to characterize that interaction.

Numerous studies have already been conducted to characterize the structure of the grafted polymer chains on the nanoparticles "in solution" using dynamic light scattering (DLS) [6, 7, 8, 9] and small angle neutron scattering (SANS) [10, 11, 12, 13]. Works using DLS have focused on the scaling of the thickness (h) with the molar mass ($M_w$) and grafting densities ($\sigma$) of the grafted polymer layers [7, 8, 9]. Scaling relations between h and $M_w$ were reported based on DLS studies, and the main factors governing

polymer conformation were found to be size of the core of a spherical particle, the grafting density, and the molar mass of grafted chains. We note that DLS probes the hydrodynamic size of the particles. SANS, on the other hand, provides direct access to the static structure of the polymer layer. In SANS studies, grafted polymer chains have been characterized via contrast matching of a core and a solvent to access the structure of the grafted polymer layer. Such measurements are also possible for grafted particles in a polymer matrix. Chevigny et al. [10] reported that the thickness of the grafted chains obtained from SANS measurements in a theta solvent were consistent with two times the radius of gyration ($R_g$) of the grafted polymer.

As for the characterization of the grafted polymer chains in a polymer matrix (PNC), the main concerns for the research studies were the particle systems grafted with polymer chains in a polymer matrix whose chemical composition is identical to that of the grafted polymer. Recent experimental efforts have been contributed for particles grafted with polymer chains in the same polymer matrix in order to investigate the dispersion state of the particles [14]. The results demonstrated that the dispersion state of the particles in the matrix polymer can be tuned by changing the ratio of molecular weight of matrix chain, $N_f$, and to that of grafted chain, $N_g$, namely $N_f/N_g$, grafting density and size of the nanoparticles, respectively. Furthermore it was reported[14], the change of the dispersion state is linked to the miscibility of the matrix with the grafted polymer, the change of the wetting properties of the matrix polymer on the grafted as stated previously. The change of the wetting property can be experimentally tracked by observing the change of the thickness of the grafted polymer layer. Chevigny et al.[15] employed SAXS to extract the thickness of the grafted layer and for that aim, $N_f/N_g$ was varied. Their results showed that the change of the conformation is closely linked to the change of the dispersion state and for a certain value of the ratio of the molecular weight of the free ($N_f$) to the grafted chain ($N_g$), in their case, $N_f/N_g$=4, the wetting-dewetting transition occurred.

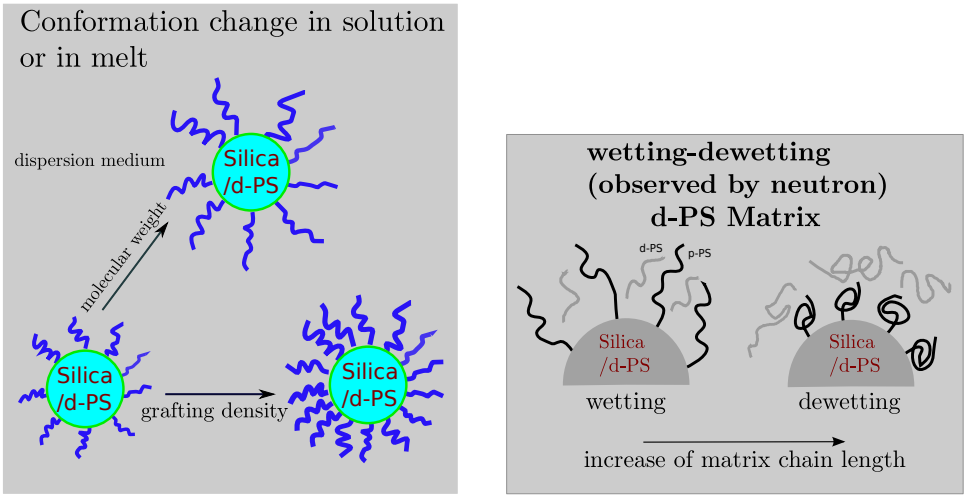


**Figure 1.2.:** (a): Schematic illustration of experiments performed on this work to reveal a conformation feature of grafted polymers on a spherical nanoparticle surface. As main strategies to see the change of the conformation, molecular weight and grafting density will be varied using two different core particles. Main tools to investigate the static structural properties of the grafted polymers will be SANS, SAXS and DLS. Polystyrene polymer (PS) will be grafted "from" the surface of the nanoparticles. (b): The expected change of the conformation of the grafted PS chain will be investigated as a function of the length of the deuterated PS polymers chemically identical with PS, using SANS experiments.

It has been clear that the conformation of the grafted chains in solution or in melt can be changed with respect to grafting density, molecular weight and size of the core. Along with the advance of the chemical methods to synthesize grafted chains on nanoparticles, scattering methods have been used, therefore, to reveal the conformation feature of the grafted chains either in solution or in melt. However we find, for the particles in solution, DLS has been a main method to characterize the conformation of the grafted

chains, since the hydrodynamic thickness of the grafted chain can be easily obtained without applying models to describe the experimental data. But the SANS investigation on the grafted particle systems, is rare due to the difficulty of the modeling process to analyze the data. Also for the particles in a melt, even though SANS can render a direct access to the grafted chain conformation, SAXS was preferred since it is easily accessible compared to SANS, and it has mainly core contrast which does not need to have a strong modeling process. Hereby, therefore, we try to combine scattering methods of SAXS, SANS and DLS to characterize the conformation and correspondingly the dispersion state. We expect, combination of scattering methods allows for revealing the conformation feature of the grafted chains more in detail throughout comparison of the scattering methods.
In the present work, the main focus will then be devoted to experimental observation of the static structural properties of spherical nanoparticles grafted with polystyrene (PS) dispersed either in a good solvent or in a chemically identical deuterated PS matrix. Silica and deuterated PS nanoparticles will be used for spherical substrates and use of different hydrophobicity will allow us to see the effect of the substrate material on the change of the conformation. Along with the different substrate materials, molecular weight and grafting density on those spherical substrates will be varied to see the change of the conformation of the grafted polymers as shown in Figure 1.2. The scattering methods of SANS, SAXS and DLS, will be combined to reveal the conformation feature of the grafted polystyrene on the nanoparticle surfaces (see Figure 1.3).

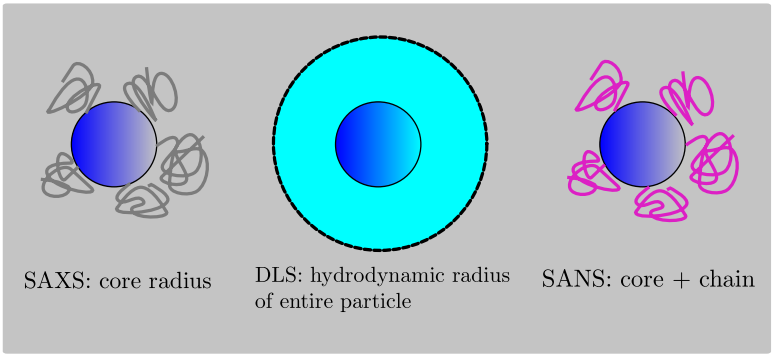


**Figure 1.3.:** Schematic illustration showing the characteristics of the different scattering methods. SAXS is well suited to determine the core radius, and DLS characterizes the hydrodynamic radius of the entire particle. SANS is sensitive to the conformation of the polymer chains. The combination of the three methods will allow a detailed understanding of the complex particle structure.

Polymers were synthesized by the “grafting from” method to obtain surface attached polymers on nanoparticle surfaces in a controllable manner. The samples were provided by Prof. Rehahn’s group in the chemistry department at TU Darmstadt. It is noteworthy that this work resulted from strong cooperation with his group. For the case of the polymer brush in contact with a chemically identical polymer melt, the molecular weight ratio of the matrix polymer to the grafted polymer is expected to contribute to the change in the conformation of the grafted polymer and that of the dispersion state of the nanoparticles. Relation of the change of the conformation and dispersion state will be addressed as another main topic in this work. The experiments performed for this work are schematically illustrated in Figure 1.2.
The outline of this work is as follows. Experimental methods will be introduced as a basic step to understand the set-up and its functionalities. The chapter on the polymer brush will elucidate the recent experimental and simulational results on the polymer brush as well as the physical concepts of the polymer brush. The description of the polymer brush will be somewhat limited to the case of a good solvent or in a melt, especially chemically identical polymer matrix. The main focus of the chapter on the polymer brush will be the scaling concepts that have been introduced and verified by a number of experiments and simulations. In chapter 4, various models for calculating the small angle scattering intensity will be given which will be used to analyze the small angle scattering data. The detailed descriptions of the

derivation of each model will be followed by the calculation of the small angle scattering intensity using the introduced models. The calculations will be based on parameters similar to those we used to analyze experimental small angle scattering data. Based on the conceptual studies of the experimental methods and the polymer brush, our experimental results for the systems investigated in our study will be given in chapters 5 and 6. The experimental results for the nanoparticles grafted with PS under good solvent and melt condition, will be addressed in chapter 5 and 6 based on our previous publications concerning those topics. After the description of the experimental results and the corresponding discussions, a summary will be given, and the chapter will include the future perspective extending the scope of the present work to other possible experiments.

# 2 Experimental Methods

Methods for the experiments performed will be described in the following sections. Instead of giving all the information on the methodology for the experiments, the factors relevant to the treatment of experimental data and their corresponding theoretical background will be described based on references [16, 17].

## 2.1 Basics of X-ray and neutron scattering

### 2.1.1 Elastic scattering

When an x-ray or neutron beam is impingent on the sample, the incoming ray will be scattered by the sample. The resulting change in the momentum and energy of the sample will be reflected in the change in the momentum and energy of the incoming ray. The change in the momentum, $\Delta\mathbf{P}$, and the energy, $\Delta E$, of the incoming ray are schematically represented in Figure 2.1. The momentum and energy transfer are expressed as

$$\Delta\mathbf{P} = \hbar\mathbf{q} \quad \text{where} \quad \mathbf{q} = \mathbf{k_i} - \mathbf{k_f} \tag{2.1}$$

$$\Delta E = \hbar\omega \quad \text{where} \quad \omega = \omega_i - \omega_f \tag{2.2}$$

$\hbar$ is the Planck constant. The wavevector and angular frequency of the incoming ray are represented as $\mathbf{k_i}$ and $\omega_i$, those of the outgoing ray are $\mathbf{k_f}$ and $\omega_f$, and $\mathbf{q}$ is the wavevector transfer, respectively. In an elastic scattering event, there is no transfer of energy, and the modulus of momentum in the initial and the final state are the same.

$$\Delta E = 0, \quad |\mathbf{k_i}| = |\mathbf{k_f}| = \frac{2\pi}{\lambda}, \tag{2.3}$$

where $\lambda$ is the wavelength of the incoming beam. The vector diagram for the elastic scattering is schematically represented by Figure 2.1. The wavevector transfer $\mathbf{q}$ is called a scattering vector when an incoming beam is deflected through an angle $2\theta$. The modulus of $\mathbf{q}$ is as shown in Figure 2.1.

$$|\mathbf{q}| = \frac{4\pi\sin\theta}{\lambda} \tag{2.4}$$

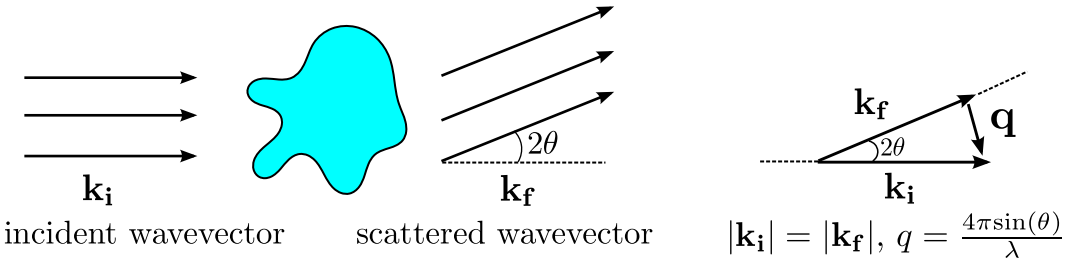


**Figure 2.1.:** Schematic diagram for the elastic scattering, $|\mathbf{k_i}| = |\mathbf{k_f}|$.

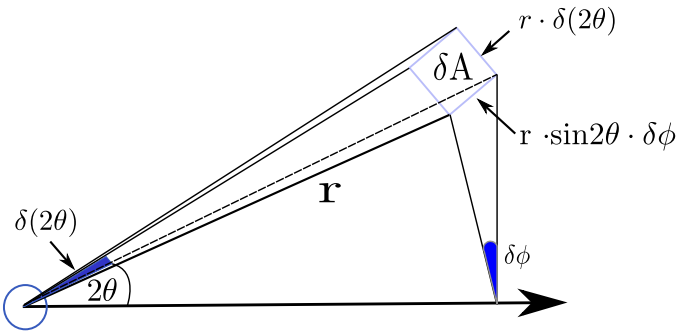


**Figure 2.2.:** Schematic illustration of solid angle

### 2.1.2 Differential cross section

Intensity in a scattering experiment is a measure of diffracted outgoing rays emerging in various directions. The geometry is defined by spherical coordinates expressed by $\theta$, $\phi$, and $r$. The basic quantity that a scattering experiment aims to measure is the fraction of incident rays that is scattered in the unit angle. As shown in Figure 2.2, the unit angle is called the solid angle, given by

$$d\Omega = \frac{dA}{r^2} = \sin(2\theta) \cdot d(2\theta) \cdot d(\phi) \tag{2.5}$$

$dA$ herein is an infinitesimally small area. Then, the rate of the outgoing rays captured in a direction of $\theta$ and $\phi$ at a small solid angle $\Delta\Omega$ per unit time and area, is a required expression for the scattering experiment, that is, a differential cross section, $d\sigma/d\Omega$, whose unit is $m^2 sr^{-1}$.

$$\frac{d\sigma}{d\Omega} = \frac{R(2\theta, \phi)}{\Phi \Delta\Omega} \tag{2.6}$$

where the equality holds at the limit of $\Delta\Omega \to 0$. $R(2\theta, \phi)$ is the rate of rays to arrive in the direction of $2\theta$ and $\phi$. $\Phi$ is the incident flux, which is the number of the particles per unit time and area in parallel with the direction of the flow with an SI unit of $m^{-2}s^{-1}$. The experimental intensity $I(q)$ is then obtained by dividing the differential cross section $d\sigma/d\Omega$ by the scattering volume V($m^3$) to yield its unit as $m^{-1}$, as given by (usually its unit is $cm^{-1}$),

$$I(q) = \frac{1}{V}\frac{d\sigma}{d\Omega} = \left(\frac{d\Sigma}{d\Omega}\right). \tag{2.7}$$

### 2.1.3 Scattering by a single atom

The above description of the differential cross section is related to the experimental scattering data. In order to describe the experimental data with the theoretical calculation, first, the diffraction by a single atom should be understood. An incident beam of an x-ray or neutron traveling in the x direction is described by the complex plane wave form

$$\psi_i = \psi_0 e^{ikx} \tag{2.8}$$

where the incident flux is $|{\psi_0}^2|$. As for the case of elastic scattering, the atom is assumed to have a fixed location. The incoming ray will then interact with the atom elastically with an unchanged wave number, k. After interaction, the amplitude of the outgoing wave will decay at a distance of r by $r^{-1}$. The scattered wave is therefore given by,

$$\psi_f = \psi_0 f(\lambda, \theta)\frac{e^{ikr}}{r} \tag{2.9}$$

where $f(\lambda, \theta)$ expresses the efficiency of the diffraction of the particles in a given direction as a function of $\lambda$ and $\theta$. As this factor is expressed in a different manner for x-rays and neutrons, they will be described separately in the following sections.

### 2.1.4 Atomic form factor (scattering of x-ray)

In x-ray scattering, the atomic form factor is the scattering amplitude of the x-ray from an atom. The interaction of the x-ray with the atom depends on the number of electrons in the atom. Therefore, for the case of x-ray, the atomic form factor, $f(\lambda, \theta)$, has a linear dependence on the atomic number. It is easily understood since the interaction relevant to the scattering event is that between the x-ray and the electron cloud of an atom. Therefore, as the number of the electrons increases, that is, as the atomic number increases, the strength of the interaction will increase. In fact, the atomic form factor is expressed as a Fourier transformation of the density distribution of electron clouds as a function of the radial distance, r, from the center of the atom.

$$f(\mathbf{q}) = \int n(\mathbf{r}) e^{-i\mathbf{q}\cdot\mathbf{r}} d\mathbf{r} \tag{2.10}$$

$n(\mathbf{r})$ is a density profile of electron clouds surrounding a nucleus in an atom. The other feature of the atomic form factor is that it decreases as $q$ increases. A decrease in the amplitude of the form factor can be explained by an increase of the interference from different parts of the electron cloud in an atom. The atomic form factor depends on $q$ and has the form of

$$f(q) = Z g(q) r_e \tag{2.11}$$

where Z is the atomic number, g(q) is a decay function, varying from one at the origin to zero as $q \to \infty$ [18], and $r_e$ is the classical radius of the electron, or the so-called Thomson scattering length:

$$r_e = \frac{e^2}{4\pi\varepsilon_0 m_e c^2} = 2.818 \times 10^{-15} m. \tag{2.12}$$

The differential scattering cross section of an electron is,

$$\frac{d\sigma}{d\Omega} = {r_e}^2 \frac{1+\cos^2(2\theta)}{2} \tag{2.13}$$

where the scattering length of an electron $b_e$ is

$$b_e = r_e \left( \frac{1+\cos^2(2\theta)}{2} \right)^{1/2} \tag{2.14}$$

If an array of atoms is considered, the differential cross section becomes

$$\frac{d\sigma}{d\Omega} = {b_e}^2 \cdot \left| \sum_{k=1}^{N_{\text{atom}}} f_k(q) e^{-iqr_k} \right|^2 \tag{2.15}$$

$f_k(q)$ is the atomic form factor of the kth atom. Note that, the quantity of $\sum_{k=1}^{N_{\text{atom}}} f_k(q)e^{-iqr_k}$ is called the form factor of a scattering object, such as macromolecules or nanoparticles, which will be described in detail in chapter 4.

### 2.1.5 Nuclear scattering length (scattering of neutrons)

For the neutron case, $f(\lambda, \theta)$ has a constant value independent of $\lambda$ and $\theta$.

$$f(\lambda, \theta) = -b \tag{2.16}$$

The constant b is called “nuclear scattering length”; in short, the scattering length for the neutron scattering experiment and the minus sign indicate that the incident and outgoing waves are out of phase. The scattering length is a measure of the scattering amplitude between a neutron and the nucleus of an atom and is usually described by a unit of $10^{-14}$m. The constant scattering length indicates that the scattering of the neutron by the atom is independent of the wavelength and the scattering angle $\theta$, not as in the case of the x-ray. The strength of interaction between the neutron and the nucleus of the atom determines the amplitude of b. This interaction originates from the short-range “strong interaction”. The strength of the interaction then depends on the details of the nuclear structure and can therefore be drastically different from neighbouring elements in the periodic table.
We now consider the scattering of neutrons by a single atom. As in the case of x-ray scattering shown in eq. 2.13, the differential cross section of a single atom is given by

$$\frac{d\sigma}{d\Omega} = b^2 \tag{2.17}$$

In order to calculate the scattering length b of an atom, the spin state of a nucleus of an atom and that of a neutron, and the presence of isotopes should be taken into account. The scattering length of an atom whose nucleus has non zero-spin is then given by

$$b = < b > \pm \Delta b \tag{2.18}$$

The standard deviation of b, $\Delta b$, is given by

$$\Delta b = \sqrt{< b^2 > - < b >^2} \tag{2.19}$$

In order to clarify the spin effect, we first consider a particular case for a nucleus of hydrogen which is isotopically pure. It has a proton and a spin of $\frac{1}{2}$. The neutron has a spin of $\frac{1}{2}$, and the combined spin state can have either a triplet or a singlet state with a probability of 3 and 1. The former triplet state is denoted by the + state and the latter singlet state -, respectively. $b^+$ and $b^-$ are then the scattering length $b$ for the triplet state and the singlet state, respectively. The average scattering length of a hydrogen nucleus is related to $b^+$ and $b^-$ as follows.

$$< b >= \frac{3}{4}b^+ + \frac{1}{4}b^- \tag{2.20}$$

Now we consider a general case, a calculation of the scattering length of a single atom, which is also isotopically pure. If the nucleus of a single atom is assumed to have a spin of $i$ and this nucleus interacts with a neutron, the total spin becomes either $i + 1/2$ or $i - 1/2$. Then, the number of states for spin $i + 1/2$ is given by

$$2(i + 1/2) + 1 = 2i + 2 \tag{2.21}$$

For spin $i - 1/2$, the number of states is given by

$$2(i - 1/2) + 1 = 2i \tag{2.22}$$

The total number of spin states therefore becomes $4i + 2$. Thus, the average scattering length of a single atom becomes

$$< b >= \frac{i+1}{2i+1}b^+ + \frac{i}{2i+1}b^- \tag{2.23}$$

and

$$< b^2 >= \frac{i+1}{2i+1}(b^+)^2 + \frac{i}{2i+1}(b^-)^2 \tag{2.24}$$

Up to now, we have considered the calculation of b of a single atom which is isotopically pure. However, the previous discussions were ideal cases since the isotopes are present in nature. The variability $\Delta b$ indeed results from the non-zero nuclear spin of an atom and the presence of the isotopes. The value of b will then deviate with the calculation only made by the spin contribution.
We now consider an assembly of n nuclei of one kind of atom. The scattering length of b will vary from nucleus to nucleus due to the presence of the isotopes and the non-zero spin of the nuclei. The differential scattering cross section for this case is given by

$$\frac{d\sigma}{d\Omega} =< b >^2 \sum_{j,k} e^{-iq(r_j - r_k)} + n\left(< b^2 > - < b >^2\right) \tag{2.25}$$

The first term contains the structural information on this example with identical scattering lengths equal to the average $< b >$. The second term does not depend on the position of an atom denoted by $r_j$ and therefore contains no information on the structure and is simply proportional to the variance of $\Delta b^2$. The second term arises from fluctuation in the scattering length of individual nuclei, resulting from the presence of isotopes and non-zero nuclear spin. Correspondingly, the coherent and incoherent scattering lengths of an element are defined as $b_{\text{coh}} =< b >$ and $b_{\text{inc}} = \Delta b$, respectively. Then, the differential scattering cross section is given by

$$\frac{d\sigma}{d\Omega} = \left(\frac{d\sigma}{d\Omega}\right)_{\text{coh}} + \left(\frac{d\sigma}{d\Omega}\right)_{\text{inc}} \tag{2.26}$$

The total scattering cross section $\sigma_{\text{total}}$ is obtained by the integration of $d\sigma/d\Omega$ with respect to $d\Omega$ (see eq. 2.6) and is equal to $4\pi b^2$. Therefore, the total coherent and incoherent cross sections are given by

$$\sigma_{\text{coh}} = 4\pi < b >^2 \tag{2.27}$$

$$\sigma_{\text{inc}} = 4\pi(\Delta b)^2 \tag{2.28}$$

where the subscripts coh and inc represent the coherent and incoherent scattering.
The differential scattering cross section, $\frac{d\sigma}{d\Omega}$, per unit volume is $\frac{d\Sigma}{d\Omega}$ (see eq. 2.7). $\frac{d\Sigma}{d\Omega}$ is the scattering intensity, obtained by dividing $\frac{d\sigma}{d\Omega}$ by the volume of a molecule. The scattering intensity therefore consists of a coherent scattering and an incoherent scattering term, as shown in eq. 2.26. The contribution of both components depends strongly on the chemical structure, especially the fraction of hydrogen and deuteron in the molecule. The total cross sections of hydrogen are $\sigma_{\text{coh}} = 1.76$ barns and $\sigma_{\text{inc}} = 79.7$ barns, and those of deuteron are $\sigma_{\text{coh}} = 5.59$ barns and $\sigma_{\text{inc}} = 2.04$ barns, respectively. A barn is defined as $10^{-28}$ m$^2$. Such a large incoherent cross section of hydrogen leads to a large incoherent background in a neutron experiment and sometimes leads to a complication in data analysis due to a dominating large background. Therefore, deuterium labeling, the replacement of hydrogen by deuteron, is often made in a neutron scattering experiment to reduce the experimental incoherent background and to focus on the structural property of a given molecule being investigated. Therefore, to this end, in our work, the solvent and the matrix were mainly deuterated ones.

### 2.1.6 Neutron and x-ray source

Typically, x-rays are generated in the laboratory by a filament tube, where electrons accelerated by high voltage (∼30-40kV) strike the metal target in an evacuated tube, and the loss of energy upon impact is transferred to either heat or x-ray irradiation. This x-ray can be classified as a white x-ray and a characteristic x-ray. A white x-ray originates from the sudden deceleration of electrons upon impact with the metal target and shows a wide range of wavelengths. A characteristic x-ray, on the other hand, is more indirectly generated. The excitation of the electrons in the inner shells of the target materials is produced by the incoming electrons, and vacancies in the inner shells are filled by the electrons at a higher level. Then, the x-ray emission is followed. For instance, $K_\alpha$ line is produced by the excitation of K-shell electrons and the transition of the electrons from the L-shell to the K-shell. A characteristic x-ray is material-specific since the excitation of the inner-shell electrons depend on the binding energy of the shell for the given material. The wavelength of the characteristic x-ray for a Cu anode is, for example, $\lambda = 1.54$ Å.
A modern x-ray source called a synchrotron x-ray source has been developed recently due to the quest for high flux and a corresponding wide variety of experiments, such as time resolved experiments. In a synchrotron, an electron beam is accelerated by alternating magnets spread over the circumference, which is up to ∼ km. When electrons are accelerated, they emit electromagnetic waves (EM). The emitted EM ranges from infra red ($\lambda \sim 10^{-2}$ cm) to hard x-ray ($\lambda \sim 10^{-1}$ nm). The advantage of the synchrotron x-ray is a tunable x-ray wavelength and a relatively short measurement time due to the high flux.
A nuclear reactor is a commonly used source for the generation of neutrons. In a nuclear reactor, a fission reaction takes place in the $^{235}U$ fuel rods by the absorption of stray neutrons [17]. The possible mechanism is given by

$$n + {}^{235}U \longrightarrow {}^{236}U^{*} \longrightarrow {}^{134}Xe + {}^{100}Sr + 2\,n$$

After the absorption of neutrons, metastable $^{236}U^{*}$ is broken down in different ways. One example is shown above. 2.5 neutrons are released on average. This reaction produces fast neutrons with energy in the 1-2 MeV range. Aside from the source, other facilities are required for actual experimental use: the moderator, the neutron shield and the neutron guide. The moderator is used to slow down the neutrons and usually comprises a pool of $D_2O$. A thick concrete wall surrounding the core is called the radiation shield, used to protect users from harmful radiation. The last adjoining part for the experiment is called the neutron guide. The neutron guide brings the neutron flux to the area where the experiment is performed. The guide is an evacuated tube with thick glass walls whose inner surface is coated with a thin evaporated metal. The neutron flux, dissipated in various directions, is "guided" by the neutron guide based on the internal reflection. The details concerning the instruments for the experiment will be described later.

## 2.2 Small angle scattering

Small angle scattering (SAS) is a diffraction method (x-ray, neutron, and light) which is operated at very small scattering angles ($2\theta$ = 0-10°). It is therefore a widely used tool to investigate the structural and dynamical properties of materials at a large scale (1 nm to 1$\mu$m) compared to conventional diffraction methods which measure relatively high scattering angles and is therefore sensitive to atomic scales. Geometrical information about the size, shape, and dispersion of macromolecules can be obtained with a small angle scattering technique. The use of small angle scattering has been popular because this technique is non-invasive and yields the physical properties averaged over the whole sample. It is noted that the statements to follow, will be restricted to elastic scattering containing only structural information.

### 2.2.1 Absolute intensities for SANS [17, 19]

Here, the methods to acquire the absolute intensity for SANS will be described. We note that, for SAXS, no attempts have been made to convert scattered intensity to absolute intensity. Therefore, the methods to acquire absolute intensity in the subsequent description will be limited to the case of SANS.
Experimental data is usually obtained with a 2D image. In order to transform this 2D image to 1D intensity and furthermore absolute scaled intensity, the 2D image is radially averaged, extending from the masked pixels due to the beam stop to the end of the periphery of the detector. The resulting 1D image, intensity, has a $q$ dependence. "Intensity" at this step represents the number of neutrons per second or counts per second. This so called raw data, can be transformed into the absolute scaled intensity in the following way.
The flux of a measured elastic scattered signal is related to the differential scattering cross section as shown in eq. 2.7. This is given by [19]

$$I(q) = \left(\frac{d\Sigma}{d\Omega}\right) = \frac{N(q)}{\Phi_0 \cdot \Delta\Omega(q) \cdot Tr \cdot t \cdot e}, \tag{2.29}$$

where $N(q)$ is the number of neutrons at the detector position and $\Phi_0$ the incident flux measured at the sample position. $\Delta\Omega(q)$ is a solid angle which was introduced previously, e the thickness of the sample, and t the length of time for data acquisition. Tr is the experimentally determined transmission of the given sample with respect to the primary beam. The incident flux can be obtained by a monitor installed at the sample position or by measuring the primary beam, namely the direct beam or empty beam, on the detector through a calibrated attenuator. Usually in a soft condensed matter, the samples are filled in a quartz cell, which contributes slightly to the scattered signal. The scattering from the empty cell, denoted by the subscript EC, is subtracted from the total scattering signal as follows [19],

$$\left(\frac{d\Sigma}{d\Omega}\right)_{\text{sample}} = \frac{1}{e_{\text{sample}} \cdot \Phi_0}\left[\frac{N_{\text{sample}}(q)}{\Delta\Omega(q) \cdot Tr_{\text{sample}} \cdot t_{\text{sample}}} - \frac{N_{\text{EC}}(q)}{\Delta\Omega(q) \cdot Tr_{\text{EC}} \cdot t_{\text{EC}}}\right]. \tag{2.30}$$

Samples with predominant incoherent scattering, such as light water ($H_2O$), vanadium, and PMMA (Poly(methyl methacrylate)), are used for absolute scaling. Water is frequently used as a standard because it is homogeneous at the scales of SANS and its scattering is mainly incoherent. It is noted that water is used as a standard, usually at ILL and PMMA is another standard at FRM 2, and their scattering patterns are almost identical. The differential cross section of light water, $(\frac{d\Sigma}{d\Omega})_{H_2O}$, can be calculated using eq. 2.30. The value of the water cross section increases with wavelength and varies slightly with temperature. It is close to $1\text{cm}^{-1}$. A scattered signal normalized with water as a standard gives an absolute intensity as follows [19],

$$\left(\frac{d\Sigma}{d\Omega}\right)_{\text{sample}} = \frac{1}{F_{\text{sc}}} \cdot \left(\frac{d\Sigma}{d\Omega}\right)_{H_2O} \cdot \frac{\left[\frac{N_{\text{sample}} - N_{B_4C}}{Tr_{\text{sample}}} - \frac{N_{\text{sample-EC}} - N_{B_4C}}{Tr_{\text{sample-EC}}}\right]\frac{1}{e_{\text{sample}}}}{\left[\frac{N_{H_2O} - N_{B_4C}}{Tr_{H_2O}} - \frac{N_{H_2O-EC} - N_{B_4C}}{Tr_{H_2O-EC}}\right]\frac{1}{e_{H_2O}}} \tag{2.31}$$

$F_{sc}$ is a scaling factor equal to 1 when the sample and water are measured with the same instrument configuration. $B_4C$ is boron carbide, which strongly absorbs neutrons. Therefore, this material is used to stop the incoming beam to measure electrical noise from the detector and the instrumental environment, which should be subtracted from the given intensity, as shown in equation 2.31. The subscript sample-EC and $H_2O$-EC represent the empty cell for the sample and the water, respectively.
The details of the structural properties of a sample is now contained in the differential cross section, $d\Sigma/d\Omega$, and it is related to the Fourier transformation of the scattering length density, $\rho(\vec{\mathbf{r}})$.

$$\left(\frac{d\Sigma}{d\Omega}\right) \propto \left|\iiint_V \rho(\vec{\mathbf{r}}) e^{i\vec{\mathbf{q}}\cdot\vec{\mathbf{r}}} d^3\mathbf{r}\right|^2, \tag{2.32}$$

$\rho(\vec{\mathbf{r}})$ usually has a unit of $cm^{-2}$ and depends on the irradiation source and the material probed. If the scattering object is suspended in a dispersion medium, $\rho(r)$ is expressed as a difference in the scattering length density between the scattering object and the solvent or medium. V is the volume of the sample in which the scattering occurs. Considering the isotropic orientation of the samples as in the dilute solutions, the eq. 2.32 becomes in spherical coordinate

$$\left(\frac{d\Sigma}{d\Omega}\right) \propto N_p(4\pi)^2 \left|\int_0^R r^2 \rho(r) \frac{\sin(qr)}{qr} dr\right|^2, \tag{2.33}$$

where $N_p$ is the number of the scattering objects in the sample. Since the concentration is usually defined by the volume fraction, usually the quantity obtained from the sample preparation, $\Phi$, is given by

$$N_p = \frac{\Phi V}{V_p} \tag{2.34}$$

$V_p$ is the volume of a particle. The common small angle experiment encompasses the scattering volume V, and the differential cross section has a unit of $cm^{-1}$. Then, expression for a dilute solution without considering interference between the scattering objects, interparticle interference at $q = 0$, becomes [17]

$$\left(\frac{d\Sigma}{d\Omega}\right)\Big|_{q=0} = \Phi \cdot V_p \cdot \Delta\rho^2 \tag{2.35}$$

$\rho(r)$ is rewritten as $\Delta\rho$, representing the difference in the scattering length density between the scattering object and the medium. This expression can be converted into following expression if molar mass is the main concern. Considering the relation $V_p = \frac{m}{\rho_{\text{den}} N_A}$, where m is the molar mass in units of $g \cdot mol^{-1}$ and $N_A$ is Avogadro's number.

$$\left(\frac{d\Sigma}{d\Omega}\right)\Big|_{q=0} = \frac{\Phi \cdot m}{\rho_{den} \cdot N_A}\Delta\rho^2 \tag{2.36}$$

$\rho_{den}$ is the macroscopic mass density. Details for the calculation of the small angle scattering data will be discussed in chapter 4.

### 2.2.2 Experimental techniques, SAXS and SANS

In this section, the experimental techniques of small angle x-ray scattering (SAXS) and small angle neutron scattering (SANS) will be described. The set up for the SAXS machine is presented in Figure 2.3. An x-ray is generated by a rotating Cu anode tube in a filament tube. The details of the generation of the x-ray were provided in section 2.1.6.

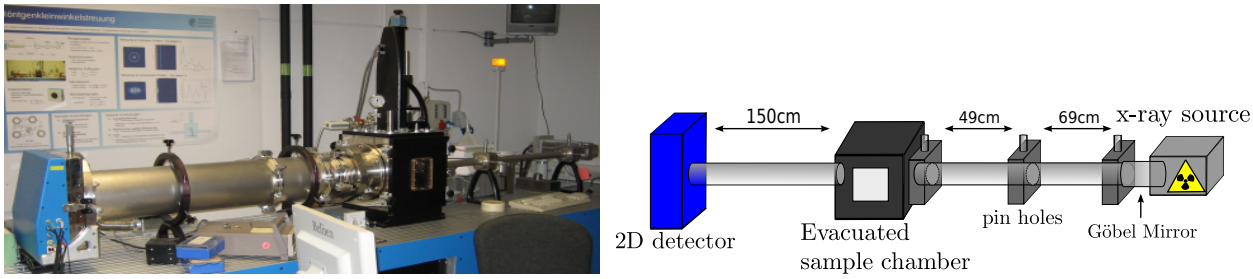


**Figure 2.3.:** Left: 2D SAXS machine (picture taken from [20]), right: schematic illustration of 2D SAXS machine

An x-ray beam generated by a rotating anode source, usually run at 40 kV and 55 mA, is monochromatized by a Göbel mirror and further collimated by three pin holes to yield characteristic Cu $K_\alpha$ line ($\lambda = 1.54$ Å, see section 2.1.6.) as shown in Figure 2.3. The detector position is varied for a long setup at a distance of 150 cm away from the sample holder to provide a $q$ range from 0.008Å$^{-1}$ to 0.25Å$^{-1}$ and for a short setup with a distance of 75 cm to provide a $q$ range from 0.014Å$^{-1}$ to 0.4Å$^{-1}$. For the experiments performed in this work, we used a long setup. The samples for the measurement can be in either solid or liquid form. The liquid sample is placed in a Mark capillary with a diameter of 1.5 mm and a solid sample is placed directly onto the sample holder. The sample chamber is kept evacuated, and temperature can be varied from -50°C to 200°C. The scattered x-ray beam is captured by a two dimensional detector (Molecular metrology), and the two dimensional scattering intensity is azimuthally averaged to yield the one dimensional intensity as a function of the scattering vector, $q$. We note that the experiments were performed at room temperature, and no attempts were made to convert the SAXS data to that absolute intensity.
SANS experiments were performed on the KWS-1 & 2 scattering instrument at FRM 2 in Munich and D11 at the institute Laue Langevin (ILL) in Grenoble in France. Figure 2.4 presents a schematic picture of a SANS instrument.
The neutron beam coming from the reactor source, as described in section 2.1.6, is monochromatized by velocity selector to have a defined wavelength with the relation

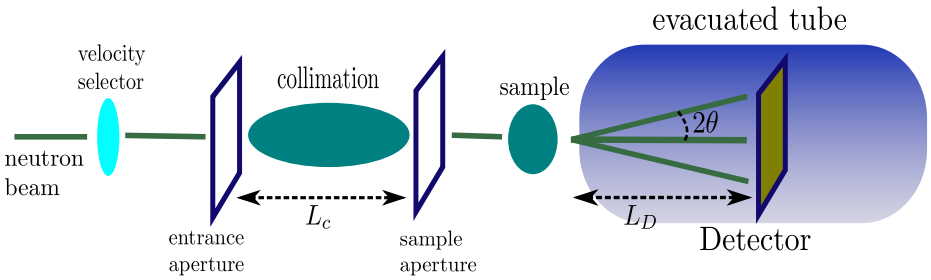


**Figure 2.4.:** Schematic illustration of a SANS instrument [21]. $L_c$ represents the collimation distance and $L_d$ the sample-to-detector distance, respectively.

$$\lambda = \frac{h}{mv} \tag{2.37}$$

The wavelength spread from the velocity selector for the KWS-2 instrument and D11, $\Delta\lambda/\lambda$, is 0.2 and 0.09 (FWHM, full width at half maximum), respectively. The monochromatized neutron beam from the velocity selector is collimated by a series of moveable glass made neutron guides (collimation in the picture above). Guide sections are inserted or removed by the requirement of the divergence of the beam in the sample area. A set of mobile apertures allows for the variation of the distance between the entrance aperture (beginning of a set of movable guides) and the sample aperture (fixed position in front of the sample) over a large interval, typically between 1 and 20 m [21]. That distance is called the "collimation distance," $L_c$, as shown in Figure 2.4. The collimated neutron beam finally enters the evacuated sample environment and is scattered, as is shown in Fig. 2.4. As in the case in the SAXS experiment, the two dimensional scattering picture is azimuthally averaged and results in an one dimensional scattering pattern having $q$ ($\text{Å}^{-1}$) dependence. In order to access various q ranges, the distance between the detector and the sample chamber ($L_D$) and the collimation distance ($L_c$) are usually varied. Accessible $q$ ranges of KWS-1, KWS-2, and D11 beamline are $1 \cdot 10^{-4}\ \text{Å}^{-1} \leq q \leq 0.2\ \text{Å}^{-1}$ and $7 \cdot 10^{-4}\ \text{Å}^{-1} \leq q \leq 0.5\ \text{Å}^{-1}$ and $3 \cdot 10^{-4}\ \text{Å}^{-1} \leq q \leq 1\ \text{Å}^{-1}$, respectively.
For the experiment at KWS-1, three configurations of the detector-to-sample distances (20 m, 4 m and 1.5 m) and three collimation distances (20 m, 4 m and 4 m) at a wavelength 4.5Å were combined to obtain a $q$ range from 0.002 to $0.4\ \text{Å}^{-1}$. The liquid samples were placed in a 1 mm hellma cuvette. The film samples used had a solid form and were directly attached to the sample holder with transparent tape, which does not influence the scattering since it was attached to the outer boundary of the sample holder. For the experiment at KWS-2, to cover a $q$ range from 0.005 to $0.3\ \text{Å}^{-1}$, two different sample-to-detector distances (8 m and 2 m) and a collimation distance (8 m) at a wavelength 4.5 Å was used. The raw data obtained by the instrument for KWS-1 and KWS-2 were treated with correction for electronic background, empty cell scattering, neutron beam transmission and sample volume. Polymethylmethacrylate was used as a standard to obtain absolute intensity. Data reduction was performed with the "Qti-KWS" program.
For the experiment at D11 at ILL in Grenoble, a $q$ range from 0.003 to $0.3\ \text{Å}^{-1}$ was acquired, combining three different sample-to-detector distances (20 m, 8 m and 1.5 m) and collimation distances (20.5, 8 and 5.5 m) at a wavelength 6 Å. For the measurement of D11, only solid film samples were measured. The raw data was corrected for empty beam scattering, electronic background, neutron beam transmission, and sample volume. Water was used as a standard to obtain absolute intensity. The data reduction process was performed with the "Lamp" program. All measurements made at ILL and FRM 2 were performed at room temperature.

## 2.3 Dynamic light scattering (DLS)

Dynamic light scattering is a widely used tool to provide information on particle sizing or its distribution in solution. Aside from obtaining structural properties, it can be used for the characterization of the dynamical behavior of the sample at different temperatures or concentrations.

### 2.3.1 Theoretical background of DLS [22, 23, 24]

Unlike static scattering, such as small angle x-ray and neutron scattering, dynamic light scattering, also known as "quasi elastic light scattering or photon correlation spectroscopy," does not measure the time averaged static intensity but a time-correlated intensity function. This depends on the fluctuation of the intensity for a given time scale, which results from "local fluctuation" in the dielectric constant of the scattering medium, as proposed by Einstein [25]. A laser is usually used as the light source, and its wavelength is more than a hundred nanometers, which is typically larger than the size of the scattering objects. Therefore, the ensemble of local fluctuations in the dielectric constant that occur in subregion of the illuminated volume are responsible for the fluctuation of the intensity. Kinetic theory tells us that molecules are constantly rotating and diffusing by thermal energy, so that the instantaneous dielectric constant of a given subregion will fluctuate in time and thus give rise to light scattering [22]. However, the fluctuation theory, in terms of the dielectric constant, is purely phenomenological and can not give the explicit dependence of this fluctuation on the molecular properties. Therefore, the molecular formulation will be useful for practical application. In Maxwell's theory, the incident light induces a dipole moment on a single molecule specified by a polarizability tensor $\alpha$, as given by

$$\mu(t) = \alpha \cdot \mathbf{E}(t). \tag{2.38}$$

According to classical radiation theory, the time varying dipole moment emits electromagnetic radiation. The scattered field at the detector with polarization $\mathbf{n_f}$ is proportional to $\alpha_{if}(t)e^{i\mathbf{q}\cdot\mathbf{r}(t)}$.

$$\alpha_{\mathbf{if}}(t) = \mathbf{n_f} \cdot \alpha(t) \cdot \mathbf{n_i}. \tag{2.39}$$

Polarization of the incident beam is specified by $\mathbf{n_i}$, and $\mathbf{r}(t)$ is the position of the molecule at a given time t and $\mathbf{q}$ is a scattering vector, whose magnitude is $\frac{4\pi n \sin\theta}{\lambda}$, where n is the refractive index of dispersion medium, usually a solvent in a light scattering experiment and $\theta$ is half of the scattering angle. $\alpha_{if}(t)$ varies in time because the molecule rotates and vibrates and the phase factor, $e^{i\mathbf{q}\cdot\mathbf{r}(t)}$, varies in time as well because the molecule performs a translational motion. The above equation tells us how the fluctuation of the intensity occurs in the light scattering experiment on molecular scale. For spherical molecules, $\alpha_{if}(t)$ is given by

$$\alpha_{\mathbf{if}}(t) = (\mathbf{n_i} \cdot \mathbf{n_f})\alpha, \tag{2.40}$$

because off-diagonal components of the polarizability tensor are zero. Therefore, in an actual DLS experiment, for a spherical molecule, only vertical-vertical polarization, referred to as VV, vertical polarization for incident and vertical polarization for the scattered beam with respect to the scattering plane, is used because the inner product of the polarization of the incident and the scattered beam for VH polarization is zero. It is therefore expected that, for spherical molecules, the scattered field is polarized. We note that, for our study, VV geometry was used for most of the experiments, since the particles for the investigation were spherical in shapes. In the case of the silica particles, the scattered beam was not analyzed with respect to its polarization.

Since the advance and development of the laser as a source, the usual method conducting the light scattering experiment is the homodyne method, where the detector captures the scattered beam. The

heterodyne method, on the other hand, captures both the scattered beam and a portion of the unscattered beam in order to gain information on the local oscillation of the samples driven by an external field. For the following theoretical description of dynamic light scattering, the homodyne method will be assumed.
Usually in a DLS experiment, the variation of intensity with time, fluctuation of intensity in time, is the property of main concern. This is given by the time correlation function of intensity:

$$\langle I(\mathbf{q},0)I(\mathbf{q},\tau)\rangle = \lim_{T\to\infty}\frac{1}{T}\int_0^T I(\mathbf{q},t)I(\mathbf{q},t+\tau)\,dt. \tag{2.41}$$

where t is the starting time and T is the time over which it is averaged. $\tau$ is the relaxation time or the correlation time, where the system is correlated. The above equation is also called an intensity autocorrelation function, which compares the intensity at time t and that after correlation time $\tau$. Intensity fluctuation over time and the time correlation function are sketched schematically in Figure 2.5. As can be expected, the intensity is correlated when the correlation time is small, and the correlation of intensity is lost as the correlation time increases as follows.

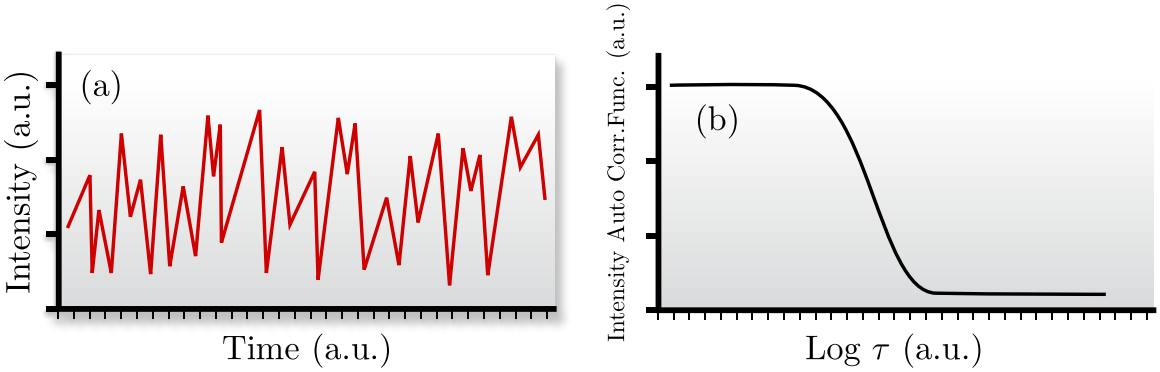


**Figure 2.5.:** (a): Intensity of scattered light in arbitrary units (a.u.) from particles in solution as a function of time. (b): Time averaged intensity-intensity correlation function as a function of relaxation time $\tau$ in a.u. Both figures were reproduced from [22].

$$\lim_{\tau\to 0}\langle I(\mathbf{q},0)I(\mathbf{q},\tau)\rangle = \left\langle I^2(\mathbf{q})\right\rangle \tag{2.42}$$

$$\lim_{\tau\to\infty}\langle I(\mathbf{q},0)I(\mathbf{q},\tau)\rangle = \langle I(\mathbf{q},0)\rangle\langle I(\mathbf{q},\tau)\rangle = \langle I(\mathbf{q})\rangle^2. \tag{2.43}$$

In order to relate the correlation function of intensity with the scattered electric field, we need the normalized time correlation function of the scattered electric field, defined by

$$g^{(1)}(\mathbf{q},\tau) = \frac{\langle E(\mathbf{q},0)E^*(\mathbf{q},\tau)\rangle}{\langle I(\mathbf{q})\rangle} \tag{2.44}$$

The normalized time correlation function of the scattered intensity is defined by,

$$g^{(2)}(\mathbf{q},\tau) = \frac{\langle I(\mathbf{q},0)I(\mathbf{q},\tau)\rangle}{\langle I(\mathbf{q})\rangle^2} \tag{2.45}$$

The Siegert relation is applied to relate the normalized time correlation function of the scattered intensity with that of the scattered electric field [23, 24].

$$g^{(2)}(\mathbf{q},\tau) = A + B \cdot \left[g^{(1)}(\mathbf{q},\tau)\right]^2 \tag{2.46}$$

A is a baseline factor which should be close to one in an actual experiment, and B is a factor that depends on the experimental geometry, which is usually close to one. In practice, a small noise in the intensity autocorrelation function can enable the value of A to be slightly different from unity ($\sim 10^{-4}$).
A molecule in a dispersion medium will follow a random path described by Brownian motion. The displacement of a molecule, $\mathbf{R}(t)$, in Brownian motion is described by the Gaussian probability function $P(\mathbf{R},t)$,

$$P(\mathbf{R},t) = \left[\frac{2\pi}{3} < \Delta R^2(t) >\right]^{-3/2} \exp\left[-3R^2/2\left\langle \Delta R^2(t)\right\rangle\right]. \tag{2.47}$$

where $< \Delta R^2(t) >$ is the mean square displacement of the particle at time t. The Fourier transform of this function is the intermediate scattering function, or the field correlation function, $g^1(\mathbf{q},\tau)$. This is given by

$$g^{(1)}(\mathbf{q},\tau) = \exp(-q^2\left\langle \Delta R^2(t)\right\rangle/6). \tag{2.48}$$

For a freely moving molecule,

$$\left\langle \Delta R^2(t)\right\rangle = \left\langle {v_p}^2\right\rangle t^2. \tag{2.49}$$

and the field correlation function becomes

$$g^{(1)}(\mathbf{q},\tau) = \exp(-q^2\left\langle {v_p}^2\right\rangle t^2/6), \tag{2.50}$$

where $v_p$ is velocity of the particle. For a diffusing particle,

$$\left\langle \Delta R^2(t)\right\rangle = 6Dt, \tag{2.51}$$

where D is a translational diffusion coefficient. For monodisperse spherical particles in a dilute solution, the normalized field correlation function, therefore, $g^{(1)}(\tau)$, decays exponentially with the relation

$$g^{(1)}(\tau) = \exp(-q^2Dt) = \exp\left(-\left(\frac{\tau}{\tau_D}\right)\right), \tag{2.52}$$

where $\tau_D$ is a characteristic relaxation time. For a diffusive motion, $\frac{1}{\tau_D} = Dq^2$.
The hydrodynamic radius, $R_H$, is obtained by applying the Stokes-Einstein relation,

$$R_H = \frac{K_B T}{6\pi\eta D}. \tag{2.53}$$

$K_B$ is Boltzmann's coefficient, T is the absolute temperature, and $\eta$ is the viscosity of the solvent medium in a dilute solution.
For a polydisperse system, $g^{(1)}(\tau)$ is no longer described by a single exponential, and the distribution of the relaxation time, $G\left(\frac{1}{\tau_D}\right)$, should be taken into account:

$$g^{(1)}(\tau) = \int_0^\infty G\left(\frac{1}{\tau_D}\right) \cdot \exp\left(-\left(\frac{\tau}{\tau_D}\right)\right) d\left(\frac{1}{\tau_D}\right). \tag{2.54}$$

It is not possible to obtain $G\left(\frac{1}{\tau_D}\right)$ directly by mathematical methods, and there are several ways to characterize $G\left(\frac{1}{\tau_D}\right)$ to result in a functional form [24]. A variety of data analysis techniques can be applied to analyze the light scattering data. Among the most common approaches, we introduce a KWW (Kohlrausch-Williams-Watts function) [16, 26, 27] and a method of cumulant proposed by Koppel [28, 29, 30].

The KWW function is an empirical expression to describe the deviation from a single exponential by means of parameter $\beta$, and it is widely used to characterize the relaxation process in various materials, such as polymer, dielectric material studied by means of mechanical and dielectric measurements [16, 26, 27]. The KWW function can also be used to characterize the DLS spectra. $g^{(1)}(\tau)$ adopts a form of a KWW function, as given by

$$g^{(1)}(\tau) = \exp\left(-\left(\frac{\tau}{\tau_D}\right)^{\beta}\right). \tag{2.55}$$

For $0 < \beta \leq 1$, the exponential function becomes stretched, and for $\beta > 1$, it is compressed. The stretched exponential function has practical importance for a colloidal suspension where the stretching arises from the polydispersity of the particles. For a monodisperse system, $\beta$ is close to one, and as a system becomes more polydisperse, $\beta$ deviates from one. The insertion of eq. 2.55 into eq. 2.46 allows us to obtain the normalized intensity autocorrelation function, as given by

$$g^{(2)}(\tau) = A + B \cdot \exp\left(-2\left(\frac{\tau}{\tau_D}\right)^{\beta}\right). \tag{2.56}$$

The mean relaxation time is given by

$$\left\langle \tau_D \right\rangle = \int_0^{\infty} d\tau \cdot \exp\left(-\left(\frac{\tau}{\tau_D}\right)^{\beta}\right) = \frac{\tau_D}{\beta}\Gamma\left(\frac{1}{\beta}\right), \tag{2.57}$$

with $\Gamma$ denoting the Gamma function. Clearly seen is that, for $\beta = 1$, $\left\langle \tau_D \right\rangle = \tau_D$. In this case, the single exponential function is recovered. In practice, the mean relaxation time is used to obtain the mean hydrodynamic radius.

For the cumulant method, the moment generating function is used to generate the cumulants to describe $g^{(1)}(\tau)$ [30]. It is given by [30]

$$g^{(1)}(\tau) = \exp\left(-\overline{\Gamma_D}\tau\right) \cdot \int_0^{\infty} G(\Gamma_D) \exp[-(\Gamma_D - \overline{\Gamma_D})\tau] d(\Gamma_D). \tag{2.58}$$

$\Gamma_D$ represents the relaxation rate, the inverse of $\tau_D$, $\Gamma_D = \frac{1}{\tau_D}$. Considering a Taylor expansion of the exponential function, the following function can be obtained [30]

$$g^{(1)}(\tau) = \exp\left(-\overline{\Gamma_D}\tau\right) \cdot \left(1 + \frac{\mu_2}{2!}\tau^2 - \frac{\mu_3}{3!}\tau^3 + \ldots\right), \tag{2.59}$$

where $\mu_m$ is the moment about the mean value, given by [30]:

$$\mu_m = \int_0^{\infty} G\left(\Gamma_D\right)\left(\Gamma_D - \overline{\Gamma_D}\right)^m d(\Gamma_D). \tag{2.60}$$

$$\overline{\Gamma_D} = \int_0^\infty G\left(\Gamma_D\right) \cdot \Gamma_D d(\Gamma_D), \tag{2.61}$$

$$\mu_2 = \int_0^\infty G\left(\Gamma_D\right)\left(\Gamma_D - \overline{\Gamma_D}\right)^2 d\Gamma_D = \overline{\left(\Gamma_D - \overline{\Gamma_D}\right)^2} \tag{2.62}$$

The expression for the intensity autocorrelation function is obtained by applying the Siegert relation as follows [30]:

$$g^{(2)}(\tau) = A + B\exp\left(-2\overline{\Gamma_D}\tau\right) \cdot \left(1 + \frac{\mu_2}{2!}\tau^2 - \frac{\mu_3}{3!}\tau^3 + \ldots\right)^2. \tag{2.63}$$

Cumulant expansion is widely used for colloidal particle systems in suspension. “Second order” cumulant expansion is often used for DLS data analysis, as a variance of $\mu_m(\mu > 2)$ usually does not result in enhanced fit quality.
Another widely used parameter in practice with respect to cumulant analysis is the polydispersity index (PDI), defined as the second moment divided by the square of the average relaxation rate, as given by

$$\mathrm{PDI} = \frac{\mu_2}{\overline{\Gamma_D}^2} = \frac{\overline{\Gamma_D{}^2} - \overline{\Gamma_D}^2}{\overline{\Gamma_D}^2}. \tag{2.64}$$

This indicates that, PDI is defined as the square of the normalized standard deviation of the relaxation rate. This can provide a measure for the size distribution of the particles.

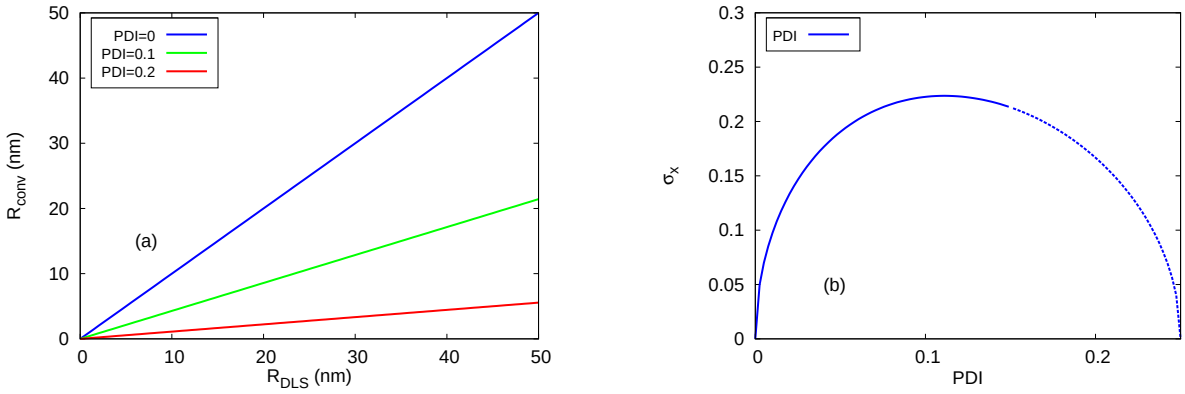


**Figure 2.6.:** Graphical presentation of eq. 2.65. In (a) converted radius is presented as a function of the radius obtained by DLS, the hydrodynamic radius, for different PDI values, and in (b) polydispersity of the size of the radius obtained, $\sigma_x$, is presented as a function of PDI values. It is noted that the converted radius deviates from the hydrodynamic radius for large PDI values as shown in (a) and a convex function to relate $\sigma_x$ and PDI shown in (b) has a maximum located at PDI $\approx 0.1$. In (b), the dotted line at PDI>0.15, indicates that the physical interpretation of $\sigma_x$ above PDI>0.15 can carry a large error (see text for details).

We now turn to the topic of the conversion of the radius obtained by DLS to that obtained by static measurements such as TEM, SANS, and SAXS. As will be discussed later, for the analysis of the static scattering measurements such as SANS and SAXS, we use a Schulz function to determine the size distribution of the radius, which is averaged with respect to the number of particles per volume. Hanus

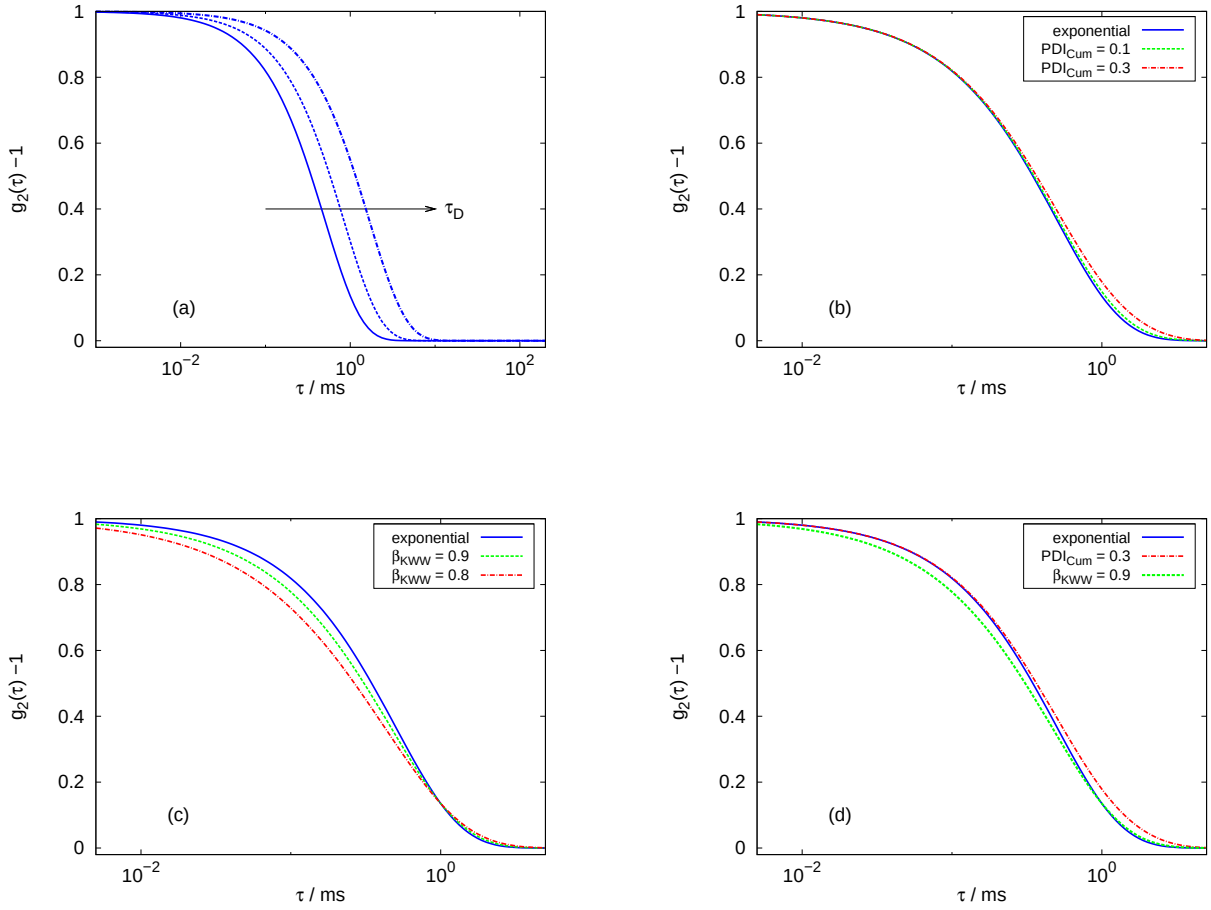


**Figure 2.7.:** Calculated results for (a): variation of the normalized intensity autocorrelation function with increasing characteristic relaxation time (arrow indicates increase of the time scale, slow dynamics). (b): variation of the correlation function generated by the cumulant function with increasing PDI index. (c): variation of the correlation function generated by KWW with decreasing $\beta$. (d) Comparison of both functions at specific values demonstrates the different behaviors of the stretching. For calculating the functions, the value of A was set to be 0 and that of B, to be 1, for all cases. The values inserted for the calculations are displayed in the legend in each figure. The exponential shown in the legend represents a single exponential, $\exp(-\tau/\tau_D)$.

et al. [31, 32] derived formulas to convert the intensity averaged quantities of the radius and the PDI obtained from cumlant analysis of DLS data to the number weighted mean and variance of the spherical particles of the assumed particle size distribution functions. The calculation was made at the limit of small particles or a small scattering angle $\theta$ (i.e. Rayleigh approximation). The mean radius ($R_{\text{conv}}$) and its standard deviation ($\sigma_x = \frac{\sqrt{\overline{R_{conv}}^2 - \overline{R_{conv}}^2}}{\overline{R}}$) can be extracted from the quantities of $R_h$ and PDI obtained by the cumulant analysis of DLS data.
The following relations for the Schulz size distribution function hold, as introduced by Thomas [31, 32]:

$$\overline{R_{conv}} = \overline{R_{\text{DLS}}}\left(\frac{1-4\cdot\text{PDI}}{1+4\cdot\text{PDI}}\right) \text{ and } \sigma_x = \frac{\sqrt{\text{PDI}\cdot(1-4\cdot\text{PDI})}}{1+\text{PDI}}. \tag{2.65}$$

According to Hanus et al. [32], the radius extracted from the above expression from intensity averaged DLS data can be compared with that from transmission electron microscopy (TEM) measurement.

The authors found that, for PDI $< 15\%$, the number averaged radius, $\overline{R_{conv}}$, obtained from the above equation, shows good agreement with the radius $R_{TEM}$ from a TEM measurement when additionally the "correction heuristics " is used (for the Schulz-Zimm distribution function, PDI/2.071). Additional heuristics was "empirically" applied to reduce the difference between $R_{TEM}$ and $\overline{R_{conv}}$. This conversion formula essentially allows DLS and other static scattering measures of size and its distribution to be compared directly and to result in a universal average unit. However, it should be noted that, for a large PDI value close to $\sim$15%, the author found the deviation between the converted size and its distribution from DLS data and those quantities from TEM data. In addition, the assumption made for the conversion formula was that the particles are at the Rayleigh limit. In reality, if the particles are not at the Rayleigh limit but above it, a scattering angle dependent form factor should be introduced. However, application of the form factor did deviate more than the correction made formula at the Rayleigh limit. This indicates that the conversion formula can be better estimated at the Rayleigh limit. In chapter 5, where the experimental results from DLS, SANS, and SAXS are compared, the radii obtained from DLS data will be converted using eq. 2.65 and the converted radii $R_{conv}$ will be compared with radii from SAXS or SANS to see whether eq. 2.65 is valid, and furthermore, the radii from each measurement can be closely approximated.

Finally, concerning the DLS data analysis methods, the intensity autocorrelation functions will be calculated by means of the KWW function and the cumulant function. This part was intended to show how variation in PDI index and $\beta$ affects the intensity autocorrelation functions. Figure 2.7 shows the calculated intensity autocorrelation functions using the cumulant (b) and KWW function (c), to see the effect of the PDI index (b) and $\beta$ (c) on the change in the correlation function. Figure 2.7 demonstrates that the PDI index from the cumulant and $\beta$ from KWW contribute to the stretching of the correlation function in a different way. A large PDI value contributes to the stretching of the correlation curve only at a large time scale, whereas a smaller $\beta$ contributes to its stretching overall. The comparison shown in Figure 2.7 (d) shows this difference clearly.

To summarize, the theoretical background of the DLS experiment has been described, and the functions to analyze the DLS data have been introduced and calculated. As will be shown in chapter 5, the experimental DLS data, with the form of the intensity autocorrelation function, will be analyzed mainly by a cumulant expansion method. For each $q$, we use equation $\overline{\Gamma} = Dq^2$ for a diffusive motion. If the results show a diffusive motion, diffusion coefficient $D$ can be obtained. The hydrodynamic radius will be then obtained by applying the Stokes-Einstein relation given in eq. 2.53. Along with the determination of $R_h$, PDI values obtained from a cumulant method will be used to obtain $R_{\text{conv}}$ from $R_h$ using eq. 2.65 to compare $R_{\text{conv}}$ with the size obtained from static scattering measurements from SANS or SAXS. The use of the cumulant method was therefore intended to obtain $R_h$ as well as PDI, which can relate $R_h$ with the size obtained from the static scattering methods. In chapter 5, the spherical particles suspended in solution will be used for the characterization. Thereby, different experimental methods of SANS, SAXS, and DLS will be used to compare the sizes obtained by each method. The size extracted from the analysis of DLS experiments will be shown and compared with that obtained from static scattering methods, SANS and SAXS. The converted size from the DLS results, $R_{\text{conv}}$, will also be shown to judge whether eq. 2.65 is valid, moreover, it can be applied to approximate the size obtained from static scattering methods. This will be dealt with as another important issue in chapter 5.

### 2.3.2 Experimental technique, DLS

DLS measurements were performed with a home-built set-up shown in Figure 2.8. A He-Ne laser (wavelength $\lambda$=632.8 nm) was used as a light source and the scattering angles ($2\theta$) could be varied from 30° to 160°. The intensity of the incident beam could be varied with an attenuator to minimize the damage to the detector, and the highest threshold of the intensity in a unit of kHz was set at 150kHz. The polarization of the incident and scattered beam was defined with a polarizer and analyzer with a

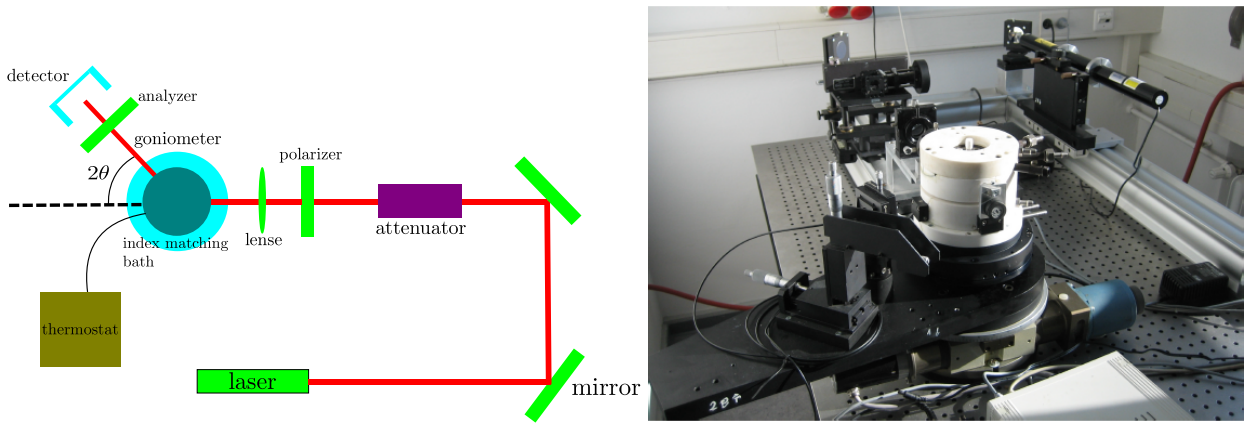


**Figure 2.8.:** Left: schematic illustration of DLS setup, right: photo of DLS setup taken from [33]

Glan-Thomson prism. Most of the experiments were performed in vertical-vertical geometry, where the polarization of both the incident and the scattered beam are defined by vertical geometry with respect to the scattering plane. Samples are placed into a cylindrical glass cuvette (Hellma) with a 10 mm diameter. Before being placed into the sample holder, samples were filtered to avoid enormous scattering from dust and other contaminants. They are filtered depending on the chemical property of the suspension, either hydrophobic or hydrophilic, with a typical pore size of 0.2 $\mu$m in diameter. The glass cuvette is then immersed in a temperature controlled index matching bath for the measurement where the temperature can be varied from 10°C to 80°C. Temperature control was performed using a Haake C25p thermostat where the liquid to be used to vary the temperature was a mixture of water and glycol. The temperature deviation was found to be ±0.2 to 0.3°C which was measured by comparing the values of the temperature inside the index matching bath and the temperature of the sample. For temperature controlled measurements, in order to maintain a stabilized temperature for the samples inside the goniometer, each measurement was done ≈ 30 minutes after inserting the samples into the goniometer.
Silicon oil was used for the index matching material and provided by Wacker Chemie AG (product name: AK 100), and it had refractive index of 1.403 at 632.8 nm [34]. Use of the index matching material was intended to avoid reflection from the surface of the glass cuvette and therefore to establish a homodyne condition instead of the heterodyne condition for the scattering experiment. It is therefore appropriate to choose silicon oil for the index matching material since it has a value close to the refractive index of a Hellma cuvette made from Suprasil quarz glass whose refractive index is 1.457 at 632.8 nm [35].
The scattered intensity was then detected with an optical fiber coupled to the two-photomultiplier tubes, where the DC output is proportional to the intensity. In this way, the background could be minimized using the cross-correlated signal from two photo tubes. The normalized intensity autocorrelation function, $g^{(2)}(q,\tau)$ -1, is calculated with an ALV 5000 autocorrelator for each scattering angle, where $q$ is the modulus of a scattering vector defined previously. For experiments with each particle system, a series of concentrations was prepared, and the correlation function was measured in a range of scattering angles $2\theta$ from 50° to 130°. The range of the scattering angles were chosen to minimize possible reflection from the glass cuvette. The correlation functions for each angle were analyzed by the cumulant expansion, shown in eq. 2.63. For each concentration, we could determine an effective hydrodynamic radius and extrapolate to zero concentration. These results will be shown in chapter 5. The concentration dependent measurements were aimed to obtain the diffusion coefficient of a single particle $D^0$. In the presence of intermolecular interactions, when the concentration is not zero, the diffusion coefficient at a certain concentration $D$ is given by [24]:

$$D = D^0(1 + K_d c), \tag{2.66}$$

where $K_d$ is a coefficient to represent the overall intermolecular interactions and c is a concentration. We note that, however, in chapter 5, $R_h$ instead of $D$ will be shown as a function of concentrations, which are correlated with respect to the Stokes-Einstein relation shown in eq. 2.53. The experimental setup and its schematic illustration are shown in Fig. 2.8.

# 3 Polymer brush

Polymer chains attached to a solid substrate may show different conformations from those of free polymer chains in the bulk state. Their physical properties also may differ from what is usually observed. The key parameter to determine the conformation of the polymer chains on the surface is the density of the attached chains on the surface, the grafting density. The polymer is expected to be stretched away from the surface when the grafting density is relatively high. Then the structure is called a "polymer brush" , which can be used for a wide variety of applications. Even though many research works have been conducted, the fundamental questions such as, "What is the threshold value of the grafting density at which the conformation of the polymer chains becomes brush like? ", or "Does the conformation of the grafted polymer chains on a curved substrate have the same conformation as that on a planar substrate?" seem not to be properly answered. Before we begin to answer this question, the basic properties of free polymer chains in the bulk state will be briefly described, while the physics of the polymer brush will be described in a subsequent section.

## 3.1 Polymer basics [1, 36]

A polymer is a macromolecule comprising many elementary repeating units: monomer. N is the polymerization index, which is simply the number of monomers in a polymer. Other relevant parameters to characterize polymers are the size of the monomer and the distance between two neighboring monomers. The end-to-end distance is one of the characteristic length scales to determine the size of a polymer. Consider a flexible polymer of N+1 backbone atoms $A_i$ with $(0 \leq i \leq N)$. When the bond vector $\overrightarrow{r_i}$ with $1 \leq i \leq N$ is the vector going from $i-1^{th}$ to $i^{th}$ backbone, then the end-to-end vector is given by

$$\overrightarrow{R_N} = \sum_{i=1}^{N} \overrightarrow{r_i} \tag{3.1}$$

The ensemble averaged end-to-end vector becomes 0 for an isotropic construction of chains. The simplest non-zero averaged value is the mean squared end-to-end distance:

$$\begin{aligned} < R^2 > = < \overrightarrow{R_N}^2 > &= \left\langle \left( \sum_{i=1}^{N} \overrightarrow{r_i} \right) \cdot \left( \sum_{j=1}^{N} \overrightarrow{r_j} \right) \right\rangle \\ &= \sum_{i=1}^{N} \sum_{j=1}^{N} < \overrightarrow{r_i} \cdot \overrightarrow{r_j} > . \end{aligned} \tag{3.2}$$

If all bond lengths have the identical lengths $l = |\overrightarrow{r_i}|$, the scalar product shown in above equation can be expressed by an angle between two neighboring bond vectors, $\theta_{ij}$:

$$\overrightarrow{r_i} \cdot \overrightarrow{r_j} = l^2 \cos\theta_{ij}. \tag{3.3}$$

For an ideal polymer, where no interaction of monomer units is assumed, the freely jointed chain model is the simplest to describe the correlation of monomers. In this simple model, no correlation is assumed. Therefore,

$$\begin{aligned} &< \cos\theta_{ij} > = 0 \text{ for } i \neq j \\ &< \cos\theta_{ij} > = 1 \text{ for } i = j \end{aligned} \tag{3.4}$$

The summation in eq. 3.2 then becomes

$$< R^2 >= Nl^2 \tag{3.5}$$

If the end-to-end distance is intended to be expressed more realistically, it can often be expressed by the Kuhn length [23], assuming that there are $N_{\text{kuhn}}$ subchains of length b instead of N subchains of length l. The Kuhn length, b, is the segment length of a polymer considering the flexibility of the real polymer chain. It tends to be larger as the polymer becomes stiffer. Therefore, the polymer is considered to be a connected sequence of identical segments rather than a sequence of monomers. It is indeed useful to introduce the Kuhn length to discuss the property of a real polymer. For that case, the end-to-end distance becomes

$$< R^2 >= N_{\text{kuhn}} b^2 \tag{3.6}$$

Another important size is the radius of gyration, $R_g$. For the case of a linear chain, the size can be characterized by the mean squared end-to-end distance. However, for the case of a ring polymer or a branched polymer, the end-to-end distance can not be used, as there are different chain ends or the chain ends do not exist at all. Therefore, another size scale should be introduced instead of end-to-end distance. A radius of gyration introduced here can characterize the size of the polymers of any architecture. The linear polymer chain is illustrated in Figure 3.1.

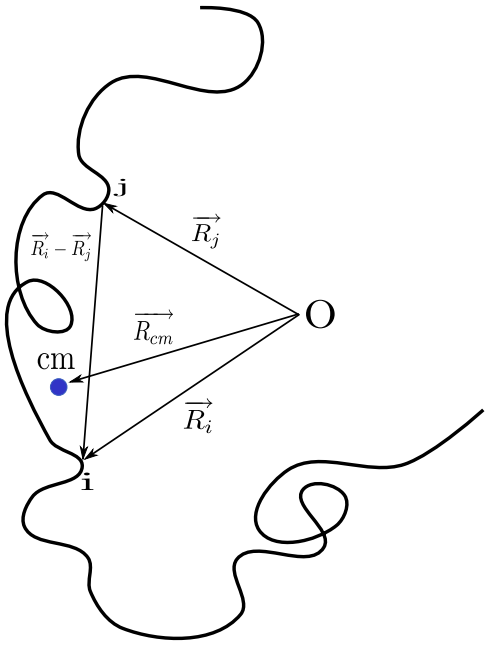


**Figure 3.1.:** Schematic illustration of a linear polymer chain with a random coil conformation. Its center of mass is denoted by cm [36].

The square radius of gyration is defined as the average square distance between monomers at a given position ($\overrightarrow{R_i}$) and the polymer's center of mass (position vector $\overrightarrow{R_{cm}}$):

$${R_g}^2 = \frac{1}{N}\sum_{j=1}^{N}(\overrightarrow{R_i} - \overrightarrow{R_{cm}})^2. \tag{3.7}$$

The position vector of center of mass is given by

$$\overrightarrow{R_{cm}} = \frac{1}{N}\sum_{i=1}^{N}\overrightarrow{R_j}. \tag{3.8}$$

The squared radius of gyration then takes the form of

$$< {R_g}^2 >= \frac{1}{N}\sum_{i=1}^{N} < (\overrightarrow{R_i} - \overrightarrow{R_{cm}})^2 >= \frac{1}{N^2}\sum_{i=1}^{N}\sum_{j=1}^{N} < (\overrightarrow{R_i} - \overrightarrow{R_j})^2 > . \tag{3.9}$$

where <...> denotes the ensemble average over allowed conformations of a polymer. For instance, the radius of gyration of an ideal linear chain is given by,

$$< {R_g}^2 >= \frac{b^2 N_{\text{kuhn}}}{6} = \frac{< R^2 >}{6}. \tag{3.10}$$

So far, the basic length scale for polymers is discussed based on the ideal chain conformation. For the ideal chain conformation, monomer-monomer and monomer-solvent interaction are not considered. However, in real chain conditions, the interaction between monomer and monomer and monomer and solvent should be taken into account. Monomer-monomer interaction is attractive at a large distance and is repulsive at a short distance, as expected from Leonard Jones' potential. The consideration of these interactions leads to the different scaling behavior between end-to-end distance and molecular weights, as given by

$$R \cong b N_{\text{kuhn}}^{\nu} \tag{3.11}$$

$\nu$ is called the Flory exponent to characterize the swelling of a chain in various conditions. In the ideal chain condition, no interaction is assumed. This situation is realized when monomer-monomer attraction cancels steric repulsion. This occurs due to the fact that a monomer can not penetrate another monomer. In this case, the Flory parameter is $\nu = \frac{1}{2}$ as shown in eq. 3.6. In a good solvent condition, monomer-solvent attraction is more favorable than monomer-monomer attraction, indicating that each monomer avoids each other, leading to a swollen configuration. In this case, the Flory parameter becomes $\nu = \frac{3}{5}$. The end-to-end distance for this case is called Flory's radius, as given by

$$R_F \sim b {N_{\text{kuhn}}}^{\frac{3}{5}} \tag{3.12}$$

The physical reason for the swelling of polymer chains in a good solvent is entropy balance between monomer-solvent interaction and the conformation of a polymer chain. As the polymer chains swell, the entropy decreases, so the polymer chain can not have maximum extension and should be balanced by a monomer-solvent interaction term. The last condition to be considered is the poor solvent condition. In this condition, the monomer-monomer attraction is stronger than the steric repulsion, resulting in collapsed conformation of a single chain. In this case, the Flory exponent becomes $\nu = \frac{1}{3}$.

## 3.2 Polymer brush [1, 37, 38]

A polymer brush is the array of polymer chains attached to the substrate with high coverage so that the polymer chains are stretched away from the surface to avoid overlapping with neighbouring chains. The behavior of the polymer chains tethered to the surface is different from that of the free polymer chains or bulk polymer in good solvents in that the chains adopt a stretched conformation instead of a random walk conformation, as will be described subsequently. People find a wide variety of applications, such as the stabilization of particles in solution or that of the surface of a planar substrate by tuning the density of the attached chains [1, 37, 38]. This stabilization of the particles or the surface is usually performed by modulating the density of the attached chains. Therefore, the density of the attached chains, so called, grafting density, is one of the most important parameters to determine the chain conformation. This point will be addressed later in detail. The usual circumstances in which a polymer brush is discussed involve good solvent conditions. This indicates that the other reason for chain stretching is the affinity of the polymer chains for the solvent.
When it comes to a polymer brush on a planar surface, polymer chains are expected to show a transition of the conformation from "mushroom" to "brush"[39, 40] with increasing grafting density. For the mushroom conformation, the conformation of the polymer chains adopts that of free polymer chains, and the average height of the polymer chains is $h \sim 2R_g$ [39, 40]. This crossover occurs when the chains begin to overlap at a grafting density, $\sigma^*$. $\sigma$ is a measure of the density of chains, that is, the number of chains per unit area. After reaching this critical value of the grafting density, the chains try to avoid the overlapping and show the stretched conformation. This is illustrated in Figure 3.2. In Fig. 3.2 (a), the mushroom conformations are shown, and the chains are well separated. At a high grafting density, on the other hand, the polymer brush shows a highly stretched conformation, and the distance between chains is small compared to the unperturbed coil size. The crossover for the polymer brush on the planar substrate is known to occur at a grafting density $\sigma^* \sim a^{-2}N^{-\frac{6}{5}}$, where N is the polymerization index as introduced previously, and a is the monomer size. The polymer brush then adopts a highly stretched conformation, exceeding the size of the unperturbed coil size, $h \sim 2R_g$.
The physical properties of the polymer brush of main concern are the scaling law between the molecular weight and the average height and the segment density or the volume fraction profile of the polymer brush. This section will be structured as follows. First, the polymer brush on the planar substrate will be described from both experimental and theoretical points of view, and the same information for the polymer brush on a curved substrate will be described subsequently. The theoretical background of the polymer brush will be briefly described, and the corresponding experimental outcomes will be described. The following description will be limited to the case of neutral grafted polymers.

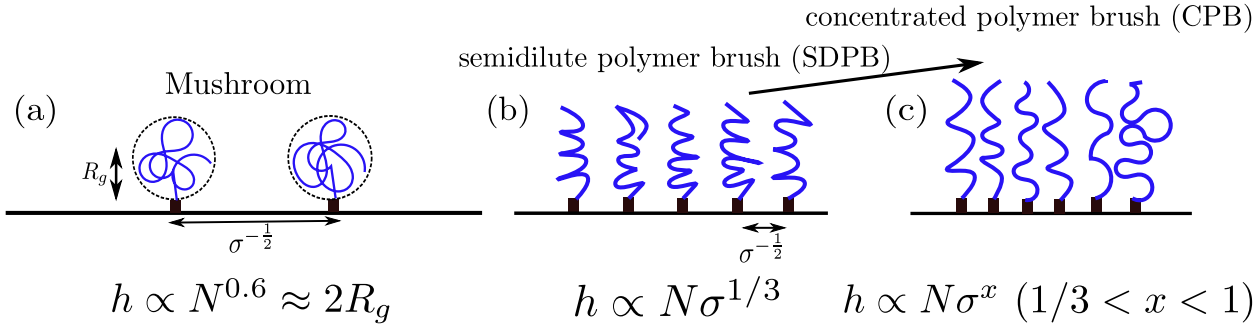


**Figure 3.2.:** (a):Mushroom regime, distance between two attached polymer chains is larger than $2R_g$ (unperturbed coil size). (b) and (c): Brush regimes; distance between them is smaller than the unperturbed coil size, and chains show a stretched conformation to avoid overlapping [1, 8].

### 3.2.1 Polymer brush in a good solvent [37]

High stretching of a polymer brush on a planar substrate under good solvent conditions, can be understood theoretically by free energy balance, which is based on Flory's argument (see also the end of section 3.1). As introduced previously, polymer chains in the bulk state have a favorable interaction with solvent molecules, while they tend to maximize the configurational entropy by adopting a random walk conformation. In the bulk state, the entropy balance between the configuration of the chains and the affinity of the chains for the solvent molecules is the physical reason for the polymer chains to adopt the swollen state. In the brush state, where the polymer chains are located at a close distance, the overlapping of chains occurs, which is energetically unfavorable. Then the polymer chains adopt a stretched conformation as an outcome of the balance of the entropy gain due to the repulsive interaction between neighbouring brush chains and entropy loss due to the chain stretching. In other words, the chains respond by choosing the chain conformation by minimizing the entropy cost. The entropy loss due to the chain stretching is proportional to $h^2/b^2$ per chain, where b is the Kuhn length of the polymer, and that due to chain overlapping is proportional to the monomer density, $\frac{\sigma N}{h}$, where h is the average height of the polymer brush and $\sigma$ is the grafting density in a unit of chains per unit area. Then, the free energy cost is [37],

$$\Delta F \sim K_B T \left[ \frac{3h^2}{2Nb^2} + \nu^* N \left( \frac{\sigma N}{h} \right) \right]. \tag{3.13}$$

$\nu^*$ is the excluded volume parameter to characterize the repulsion of chain units, and $K_B$ is the Boltzmann constant. Then, the minimization of eq. 3.13 leads to the average height of the brush on the planar substrate as given by [37]:

$$h \sim N(\nu^* \sigma b^2)^{\frac{1}{3}}, F \sim K_B T N(\nu^* \sigma b^{-1})^{\frac{2}{3}}. \tag{3.14}$$

This is a rather striking result in that, at a constant grafting density, the average height scales linearly with the polymerization index, N, unlike the polymer chains in the bulk state, $R \propto N^{\frac{3}{5}}$. This represents the high stretching of the chains compared to those in the bulk state. This simple theoretical consideration was confirmed by experimental observations [39, 40]. The average height of the polymer brush on a planar substrate was found to show a transition of the scaling law depending on the variation in the grafting density. At a low grafting density, where chains are not overlapped, the average height is scaled as $h \sim N^{\frac{3}{5}}$. At a grafting density above the threshold, where chains are starting to overlap, the average height is scaled as $h \sim N\sigma^{\frac{1}{3}}$. It should be noted that, for monomer density calculation, the equally distanced chain ends were assumed, leading to the step like density profile for a simplification. However, the application of more advanced density profiles of a parabolic type did not lead to different results for the scaling of thickness, as will be shown subsequently.
This scaling law is valid until the intermediate grafting density, where interaction between the chains is pairwise (semidilute polymer brush regime, SDPB). At even higher grafting densities, where higher orders of interaction become important (concentrated polymer brush regime, CPB), the scaling of the brush height becomes [8, 41]

$$h \propto N\sigma^x \quad (1/3 < x < 1). \tag{3.15}$$

The equation indicates that, in the CPB regime, the exponent of the grafting density varies from 1/3 to 1 as the grafting density increases. When the grafting density approaches the highest coverage limit, where the grafted chains are fully stretched, the brush height may no longer depend on the grafting density and retain the saturated value [41]. The scaling behavior of the brush height is summarized in Figure 3.2.

A polymer brush on a curved substrate is expected to show similar behavior as a polymer brush on a planar substrate [8]. The transition from mushroom throughout SDPB to CPB is also expected. The salient difference in the conformation of the polymer brush on the curved substrate arises from the curvature. Due to the curvature of the substrate, the conformation of the polymer brush on the curved substrate at a rather small curvature is expected to be similar to that on a planar substrate. On the other hand, at a large curvature, the conformation of the polymer brush is treated in analogy with the conformation of a star polymer. The latter approach was first introduced by Daoud and Cotton [42]. This model assumes that all chains are bonded to a central point and that the chain ends are stretched away from the core to an identical distance. The schematic illustration is shown in Fig. 3.3. Every branch of the star polymer in a solvent is assumed to consist of a succession of blobs extending from the core to the media. A blob is a sphere containing parts of polymer chains away from the core at a distance r. The size of each blob at a given distance r is assumed to be identical in size, $\xi(r)$, and the swelling parameter of each blob is denoted by $\alpha(r)$. For an important hypothesis, they assumed that $\alpha(r)$ decreases as distance decreases, representing unswelling at a distance close to the core and swelling at a distance far away from the core. This $\alpha(r)$ is defined simply by

$$\alpha(r) = \frac{\xi(r)}{\xi_0(r)}, \tag{3.16}$$

where $\xi_0(r)$ is the unperturbed size of the blob at a distance r. The dimensionless volume fraction profile of the polymer segments for each region is given by

$$\phi(r) = \begin{cases} 1 & (r < R_c \sim f^{\frac{1}{2}} b) \\ \left(\frac{r}{b}\right)^{-1} f^{\frac{1}{2}} & (R_c < r < R_1 \sim f^{\frac{1}{2}} \nu^{*-1} b) \\ \left(\frac{r}{b}\right)^{-\frac{4}{3}} \nu^{*-\frac{1}{3}} f^{\frac{2}{3}} & (r > R_1) \end{cases} \tag{3.17}$$

$b$ is a segment length, $f$ is the number of arms of a star polymer, and $\nu^*$ is an excluded volume parameter. $R_c$ is a core radius and $R_1$ is a radial distance away from the center of a star polymer where swelling occurs. In Figure 3.3, a volume fraction profile and the schematic illustration of the blob picture are shown. For a clear understanding, each parameter will be chosen to have a finite number, and these parameters are given in the caption of Figure 3.3 (b).
The volume fraction profile is directly related to the brush height $h$ for each region considered above. They are [42, 43]

$$h \sim {N_{\text{kuhn}}}^{1/2} f^{1/4} b \quad \text{for the unswollen region ,} \tag{3.18}$$

and

$$h \sim {N_{\text{kuhn}}}^{3/5} \nu^{*\frac{1}{5}} f^{1/5} b \quad \text{for the swollen region .} \tag{3.19}$$

More generally, if the volume fraction profile is of the form $r^{-\alpha}$ [42, 43] for a fixed chain length, the brush height scales as,

$$h \propto f^{(2-\alpha)/2(3-\alpha)} \tag{3.20}$$

The volume fraction profile introduced by Daoud and Cotton, has motivated many researches on the investigation of the conformation of the grafted polymer chains on the surface of nanoparticles. SANS is one of the most powerful tools to investigate the concentration profile of a brush layer on a nanoparticle surface. Förster et al. [43] made use of the hyperbolic profile in a form of $r^{-\alpha}$ shown in eq. 3.17 to model

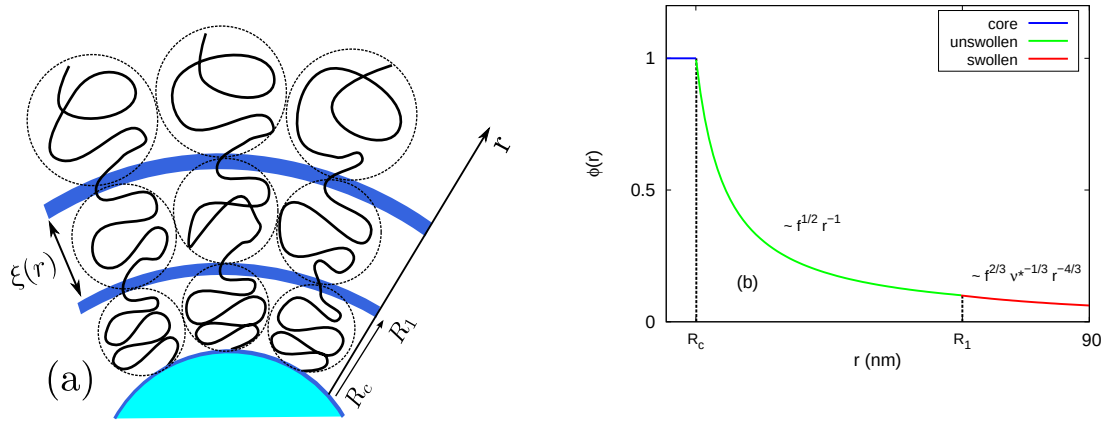


**Figure 3.3.:** (a): Schematic illustration of blob picture introduced by Daoud and Cotton [42]. (b): The volume fraction profile [42]. For the volume fraction profile, three regions appear. In the core ($r < R_c \sim f^{\frac{1}{2}} b$), the volume fraction is constant. In the intermediate region ($R_c < r < R_1 \sim f^{\frac{1}{2}} \nu^{*-1} b$), the chains are not swollen and the concentration of each blob is relatively high. In the outside region ($r > R_1$), the chains are swollen and the excluded volume effect is present. To generate the volume fraction profile shown in (b), f=10, b=2nm, and $\nu^*$=0.1 were used. b was for PS in a good solvent and set to be 2 nm [44]. Values of $R_c$= 6.3 nm, $R_1$=63.2 nm could be obtained using the relations $R_c = f^{\frac{1}{2}} b$ and $R_1 = f^{\frac{1}{2}}$. Note that, unlike the original expression in eq. 3.17, equality was considered for obtaining those parameters. Each volume fraction profile in three regions was calculated using eq. 3.17 considering equality for each region and was not scaled.

the form factor of a spherical polymer brush to analyze the experimental data from spherical micelles in a good solvent. Spherical micelles are formed from the asymmetric block copolymers $A_l B_{1-l}$ with $l << 1$ in a selective solvent, which is bad for the A block and good for the B block. The A monomers form a dense core, and the A-B interface can be well approximated as a spherical shape onto which B block polymers form a corona. The form factor consisting of a dense core and a corona was successfully modeled by the hyperbolic density profile for the corona with a solid core with homogeneous density. Förster et al. [43] found the general relation between $h$ and f with a fixed $N_{\text{kuhn}}$, shown in eq. 3.20 for their system investigated by SANS.

### Curvature dependence of the brush conformation [45]

The scaling law and the segment density profile for a polymer brush on a curved substrate have been intensively studied, especially by simulations. As an extension of the study from Daoud and Cotton, Wijmann and Zhulina [45] used a self consistent field (SCF) lattice model to investigate the effect of the curvature of the surface of a curved substrate on the density profile of the segments and free end chains of the polymer immersed in various qualities of solvents. The following statements for the polymer brush will be restricted to the case of a spherical surface. According to their results, at a small curvature, large radius, the scaling law and volume fraction profile are similar to those of a polymer brush on a planar substrate and at a large curvature, on the other hand, these properties are similar to the case of the star polymer.

### Large curvature

The volume fraction profile for a polymer brush at a large curvature under good solvent conditions is given by [45]

$$\phi(r) = \left(\frac{3\sigma^2}{4\nu^*}\right)^{\frac{1}{3}} \left(\frac{R_c}{r}\right)^{\frac{(2d-2)}{3}}. \tag{3.21}$$

$R_c$ is a core radius, $\sigma$ is the grafting density, and $\nu^*$ is the excluded volume parameter and the second virial coefficient (within the Flory theory, $\nu^* = 1/2 - \chi$). The dimensionality parameter $d$ is determined by the geometry, which is given by 1,2, and 3 for planar, cylindrical, and spherical surfaces. As introduced at the beginning of this section, the average brush height is obtained by the minimization of the free energy contribution from the elastic chain stretching and the repulsive interaction between chains attached to the surface driven by chain overlapping and the affinity of the chains for the solvent molecules. This minimization leads to the scaling law for the brush height, as given by [45]

$$h \sim \left(N^3 {R_c}^{d-1} \sigma \nu^*\right)^{\frac{1}{(d+2)}} \tag{3.22}$$

Here, N is a degree of polymerization. In a $\Theta$ solvent case, the volume fraction profile is given by [45]

$$\phi(r) = \left(\frac{\sigma^2}{2w}\right)^{1/4} \left(\frac{R_c}{r}\right)^{\frac{(2d-2)}{4}}, \tag{3.23}$$

where $w$ is the third virial coefficient to characterize the free energy of the system (within the Flory theory, $w = 1/6$). Here, it is noteworthy that the volume fraction profile for the case of the good solvent shown in eq. 3.21 is consistent with that obtained from Daoud and Cotton in the swelling regime, as introduced in eq. 3.17. As a last case, in a bad solvent case, the volume fraction profile becomes constant, representing the collapsed conformation of the polymer. The volume fraction profile for this case is given by [45]

$$\phi(r) = \frac{|\nu^*|}{2w} \tag{3.24}$$

**Small curvature**

For a small curvature, as discussed previously, the density profile of the polymer segments and the scaling law are similar to those on a planar substrate. The volume fraction profile is a parabolic type, given by [45]

$$\phi(r) = \frac{3\sigma N a^3}{H_0} \left(\frac{h}{H_0}\right)^2 \left(1 - \left(\frac{r - R_c}{h}\right)^2\right) \tag{3.25}$$

Here, a is the monomer length. The brush height on a planar substrate $H_0$ has been derived with a similar form using eq. 3.14 [45]

$$H_0 = \left(\frac{8}{\pi^2}\right)^{1/3} aN \nu^{*1/3} (a^2\sigma)^{1/3} \tag{3.26}$$

The brush height at a given curvature is obtained by considering the relative curvature, which is the ratio of the radius of the curvature of the surface to the brush height, $R_c/h$. In a good solvent condition, the following equation determines the brush height at a given curvature value, $R_c/h$ [45].

$$\left(\frac{h}{H_0}\right)^3 \left(1 + \frac{3}{4} \cdot \frac{h}{R_c} + \frac{1}{5} \cdot \left(\frac{h}{R_c}\right)^2\right) = 1 \tag{3.27}$$

Figure 3.4 shows the volume fraction profile $\phi(r)$ to clarify the effect of the curvature and excluded volume parameter $\nu^*$ on the brush height. Eq. 3.25 is used to generate the volume fraction profile. It is clear that grafted chains are more stretched as $\nu^*$ increases since an increase in $\nu^*$ corresponds to that of the solvent quality and excluded volume interaction. As for the effect of the curvature, as the curvature increases, the conformation freedom of the free ends of the grafted chains will increase, thus leading to the relaxation of the stretched conformation of the grafted chains. The following plots show the effect of the curvature and $\nu^*$ for realistic sets of parameters. The parameters are given in the caption together with a detailed description of the plots.

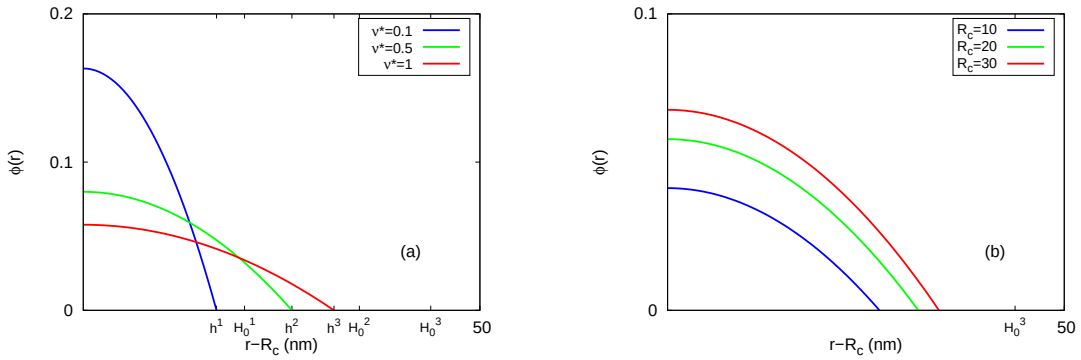


**Figure 3.4.:** The volume fraction profile generated from eq. 3.25 as a function of r to see the effect of $\nu^*$ (a) and $R_c$ (b). For both plots, $\sigma$ and N are set to be 0.1 chains/nm$^2$ and 1000. Length of a styrene monomer, named a, was set to be 0.253nm [46]. For the plots in (a), the values of $\nu^*$ are set to be 0.1, 0.5, and 1 to see the effect of the excluded volume parameter on the volume fraction profile and the radial extension of the brush height at a fixed radius, $R_c = 20$ nm. For the plots in (b), the values of $R_c$ are set to be 10, 20, and 30 nm to see the effect of variation in $R_c$. $\nu^*$ is fixed at 0.1. In (a) ${H_0}^1$, ${H_0}^2$, and ${H_0}^3$ are the brush heights on the planar substrate given by eq. 3.26 for $\nu^* = 0.1$, 0.5, and 1. $h^1$, $h^2$, and $h^3$ are the corresponding values of the brush heights at a fixed radius $R_c = 20$ nm. $h$ was numerically obtained using eq. 3.27 with a precision of 0.1. In (a), it is observed that $H_0$ is significantly larger than $h$ due to the curvature effect (see the text). In (b), it is apparent that, as the curvature increases, the brush height decreases.

Most essentially, Zhulina and Wijmann stated that the dead zone, where chain ends do not exist, is located near the surface and grows as the radius is increased, but not monotonously. This indicates that the tethered chains are stretched away from the surface as the radius increases.

### Conformation of tethered polymers on the spherical substrate and review of recent results

The overall profile of the conformation feature of the tethered polymers on a spherical substrate with variation in the grafting density and the molecular weight was schematically explained in the work of Dukes et al. [8]. It is summarized in Figure 3.5. The grafted chains on the curved substrate exhibit a transition from mushroom to SDPB and CPB regimes, similar to the case of a planar substrate. However, for the SDPB and CPB regimes, the stretched conformation of the chains on the curved substrate becomes relaxed compared to that on the planar substrate. This is seen in the scaling behavior of the height of the chains with other parameters, such as molecular weight, curvature, and grafting density (compare Figure 3.2 and Figure 3.5). The physical reason for the relaxation of the stretched conformation is the curvature of the radius of the core, as described previously. The scaling concept for the SDPB regime in Figure 3.5 is from eq. 3.22, which clearly demonstrates that the brush height scales as $h \propto N^{0.6}\sigma^{0.2}$, not as $h \propto N\sigma^{1/3}$, reflecting the curvature effect. For densely tethered long polymer chains, the conformation transition occurs as the chain length increases, and it is to be decomposed into two parts, CPB for

short parts and SDPB for long parts. It is noteworthy that the exponents of N and $\sigma$ to scale with the brush height in the CPB regime are smaller than those in the planar case.
For the experimental verification of the conformation of the densely tethered long polymer chains, Dukes et al. [8] used silica particles (diameter = 14nm) grafted with polystyrene (PS) for their DLS experiments. The ATRP (atomic transfer radical polymerization) method was applied for grafting PS from the silica nanoparticles. Three different grafting densities, 0.05, 0.39, and 0.55 chains $\cdot\, nm^{-2}$, were applied to the surface of the particles along with variations in the molecular weights of the grafted chains. The hydrodynamic brush thickness was defined as the difference between the $R_h$ of the polymer grafted particle and that of the particle core. Their experimental findings showed that the transition from the CPB regime, where the hydrodynamic brush thickness, h, scales as, $h \sim N^{4/5}$ for short chains, and to the SDPB regime, where h scales as, $h \sim N^{3/5}$ at a constant grafting density, high grafting density regimes, 0.39 and 0.55 chains $\cdot\, nm^{-2}$. Then, they applied eq. 3.27 to investigate the chain conformation and found that the experimental data deviated from the theoretical prediction at low molecular weights but matched quite well at large molecular weights. Therefore, they concluded that the theoretical prediction from eq. 3.27 can explain the conformation feature of the SDPB regime, as the interaction assumed was pairwise and the curvature was designated to be small, as the scheme in Figure 3.5 shows.
Ohno et al. [7] used rather large silica particles (diameter = 130 nm) grafted with PS ($M_w$ = 88,000 g/mol to 126,000 g/mol), where the grafting densities ranged from $\sigma$ = 0.6 to 0.7 chain/nm$^2$. The hydrodynamic thickness extracted from DLS increased with increasing $M_w$ with an exponent of 0.83. The exponent on the grafting density, 0.83, found in their experiment, seems to show that the grafted polymer has a CPB brush conformation due to a large grafting density and a rather small curvature, large radius.

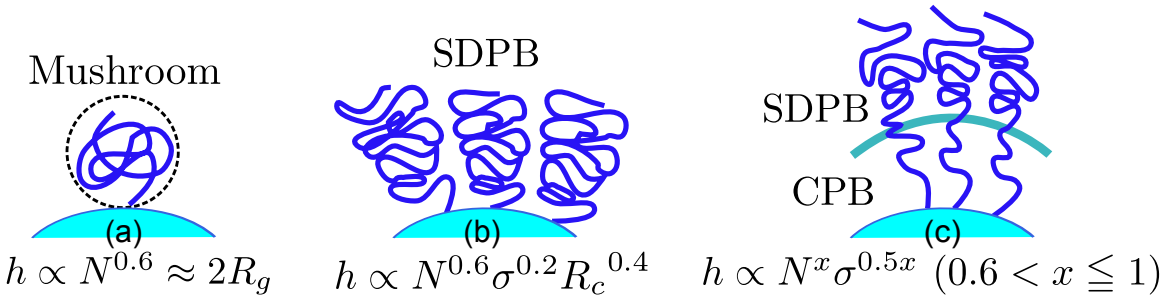


**Figure 3.5.:** Schematic illustration of different conformations of the polymer attached to the surface of a spherical particle depending on the grafting density and length of the chain [8].

Lo Verso et al. [47] investigated the conformation of a polymer brush and the corresponding volume density profile of the polymer segments under good solvent conditions using density functional theory (DFT) and a coarse-grained model. In their study, the radius of gyration of the tethered polymer chains was comparable with the size of the core. They claimed that the tethered chains are less stretched in radial directions than expected Daoud and Cotton picture and that there is a gradual crossover regime to describe the scaling behavior of the polymer brush between two extremes, a flat substrate and a star polymer, as neither the scaling law of eq. 3.19 or eq. 3.22, could explain the scaling behavior of their data.
So far, simulation studies of the conformation of a polymer brush on a spherical interface and some experimental studies related to the former simulation have been introduced and reviewed. To summarize chain stretching is strongly affected by the grafting density, molecular weight, and the relative curvature, $R_c/h$, as introduced previously. For a polymer brush on a curved and a flat substrate, the height of the polymer brush increases as the grafting density increases due to the interaction between neighbouring tethered chains. An experimental study from Dukes et al. [8] demonstrated, for a spherical brush at a rather high grafting density, due to the increased volume at a distance away from the core, the conformation features should be described separately depending on the distance close to the core (CPB)

and close to the interface between the chains and the medium (SDPB). Based on a theoretical study from Wijmann and Zhulina [45], the volume density profile and the corresponding scaling law of the brush height with the relevant parameters have been reviewed, depending on the different curvatures. Here, it is noted that the scaling law derived from the theory assumed a pairwise interaction. As for the curvature effect Lo Verso et al. [47] reported that there is a broad range of radii to explain the scaling behavior of the intermediate regime between two extreme cases of a brush on a flat surface, shown in eq. 3.22 and the star polymer brush, shown in eq. 3.19. A number of the experimental works relate to a polymer brush on a spherical surface under good and theta solvent conditions but it will be discussed later with our experimental results.
In the next section, the conformation feature and its possible variation in a polymer brush on spherical particles in a chemically identical polymer matrix will be described. The variation in the conformation feature can be achieved by tuning the ratio of the molecular weight of the matrix polymer to that of the grafted polymer, grafting density, and curvature. By tuning these parameters, the nanoparticle dispersion and the wettability of the matrix polymer on the grafted polymer are known to be changed. Change in the wettability of a free matrix polymer is designated as the wetting-dewetting transition. The effect of these parameters on the dispersion and wettability will be a main issue, and the physical behavior of the grafted and matrix chains will be either theoretically or experimentally reviewed.

### 3.2.2 Grafted polymer in a melt

The physical properties of polymers can be considerably enhanced by the addition of nanoparticles, named fillers, to a polymer matrix. The resulting material, identified as a polymer-nanoparticle composite (PNC), can be implemented as a new functional material when the specific material properties of a polymer and organic or inorganic nanoparticles are combined. It has been recently recognized that the dispersion state of nanoparticles in a polymer matrix plays an important role in triggering or tuning the optical, electrical, and mechanical properties of the resulting PNC materials [5, 14, 15, 48, 49, 50, 51, 52, 53]. These macroscopic properties are related to the local organization of the nanoparticles in a polymer matrix, well dispersed or aggregated state. On the other hand, the properties of PNC can be greatly improved when the size of the nanoparticles is reduced to the nanoscale due to the augmented surface area. The investigation of the microscopic or mesoscopic organization of the nanoparticles is therefore important, to gain insight into the resulting properties of the PNC materials. The dispersion state can be triggered either externally by applying a magnetic field or an electric field during film processing [15, 49], or internally by chemically grafting the polymers onto the nanoparticles. The latter method is favored due to the advancement of chemical methods to generate grafted polymers and relatively easy control of the internal parameters, such as grafting density and the molecular weight of polymers. Recent research efforts have contributed to cases where these grafted nanoparticles are dispersed in a chemically identical polymer matrix. The use of the chemically identical polymer for the matrix material was attributed to the well-developed theoretical base for the behavior of the homopolymer on the grafted polymer on a planar substrate. The following theoretical description of the behavior of the free polymer on the grafted polymer on the curved substrate will be restricted to the case where the free and grafted polymers are chemically identical. As in the case of polymer grafted nanoparticles in good solvents, the conformation of the grafted polymers depends on the grafting density, molecular weight, and curvature. The additional parameter to affect the conformation considered is the ratio of the chain length of free ($N_f$) to that of grafted chain ($N_g$). The former denomination, $N_f$, for free chain, corresponds to the degree of polymerization of the free matrix polymer chain and that of the latter, $N_g$, that of the grafted chain, respectively.
Most theoretical descriptions of the behavior of free chains on grafted chains on a curved substrate have been based on the simple case of a free polymer on a grafted polymer on a planar substrate. This theoretical description can be transferred to colloidal particle systems, so the theoretical description will be momentarily limited to the case of the planar substrate. As the free chain is chemically identical to

the grafted chain, the driving interaction between the free and the grafted chain is purely entropical in nature. The balance between the entropy gain due to the penetration of the free chains into the grafted chains and the entropy loss due to the stretching of the grafted chains, the elastic stretching term, is the physical reason for the interaction, the balance between the mixing-demixing and chain configurational entropy. The free energy per chain is given by [54]:

$$\frac{F}{K_B T} = \frac{h^2}{a^2 N_g} + \frac{a^3}{N_f} \cdot \frac{{N_g}^2}{hd^2}. \tag{3.28}$$

Here, a is the monomer length, $K_B$ is the Boltzmann constant, and d is the average distance between the grafted sites. The first term represents the elastic contribution and the second the mixing-demixing term. The result of the above free energy description will be discussed with a phase diagram by Leibler et al. [55]. Note that the above eq. 3.28 is similar to eq. 3.13, in that both equations contain the elastic contribution term and the interaction term.

**Qualitative phase behavior of polymer grafted nanoparticles in a polymer matrix [50, 57, 58]**

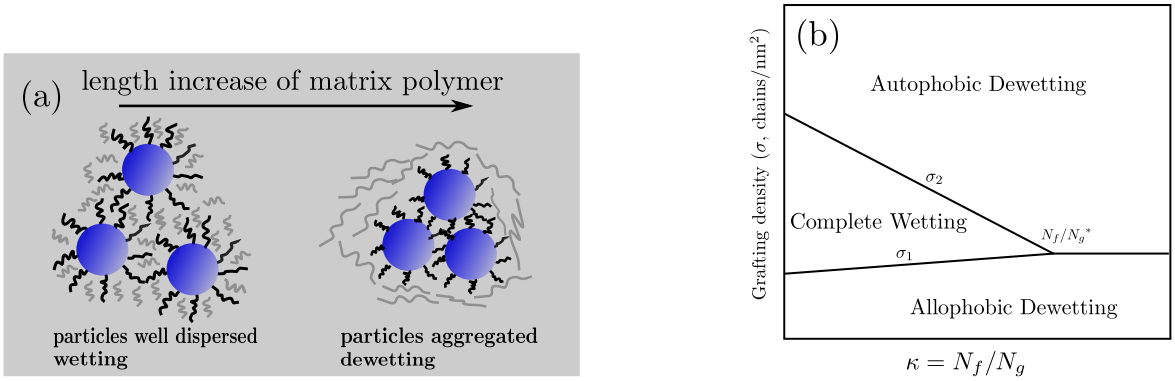


**Figure 3.6.:** (a): Schematic illustration of the behavior of the wetting-dewetting transition of free polymers on polymers grafted to the spherical nanoparticles. The free and graft polymers are chemically identical. See text for the details. (b): Schematic illustration of a phase diagram for particle stability as a function of the molecular weight ratio, $\kappa = N_f/N_g$, and $\sigma$, the grafting density (chains/nm$^2$) [50, 57, 58]. Three regions are identified with different combinations of $\kappa$ and $\sigma$. The free chains are de-wetted from the brush at low grafting densities (allophobic dewetting) and at intermediate to high grafting density (autophobic dewetting). For a detailed explanation, see text.

The behavior of the free chain on the grafted chain on the planar substrate can be described by the phase diagram, characterized by the chain length ratio ($N_f/N_g$, named $\kappa$) and the grafting density ($\sigma$, chains/nm$^2$), originally introduced by Green et al. [50, 57, 58]. The corresponding phase diagram is shown in Figure 3.6. When $N_f \leq N_g$, the free chains can penetrate the space between the grafted sites, and this penetration causes the grafted chains to swell, leading to a good dispersion of nanoparticles in a matrix. This penetration is represented by the "wetting" of the free chains. This region in the phase diagram is bound by two grafting density limits, $\sigma_1$ as a lower limit and $\sigma_2$ as an upper limit. When $N_f \geq N_g$, however, the interpenetration of the free and grafted chains is weakened and nanoparticles are aggregated. In this case, the elastic stretching entropy term dominates so that the free chains are expelled by the grafted chains, and correspondingly, the grafted chains adopt a collapsed conformation different from the "wetting" case. The behavior of the free chain is named the "de-wetting state". The autophobic dewetting occurs at moderate to high grafting densities and is driven by a variation in $\kappa$ when the free chains are expelled from the grafted chains. The allophobic dewetting takes place at low grafting densities when the van-der-Waals interaction between cores is still large

and the interaction mediated by the free chain is not yet relevant. The behavior of the free chain as a function of $\kappa$ is schematically illustrated in Figure 3.6, along with the phase diagram described previously.

**Quantitative phase behavior of the grafted homopolymer on a spherical substrate [54, 55]**

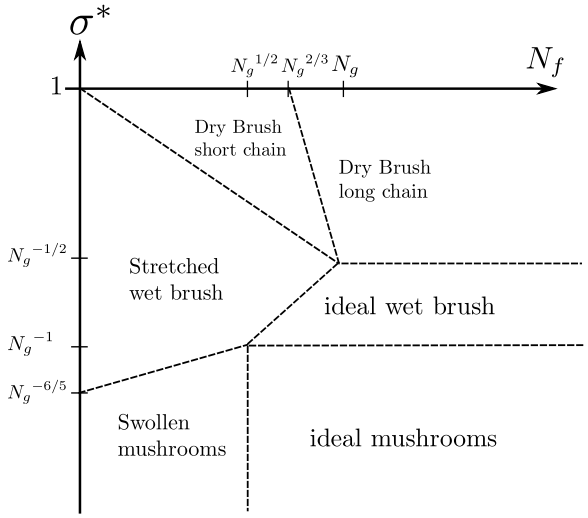


**Figure 3.7.:** Phase diagram of a spherical grafted polymer in contact with a chemically identical polymer matrix. The grafting density is $\sigma^*/a^2$, where a is the size of a monomer [54, 55].

So far, the phase diagram and corresponding wetting behavior of the free chains has been described qualitatively, not quantitatively. The quantitative description of the phase behavior of a grafted homopolymer on a spherical substrate was introduced Leibler et al. [55] based on an approach similar to those on a planar substrate introduced by Aubouy et al. [54, 56].
Leibler et al. [55] predicted the scaling relation of the thickness of the grafted polymer on a spherical substrate in contact with a chemically identical free polymer. Motivated by Aubouy et al. [54], who investigated the scaling relation of the grafted polymer in a chemically identical polymer melt on the planar substrate, their phase diagram contained five regions specified with a variation of $\kappa$ and $\sigma^*$. Here, $\sigma^* = \sigma \cdot a^2$, where a is the size of a monomer. At low enough grafting densities, the grafted chains show the transition from the swollen mushroom conformation to the ideal mushroom conformation, as in the case of the planar substrate. The thickness of the swollen mushroom conformation at $N_f < {N_g}^{1/2}$ is given by [55]

$$h \cong {N_g}^{3/5}/{N_f}^{1/5}. \tag{3.29}$$

For a large free chain, the grafted chain adopts the ideal mushroom conformation at $N_f > {N_g}^{1/2}$, as given by [55]

$$h \cong a{N_g}^{1/2}. \tag{3.30}$$

Above a threshold value of reduced grafting density of $\sigma^* \cong {N_f}^{2/5}/{N_g}^{6/5}$, that is, above the swollen mushroom regime, the size of the grafted chain becomes [55]

$$h \cong N_g {N_f}^{-1/3}{\sigma^*}^{1/3}. \tag{3.31}$$

Above the ideal mushroom regime, when $\sigma^* \cong 1/N_g$, the grafted chain adopts the ideal chain conformation.

$$h \cong a{N_g}^{1/2}. \tag{3.32}$$

At even higher grafting densities, the dry brush regime is reached, where the free chains are almost completely expelled from the brush. As in the case of the planar surface, the size of the brush is $h \cong N_g \sigma^* a$. The volume fraction up to the penetration depth is the order of unity. The penetration depth for short free chains is $\lambda \cong N_g/\sigma^* N_f$, and for large free chains, $\lambda \cong {N_g}^{1/3}{\sigma^*}^{1/3}$. It is noteworthy that the penetration depth for large free chains is independent of the length of the free chains, different from the case of the short free chains.
However, the scaling relation provided by Leibler et al. [55] is quite similar to that of a planar substrate and does not include the curvature effect. Additionally, the phase diagram developed by Leibler et al. displays only an approximation to scale the thickness and other parameters, and the interaction between the particles was not considered, which will also induce the dewetting state. Therefore, the experimental data for our particle systems will not be quantitatively compared with the scaling law introduced here but, rather, qualitatively.

**Review of recent results**

The dispersion state and conformation of the grafted polymer in a chemically identical polymer melt on a spherical nanoparticle were experimentally investigated by several groups, mostly by SAXS and TEM and sometimes by rheology measurement [15, 48, 50, 53]. Hasegawa et al. [48] used rheology and SCF (self consistent field calculation) to show that there is an optimum grafting density in acrylonitrile-co-styrene (AS) grafted cross-linked polybutadiene (PB) particles (diameter, D = 170 and 350 nm) dipsersed in the same AS polymer matrix. Below this critical grafting density, the particles were aggregated due to the van der Waals interaction between the particles, and above that, the particles were aggregated possibly due to the attractive interaction between the brush. Chevigny et al. [15] used PS grafted silica nanoparticles ($R_c$=13 nm) in PS matrices to investigate the dispersion and the thickness of the grafted PS. $\kappa, N_f/N_g$ was modulated from 2.8 to 28 at a fixed grafting density $\sigma \cong 0.2$ chains/nm$^2$. They found that, for $\kappa < 4$ the particles were homogeneously dispersed, while for $\kappa > 4$, the particles were aggregated and phase separated, corresponding to a transition from the "wet" for the former case to the "dry" brush for the latter case. Their observation implies that the penetration of the short free PS chains induces the wet brush conformation, while the large free chains expelled from the brush induce the dry brush conformation, as stated in the aforementioned theory part. Sunday et al. [50] developed a phase diagram for a similar system of PS grafted silica nanoparticles ($R_c$ = 9 nm) in PS matrices which was extracted from results from USAXS (ultra small angle x-ray scattering) and TEM. $\kappa$ was varied from 0.6 to 7.7 and grafting densities were varied from $\sigma$= 0.1 to 0.7 chains/nm$^2$ to construct a wide variety of parameters for the phase diagram. The phase transition from complete wetting (wet brush) to an autophobic dewetting region (dry brush) was displayed as a function of $\sigma$ and $\kappa$. The intersection molecular weight ratio, $N_f/{N_g}^*$, called the critical molecular weight ratio, $\kappa_c$, was found to be ≈4. They reported that $\kappa_c$ may range between 1 and 4. The lower limit may correspond to the planar interface or the large particle ($R_c$, larger than 100 nm) and the upper limit, the small particles ($R_c$ = 2-16 nm).
For similar systems, but using PEG (polyethylene glycol) grafted silica nanoparticles ($R_c$=5 nm) in PEG matricies, the phase transition was investigated by combination of SAXS and TEM [53]. The range of $\kappa$ was varied from 1 to 19, and $\sigma$ was varied from 0.8 to 2 chains/nm$^2$. They found that, for the high grafting densities used in their experiments, the particle dispersion was not sensitive to the grafting density variation but to the curvature of the radius of the core, characterized by a parameter, $D/R_g$, where D is the diameter of the spherical core and $R_g$ is the radius of gyration of the grafted polymer chain in a bulk state. The phase transition from the wetting state to the phase separated state, the latter of which may represent the autophobic dewetting region, was observed at a high molecular weight ratio, $\kappa$=5 [53]. The critical molecular weight ratio, $\kappa_c$, observed in their experiment was found to

be larger than the value reported by Chevigny et al. [15]. The smaller value of $D/R_g$ used for their study (≈3.7) compared to that of Chevigny et al. (larger than ≈4) was claimed to be a reason for the larger $\kappa_c$ value (≈5) compared to (≈ 4) in Chevigny et al. [15]. Intuitively, the conformation freedom for a grafted chain on the spherical nanoparticle increases as the radial distance increases. Therefore, the chain crowding will be relaxed as the radius of the core increases, and this relaxation at the free ends of the grafted chains will permit interpenetration of the free and grafted chain to be more facile than in the case of the planar substrate. Even though the grafted chains are highly stretched due to the high grafting density, the conformation freedom at the interface will play a significant role in the interpenetration of the free and grafted chains. This curvature effect seems to be reflected in the experimental observations reviewed so far, and it can be conjectured that, as the radius of the core decreases, the wetting-dewetting transition occurs at larger $\kappa_c$, as the free chains may have more freedom for penetration into the brush. This phenomenological behavior of the deceleration of the transition as the curvature increases, that is, as the radius decreases, was also verified by SCFT simulation by Trombly et al. [59]. They additionally claimed that the decreased interpenetration of the free and grafted chains leads to the increased attraction between the particles, implying that the dewetting of the free chains on the grafted chains leads to the increased attraction between the particles, as shown in Figure 3.6.
So far, theoretical and experimental studies of the wetting behavior for systems of polymer grafted nanoparticles have been reviewed. Most of the experimental studies have focused on the dispersion of the grafted nanoparticles with a variation of $\kappa$ and $\sigma$, and detailed study of the scaling relation as a function of $\kappa$ and $\sigma$ is now lacking. SANS is a powerful tool to investigate the structure of the grafted polymer due to the enhanced contrast between the grafted and matrix polymers driven by selective deuterium labeling. In our results section, PS grafted silica and deuterated PS particles in deuterated PS matrices will be prepared to study the wetting-dewetting transition as well as the scaling relation of the thickness of the grafted polymer layer with other parameters, $\kappa$ and $\sigma$. SANS will be a method to extract the structural properties, such as the thickness and the dispersion state.

### 3.2.3 Conclusion

The conformation of the tethered polymer chains on a spherical substrate in a good solvent or in a chemically identical polymer melt with tethered chains has been described and reviewed. For tethered polymers under good solvent conditions, the main focus of this chapter was prediction of the conformation feature of tethered chains for the parameters known to affect, namely the grafting density, molecular weight, and curvature. The description of the conformation feature of the tethered polymers on the curved substrate was limited to the case of a spherical substrate. The conformation transition from mushroom to SDPB and CPB expected based on theory with increasing grafting density was observed by experiments involving both planar and spherical substrates. The stretching of the tethered polymers on a spherical substrate was predicted and found to be relaxed compared to those on a planar substrate. The curvature is responsible for the different conformation feature of the tethered polymer on the curved substrate and reflected in the low amplitudes of the exponents for the grafting density and the molecular weight employed to scale the thickness. The experimental study of Dukes et al. [8] explicitly showed that the conformation transition occurred for large molecular weight chains at relatively high grafting densities.
The dispersion of the particles and the change in the conformation of the grafted chains were the main topics of the section on the polymer brush in the melt. It is widely accepted that the particle dispersion and the change in the conformation, namely the wetting-dewetting transition, is correlated, and this was proved by the simulation and experiments. The additional parameters to affect the chain conformation herein were the molecular weight ratio, $\kappa, N_f/N_g$, as well as the previously mentioned parameters, the grafting density, curvature, and molecular weight of the grafted chain. The experimental studies showed that the wetting-dewetting transition for the spherical nanoparticle systems occurred at a relatively large molecular weight ratio, $\kappa$, compared to the planar substrate case. The authors insisted that the criti-

cal molecular weight ratio, where the transition occurs, is affected by the curvature. As the curvature increases, the transition occurs at large molecular weight ratios. However, most studies have used the dispersion state as a criterion to judge the wetting-dewetting transition, and to our knowledge there has been no detailed study of the change in size of the grafted chains for each transition regime. Therefore, we will investigate both the variation of the dispersion state and the thickness as a function of $M_w$ of d-PS matrices. SANS may be a well-suited method to extract the structural properties of the thickness and the dispersion state simultaneously.

# 4 Form factors for the various density profiles

The structure of nanoparticles and macromolecules such as micelles and proteins can be characterized by small angle scattering. The size and form of the scattering objects of concern, their distribution, and additionally their interaction behavior can be analyzed by a small angle scattering technique. These basic informations are thus inherently required to understand the idea of the physical or biological process. In this chapter, the intensity calculation for the general analysis of small angle scattering curves will be discussed, and the form factors to calculate the SANS scattering curves for polymer coated nanoparticles, as a central theme, will be addressed in detail.

## 4.1 Intensity calculation of small angle scattering curves [17, 60, 61]

Previously in order to calculate the intensity of the small angle scattering, the interparticle interaction was not considered as the assumed solution would have a high dilution. However, if the concentration is not low and the interparticle interference should be considered, the intensity is not simply a function of the form factor but of the form and structure factor. Additionally, the distribution of the particle sizes should be taken into account to calculate the intensity. Here, it is noted that the particle sizes and orientations are not correlated with the position of the particles. The differential cross section, intensity is then given by

$$\left(\frac{d\Sigma}{d\Omega}\right) = V^{-1}\left\langle \sum_{i=1}^{N_p}\sum_{j=1}^{N_p}\left\langle F_i(\vec{q})F_j{}^*(\vec{q})\right\rangle \times \exp\left(\vec{q}\cdot(\vec{r_i}-\vec{r_j})\right)\right\rangle, \tag{4.1}$$

where V is the sample volume and $N_p$ is number of particles in the sample volume. The inner bracket represents an average weighted by the size distribution and orientation of the particles. The systems investigated in the following will be isotropic with a homogeneous shape. Therefore, $\vec{q}$ will be replaced by $q$. For a monodisperse system, $F(q)$ is as previously introduced in eq. 2.32:

$$F(q) = 4\pi\int_0^R \left(\rho(r)-\rho_s\right)\frac{\sin(qr)}{qr}dr, \tag{4.2}$$

where $\rho(r)$ is the distribution of the scattering length density within a particle and $\rho_s$ is the scattering length density (SLD) of a solvent. Note that $\rho(r)$ in eq. 2.32 is replaced by $\rho(r)-\rho_s$ here, to describe the excess $\rho(r)$ of the SLD of the particle over the $\rho_s$ throughout the system. Here, the form factor of the spherical shape was assumed. From now on, the polydisperse system will be discussed. For the polydisperse system, inner bracket in eq. 4.1 can be decomposed into

$$\left\langle F_i(q)F_j{}^*(q)\right\rangle = \left[\left\langle\left|F(q)\right|^2\right\rangle - \left|\left\langle F(q)\right\rangle\right|^2\right]\cdot\delta_{ij} + \left|\left\langle F(q)\right\rangle\right|^2, \tag{4.3}$$

where $\delta_{ij}$ is the Kronecker delta, which is equal to 1 if i=j and equal to 0 otherwise. Then, the intensity in eq. 4.1 takes the form

$$\left(\frac{d\Sigma}{d\Omega}\right) = n_p\left[\left\langle\left|F(q)\right|^2\right\rangle - \left|\left\langle F(q)\right\rangle\right|^2\right] + n_p\left|\left\langle F(q)\right\rangle\right|^2 S(q). \tag{4.4}$$

$n_p$ is the average number density of particles in the sample, which is defined by $n_p = N_p/V$. The first term denotes $q$-dependent Laue diffuse scattering term which arises from size distribution of the particles. $S(q)$ is the structure factor to describe the interparticle interference in the scattering data. $S(q)$ is a measure of spatial distributions between different particles which arises from mutual interaction between a pair of particles. For a dilute system, therefore, $S(q)$ reduces to ≈1 and as the concentration of the particles in the sample increases, the interaction between the particles contributes to the scattering intensity. It is defined as the Fourier transformation of the pair correlation function or the pair distribution function $g(r)$, which is the dimensionless parameter of the radial distribution of a particle pair. In spherical coordinates, it is given by

$$S(q) = 1 + \frac{4\pi n_p}{q} \int_0^\infty r[g(r) - 1]\sin(qr)dr. \tag{4.5}$$

$S(q)$ is obtained by solving the Orstein-Zernike equation using the Percus-Yevnic approximation for an interaction potential between a pair of particles [61]. However, explicit expressions for $S(q)$ will not be given in this work since our work focuses on a dilute situation where the particular interactions are negligible.
The following expressions were introduced in eq. 4.4 to take polydispersity into account.

$$\left\langle \left|F(q)\right|^2 \right\rangle = \int_0^\infty \left|F(q,R)\right|^2 f(R)dR. \tag{4.6}$$

$$\left|\left\langle F(q)\right\rangle\right|^2 = \left| \int_0^\infty F(q,R) f(R)dR \right|^2. \tag{4.7}$$

$f(R)$ is a particle size distribution function, and $f(R)d(R)$ is the probability of a particle having a radius between $R$ and $R+dR$. For a particle size distribution function, the Schulz-Zimm function was employed for this work. The Schulz distribution function is a two-parameter function as given by

$$f_s(R) = \left(\frac{Z+1}{\overline{R}}\right)^{Z+1} R^Z/\Gamma(Z+1) \cdot \exp\left[-\left(\frac{Z+1}{\overline{R}}\right)R\right], \quad Z > -1, \tag{4.8}$$

where $\overline{R}$ is the mean radius and $Z$ is the width parameter. $\Gamma(X)$ is the gamma function. The function approaches a delta function as Z approaches infinity and becomes a Gaussian form at a large value of Z. To determine the polydispersity root mean square deviation from the mean radius, $\sigma_R$ is introduced.

$$\sigma_R = \left(\overline{R}^2 - \overline{R^2}\right)^{1/2} = \overline{R}/(Z+1)^{1/2}. \tag{4.9}$$

The polydispersity ($\sigma_x$) is given by

$$\sigma_x = \frac{\sigma_R}{\overline{R}} \tag{4.10}$$

In some cases where aggregation of particles exist, two types of "phenomenological" functions can be implemented. In the presence of aggregation, scattering from a system containing aggregates consists of two components. In addition to the scattering from the single particle, one also finds the scattering from aggregates, and the particles in the system are not spatially distributed. Therefore, scattering data for a system containing aggregation is not described by a structure factor $S(q)$ but instead can be described by a superposition of a form factor and a term for aggregation [52, 62]. They are:

$$Cq^{-\alpha} \tag{4.11}$$

$$\frac{A}{(1+q^2{\xi_{\mathrm{DB}}}^2)^2} \sim \begin{cases} \frac{1}{q^4} & \text{if } q\xi_{\mathrm{DB}} \gg 1 \\ A & \text{if } q\xi_{\mathrm{DB}} \ll 1 \end{cases} \tag{4.12}$$

where $\alpha$ is a power law exponent, A and C are constants, and $\xi_{\mathrm{DB}}$ is a correlation length. The term in eq. 4.12 is the Debye-Bueche function, which was originally introduced to describe the length scale of the structural heterogeneities of the random two-phase model [63]. The Debye-Bueche function is expected to describe the scattering behavior of the aggregates [62] showing a constant amplitude at low $q$ and $q^{-4}$ decay at high $q$ from the Porod scattering from the aggregates. Therefore, as shown in eq. 4.12, extending from the constant amplitude of the scattering curves, the curves decay as $q^{-\alpha}$ and finally reach $q^{-4}$ behavior. Therefore, the term of $Cq^{-\alpha}$ can be used when the data is not extended to lower $q$ to cover the whole profile of the scattering curves from the aggregates; a plateau and a decay following a plateau, and Debye-Bueche function can be used when the data covers the whole profile of the scattering curves from the aggregates. The application of the Debye-Bueche contributions is expected to allow characterization of the average size of the aggregates with the parameter $\xi_{\mathrm{DB}}$ [62]. When the data contains information on the aggregation, these two types of fit functions will be used to describe the low $q$ scattering from experimental SAS data, and the corresponding results will be shown in chapter 5 and 6.

As the last part of the intensity calculation, the prefactor shown in eq. 4.4 and eq. 2.35 will be compared to determine its physical meaning. Since an equality of the prefactors of eq. 2.35 and eq. 4.4 should hold, we consider the case of eq. 4.4 at $q = 0$ in a high dilution ($S(q) = 1$) using a simple form factor of a solid sphere with a homogeneous SLD in the core. The form factor of a solid sphere is given by

$$F(q,R) = (4\pi/3)R^3(\rho_{\mathrm{core}} - \rho_{\mathrm{sol}})3\frac{\sin(qR) - qR\cos(qR)}{(qR)^3}. \tag{4.13}$$

where $\rho_{\mathrm{core}}$ and $\rho_{\mathrm{sol}}$ are the SLD of the core and the solvent, respectively. An experimentally accessible parameter, $\phi$, the volume fraction, is related to the number density $n_p$ as given by

$$n_p = \frac{\phi}{V_p}, \tag{4.14}$$

where $V_p$ is the particle volume, for the case of a sphere, simply $(4\pi/3)R^3$. If the form factor of the sphere shown above for a dilute situation, $S(q) = 1$, is inserted into eq. 4.4 and the prefactor, representing when $\lim_{q\to 0}\left\langle |F(q,R)|^2 \right\rangle$ becomes

$$n_p {V_p}^2 \Delta\rho^2 = \frac{\phi}{V_p} \cdot {V_p}^2 \Delta\rho^2. \tag{4.15}$$

Here, $\Delta\rho$ is $\rho(r) - \rho_s$ as discussed before. It means that, in order to determine the volume fraction of the particles in the sample, $\phi$, the form factor should be divided by the distribution of volume with a dependence on R as follows.

$$\left\langle V_p \right\rangle = \int_0^R \frac{4}{3}\pi R^3 f(R) dR. \tag{4.16}$$

Finally the intensity at $q = 0$ becomes

$$\left(\frac{d\Sigma}{d\Omega}\right)\Big|_{q=0} = \Phi \cdot V_p \cdot \Delta\rho^2 \tag{4.17}$$

## 4.2 Model independent analysis of small angle scattering spectra [16]

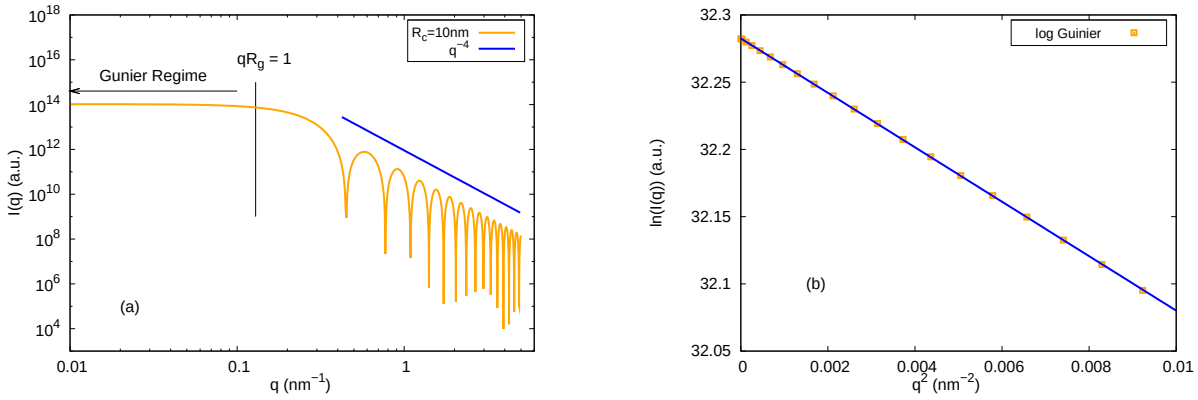


**Figure 4.1.:** (a): Calculated SAS intensity of spherical particles with a homogeneous SLD using eq. 4.13. Guinier regimes, where $qR_g < 1$ is satisfied, and Porod's law at high $q$ with a $q^{-4}$ decay are presented. Overall, the intensity of the spherical particles, decay as a function of $q^{-4}$ as presented in the plot, and Porod's law for the surface scattering is followed at high $q$ ranges. For the calculated curve, the core radius, $R_c$, is set to be 10 nm without polydispersity. (b): Typical logarithmic Guinier plot, i.e. $\ln I(q)$ vs $q^2$, of the curve given in (a), in a linear-linear scale to obtain $R_g$ with a curve fit. $R_g$ is found to be 7.8 nm which corresponds to $R_c$=10 nm by applying eq. 4.19 and shows good agreement with the set core radius. We note that, to obtain $R_g$, the range of scattering vectors is restricted to $qR_g \leq 1$, for which the Guinier law is valid.

In the previous description of the intensity, the form factor had a known shape, a sphere. However, when the particle shape is not easily describable or expectable from the scattering data, the model independent characterization could be useful to obtain an idea of the size or the shape of the particles. The first method to describe the size of particles of unknown shape is called "Guinier's law". This is given by

$$\left(\frac{d\Sigma}{d\Omega}\right) = \Delta\rho^2 {V_P}^2 \exp\left(-\frac{1}{3}q^2 {R_g}^2\right). \tag{4.18}$$

$\Delta\rho$ is the SLD contrast between the particle and the dispersion medium. This allows determination of the particle size $R_g$, irrespective of shape, from the scattering experiment. The Guinier law is valid when (1) $qR_g < 1$, (2) the system is dilute, and (3) the system is isotropic. An additional constraint needed is that the dispersion medium, such as a solvent, should be of constant density and lack of an internal structure so that only the contrast between the particles and dispersion medium exists. For example, if the particle shape is supposed to be spherical, $R_g$ is given by

$$R_g = \sqrt{\frac{3}{5}}R. \tag{4.19}$$

For an ellipsoid with principal axes of half-length a and b,

$$R_g = \sqrt{\frac{2a^2 + b^2}{5}}. \tag{4.20}$$

Guinier's law describes the overall size of the unknown particle, and the information is obtained at low $q$ range. However, the detailed information of the particle is usually obtained at high $q$ range. The shape of the particle is usually obtained by fitting of the data, but close inspection of the decay as a function of $q$ also at low q extending from the Guinier plateau allows determination of the shape of the particle, as given by

$$\left(\frac{d\Sigma}{d\Omega}\right) \sim q^{-\alpha}. \tag{4.21}$$

The exponent $\alpha$ is equal to 4 for spheres, 2 for thin disks, and 1 for thin rods, reflecting the dimensionality of the particles. At high $q$, the intensity decays as a function of $q^{-4}$, so called Porod scattering. This Porod scattering is the scattering from the surface of the particles irrespective of the particle shape, which is originally derived from the ideal two-phase model. The ideal two-phase model indicates that two phase, or two domains are well separated, with a smooth interface. Therefore, Porod's law should be related to the surface area of the particle. Then, the Porod's law prediction holds for $q \to \infty$ and is given in absolute scale [23]

$$\left(\frac{d\Sigma}{d\Omega}\right) \to n_p \frac{2\pi S_P}{q^4} \Delta\rho^2, \tag{4.22}$$

where $S_p$ is the surface area of the particle ($4\pi R^2$ for a sphere). In practice, the Porod scattering is seen at the $q$ range, preceded by scattering from the background. A special example is the form factor scattering from a sphere which falls off as $q^{-4}$ at a high $q$ range as previously introduced. It should be stressed that this law allows determination of the surface area at high $q$ range if (1) the intensity is scaled in absolute unit, and (2) experimental background is correctly subtracted. It should be noted that, $q^{-4}$ decay of the curve contains the important information in that it represents the scattering from the surface of the particles in the scattering medium. It is additionally noted that, for a diffuse interface between the particle and the dispersion medium, usually a solvent, the intensity falls off much more rapidly, as given by [23]

$$\left(\frac{d\Sigma}{d\Omega}\right) \sim \frac{\exp(-\sigma^2 q^2)}{q^4}. \tag{4.23}$$

$\sigma$ is the rms measure of the interfacial roughness, which has a similar form to a Debye-Waller factor. The regimes for the characteristic scattering are explicitly shown in Figure 4.1. Up to now, the model independent methods to analyze the scattering data have been introduced. However, the methods described so far merely contain a rough idea of the particle structure. Therefore, for a detailed study of the structure of the particle, the appropriate model should be introduced. In the next section, the main focus will be the application of the model for SANS data analysis of polymer coated particles, and it will be based on the previous theoretical description of the polymeric layer, the so-called diffuse layer, on the surface of the nanoparticle.

## 4.3 Form factor calculation for the polymer coated nanoparticle

The volume fraction profile of the polymeric corona on the surface of the spherical particle or micelle has been intensively studied either theoretically or experimentally, as discussed in the previous chapter 3. The profile of the polymeric layer mainly concerns with the polymer brush, a strongly stretched polymer compared to bulk polymer or free polymer chain. This volume fraction profile is indeed related to the SLD profile of the polymer layer, diffused layer and allows determination of the grafting density and the chemical properties. The grafting density can also be obtained with a more direct method, the thermal gravimetric analysis (TGA). Via comparison, the conformational property will be more efficiently revealed. In this section, the main focus will be on the form factor calculation based on different SLD profiles introduced by several authors with a description of the theoretical background of the model introduced. The detailed calculations of form factors will be explicitly shown, and the corresponding results for different profiles will be compared with one another.

### 4.3.1 Core-shell-chain model

**Gaussian density profile of shell – model 1**

First, the form factor of a core-shell-chain model will be introduced. This model was originally derived by Pedersen [64, 65, 66] to describe the form factor of a diblock copolymer micelle (A-B block) in a good solvent. A diblock copolymer micelle having the shape of a sphere motivated the use of this model. The spherical diblock copolymer micelle is comprised by the insoluble part of a core (A-block) surrounded by a shell of dissolved chains (B-block). This shell is similar to the outer region of a star polymer or a polymer brush on a spherical substrate. The polymeric layer, more generally diffused layer on the surface of the core, is assumed to have a Gaussian density profile. Additionally, the attached chains are supposed to be non-interacting. The model is schematically illustrated in Figure 4.2 (a). This model consists of four terms: the contribution from the spherical core, that of the chains, the correlation between the chains, and that of the core and chains. First, the contribution from the spherical core is given by $P_{\text{core}}(q,R_c) = \Phi(q,R_c)^2$. $\Phi(q,R_c)$ is the form factor amplitude of a sphere without the factors of volume and SLD contrast (cf. eq. 4.13):

$$\Phi(q,R_c) = \frac{3\left[\sin(qR_c) - qR_c\cos(qR_c)\right]}{(qR_c)^3}. \tag{4.24}$$

The contribution from the chains is for chains with Gaussian statistics, the Debye function:

$$P_{chain}(q,R_g) = \frac{2\left[\exp(-{R_g}^2q^2) - 1 + q^2{R_g}^2\right]}{q^4{R_g}^4}. \tag{4.25}$$

$R_g$ is the radius of gyration of the Gaussian chain. It is assumed that the chains with Gaussian statistics extend from the surface of the core and that the center of the Gaussian profile is located at R+$R_g$ (see Figure 4.2 (b)). The correlation term between the chains, $S_{\text{chain-chain}}$, is then given by

$$S_{\text{chain-chain}}(q) = \left(\frac{1-\exp(-q^2{R_g}^2)}{q^2{R_g}^2}\right)^2 \cdot \left[\frac{\sin(q[R_c+R_g])}{q[R_c+R_g]}\right]^2. \tag{4.26}$$

The core-chain term, $S_{\text{core-chain}}$, is given by

$$S_{\text{core-chain}}(q) = \Phi(q, R_c) \cdot \left( \frac{1 - \exp(-q^2 {R_g}^2)}{q^2 {R_g}^2} \right) \cdot \left( \frac{\sin(q[R_c + R_g])}{q[R_c + R_g]} \right). \tag{4.27}$$

The terms introduced so far allow calculation of the form factor of the sphere attached with the chains with a Gaussian density profile. It is assumed that the sphere has $N_c$ chains attached onto the surface with a Gaussian density profile, which will be shown in Figure 4.2 (b). The following form factor has a form already squared, $P(q) = |F(q)|^2$, and this is given by

$$\begin{aligned} P(q) = {} & {V_{\text{core}}}^2 \Delta {\rho_{\text{core}}}^2 P_{\text{core}}(q) + N_c {V_{\text{chain}}}^2 \Delta {\rho_{\text{chain}}}^2 P_{\text{chain}}(q) \\ & + 2 N_c V_{\text{core}} V_{chain} \Delta \rho_{\text{core}} \Delta \rho_{\text{chain}} S_{\text{core-chain}}(q) \\ & + N_c (N_c - 1) {V_{chain}}^2 \Delta {\rho_{\text{chain}}}^2 S_{\text{chain-chain}}(q) \end{aligned} \tag{4.28}$$

Here, $V_{\text{core}}$ is the volume of a sphere, $4/3\pi {R_c}^3$, $V_{\text{chain}}$ is the volume of a single chain, and $N_c$ number of chains attached to the surface of the particle. $V_{\text{chain}}$ is calculated from $V_{\text{monomer}}$:

$$V_{\text{monomer}} = \frac{M_{\text{monomer}}}{\rho_{\text{polymer}} N_{\text{A}}}, \tag{4.29}$$

where $\rho_{\text{polymer}}$ is the mass density of the polymer chain, $M_{\text{monomer}}$ is the molecular weight of a monomer and $N_{\text{A}}$ is Avogadro's number. $V_{\text{chain}}$ is obtained by $V_{\text{chain}} = N_x V_{\text{monomer}}$, where $N_x$ is the degree of polymerization of the polymer segments. This volume is called the segment volume, representing the volume occupied by the polymer segments. $\Delta\rho_{\text{core}}$ is excess scattering length density between the core and the solvent and $\Delta\rho_{\text{chain}}$ is that between the chain and the solvent. The polydispersity can be included by integrating the expression given in eq.4.28 with a Schulz distribution as shown in eq. 4.6. It is noted that the expression for the spherical micelle is different from eq. 4.28 as $N_c$ for the spherical micelle represents the aggregation number, that is, number of chains constructing a spherical micelle, which is not simply the number of chains attached to the surface of the particle as in the present case.

This model was successfully applied to analyze small angle scattering data for systems of spherical micelles and polymer grafted nanoparticles in a good solvent as well as in a theta solvent. The conformation of grafted polymer chains or chains on a spherical core in the micellar structure is expected to have a hyperbolic (power law-like) or parabolic profile depending on the curvature, as introduced previously. While the theoretical expectation for the volume fraction profile of the grafted chains on a spherical core is different from the Gaussian profile, this function was successfully implemented to analyze the systems in both a theta solvent and a good solvent [10, 66, 67, 68]. It is noted that this function is often limited in use due to the information required to analyze the data, especially the molecular weight of the chains and the number of chains. Parameters relevant to the molecular weight, $N_c$ and $V_{\text{chain}}$, can also be used as fit parameters, but it is always difficult to acquire a stabilized fit for the data with many free parameters. It is therefore essential to have supplementary chemical information for the polymer chains attached to the core to have a reliable fit.

In the following, the data will be generated from the given model function in order to see the effect of the change in the scattering curves on different parameters, such as $N_c$ and $R_g$ for a fixed SLD contrast. The parameters will be chosen based on proximity to the systems of this work. The calculated intensity is based on eq. 4.4 with $S(q) = 1$, assuming that there is no interparticle interference, namely a high dilution limit. The volume and squared form factor are averaged with a Schulz distribution function, as previously introduced:

$$\left( \frac{d\Sigma}{d\Omega} \right) = \phi \cdot \frac{\langle P(q) \rangle}{\langle V_{\text{total}} \rangle} + I_b. \tag{4.30}$$

Here, $V_{\text{total}}$ is the total volume of the core-shell particles and $I_b$ is the experimental background, but this parameter was set to zero for the generated data. $V_{\text{total}}$ is given by

$$V_{\text{total}} = V_{\text{core}} + N_c V_{\text{chain}}, \tag{4.31}$$

where $V_{\text{core}}$ is the volume of the core.
Figure 4.2 (c) and (d) shows the scattering intensity from eq. 4.30 calculated for the form factor of a core-shell-chain model for a Gaussian density profile of a shell with different sets of structural parameters. The core radius is set to be 30 nm and $R_g$ of the chain is varied with a size of 10, 20, and 30 nm. The relatively moderate polydispersity of $\sigma_R/R_c = 0.1$ is used, and the number of chains, $N_c$, is fixed at 1,000 which corresponds to the grafting density, $\sigma = 0.09$ chains/nm$^2$. The SLD of the core, shell and solvent are set to be 0.6,0.1,and 0.6 for Figure 4.2 (c), (d) and (e). SLD values are selected for the case of shell contrast only to see the shell. For the generated data in (d) the effect of the parameter, $N_c$, for the shell contrast is shown. In (e) the constituent parts of the scattering curves, chain-chain correlation, and chain term for the shell contrast with a thickness 10 nm are displayed. The Volume of the chain is set to be $V_{\text{chain}}$ = 100,000 Å$^3$ and was not varied for different thicknesses only to see the effect of the parameters used. It is noted that, for the fit of the experimental data, the volume of the chain is extracted from the molecular weight based on eq. 4.29.
Figure 4.2 (c) clearly shows that the scattering curves are shifted to lower q ranges as the thickness of the chains increases. The $q^{-2}$ behavior at high $q$ is characteristic of the Gaussian chains, described by the chain term, the Debye function. This term is called a density fluctuation term representing the fluctuation of the SLD of the polymeric shell. This $q^{-2}$ behavior at high $q$ is often shown in the scattering curves for polymer grafted particles or spherical micelles in a good solvent or a theta solvent. This term motivated the addition of the Debye function with a core-shell form factor in the scattering intensity. This will be described in the next section. Note that the variation of $N_c$ shown in Figure 4.2 (d) does not lead to a horizontal shift but leads to a vertical shift of the scattering curves as $N_c$ increases.
The aforementioned form factor had a corona shell with a Gaussian density profile and a single chain form factor without considering the interaction between chains. Pedersen [69, 70, 71] introduced form factors for models of spherical particles attached with interacting chains. The radial density profile of the corona shell was assumed to be of various types, and the chains were assumed to be interacting each other. The form factor squared, $P_{\text{int}}(q)$, is given by [69],

$$\begin{aligned} P_{\text{int}}(q) = {} & {V_{\text{core}}}^2 {\Delta\rho_{\text{core}}}^2 \cdot P_{\text{core}}(q) + N_c {V_{\text{chain}}}^2 {\Delta\rho_{\text{chain}}}^2 \cdot P'_{\text{chain}}(q) \\ & + 2N_c V_{\text{core}} V_{chain} \Delta\rho_{\text{core}} \Delta\rho_{\text{chain}} \cdot S_{\text{core-chain}}(q) \\ & + N_c (N_c - P'_{\text{chain}}(q=0)) \cdot {\Delta\rho_{\text{chain}}}^2 \cdot S_{\text{chain-chain}}(q) \end{aligned} \tag{4.32}$$

Note the difference between eq. 4.28 and eq. 4.32. The $P'_{\text{chain}}(q)$ used in eq.4.28, was a Debye form factor for a non interacting Gaussian chain. This is replaced by an effective single chain form factor to describe self-avoidance of the chains reflecting the interaction between grafted chains. This is given by [69]

$$P'_{\text{chain}}(q) = \frac{P_{ex\nu}(q)}{1 + \nu P_{ex\nu}(q)} \tag{4.33}$$

Here, $\nu$ is a parameter which increases with increasing concentration of the grafted chains and is related to the interaction between the grafted chains within the corona. Note that $P'_{\text{chain}}(q=0) = 1/(1+\nu)$. The other difference between eq.4.28 and eq.4.32 is a factor to scale $S_{\text{chain-chain}}(q)$, where $N_c(N_c-1)$ in eq. 4.28 is replaced by $N_c(N_c - P'_{\text{chain}}(q=0))$. The use of a term of $P'_{\text{chain}}(q=0)$ was intended to present the interaction between the chains. $P_{ex\nu}(q)$ is the form factor of self-avoiding chains with excluded volume interaction; the expression is given by [69]

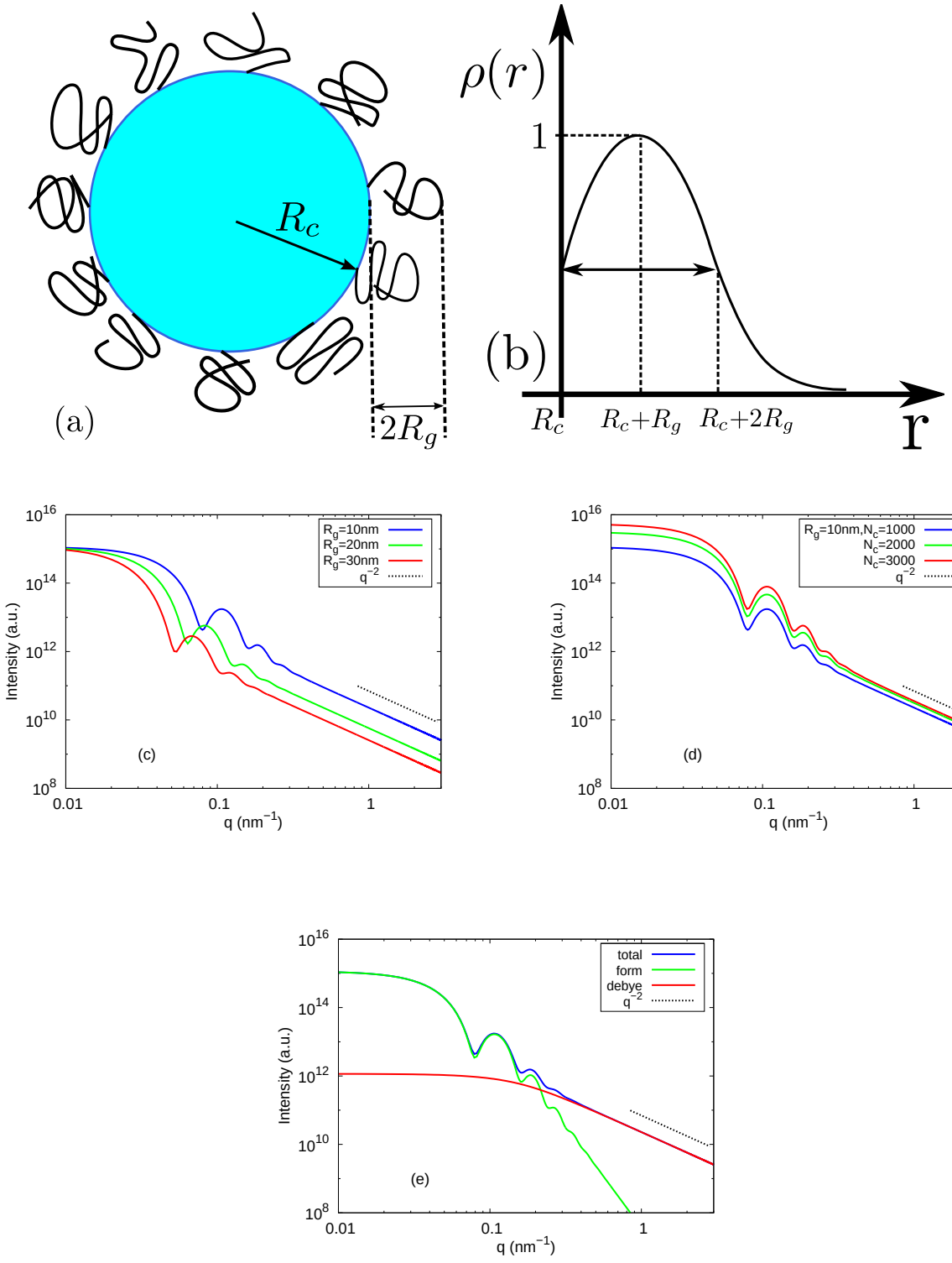


**Figure 4.2.:** (a): Schematic illustration of the spherical core-shell-chain model for a Gaussian density profile of a shell (model 1) [65] (b): Schematic representation of the Gaussian density profile of a shell, $\rho(r)$ [65]. (c): Calculated scattering intensities generated by eq.4.30 based on the core-shell-chain model for Gaussian density profile of a shell (model 1) in terms of eq.4.28 for a shell contrast with different $R_g$s (d): Those for a shell contrast with different $N_c$. (e): Scattering curves from $R_g = 10$ nm shown in (c) are decomposed into the contribution of chain-chain correlation and chain with a total scattering function.

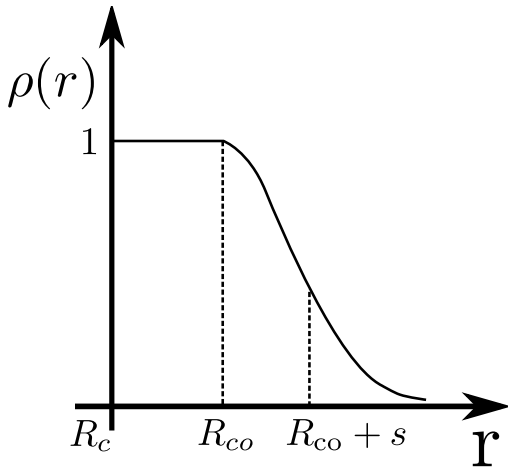


**Figure 4.3.:** Schematic illustration of box-Gaussian density profile of a shell shown in eq. 4.36.

$$P_{exv}(q) = \left[1 - w(qR_g)\right] \cdot P_{\text{debye}}(q) + w(qR_g) \cdot \left[C_1(qR_g)^{-1/\nu} + C_2(qR_g)^{-2/\nu} + C_3(qR_g)^{-3/\nu}\right] \tag{4.34}$$

$\nu$ is a Flory exponent to characterize the behavior of a single chain (see section 3.1), where $\nu$=0.5 is related to the ideal chain, the chain in a theta solvent, and $\nu$=0.6 to the real chain, namely the chain in a good solvent [69].

$$w(x) = \left[1 + \tanh((x - C_4)/C_5)\right]/2 \tag{4.35}$$

Constants of $C_1$, $C_2$, $C_3$, $C_4$, and $C_5$ were determined by the least square fit of the generated data from a Monte Carlo simulation. The least square fit gave $C_1$=1.22, $C_2$=0.4288, $C_3$=-1/651, $C_4$=1.523, and $C_5$=0.1477. Here, we note that, without excluded volume interaction, in the Gaussian configuration of a single chain, eq.4.34 is replaced by a classical Debye form factor. Eq.4.32 is a rather complicated approach to analyze data, and in our data, which will be shown in section of 6.1, there was a simple Gaussian chain behavior at high $q$ ranges. Consequently, we used $\nu = 0$ and disregarded the contribution of the chain-chain interaction. Then, the expression in eq.4.32 is reduced to eq.4.28, and the effective single chain form factor shown in eq.4.33 is replaced by eq.4.25, the classical Debye form factor.

**Box-Gaussian profile of shell – model 2**

Besides a description of the high $q$ scattering, to describe the low to intermediate $q$ scattering behavior of the given scattering curves, different forms of the radial density profile, $\rho(r)$, were introduced [69]. They are box-Gauss, a box function followed by a half Gaussian function, spline 2 and 3, the sum of two or three partial cubic b spline functions, the power law function, etc. Here, we introduce the box-Gaussian profile which will be used in the analysis of the experimental SANS data. This profile is schematically shown in Figure 4.3.
The box-Gauss profile has a box part between the core radius, $R_c$, and $R_{\text{co}}$ followed by the half Gaussian function with a width given by s (see Figure 4.3). Subscripts, c and co, denote the core and the corona. The corona denotes a part of the box-Gaussian profile having a constant density variation of the shell extended from r=$R_c$. The profile is [69]

$$\begin{aligned} \rho(r) &= 1 \text{ for } R_c \le r < R_{\text{co}} \\ \rho(r) &= \exp\left[-(r - R_{\text{co}})^2/(2s^2)\right] \text{ for } r \ge R_{\text{co}} \end{aligned} \tag{4.36}$$

The chain-chain correlation term, mentioned before, is described by [69]:

$$S_{\text{chain-chain}}(q) = A_{\text{chain}}(q)^2 \tag{4.37}$$

and

$$A_{\text{chain}}(q) = \left[4\pi \int \rho(r) \cdot \frac{\sin(qr)}{qr} \cdot r^2 dr\right] / \left[4\pi \int \rho(r) \cdot r^2 dr\right] \tag{4.38}$$

is the normalized Fourier transformation of the radial density profile of the corona chains on a spherical core. This can be analytically calculated as follows [69].

$$A_{\text{chain}}(q) = \frac{S_g(q) + V(R_{co})\Phi(qR_{co}) - V(R_c)\Phi(qR_c)}{V_0 + V(R_{co}) - V(R_c)} \tag{4.39}$$

where $V(R) = 4\pi R^3/3$, $V_0 = 2\pi[4R_{co}s^2 + \sqrt{2\pi}({R_{co}}^2 + s^2)s]$. $V_0$ is a volume of a part of the Gaussian profile.
Component $S_g(q)$ is as given by [69]:

$$\begin{aligned} S_g(q) = {} & \frac{4\pi s^2 \sin(qR_{co})}{q} + \frac{2\pi s}{q}\Big[\sqrt{2\pi} \cdot \exp(-q^2s^2/2) \cdot \left(qs^2\cos(qR_{co}) - R_{co} \cdot \sin(qR_{co})\right) \\ & + 2\sqrt{2}D(qs/\sqrt{2})\left(R_{co}\cos(qR_{co}) - qs^2\sin(qR_{co})\right)\Big] \end{aligned} \tag{4.40}$$

The function D(x) is the Dawson integral for which a numerical expression is found in [72].

$$D(x) = \exp(-x^2)\int_0^x \exp(t^2)dt \tag{4.41}$$

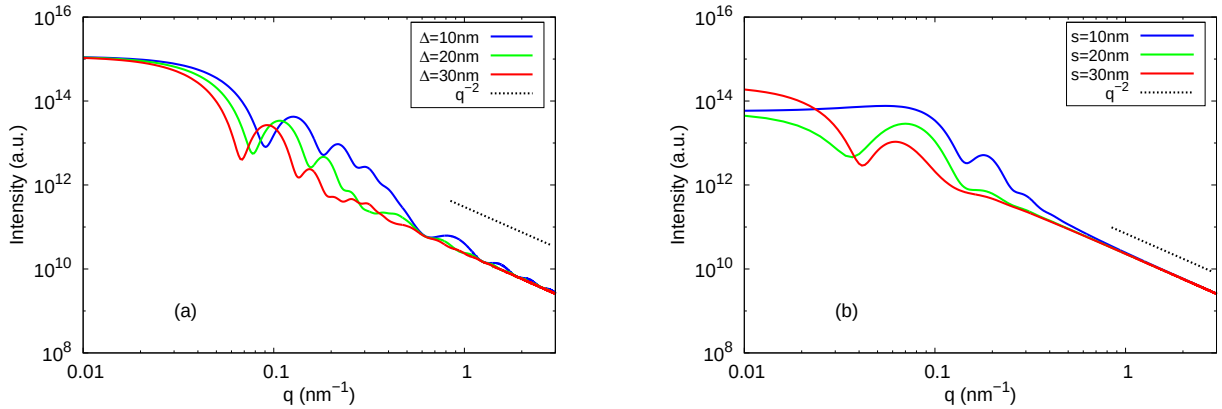


**Figure 4.4.:** (a): Calculated scattering intensities from eq. 4.30 based on the core-shell-chain model for box-Gaussian density profile of a shell (model 2) in terms of eq.4.28 with a variation of $R_{co}$ - $R_c$ = Δ, that is, the size of the corona by the model for shell contrast (b): Calculated intensities using the same function with a variation of s for shell contrast.

Figure 4.4 shows the scattering intensity from eq.4.30 calculated for the core-shell-chain model for the box-Gaussian density profile of a shell using eq. 4.28. Similar parameters to those in the previous calculation for the model for the Gaussian density profile of a shell, were chosen. The core radius, $R_c$ was

set to be 30 nm and for Figure 4.4 (a), corona thickness, defined by $R_{co}$ - $R_c$, namely $\Delta$, was varied and for Figure 4.4 (b), the size of gaussian profile, namely $s$, extended from the end of the corona shell, was varied (see Figure 4.3).
The input parameters for thickness, $\Delta$ for the former case and $s$ for the latter case, were 10, 20, and 30 nm and one given parameter for each case was varied only to see the effect of the given parameter for each calculation. As in the previous case of the core-shell-chain model for the Gaussian density profile of a shell, the polydispersity was set to be 0.1 which is a moderate value, and the number of chain, $N_c$, was set to be 1000, to yield a grafting density ∼0.09 chains/nm$^2$. The volume of the polymer chain was set to be 100,000 Å$^3$, and $R_g$ was fixed at 10 nm. The variation of parameter $\Delta$ in Figure 4.4 (a) shows the expected behavior of the scattering curves where an increase in $\Delta$ results in a shift of minima of the scattering curves to lower $q$ ranges. However, the variation of $s$ in Figure 4.4 (b) does not result in a shift of the minima to lower $q$ ranges. It is observed that the minimum shown at $q$ ∼0.1nm$^{-1}$ becomes smeared as the size of $s$ increases and the scattering pattern at low $q$ smaller than ∼0.03nm$^{-1}$, changes drastically as s increases. It is shown in the plot in Figure 4.4 (b) that characteristic oscillations at $q$ larger than $q$ ∼0.2nm$^{-1}$ become smeared as s increases. If the calculated scattering curves in Figure 4.4 do reflect the grafted polymer chains, the SLD profile of the corona shell substantially, will not be linear or step-like but contain tails at its end, such as a parabolic or a hyperbolic profile. Therefore, smearing of curves as $s$ increases may precisely reflect the density profile of stretched polymer brush chains and can be applied to analyze the experimental small angle scattering data, as will be shown later.

### 4.3.2 Core-shell model added with chain form factor

**Core-Shell form factor**

We now introduce simple models for the description of the polymer grafted nanoparticles in a dispersion medium, compared to the models introduced by Pedersen. Various model functions for the description of SANS data from the polymer layer attached to the nanoparticle or spherical micelle in a good solvent or a theta solvent have been implemented [10, 43, 67, 73]. Besides the models introduced by Pedersen, most approaches have implemented the core-shell form factor with an additional term to describe a high $q$ scattering, usually $q^{-2}$ decay as a function of $q$. For the core-shell form factor, the radial density profile for the shell was theoretically expected to be a power law type [42] or a parabolic type [45] as introduced previously. The power law [43] or parabolic type [73] density profile have been successfully applied to analyze the SANS data. It is noted that the radial density profile is assumed to be centrosymmetrical and that the core-shell form factor contributes to a $q^{-4}$ decay, usually at the low to intermediate $q$ range.
We applied the linear density profile, as the application of the linear density profile is expected to become reliable for the low SLD contrast between the shell and dispersion medium, the solvent, as the low contrast does not lead to fine variation in the density profile [74]. The various models for the analysis of the SANS data of polymer coated particles will be discussed again in section 5.1. The form factor of the spherical core surrounded by a shell with a linear density profile can be calculated as a homogeneous spherical core with a linear extension of the SLD variation from the surface of the particle to the size of the corona shell, $\Delta$, which is given by

$$F_{cs}(q,R) = (\rho_{core} - \rho_{sol}) \cdot F_{core}(q,R_c) + (\rho_{sh} - \rho_{sol}) \cdot (4\pi \int_{R_c}^{R_c+\Delta} \rho(r) \frac{\sin(qr)}{qr} r^2 dr) \qquad (4.42)$$

The subscripts cs, core, and sol represent the core-shell, core, and solvent, respectively. Correspondingly, $\rho_{core}$ and $\rho_{sol}$ are the SLD of the core and solvent, respectively. $\rho_{sh}$ is the SLD of the shell at the core-shell interface. $F_{cs}(q,R)$ is a core-shell form factor with a core with a homogenous SLD with a shell with various density profiles and $F_{core}(q,R)$ is the form factor amplitude of a sphere without contribution of

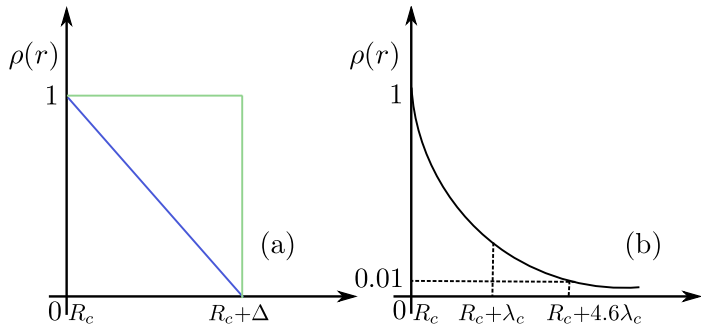


**Figure 4.5.:** Schematic representation of density profiles of (a): linear (blue) and step-like (green) and (b): exponential. For the exponential density profile, the characteristic length scale $\lambda_c$ was introduced, as shown in (b). 1% in amplitude of the exponential function corresponds to the radial extension of $R_c+4.6\lambda_c$. In the following calculated data in Figure 4.6, $4.6\lambda_c$ from the exponential density profile was set to be $\Delta$ for other profiles to obtain a commensurate thickness parameter.

volume and SLD contrast shown in eq.4.24.
$\rho(r)$ is the SLD profile of the corona from the core surface to the radial extension $\Delta$ to the dispersion medium. The above expression in eq. 4.42 can be analytically calculated (see appendix). The linear density profile of the corona is given by

$$\rho(r)^{\text{lin}} = 1 - \frac{r - R_c}{\Delta} \ (R_c < r < R_c + \Delta). \tag{4.43}$$

The core-exponential shell model is introduced for a description of the polymer coated nanoparticle systems as a second alternative. As in the previous case, the core is assumed to have a homogeneous SLD profile, while the shell has exponential decay as a function of the distance r extending away from the surface of the core. The core-exponential shell is also analytically calculated using eq. 4.42 (see appendix). The exponential density profile is given by

$$\rho(r)^{\text{exp}} = \exp(-\frac{r - R_c}{\lambda_c}) \ (r > R_c). \tag{4.44}$$

The superscript of "exp" represents the exponential density profile of the shell. $\lambda_c$ is a characteristic thickness parameter for the exponential profile. For a comparison, the most commonly used core-step-like shell model will be introduced. The core-step-like shell model has a constant density profile of the shell as given by,

$$\rho(r)^{\text{step}} = 1 \ (R_c < r < R_c + \Delta). \tag{4.45}$$

If the density profiles in eq. 4.43, eq. 4.44 and eq. 4.45 are inserted into eq. 4.42, core-shell form factor is constructed. Each density profile is schematically shown in Figure 4.5.
The differential scattering cross section, the scattering intensity, can be calculated by means of the core-shell form factor shown in eq. 4.42, as given by

$$\left(\frac{d\Sigma}{d\Omega}\right) = \phi \cdot \frac{\left\langle \left| F_{\text{cs}}(q,R) \right|^2 \right\rangle}{\langle V_{\text{total}} \rangle} + I_b. \tag{4.46}$$

$I_b$ is the experimental background. $V_{\text{total}}$ is the volume of the core-shell particle and is calculated by

$$V_{\text{total}} = \int_{R_c}^{R_c+\Delta} \rho(r) \cdot 4\pi r^2 dr \tag{4.47}$$

where $\Delta$ is a radial extension of the corona shell, and for the core-exponential shell model, an equality of $\Delta = 4.6\lambda_c$ was used to calculate the total volume. The volume $V_{\text{total}}$ and the squared form factor $\left|F_{\text{cs}}(q,R)\right|^2$ were then averaged with respect to the Schulz distribution function, as previously introduced. The contribution of the structure factor will not be considered as before since $S(q) \approx 1$ at a high dilution limit.

In the following, the scattering intensity from the form factor of the core-step-like shell, the core-linear- and the core-exponential-shell will be calculated, based on proximity of the experimental data as done previously. The scattering intensity will be calculated in terms of eq. 4.46 for each density profile. The calculated scattering curves are expected to show different behavior for the same set of parameters. For the whole models investigated here, the core radius is set to be 30 nm and relatively moderate polydispersity of $\sigma_x = 0.1$ is used. The SLD of the core, shell and solvent are set to be 0.6,0.1,and 0.6 for the shell-contrast situation for Figure 4.6. For the linear and step-like shell model, $\Delta$ is set to be 10 nm. For the exponential model, $\lambda_c$ instead of $\Delta$ will be used as a measure of the thickness. $\lambda_c$ will have a size of 2.2 nm, a small size compared to the linear and step-like shell model. It is noted that the exponential function decays rapidly compared to the linear and step function. If the exponential function in eq. 4.44 decays to 1% in amplitude, the radial extension $r$ becomes $R_c + 4.6\lambda_c$ (see Figure 4.5). Therefore in order to satisfy an equality of $\Delta = 4.6\lambda_c$, the thickness value of 10 nm was divided by 4.6 to obtain the same value compared to other models.

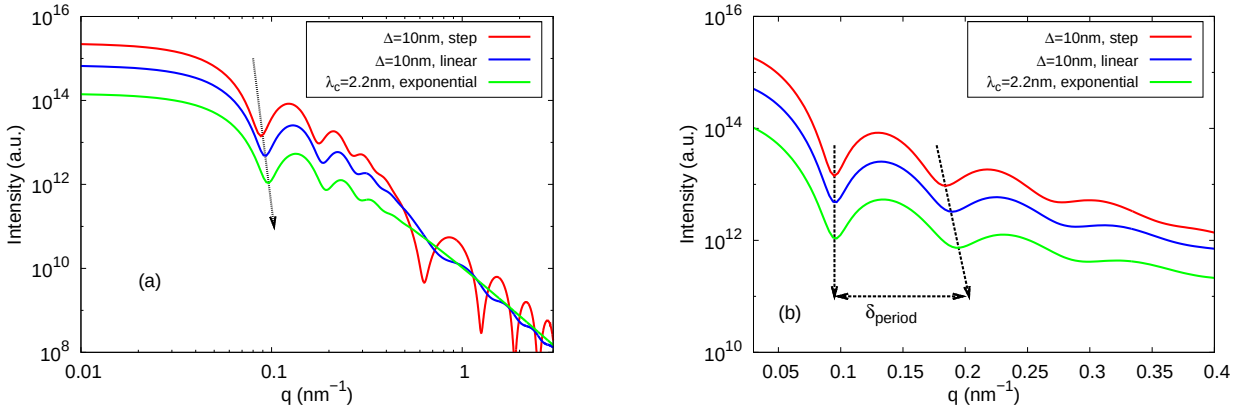


**Figure 4.6.:** (a): Comparison of calculated scattering curves from eq.4.46 for the core-linear, the core-exponential and the core-step like shell model, respectively. The thickness for the linear and step-like shell model was set to be 10 nm. The thickness parameter $\lambda_c$ from the exponential density profile was set to be 2.2 nm to have a commensurate value with $\Delta$= 10nm. Arrow indicates the shift of the first minimum (see text). (b): Scattering curves based on core-step like and -linear profile were horizontally shifted to have the same position of the first minimum as the scattering curves based on the core-exponential shell model, in order to see the change in the period between the first and second minimum. Note that, for (a), the plots are presented in log-log scale, for (b), in linear-log scale.

In Figure 4.6 (a), (1): the position of the first minimum is shifted to a higher $q$, and in Figure 4.6 (b) (2): the period $\delta_{\text{period}}$ between minima increases, as the model is varied from the core-step like shell, -linear to -exponential shell model. In order to compare the period, the scattering curves based on the core-step-like shell and -linear shell were horizontally shifted to have the same position for the first minimum as the curves based on the core-exponential shell. Besides these two features, at a large $q$, the scattering

curve from the core-step-like shell model is distinguished by the pronounced oscillation pattern, while the scattering curve from core-linear and -exponential shell model exhibit damped oscillation. Note that the intensity at $q \to 0$ goes to $\Phi \cdot V_p \cdot \Delta\rho^2$ as shown in eq. 2.35; therefore, the largest amplitude of intensity at low $q$ for the core-step like shell model stands to reason since the calculation of volume (see eq.4.47) and density (see Figure 4.5) for the core-step-like shell will be largest if different density profiles in Figure 4.5 are considered.

**Density fluctuation term**

$q^{-2}$ behavior of the scattering curve arises from the thermal density fluctuation within the polymer layer on the surface of the nanoparticles, which is experimentally observed at a high $q$ range with a small angle scattering experiment. This behavior was first introduced to describe the thermal fluctuation of a semidilute polymer in a good solvent [75]. In order to express $q^{-2}$ behavior for a scattering curve from polymer grafted nanoparticles, also motivated by Pedersen's approach described in the previous section, the Debye function has been implemented [10, 74, 76, 77].

$$I_{\text{fluct}}(q,\xi) = 2G\frac{\exp(-q^2\xi^2) - 1 + q^2\xi^2)}{q^4\xi^4}. \tag{4.48}$$

Here, $\xi$ is a correlation length and G is a constant. The size of $\xi$ may show the detailed conformation of the grafted polymer, and this has been used for grafted chains in good solvents [76, 77] and in a theta solvent [10]. Over the whole range of $q$, eq. 4.48 can be approximated well by [16]

$$I_{\text{fluct}}(q,\xi) \approx G\frac{1}{1 + q^2\xi^2/2} \tag{4.49}$$

In order to analyze the SANS data, the fluctuation term introduced here was superimposed on the intensity described in eq. 4.46 to describe the $q^{-2}$ behavior of the scattering curves from polymer grafted nanoparticles suspended in either good solvents or polymer matrices. The overall intensity of the polymer grafted nanoparticles is finally given by

$$\left(\frac{d\Sigma}{d\Omega}\right) = \phi \cdot \frac{\left\langle \left|F_{\text{cs}}(q,R)\right|^2 \right\rangle}{\langle V_{\text{total}} \rangle} + I_{\text{fluct}}(q,\xi) + I_b. \tag{4.50}$$

It has been reported that the contribution from the fluctuation term in the scattering curves for the grafted chains in good solvents becomes larger as the grafted chains become more swollen and smaller when the grafted chains become unswollen [11]. In chapter 5, the $\xi$ obtained from SANS data fits will be explicitly shown for the systems of PS grafted silica and d-PS nanoparticles and discussed in more detail.

## 4.4 Conclusion

Based on the calculation of SAS intensity introduced in the beginning, this chapter was devoted to introducing the form factors of the core-shell-chain model and the core-shell model added with a fluctuation term, used in the analysis of the experimental small angle scattering data of more specifically polymer coated nanoparticles, and to investigating the effect of the various parameters on the change in the scattering curves. Model independent approaches of Porod's law and Guinier's law were first introduced and are often used to obtain physical quantities, such as the specific surface and radius of gyration. Analysis beyond these basic theories, the complete fitting of the scattering data, will be enabled by applying the geometrical models to study the structure of the materials of concern in more detail.

Various models were then introduced to calculate the small angle scattering intensities of the spherical core with a diffused corona shell as a function of $q$ in a shell contrast condition. First the spherical core-shell-chain model for the Gaussian SLD profile of a shell (model 1), introduced by Pedersen, was introduced, and data have been generated for the various sets of the parameters for the shell contrast. The effects of the parameters of thickness and the number of attached chains, on the change in the scattering curves were investigated. Especially for this model description, the characteristic high $q$ scattering term, $q^{-2}$ decay at high $q$ ranges, was included as a form of Debye function, phenomenologically. A more advanced model by Pedersen was introduced, where the corona shell has the radial distribution of box Gaussian profile and the chain form factor is described by an effective single chain form factor. However, for simplicity in the data analysis, the rather complicated effective single chain form factor was not used for the calculation, as a high $q$ scattering often displays only Gaussian chain behavior, $q^{-2}$ behavior. This simple approach will be implemented in the analysis of our SANS data. For the core-shell-chain model for a box-Gaussian profile of a shell (model 2), data were generated to see the effect of the parameters, especially corona thickness, $\Delta$, and the width of the Gaussian profile extended from the end of the corona thickness, named s, on the change in the scattering curves. An increase in $\Delta$ resulted in a shift of the minima of the scattering curves to characterize the size of particles, to the lower $q$ range, but that of $s$ did not lead to a shift of the minima to lower $q$ ranges and resulted in smearing of oscillations appeared at the intermediate to the high $q$ range.

As a second approach, the model of the core-linear and exponential shell as well as -step-like shell were introduced, and the corresponding form factors have been calculated. We note that, for generated data, the high $q$ scattering term, which can be simply added to the total intensity calculation, was not included. It was seen from the calculated curves that the position of the first minimum is shifted to a higher $q$ and the period between minima increases as the model varies from core-step-like shell, linear and exponential shell. Additionally, at large $q$, damped oscillation appears as the model varies from core-step-like shell, linear and exponential shell.

Among the various models introduced here, the core-linear shell model and the core-shell-chain model for a box-Gaussian or Gaussian profile of a shell will be implemented for the SANS data analysis from PS grafted silica and d-PS particles and the resulting fits from the functions will be shown, in order to judge whether the used fit functions described the experimental data effectively well. The fit function will then be chosen based on the fit quality and fit parameters, which should physically make sense. The detailed explanation and discussion for choosing a fit function for data analysis will be another issue in the experimental results, which will be shown in chapter 5 and 6.

# 5 Polymer grafted nanoparticles in a good solvent

The conformation of grafted chains may differ from that of the free chains in the bulk state. Depending on the grafting density, the length of the chains (molecular weight), and the curvature, the conformation of the grafted chains will become drastically different from that of free chains in a good solvent. Here, the conformation of grafted polymers (PS) on spherical nanoparticles (silica or deuterated PS) will be investigated extensively by experimental methods. SANS, SAXS, DLS, and TEM will be combined to reveal the conformation feature of the grafted PS chains in good solvents, toluene or THF. Nanoparticles of rather large sizes (diameter = 40 to 60 nm) will be provided for spherical substrates, and the grafting density and molecular weights will be varied to determine the impact of those parameters on the change in the conformation of the grafted PS chains. The use of silica and d-PS spherical particles is also expected to contribute to the change of the grafted PS chain conformation and the effect of difference in the substrates will be experimentally investigated as well.
The scaling concepts introduced in section 3.2.1 can be easily used in the experiments to gain insight into the conformation feature of the grafted chains. Therefore, in our study, we applied the scaling concepts to describe the relation of the thickness of the grafted chains with the grafting density, the length of the grafted chains, and the curvature, so that theoretical expectation included in the scaling concepts will be validated by the experiments. Furthermore, the information on the conformation will be correspondingly revealed by the experimentally acquired scaling relation. In addition to the characterization of the grafted PS chains, a brief description of the synthesis of each particle system will be given as well.

## 5.1 PS grafted silica in a good solvent

The characterization of polystyrene (PS) grafted silica particles will be a topic of this chapter. This section will be written, based on our previous publication [74]. The methods used for the characterization will be SAXS, SANS, DLS, and TEM. Chemical details concerning synthesis of the bare, surface modified and grafted particles will not be described in detail but briefly.

### 5.1.1 Synthesis

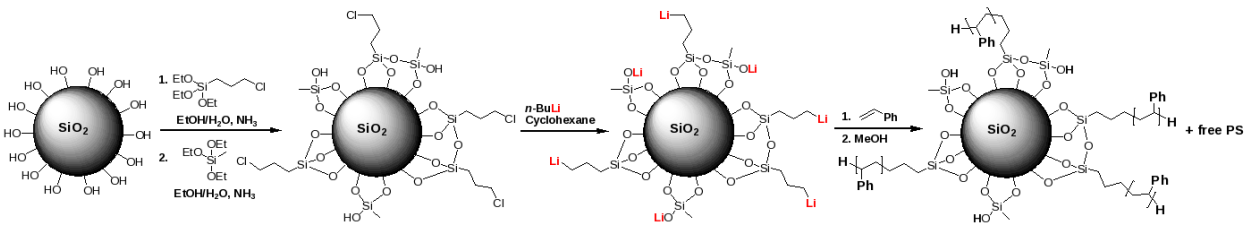


**Figure 5.1.:** PS on silica nanoparticles: applied surface-initiated anionic polymerization of styrene [78]

A suspension of bare silica particles was used as received from Merck (Monospher-Nano-Mü-145, step 1 in Figure 5.1). Bare silica particles originally dispersed in a mixture of ethanol and water (volume fraction = 7:3) were treated with (3-chloropropyl) triethoxysilane (step 2 in Figure 5.1) for the functionalization of the surface of the particles. For transferring in a nonpolar solvent, toluene was added

continuously, while ethanol was removed by vacuum distillation. The silica dispersion in toluene was diluted by adding dry cyclohexane. For surface initiated anionic polymerization styrene, n-BuLi was used as an initiator material and reaction was made in THF. Styrene was added in order to be terminated as a polystyrene of a desired molecular weight (step 4 in Figure 5.1). Free PS was removed by nanofiltration using an Anodisc 47 membrane from Whatman in cyclohexane. For characterization of surface-grafted PS, the chains were detached via etching the silica core with hydrofluoric acid.

### 5.1.2 Experimental methods

For SAXS and SANS measurements the reader can refer to section 2.2.2. A detailed description of DLS measurements can be found in section 2.3.2. TEM experiments were carried out on a Zeiss EM 10 electron microscope operating at 80 KV. All images shown were recorded with a slow-scan CCD camera obtained from TRS (Tröndle) in bright field mode. The camera control was computer aided using the ImageSP software from TRS.
Size exclusion chromatography (SEC) was performed with THF as the mobile phase (flow rate 1 mL $min^{-1}$) with a styrene-divinylbenzene (SDV) column set from Polymer Science Service (PSS) (SDV 1000; SDV 100,000 ; SDV 1,000,000) at 30°C. Calibration was carried out using PS standards from PSS, Mainz. For TGA (Thermogravimetric analysis), a TA instruments TGA Q-500 was used, and a temperature range from 35 to 750 °C and a heating rate of 10 $K \cdot min^{-1}$ under oxygen atmosphere was applied.

### 5.1.3 Results and discussion

#### Characterization of bare and surface modified silica nanoparticles

The different experimental methods of SAXS, SANS, DLS and TEM will be combined to characterize bare and surface modified silica particles and allow a comparison of the results of different experimental approaches. DLS determines the hydrodynamic radius of the bare and surface modified particles. The particles were synthesized in an ethanol/water mixture (7:3 volume ratio; see step 1 and 2 in Figure 5.1.). A series of concentrations was prepared by merely adding solvent mixture to dilute the initially made suspension in ethanol and water to obtain the desired weight fraction. The correlation function was measured in a range of scattering angles, usually from 50° to 130° and analyzed by the second order cumulant method shown in eq. 2.63.
To begin with, DLS results of the bare particles will be shown. Figure 5.2 (a) shows representative results for a concentration of c=0.08 wt%. The correlation functions are found to be very close to single exponential. For each $q$, we use equation $\overline{\Gamma} = Dq^2$ for a diffusive motion. Here, D is a diffusion coefficient, $q$ is a scattering vector, and $\overline{\Gamma}$ is a mean relaxation rate as described in section 2.3.1. In Figure 5.2 (b), the variation of $\overline{\Gamma}$ is shown in dependence on $q^2$. The data follow the expectation for the particle diffusion and thus allow the determination of a diffusion coefficient and a hydrodynamic radius applying eq. 2.53 in section 2.3.1. For each concentration we can determine an effective hydrodynamic radius and extrapolate to zero concentration. The extrapolations for the bare and surface modified silica particles are shown in Figure 5.2 (c) and (d), respectively. The extrapolated value is $R_H$ = (38.3 ± 1.1) nm. The viscosity ($\eta$) and the refractive index (n) of the ethanol and water mixture were interpolated, considering the mole fraction of ethanol in aqueous solution, which were found to be 2.433 cP ($10^{-3}$ Pa·$s$ = kg/(s · m). ) [79] and 1.3645 [80, 81, 82] at 20°C. The refractive index of the mixture was taken for $\lambda$ =589.3 nm (in our case $\lambda$ =632.8 nm) which was found to deviate slightly for $\lambda$ =632.8 nm, with a negligible deviation ≈ $10^{-3}$ [82]. Measurements were carried out at 20°C.
In the next step, the silica particles were surface-modified with (3-chloropropyl) triethosilane to yield the precursor groups, and the particles were dispersed in the same ethanol/water mixture. Here, the hydrodynamic radius determined by DLS was found to be $R_H$ = (35 ± 0.8) nm. It is thus smaller

than the $R_H$ of the unmodified particles. The variation of $\overline{\Gamma}$ with $q^2$ is included in Figure 5.2 (b). The difference between $R_h$ of the bare particle and that of the surface modified particle may be attributed to the different surface structures. The smaller number of OH bonds on the surface of the modified particles results in a faster diffusion and thus in a smaller $R_H$. Close inspection of the data in Figure 5.2 (b) shows that the data deviate from the straight line at a small $q$. This may be caused by the slightly non-spherical shape of the particles, which is also observed in TEM (see Figure 5.4).

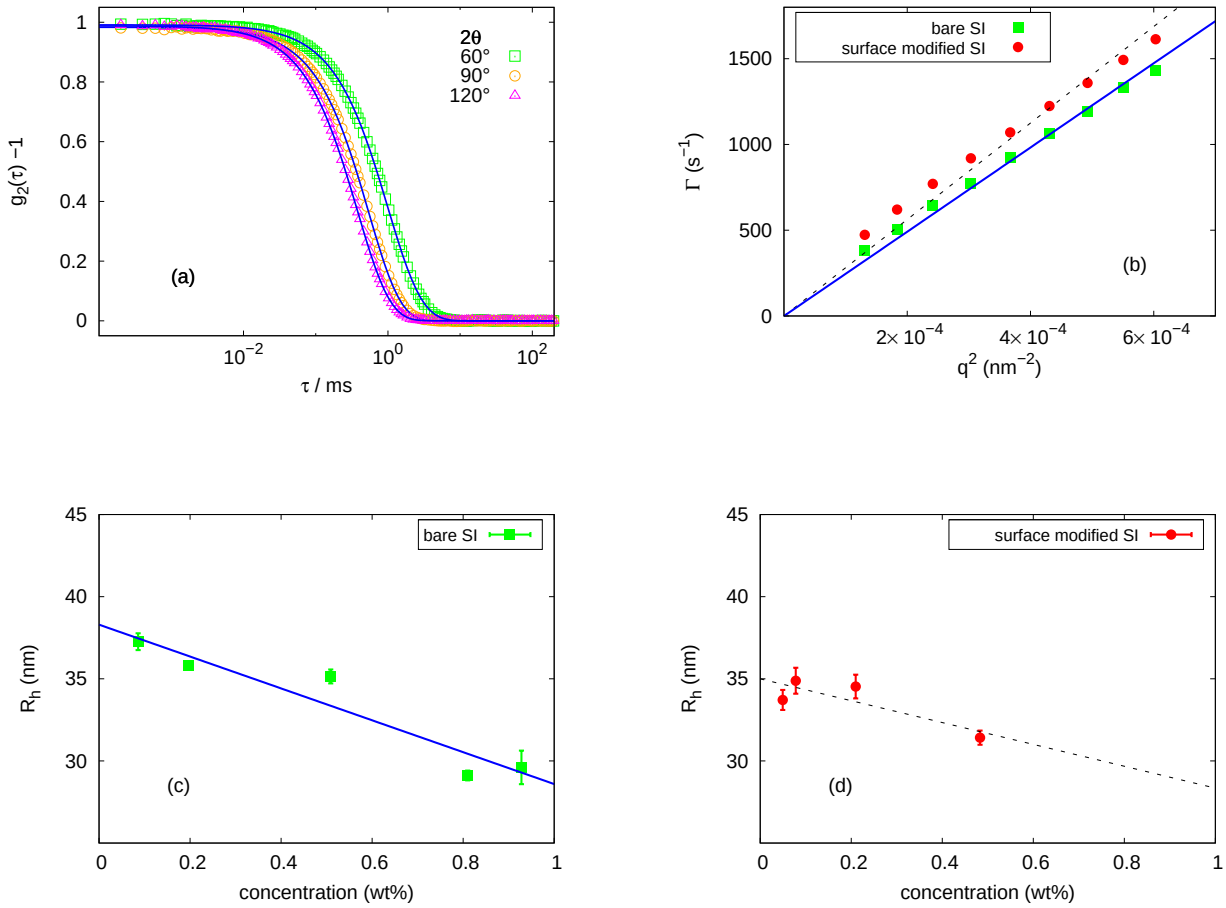


**Figure 5.2.:** (a): Intensity autocorrelation function of a bare silica in an ethanol/water mixture (0.08wt%) at selected angles as an example. Solid line presents fits using a cumulant analysis. (b): $q^2$ dependence of $\Gamma$ to determine the diffusion coefficient for a bare silica particle (square, green) and a surface modified particle (circle, red). Solid and dotted line present the linear fit to obtain D. (c): Concentration dependence of $R_h$ to obtain an extrapolated value for the bare particle. (d): Concentration dependence of $R_h$ to obtain an extrapolated value for the surface modified particle.

The same bare and surface-modified particles dispersed in an ethanol and water mixture at a concentration of 0.2 wt% were also analyzed by SAXS. Figure 5.3 compares these results for both systems in ethanol/water. It is obvious that the scattering pattern for the two samples is very similar. It shows the features of single particle scattering with a shoulder in $I(q)$ resulting from intraparticle interference. We therefore used a single particle scattering function to fit the data. The total intensity is then given as,

$$I(q) = k\left\langle |F(q,R)|^2 \right\rangle + I_b. \tag{5.1}$$

The patterns are well described using a model of a solid spherical particle with a form factor $F(q,R)$, as introduced in eq. 4.13 in section 4.1. The intensity is scaled with k, and a flat background (in the

neutron case arising from incoherent scattering, usually from the solvent) with a parameter $I_b$. The former description is a general calculation encompassing SAXS and SANS since the intensity of SAXS is not in an absolute unit. For the neutron case, the calculation is

$$I(q) = \phi \frac{\left\langle |F(q,R)|^2 \right\rangle}{\left\langle V_{\text{particle}} \right\rangle} + I_b \tag{5.2}$$

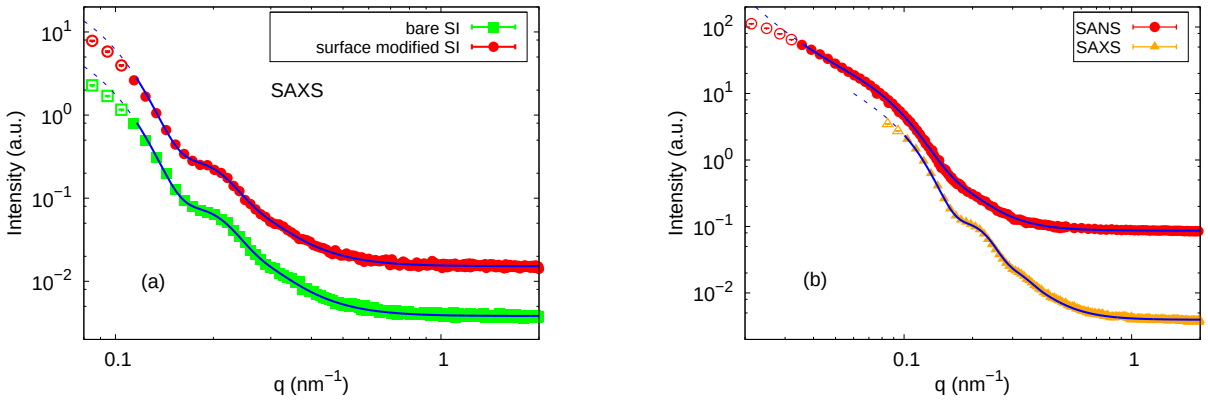


**Figure 5.3.:** (a): SAXS data of bare (lower, green) and surface modified silica (upper, red) dissolved in 0.2wt% ethanol and water mixture. Solid lines are fits with the spherical form factor. The curve of surface-modified silica was vertically shifted for clarity. Open symbols indicate those that were not taken into account in the data analysis. (b): SAXS (lower, orange) and SANS (upper, red) data from surface modified silica dissolved in 0.5 wt% deuterated THF. Solid lines are fits with eq.5.1 including term $Cq^{-\alpha}$ in eq.4.11. Open symbols were not taken into account to fit the data.

$\phi$ is the volume fraction of the particles. The brackets <..> in eq. 5.1 and 5.2 denote an average with respect to the size distribution, a Schulz distribution of particle radii as discussed in section 4.1. In Figure 5.3 (a) the fits using eq.5.1 are included as a line. It is seen that the model of a spherical particle describes our data very well. As a result of the fits, we find the average radius for both samples to be ∼26 nm and the width of the size distribution is ≈18%. The width of the size distribution from SAXS is found to be significantly larger than PDI obtained from DLS, which are found to be ≈2 % for the bare and ≈3% for the surface modified, respectively. As discussed in section 2.3.1, a low value of PDI provides a small deviation between $R_{\text{conv}}$ and $R_h$. Therefore, for the surface modified particle, $R_h$ showed a small difference with $R_{\text{conv}}$ obtained by eq. 2.65.
If however $R_{\text{conv}}$ and $R_c$ from SANS or SAXS are compared, a large deviation between two sizes is observed clearly. The reason for the deviation between $R_{\text{conv}}$ and $R_c$ for the surface-modified particle, may be due to a non-spherical shape of the surface modified particle as is seen in Figure 5.4 since the conversion formula shown in eq.2.65 was assumed to be applied to the "spherical" particles.
The polystyrene grafted particles will be characterized in THF. Therefore, we also investigate the structure of surface-modified particles in the same solvent. Here, SAXS and SANS results will be compared for the surface-modified particles dispersed in deuterated THF (d-THF). Figure 5.3 (b) compares the results from SANS and SAXS for surface-modified particles at c=0.5 wt%. Data from SANS extend to a much lower $q$ and reveal the existence of aggregates in the sample. The scattering curve from the SAXS measurements clearly shows a better resolution as shown in the more pronounced shoulder in $I(q)$ compared to that from the SANS measurement. At a small $q$, a contribution of scattering from aggregates is seen in particular in the SANS data. In order to account for this additional scattering in the low $q$ range, the phenomenological $Cq^{-\alpha}$ term shown in eq. 4.11 is added to eq. 5.1. It is then possible to obtain a

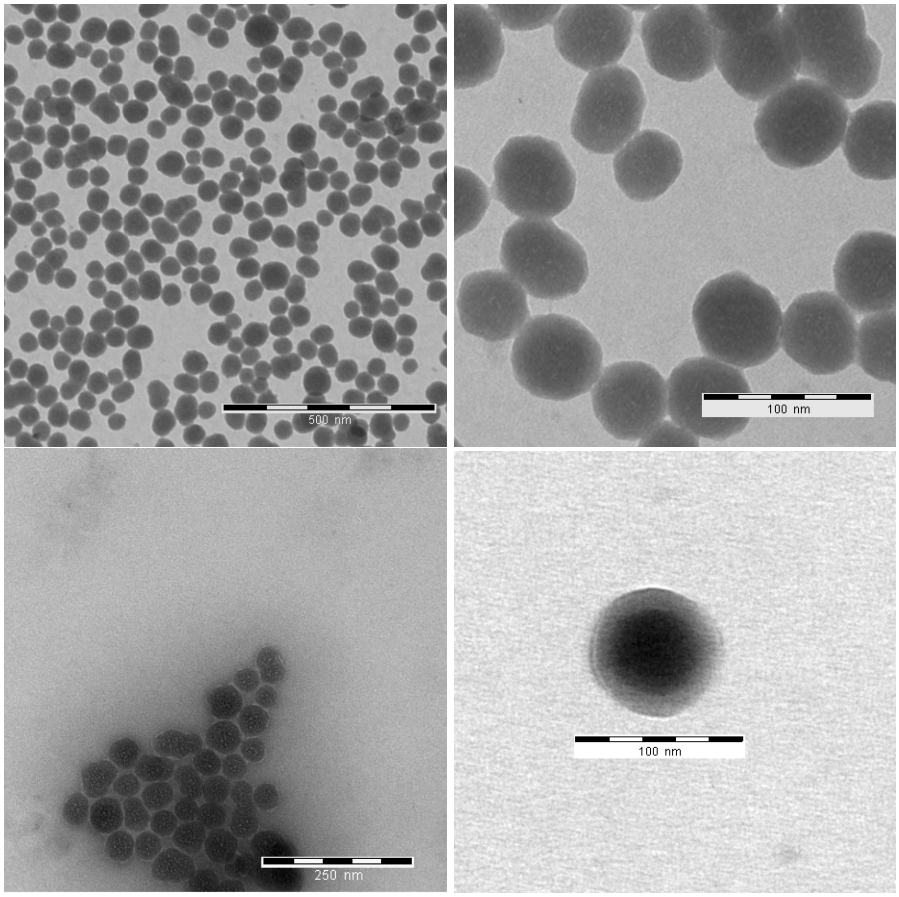


**Figure 5.4.:** TEM images of bare silica nanoparticles (upper images) and PS grafted silica nanoparticles (images below) prepared by using the drop-cast method of their dispersion on carbon-coated copper grids

good fit within a wide $q$ range, as demonstrated by the lines included in Figure 5.3. Porod's law for the scattering from large particles would result in an exponent $\alpha = 4$. Fitted values are $\alpha \approx 3.6$ for SAXS and $\alpha \approx 3.4$ for SANS. The particle sizes obtained from the fits are ∼25.6 nm for SAXS and ∼23.3 nm for SANS. The SAXS value is consistent with the result obtained in ethanol/water. The slightly smaller value obtained in the SANS experiment may be caused by the rather wide wavelength distribution of KWS-2 [83]. We do not attempt to correct for this effect, but the value obtained here for the surface-modified silica particles will be used in the modeling of data for the grafted particles.
TEM investigations of both the bare and the polymer grafted nanoparticles are shown in Figure 5.4 and clearly reveal a shell for the PS grafted silica nanoparticles. Grafted particles are well dispersible in common organic solvents and tend to form films during the drying process of the TEM sample preparation. The picture shows that the bare particles are not completely spherical in shape, as discussed in the analysis of DLS data for bare and surface modified particles. The mean size of the bare particle was estimated to be (25.7 ± 4.7) nm along the major axis and (23.6 ± 4.7) nm along the minor axis, showing that the particles are slightly ellipsoidal in shapes. Therefore, the deviation of the converted radius $R_{\mathrm{conv}}$ and $R_{\mathrm{c}}$ from static scattering of the surface modified particle due to the non spherical shape of the particle could be verified by the TEM picture.

### Investigation of the conformation of grafted PS chains on silica nanoparticles

In this section, the main focus will be the determination of the conformation of grafted PS chains on silica nanopartciles in a good solvent, THF. SANS, SAXS, and DLS will be combined to reveal the structural properties experimentally in detail. Prior to these characterization, free PS and grafted PS chains were

investigated by SEC. We note that the molar mass of "free PS" was taken from freely formed bulk PS by a sacrificial initiator, and that of grafted PS was taken from PS detached from the silica core with hydrofluoric acid (HF). The results are shown in Table 5.1 with a corresponding diagram of the molecular weight distribution of grafted PS in Figure 5.5. In Table 5.1, it can be concluded that the molar masses of chains are slightly lower than those of freely grown chains and additionally show higher polydispersities, similar to the work of Zhou et al. [84].

**Table 5.1.:** Molar masses were determined with SEC. In the case of surface-grafted PS, the chains were detached via etching the $SiO_2$ particles with hydrofluoric acid. For sample 1, no grafted PS chains could be obtained after etching due to a very low grafting density.

| **Sample** | $\mathbf{M_{w,grafted}}$ $[g \cdot mol^{-1}]$ | $\mathbf{PDI^{grafted}_{SEC}}^{a}$ | $\mathbf{M^{w,free}}$ $[g \cdot mol^{-1}]$ | $\mathbf{PDI^{free}_{SEC}}^{a}$ | **Grafting Density**$^{b}$ $[chains \cdot nm^{-2}]$ |
|---|---|---|---|---|---|
| 1 | — | — | 17,200 | 1.13 | — |
| 2 | 25,400 | 1.23 | 31,800 | 1.08 | 0.032 |
| 3 | 42,000 | 1.29 | 55,200 | 1.12 | 0.015 |

a) PDI indices shown here were determined by SEC measurements. $PDI_{SEC} = \frac{M_w}{M_N}$ where $M_w$ is weight average molar mass and $M_N$ is number averaged molar mass, respectively. b) Grafting density determined by TGA compared with initiator-functionalized silica nanoparticle. The weight loss used was estimated in the temperature range between 260°C to 750°C.

In the case of SEC measurements of the surface-detached PS after etching, a shoulder in the molecular weight distributions appeared. The maxima of the curves agree quite well with the maxima obtained from SEC measurements for the free PS chains. An overlay for samples 2 and 3 is shown in Figure 5.5. The first explanation is that preliminarily purified particles still contain free PS, which is not attached to the particle's surface and generated by free living anionic polymerization initiated by the sacrificial initiator. Hence, an exemplary sample was, additionally, after the previously described purification steps involving nanofiltration, treated in the following way by ultracentrifugation. Ultracentrifugation of the polymer-grafted particle aliquot dispersed in THF was performed with an Avanti J-30I from Beckman Coulter for half an hour at a speed of 17,000 rpm. The supernatant THF was concentrated and investigated via SEC measurements. That step was repeated 12 times, and in no case could free polymer be observed. It can, therefore, be assumed that the bimodal distribution is proved to be of the origin of definitely surface attached PS chains. Due to the low grafting densities of the herein characterized polymers on the particles, which have been generated by the grafting-from approach yielding lower molar masses and broader molecular weight distributions, it turns out that freely polymerized styrene is able to attach by a subsequent grafting-onto process to the particle's surface. This would explain the bimodal distributions and, additionally, the difference in their shape, as surface-initiated anionic polymerizations typically reveal less defined polymers. Nevertheless, both- still narrowly distributed-polymers are covalently surface-attached, and all values obtained by following characterization methods can be attributed to surface-attached PS chains.

For silica nanoparticles, Prucker and Rühe [85, 86] and Böttcher et al. [87] reported that TGA is a reliable method to determine the amount of surface-attached initiators and polymers. Therefore, weight loss in the range of 260 to 750 °C was taken for calculation. As in the case of the bare and surface-modified particles, we applied DLS and SAXS for characterization of the grafted particles. In order to obtain more detailed information on the structure of the polymer layer, we make use of SANS. Using deuterated THF as a solvent, the contrast between the polymer layer and the solvent is enhanced.

In order to calculate the electron density and scattering length density, the mass density of silica was

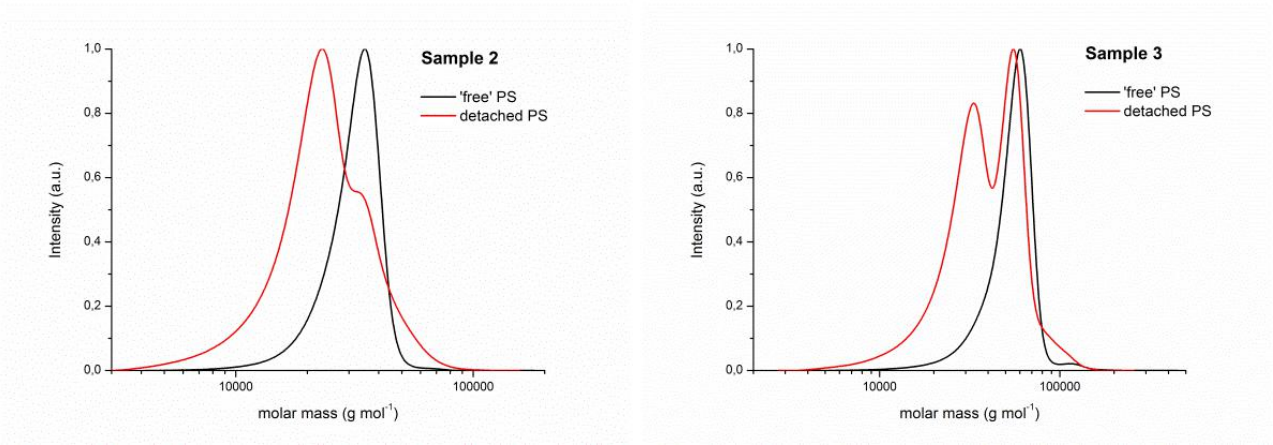


**Figure 5.5.:** Overlay molecular weight SEC measurement obtained for sample 2 (left) and sample 3 (right). The broader bimodally distributed curves (red) correspond to the surface attached PS, which have been detached by etching. The narrow monomodal distributions (black) correspond to free PS, which was initiated by the sacrificial initiator in solution.

taken as 1.85 g/ml [88]. The scattering length densities will be used for the fit of SANS, and the electron densities for SAXS data are discussed below. The electron density of PS is significantly closer to that of THF than to the silica core. The difference in contrast for SAXS and SANS experiments is seen directly by comparing the scattering length densities or electron densities given in Table 5.2. Therefore, a SAXS experiment will be more sensitive to the silica core. The SANS experiment, however, will have stronger contrast between the polymer and the surrounding matrix.

**Table 5.2.:** Scattering length densities and electron densities used for data fitting.

| compound | scattering length density ($10^{-4}$ nm$^{-2}$) | electron density (nm$^{-3}$) |
|---|---|---|
| $SiO_2$ | 2.92 | 556 |
| PS | 1.41 | 340 |
| d-THF | 6.35 | 296 |

In Figure 5.6 (a) and (b), we compare the results from both types of small-angle scattering experiments. Just as in the case of surface-modified particles, we find the SAXS data to be compatible with the model of spherical particles. THF as a good solvent apparently mixes so well with the grafted polymer layer, that a contrast between the swollen layer and the solvent is not seen in SAXS. That THF can be assigned as a very good solvent for PS can also be pointed out from the Hansen solubility parameters, whose values are very similar (PS, 22.7 MPa$^{0.5}$; THF, 19.4 MPa$^{0.5}$) [89, 90]. Fits of this model are included as full lines in Figure 5.6. We thus determine the core radius of the grafted particle, making use of the particular scattering contrast of SAXS to be (26.2± 0.1 nm), which is in good agreement with the value found for the bare particles. The SANS data shown in Figure 5.6 (b) display a variation in intensity with a $q$ that differs clearly from the SAXS data. A steep decrease in intensity at low $q$ is followed by a variation $\sim 1/q^2$ at larger $q$. This is a strong indication of the existence of a polymer layer on the outside of the silica particle. Indeed, a detailed fit of the data is no longer possible with the model of a simple sphere with homogeneous scattering length density. In addition, the extension of this model to core-shell particles with a shell of contrast density fails to describe the data adequately. This model would not be able to account for the $\sim 1/q^2$ variation of intensity at a large $q$. We are, therefore, led to apply a more detailed model for the variation of scattering length density within the polymer layer that

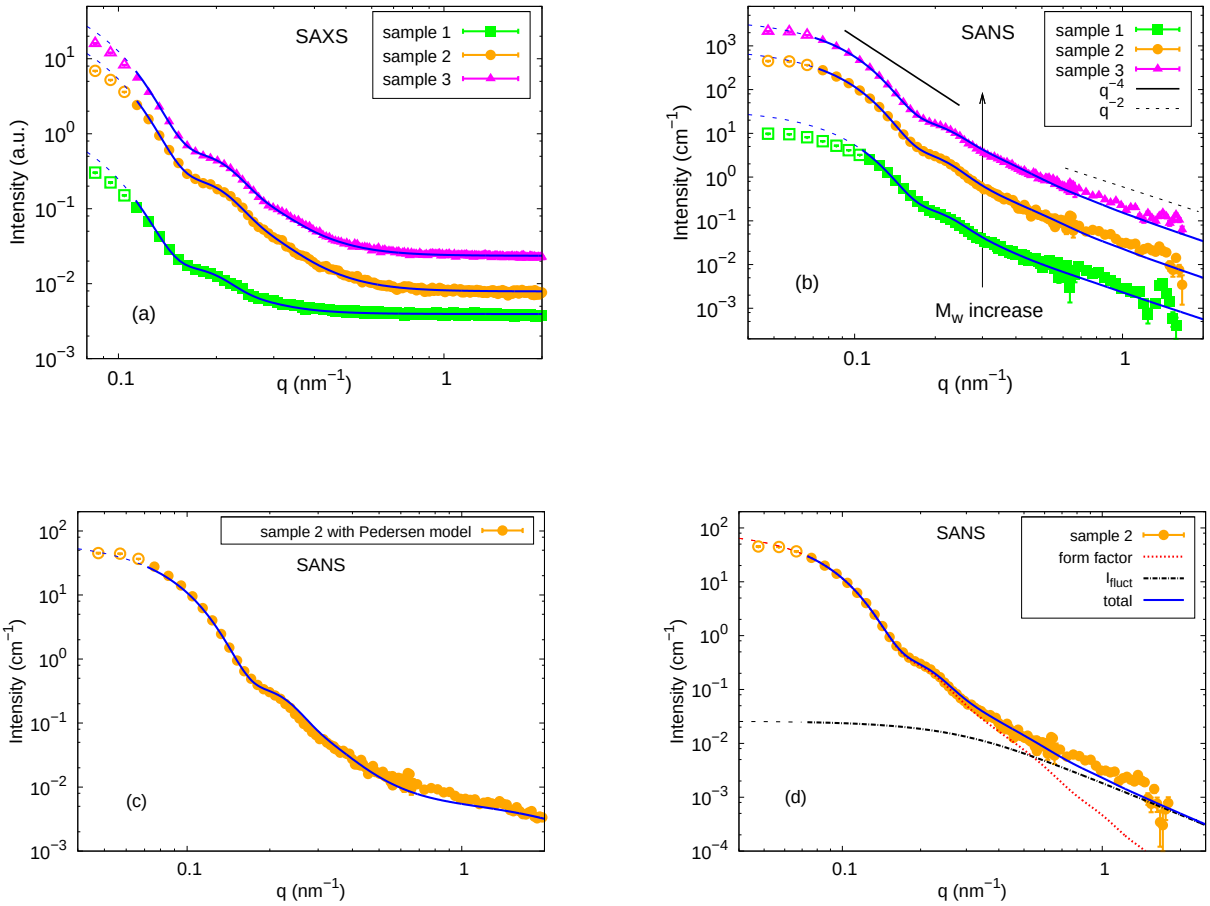


**Figure 5.6.:** SAXS (a) and SANS (b) data for PS-grafted silica dissolved in d-THF (c=0.2 wt%). The full curves are fits using the linear profile model (see text) for SANS data and the solid sphere model for SAXS data. Straight line demonstrates $q^{-4}$ dependence for low $q$ and $q^{-2}$ for high $q$ regimes. Open symbols indicate those that were not considered in the data analysis. SANS data have been corrected for the flat incoherent background. The curves of samples 2 and 3 were shifted for clarity. (c): A scattering curve of sample 2 in d-THF (0.2 wt%) analyzed by the core-shell-chain model for a Gaussian density profile of a shell (model 1). (d): Two contributions of the fit function are presented. Data are from sample 2. Dotted line: contribution from radial density profile; dashed dotted line: density fluctuation term described in Eq.4.48; full line: total fit function. Note that the experimental backgrounds were determined by fits and the different fit functions used for (c) and (d) resulted in slightly different backgrounds.

takes the conformation of the polymer chain into account.
As discussed in section 4.3.1, the problem of scattering from Gaussian polymer chains attached to a spherical particle has been addressed by Pedersen [64, 65]. This model is composed of a spherical dense core and a shell having a Gaussian density profile grafted to the surface (named the core-shell-chain model for a Gaussian profile of a shell-model 1 in section 4.3.1). As shown in Figure 5.6 (c), the form factor based on this approach describes our data only approximately. There are clear deviations in the intermediate $q$ range (0.2 nm$^{-1}$ $\leq q \leq$ 0.35 nm$^{-1}$) and high $q$ range ($q \geq$ 0.4nm$^{-1}$). Moreover, the fitting parameters obtained from this fit were unphyiscal. For example, the thickness was found to be significantly smaller than the radius of gyration of PS chains in the same solvent, THF. Chevigny et al. [10] applied this model for the case of PS-grafted silica particles dispersed in a theta solvent. They could well describe the shell structure for the protonated PS shell but not for the deuterated PS shell.

As discussed in section 3.2, Förster et al. [43, 91] introduced a power law type $r^{-\alpha}$ density profile to analyze the scattering from polymer chains on the spherical dense core. This model was inspired by the work of Daoud and Cotton [42], who further developed a model for star-like polymer which has a power law type of density profile, $\rho(r) = r^{-\alpha}$. They found that the exponent $\alpha$ obtained by their fit results was consistent with the argument by Daoud and Cotton who claimed that the exponent should lie in the range between 1 and 1.34. However, their data were not taken to the high $q$ range. Won et al. [92] used a Fermi-Dirac-type density profile to describe the polymeric shell on the spherical core. The advantage of this model is its ability to describe the density profile spanning from the typical step-like core-shell structure throughout the parabolic and the hyperbolic (power law) types of shell structure. The model, however, did not fit our data at high $q$. In an attempt to describe the full $q$ range with a simple model for the variation of scattering length density, we have therefore chosen to superimpose two scattering components. As discussed in section 4.3.2, the variation of density within the polymer layer is described by a concentration profile $\rho(r)$. The resulting form factor calculation was made analytically, as introduced previously in section 4.3.2. Besides the contribution from the radial density profile to describe the scattering intensity at low to intermediate $q$ regimes, $q^{-2}$ decay seen at a high $q$ range from our SANS data in Figure 5.6 (b), was discussed intensively in section 4.3. This contribution was approximated by an additional Debye term as described in eq. 4.48. Clearly, the restricted $q$ range does not allow us to fit $\xi$. We, therefore, use a fixed value calculated on the basis of ref. [93] that was determined for PS in a good solvent, toluene:

$$R_g = (0.0125){M_w}^{0.595}(nm) \tag{5.3}$$

As an example of the quality of fit provided by this model, Figure 5.6 (d) shows data obtained for sample 2 with curves displaying the contribution from both components in our model. The linear model obviously provides a very good description of the experimental data. The core radius was fixed to the value obtained for the surface-modified particle in d-THF. As introduced in section 4.3.2, the linear extension of the SLD of the shell, $\rho(r)$, is given by

$$\rho(r) = \frac{\rho_{\text{d-THF}} - \rho_{\text{sh}}}{\Delta}(r - R_c) + \rho_{\text{sh}} \tag{5.4}$$

where $\Delta$ is the shell thickness, $\rho_{\text{sh}}$ is the SLD of the corona shell at the interface between the core and the corona shell, and $\rho_{\text{d-THF}}$ is that of d-THF, respectively. The results of these fits are compiled in Table 5.3. It is seen that the layer thickness $\Delta$ increases with the molar mass of the grafted polymer. The scattering length density $\rho_{\text{sh}}$ appears to be independent of the molar mass. Its value is only slightly below that of d-THF, indicating a strong swelling of the polymer layer in the solvent used, THF. The remaining small contrast between the polymer layer and the solvent obviously does not allow determination of fine variations in density. The use of the simple linear model is therefore adequate. We can use the scattering length density profile to estimate the grafting density of the polymer chains.
Let $\Phi_{\text{PS}}(r)$ denote the volume fraction of PS segments at a distance r from the particle center.
The volume fraction profile of PS within the PS shell is related to the scattering length density profile of the shell, as given by

$$\rho(r) = \rho_{\text{PS}} \cdot \Phi_{\text{PS}}(r) + \rho_{\text{THF}} \cdot (1 - \Phi_{\text{PS}}(r)). \tag{5.5}$$

$\Phi_{\text{PS}}(r)$ is then obtained:

$$\Phi_{\text{PS}}(r) = \frac{\rho_{\text{d-THF}} - \rho_{\text{sh}}}{\Delta \cdot (\rho_{\text{PS}} - \rho_{\text{d-THF}})}(r - R_c - \Delta) \tag{5.6}$$

Integration over the shell volume allows for the volume of the polymer layer, $V_{\text{polymer}}$, to be calculated as follows

$$V_{\text{polymer}} = 4\pi \int_{R_c}^{R_c+\Delta} r^2 \Phi_{\text{PS}}(r) dr. \tag{5.7}$$

The ratio of $V_{\text{polymer}}$ to $V_{\text{chain}}$ gives the number of chains, $N_c$. $V_{\text{chain}}$ is denoted as the volume occupied by the polymer segments, as given by

$$V_{\text{chain}} = N_{\text{chain}} \cdot V_{\text{monomer}}. \tag{5.8}$$

Here, $N_{\text{chain}}$ is a degree of polymerization and $V_{\text{monomer}}$ is the volume of PS monomer given in the literature [69], 166.1 Å$^3$. Finally, grafting density is obtained by

$$N_{\text{chain}}/(4\pi {R_c}^2) = \sigma \text{ (chains}/nm^2). \tag{5.9}$$

The grafting density obtained by this method is $15(\pm 3)10^{-3}$ chains per nm$^2$ for sample 1, $20(\pm 0.3)10^{-3}$ chains per nm$^2$ for sample 2, and $10(\pm 0.2)\ 10^{-3}$ chains per nm$^2$ for sample 3. We note that the grafting densities of sample 2 and 3 are compatible with TGA, as shown in Table 5.1.

| | SAXS | | SANS | | | | | DLS | |
|---|---|---|---|---|---|---|---|---|---|
| sample | $R_c$(nm) | $\sigma_x$ | $R_c$(nm) | $\Delta$(nm) | $\sigma_x$ | $R_g$(nm) | SLD($10^{-4}$ nm$^{-2}$) | $D_h$(nm) | PDI |
| sample 1 | 27 ± 0.2 | 0.18 | 23.3 | 8.4 ± 0.3 | 0.21 | 4.2 | 5.96 ± 0.07 | 15.3 ± 1.5 | 0.16 |
| sample 2 | 26.2 ± 0.1 | 0.18 | 23.3 | 13.4 ± 0.03 | 0.21 | 5.2 | 5.87 ± 0.01 | 20.9 ± 1.1 | 0.14 |
| sample 3 | 25.8 ± 0.1 | 0.18 | 23.3 | 17.4 ± 0.06 | 0.21 | 7.0 | 6.11 ± 0.01 | 25.8 ± 1 | 0.16 |

**Table 5.3.:** Structural parameters derived from SAXS, SANS, DLS

$R_c$: particle core radius
$\sigma_x$: polydispersity of the core size of the particle for SAXS and SANS
$\Delta$: thickness of the grafted polymer layer from SANS
SLD: scattering length density of the interface between the core and the shell
$R_g$: radius of gyration of free PS chain obtained from eq. 5.3
PDI: polydispersity index for DLS

| | DLS | |
|---|---|---|
| | $R_{\text{conv}}$ (nm) | $R_h$ (nm) |
| sample 1 | 26.1 ± 0.7 | 50.3 ± 1.3 |
| sample 2 | 31.9 ± 0.9 | 55.9 ± 0.6 |
| sample 3 | 31.8 ± 1.6 | 60.8 ± 0.5 |

**Table 5.4.:** Conversion of intensity-weighted averaged particle radii from DLS to the number-weighted average particle radii

$R_{\text{conv}}$: converted radius from hydrodynamic radius for a given sample.
$R_h$: hydrodynamic radius for a given sample.

We now turn to the determination of the polymer layer thickness using DLS. For the sample preparation, the particles were dried by the evaporation of the initially made suspension in THF and re-dispersed by applying ultrasonication for four hours at the desired weight fraction in the solvent, THF. The viscosity ($\eta$) [94, 95] and the refractive index (n) [96, 97] of THF were taken from the literature. As we determined hydrodynamic radii of the particles before the grafting process, we can now apply the same measurement to obtain these values for the PS-grafted system. In Figure 5.7, we show representative

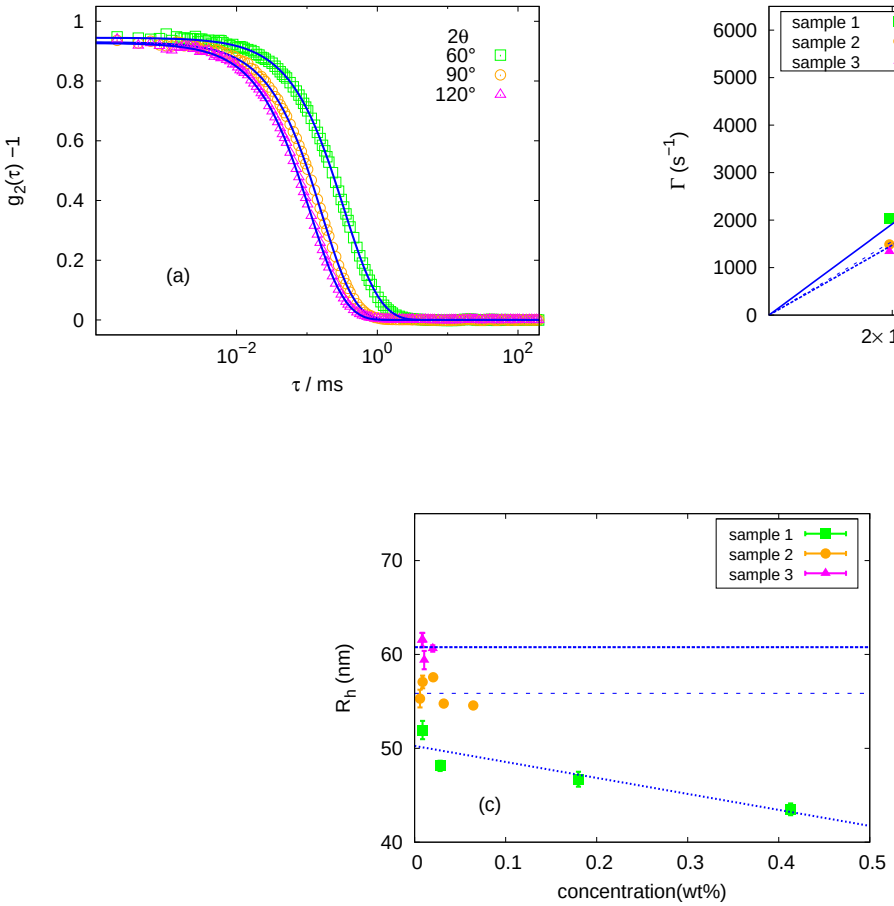


**Figure 5.7.:** (a): Intensity autocorrelation function for sample 2 in THF at selected scattering angles. Solid line represents fit using a second order cumulant analysis introduced in eq. 2.63. (b): Relaxation rate Γ vs. $q^2$ to obtain diffusion coefficient D of sample 1 (square, green), sample 2 (circle, orange), and sample 3 (triangle, violette) in THF (concentration of 0.02 wt%). Solid, dashed, and dotted lines represent linear fits to obtain D for sample 1, 2, and 3. (c): Concentration dependence of $R_H$ to extract the extrapolated values of $R_H$ for the given samples.

results for one sample. Relaxation functions are again very close to single exponentials, and we use the second order cumulant analysis to determine the mean relaxation rates for each $q$. Figure 5.7 (b) shows that, for all samples, we find a simple diffusive behavior, and we are thus able to obtain the diffusion coefficient D. As in the previous cases of the bare and surface modified particles, $R_H$ values for each sample were obtained by extrapolating an effective $R_H$ to zero concentration, as shown in Figure 5.7 (c). Table 5.3 compiles the results from three experimental methods used to characterize the structure of the grafted particles in d-THF. The radius of the silica core is systematically found to be larger in the SAXS than in the SANS experiments. This may be caused by the rather large width of the wavelength distribution in the SANS measurement. This spread also contributes to the apparent size distribution, which is larger in the SANS than in the SAXS measurement. The lowest values for polydispersity are obtained from DLS. In the previous section, the radius and its distribution from static scattering such as SAXS and SANS can be converted to the hydrodynamic radius and its distribution by applying the conversion formula which were shown in eq. 2.65. For example, the converted mean radius $R_{conv}$ from $R_H$ for sample 1 is 26.1 nm ($R_H$ = 50.3 nm). We note that, for the conversion the division factor, 2.071, was applied to PDI, PDI/2.071. If this value is compared with the value from SANS, $R_c + \Delta$, 31.7 nm, they show

comparable results. However, the converted radius from DLS data for the surface modified particle was ∼31 nm while the radius from SANS data was 23.3 nm. If the converted value from DLS data for the surface modified particle is used to extract the thickness of the grafted PS, the thickness of the PS layer becomes "negative" value, which is not physically meaningful. As discussed previously, a non-spherical particle shape, as shown in Figure 5.4, may cause a possible deviation of $R_{\mathrm{conv}}$ converted from $R_h$ of the surface modified particle by means of eq. 2.65, and $R_c$ from a static scattering experiment such as SAXS or SANS. Thereby $R_{\mathrm{conv}}$ of the surface modified particle was estimated to be large compared to $R_c$ from SANS, and the difference in $R_{\mathrm{conv}}$ between the grafted and surface modified particle will therefore become an unphysical value. It is, however, noteworthy that the radius and its distribution from DLS data can be converted to those quantities from SANS or SAXS measurements, but direct comparison should be handled with great care. The results of conversion of the mean sizes are summarized in Table 5.4.
Table 5.3 provides a layer thickness $\Delta$ as obtained from SANS. Moreover, the difference in hydrodynamic radii before and after grafting $D_{\mathrm{h}}$ is a measure of polymer layer thickness. We also include this result for our grafted particles in Table 5.3. The measures of the layer thickness thus are of the same order of magnitude as the radius of the supporting particle. We now compare the results for the apparent thickness of the polymer layer on the silica particles. Results from DLS provide a measure of the thickness as the difference in the hydrodynamic radii of surface modified and grafted particles. On the other hand, SANS allows us to derive the thickness as a static quantity, and we used the parameter $\Delta$ introduced above.

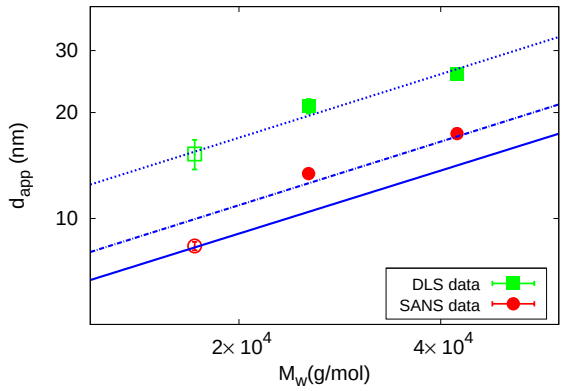


**Figure 5.8.:** Variation in the apparent thickness ($d_{\mathrm{app}}$) of the grafted PS layer on the surface of spherical silica particle in THF, obtained by SANS (circle, red) and DLS (square) with molar mass. The solid line is $d_{\mathrm{app}}$ as calculated for PS in toluene (see eq. 5.3). Dotted and dashed dotted lines are trend lines proportional to ${M_w}^{0.6}$ for $d_{\mathrm{app}}$ obtained from DLS and SANS, respectively. The open symbol is used for sample 1, as its molar mass was not taken from that of the grafted chain.

In Figure 5.8, we collect these results. The molar masses of sample 2 and 3 were taken from those of the grafted chains shown in Table 5.1. The molar mass for sample 1, on the other hand, is that of the free chain. According to Figure 5.8, the DLS results are 1.5 times larger than the SANS results. However, their variation with molar mass follows the same law. Note that the thickness obtained from DLS and SANS are weighted differently, therefore the results deviated as discussed previously. However, we did not attempt to use the converted radii $R_{\mathrm{conv}}$ from DLS, in order to compare $d_{\mathrm{app}}$ from SANS since the converted and static radius of the surface modified particle may have deviated due to the non-spherical shape of the particle. Additionally, we note that the difference of $d_{\mathrm{app}}$ from DLS and SANS may be in part caused by the adherence of solvent molecules to the particles, thus decreasing its diffusion coefficient [98].
In order to compare the layer thickness with the size of the grafted polymer chains, we calculated the

radii of gyration of free PS chains as introduced previously. $2R_g$ was taken as $d_{app}$ for comparison with $d_{app}$ from SANS and DLS measurements, in order to compare the thickness of the dilute polymer brush regime $2R_g$, as discussed in section 3.2. In Figure 5.8, we plot the results for $d_{app}$ from SANS ($\Delta$), DLS ($D_h$), and $2R_g$ from eq. 5.3 as a function of the molar mass of the grafted PS chains. Both experimental methods result in a variation in size with molar mass compatible with $d_{app} \propto {M_w}^{0.6}$. The deviation in sample 1 may be attributed to the molar mass taken from the free polymer chains, which tends to be larger than that of the grafted chain. Therefore, within the range of the molar masses investigated in our study, the PS chains are swollen by the good solvent. Their size scales with molar mass just as for free chains in a good solvent.
In section 3.2, it was stated that the conformation of the polymer brush can be decomposed into three regimes, namely the dilute polymer, semi-dilute (SDPB) and concentrated polymer brush (CPB) regimes. In the dilute polymer regime, the thickness of the polymer layer is compatible with $2R_g$, showing the conformation of the bulk polymer, and in the semi-dilute and concentrated polymer brush regimes, the polymer chains adopt a more stretched conformation in order to minimize the overlapping of the chains. In our experimental observation, the thickness determined by SANS was slightly larger than $2R_g$ of free PS chains in the same solvent and increased with ${M_w}^{0.6}$ as in the case of free PS chains. Both statements demonstrate that the PS chains studied in our experiment have a SDPB conformation. As discussed in section 3.2, a more general scaling concept was introduced, which includes not only the effect of the length of the grafted chains and the grafting density but also that of the curvature of the particle on the size of the grafted chains. The scaling law of the thickness of the grafted layer h with the length of the grafted chains, the grafting density, and the size of the core for the spherical surface is then given by [42, 45, 47] (see also section 3.2):

$$h \propto \sigma^{0.2} N^{0.6} {R_c}^{0.4}. \tag{5.10}$$

where N is the degree of the polymerization and $R_c$ is the radius of the core. The scaling law introduced in eq. 5.10 is expected to correct the deviation between data points and guide lines shown in Figure 5.8 due to the multiplication of $\sigma^{0.2}$ on the molar mass. However, we did not attempt to plot the results using eq. 5.10 and this will be done in the next section, combining the results from PS grafted d-PS particles in good solvents.

### 5.1.4 Conclusion

In this section, the synthesis of PS grafted silica nanoparticles has been briefly introduced and the particles have been experimentally characterized. The main focus has been the investigation of the conformation of PS chains on the surface of the silica nanoparticles. Three methods were combined: SAXS, DLS, and SANS. In particular, SANS permitted a detailed investigation of the PS chain conformation due to the enhanced contrast achieved by using protonated PS chains in deuterated solvent, d-THF media. In order to describe the form factor of the shell of PS grafted silica particles, a simple linear density profile was found to describe the low $q$ regime adequately. Additional scattering at high $q$ was attributed to the coil structure of the polymer chain. Grafting densities were determined from SANS and TGA. They were found to be low (less than 0.1 chains/nm$^2$). Our measurements from DLS and SANS revealed that the thickness of PS chains in a good solvent, THF, scales with ${M_w}^{0.6}$, displaying behavior similar to that of free polymer chains in the same solvent, and the thickness determined by SANS was slightly larger than the $2R_g$ of the free PS chains in the same solvent. Both results demonstrate that the grafted PS chains have a "SDPB" conformation. In this section, the results from DLS and SANS were plotted in variation with the molar mass only to see the scaling law between the thickness and the molar mass. However, as discussed in section 3.2, the curvature and grafting density are expected to contribute to the grafted chain conformation, as well. To this end, in the next section, the parameters of curvature and grafting

density, as well as molar mass, will be employed to reveal their effect on the grafted chain conformation as the results from PS grafted d-PS particles are combined with the present results.

## 5.2 PS grafted d-PS in a good solvent: "ATRP grafting from" method

In the previous section, PS grafted silica particles (diameter ≈ 50 nm) in THF were characterized by SAXS, DLS, SANS, and TEM. The thickness of the grafted PS chains obtained by SANS and DLS, scaled with $M_w^{0.6}$ which displays a slightly stretched conformation with respect to free PS chains in the same solvent, THF.
As an extension of the previous section, we chose an organic particle instead of an inorganic silica with a similar diameter in order to see the effect of the different substrate material. Additionally, more varieties of molecular weights of grafted PS used for this part will allow the conformation feature of grafted PS to be revealed more in detail. For the particles used for these experiments, we used the "grafting from" method to graft PS from the d-PS nanoparticle's surfaces. Controlled radical polymerization following atomic transfer radical polymerization (ATRP) was chosen to grow the linear PS from the d-PS latex particle surface. The ATRP method for grafting polymer from particles has been widely used and proven to be an appropriate method to obtain well defined molecular weight and grafting density for the grafted polymer chains [6, 7, 8, 99]. In the following, the chemical synthesis of the d-PS particles grafted with PS will be described briefly, and main focus will be the characterization of the conformation of systems of the d-PS latex particles grafted with PS by a combination of SANS, SAXS, and DLS.

### 5.2.1 Synthesis

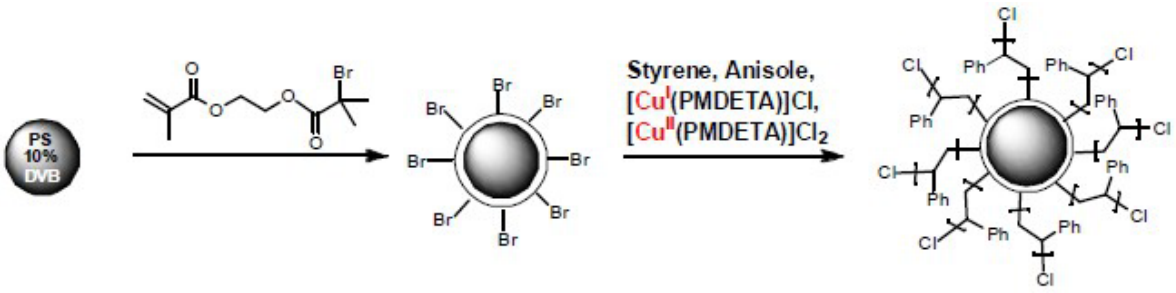


**Figure 5.9.:** Schematic illustration of synthesis of d-PS particles grafted with PS using ATRP methodology [100]

Highly cross-linked latex particles of around 40 nm diameter and a narrow size distribution were synthesized via batch emulsion polymerization using mixtures of deuterated styrene (90 wt%) and divinylbenzene (10 wt%). Sodium dodecylsulfate was used as a surfactant, and mixtures of sodium peroxodisulfate and sodium dithionite were used as the initiators (step 1). Bare d-PS particles were functionalized with ATRP inimer by adding aqueous emulsions containing variable amounts and ratios of styrene, divinylbenzene, and ATRP inimer, as well as small amounts of sodium dodecylsulfate to the seed latex dispersions. The use of a variety of ATRP inimer densities was aimed to obtain a variation in grafting densities (step 2). Before synthesizing the grafted particles, ATRP initiators were converted into those of RAFT termini by treatment with bis(thiobenzoyl) disulfide (BTBD) in the presence of ATRP-active copper complexes. The linear PS corona chains were grown from the initiator functionalized d-PS particles with different lengths and grafting densities using the ATRP methodology. The functionalized particles in anisole as a solvent, styrene, Cu(1)- and Cu(2)-salts, and ligands were added. The mixtures were stirred and heated to induce PS chain growth (step 3). The freely grown chains parallel to the grafted chains using sacrificial initiators, were taken as the representatives to evaluate the molecular weights of the grafted chains. Subsequent SEC characterization was applied to determine the molecular weights of the freely grown PS chains. The resulting molecular weights are listed in Table 5.6.

### 5.2.2 SANS data fitting

As our experiments were made at a high dilution limit, interparticle interference was not taken into account, so the structure factor, $S(q)$, was not used to fit our experimental data, $S(q) \sim 1$. For some cases where the aggregation of particles exists, an additional term $Cq^{-\alpha}$, shown in eq. 4.11 has been superimposed on the intensity calculation, where C is a constant. $Cq^{-\alpha}$ was used because the low $q$ scattering from the data merely shows $q^{-\alpha}$ decay, a part of the scattering from the aggregates, not the whole profile of the scattering from aggregates (see section 4.1 for details).
The calculated intensity used for the analysis is given by the following expression in an absolute unit ($cm^{-1}$):

$$I(q) = \phi \cdot \frac{\left\langle |F(q,R)|^2 \right\rangle}{\langle V_{\text{total}} \rangle} + (Cq^{-\alpha}) + I_b \tag{5.11}$$

Here, $\phi$ is the volume fraction of the particles in solution, $I_b$ is the background, and $F(q,R)$ is a form factor. $V_{\text{total}}$ is the volume of a core-shell particle. The modulus of the squared form factor and the volume of the particle are number-averaged with respect to the particle size distribution function, in our case a Schulz function. For the bare and surface modified d-PS particles, we apply a spherical form factor without a shell in the form of eq. 4.13.
For PS grafted d-PS particles, we apply a form factor $F(q,R)$ from a spherical core-linear shell model given in eq. 4.42 using the linear profile of the shell introduced in eq. 4.43 in section 4.3.2. In the case of the PS grafted d-PS particles, interchain correlations contribute additionally to the intensity, which we approximate with a Debye-type function, as introduced in eq. 4.48 and named $I_{\text{fluct}}(q)$.
The overall intensity for PS grafted d-PS is finally given by

$$I_{\text{total}}(q) = I(q) + I_{\text{fluct}}(q) + I_b. \tag{5.12}$$

### 5.2.3 Results and Discussion

The details of the methods of SAXS, SANS and DLS measurements were described in sections 2.2.2 and 2.3.2. The model functions to calculate the SANS intensity were introduced previously. For SAXS, SANS, and DLS measurements, the particles were dried by evaporation of the initially made suspension and re-dispersed by magnetic stirring for one day at the desired weight fraction in the solvent. For DLS measurements, ultrasonication was additionally applied for two hours.
Figure 5.10 (a) shows the SANS data from bare, surface modified, and PS grafted particles in d-toluene and Figure 5.10 (b) shows the SANS data from surface modified d-PS particles of three initiator densities. The denoted scattering curves in Figure 5.10 (a) are from surface modified particles with an intermediate initiator density and from a molecular weight of 28.5 kg/mol PS grafted d-PS particles, respectively. In Figure 5.10 (c), SAXS data from surface modified particles of three different initiator densities (0.3, 0.6, and 0.9 initiators/$nm^2$) are shown for a comparison of the structural information on the application of different scattering methods. The surface modified particles of the initiator density of 0.9 initiators/$nm^2$ are assigned as d-$PS_{high}$, those of the initiator density of 0.6 initiators/$nm^2$, as d-$PS_{mid}$, and those of the initiator density of 0.3 initiators/$nm^2$, as d-$PS_{low}$, respectively. All particles shown in Figure 5.10 were dispersed in d-toluene for SANS and toluene for SAXS. The variation of initiator densities on the particle surfaces was intended to obtain that of grafting densities. For the SANS measurements, the concentration was set to be c=0.5 wt% for the bare and surface modified particles and c=0.2 wt% for the grafted particles. The concentration used for SAXS measurements was c=0.3 wt%.
The SANS scattering pattern for bare d-PS particles in d-toluene is shown in Figure 5.10 (a). At low $q$, additional scattering is due to the presence of aggregates. Data fit was made using eq. 5.11 with a

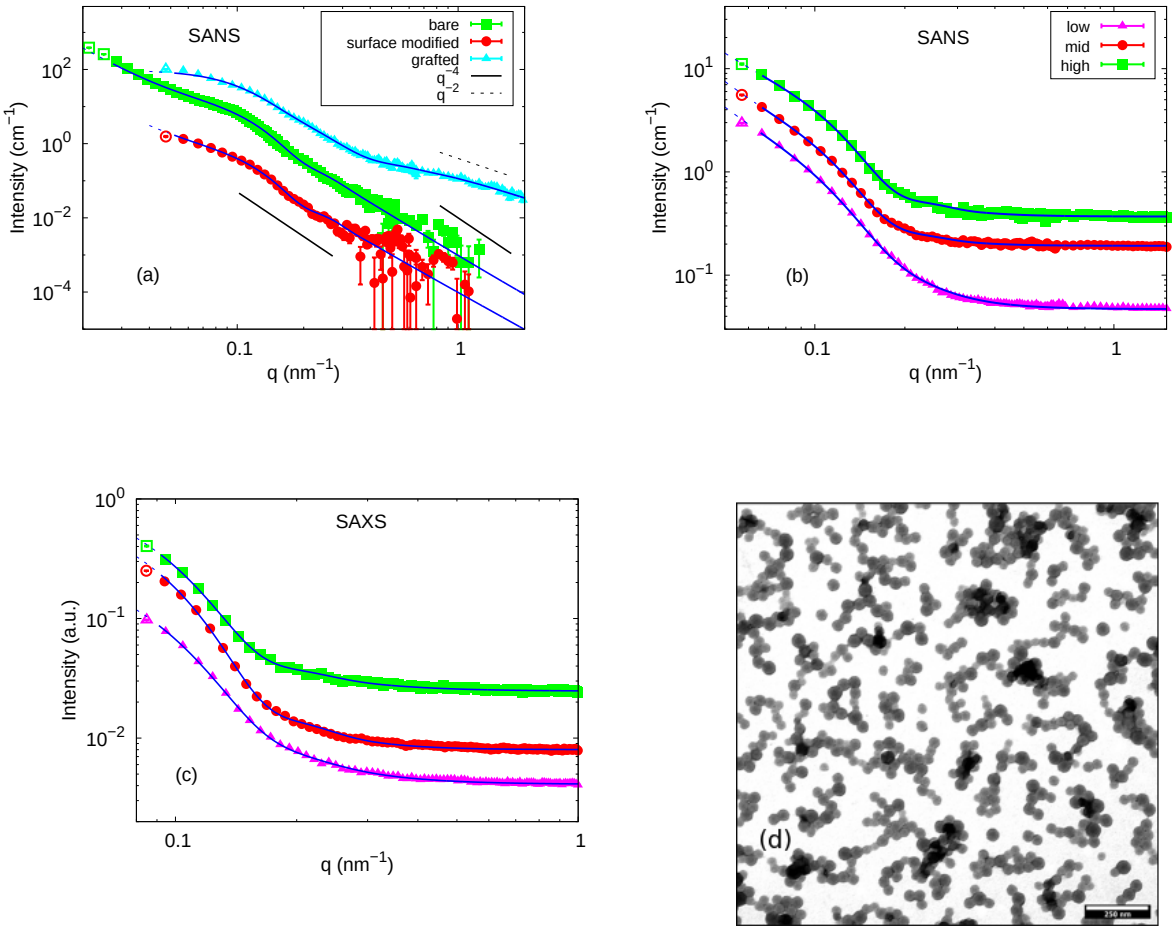


**Figure 5.10.:** (a): Comparison of SANS data for surface modified, bare (c=0.5 wt%) and grafted d-PS particles (c=0.2 wt%) dispersed in d-toluene. (b): SANS data of surface modified d-PS particles of different initiator densities dissolved in c=0.5wt% d-toluene. Solid lines are fits using eq.5.11. (c):SAXS data for surface modified d-PS particles of different initiator densities dissolved in c=0.3 wt% toluene. (d): TEM picture of bare d-PS particles prepared via the drop-cast method of particle dispersion in water on carbon-coated copper grids (scale bar 250nm). For (a), the incoherent background was subtracted from the experimental intensity and the curves were vertically shifted for clarity. Open symbols were not considered to analyze the data. For (b) incoherent background was not subtracted from the intensity for a comparison of SANS and SAXS data for the same data set.

solid sphere model shown in eq.4.13. The phenomenological intensity contribution $Cq^{-\alpha}$ introduced in eq. 4.11 was additionally used to fit low $q$ contribution and gives an exponent, $\alpha$=3.4, slightly smaller than the expected Porod exponent of the aggregates. Porod's law for the scattering from aggregates would result in an exponent of $\alpha$=4. As discussed previously in section 4.1, values of $\alpha$ smaller than 4 indicates the existence of the aggregates. It is noted that the existence of aggregates may originate from the surfactant from the synthesis on the surface of the nanoparticle, and this is expected to lead to worse solubility. At a large $q$, the data decays as $q^{-4}$, indicative of the smooth surface of the particles. The line through the data is a fit in terms of a spherical form factor in eq. 4.13. $R_c$ was found to be $\approx$ 20nm comparable to the radii found for silica nanoparticles in section 5.1.
Moreover, the bare particles were studied using TEM (see Figure 5.10). Here, the spherical shape of the particles could be verified.
As shown in Figure 5.10 (a) and (b), the SANS scattering from surface modified particles displays a similar pattern as the bare particle case: an excess of the scattering at a low $q$ and $q^{-4}$ decay at a large

$q$. The fit function to calculate the data from surface modified particles were the same as in the case of the bare particles. The power law exponent for this case was $\alpha$=3.2, slightly smaller than the expected Porod's exponent of the aggregates. The radii for the surface modified particles are ∼21 nm comparable to the size of the bare particles in d-toluene.
The SAXS scattering curves from the surface modified particles display a similar pattern as the SANS curves as shown in Figure 5.10 (b) and (c). To fit the data, the same fit functions were used to extract the structural information as in the case of SANS. The average sizes and distribution of the radii of cores of surface modified particles were slightly larger than those from SANS measurements, while $\alpha$ values were found to be slightly smaller than those by SANS measurements. The larger radius and smaller size distribution from SAXS are expected due to the rather large wavelength distribution at the KWS-2 beam line [83]. Different $\alpha$ and polydispersity values from the two scattering methods may, therefore, be attributed to the solubility of the particles in d-toluene or toluene and the available $q$ ranges. We note that the lowest $q$ achieved by SAXS is larger than that by SANS. The resulting parameters obtained by data fits are listed in Table 5.5.
In the final step, d-PS particles were grafted with protonated PS. Molecular weights were obtained from the freely grown polymer chains using a sacrificial initiator which is suitable to obtain a close value for the grafted molecular weight of the organic cores. For scattering experiments, the grafted particles were dissolved in d-toluene in one series of experiments and in d-THF in another series of experiments at a concentration of c=0.2 wt%. This is a dilute situation where all interparticle interferences are negligible. With the variation of solvents, we intended first to impose a contrast situation where the core and the grafted polymer shell both have the contrast to the matrix (d-toluene as the solvent) and achieve a stronger shell contrast (d-THF as the solvent) than in the d-toluene case. In Figure 5.10 (a), we compare three cases where the scattering patterns from the bare, surface modified, and grafted particles are shown. From low to intermediate $q$, the three scattering curves decay as $q^{-4}$, an indication of a smooth interface, and only for the coated particles is this steep decrease in the intensity followed by the $q^{-2}$ behavior. This behavior is due to the existence of the polymer layer and led to use of the Debye term, as introduced in eq. 4.48.

| | SANS | | | SAXS | | | DLS | | |
|---|---|---|---|---|---|---|---|---|---|
| | $R_c$(nm) | $\sigma_x$ | $\alpha$ | $R_c$(nm) | $\sigma_x$ | $\alpha$ | $R_h$(nm) | PDI | $R_{\text{conv}}$ (nm) |
| d-PS$_{\text{high}}$ | 20.8 ± 0.6 | 0.14 | 2.8 | 23.3 ± 0.2 | 0.18 | 2.2 | 36.7 ± 1.3 | 0.16 | 19.7 ± 3.3 |
| d-PS$_{\text{mid}}$ | 20.8 ± 0.5 | 0.16 | 3.2 | 23.2 ± 0.1 | 0.19 | 2.7 | 35.4 ± 0.5 | 0.14 | 20.7 ± 1.9 |
| d-PS$_{\text{low}}$ | 19.6 ± 0.4 | 0.2 | 3 | 21.7 ± 0.1 | 0.23 | 2.4 | 38.4 ± 0.2 | 0.08 | 28.2 ± 1.6 |

**Table 5.5.:** Physical parameters obtained by SANS, SAXS, and DLS of surface modified d-PS particles in d-toluene (SANS) and in toluene (SAXS and DLS). $\sigma_x$ and PDI denote the polydispersity index from SAS and DLS, respectively. PDI indices were obtained from the results of the particles in the lowest concentration investigated (c≈0.01 wt%). The subscript index for d-PS represents the density of the initiator used. $R_{\text{conv}}$ denotes the core radius converted from DLS results using eq. 2.65 using the heuristics PDI/2.071, as introduced in section 2.3.1.

DLS measurements were performed to characterize the size of the bare, surface modified, and grafted d-PS particles. All of the DLS results are compiled in Figure 5.11. The measurements were made at room temperature. A series of concentrations was prepared, and the correlation function was measured in a range of scattering angles (50° to 130°). For each concentration, an effective hydrodynamic radius could be determined and extrapolated to zero concentration. The intensity autocorrelation function was analyzed by second order cumulant analysis, shown in eq. 2.63. The correlation functions for the bare, surface-modified and PS grafted particles, displayed one mode, and the linear variation of $\overline{\Gamma}$ with $q^2$, representing the translational diffusion, was employed to obtain an effective hydrodynamic radius for a single measurement. Bare particles were dispersed in water, and surface-modified particles were dispersed in toluene. The $R_h$ of the bare particle in water at zero concentration was found to be ∼25 nm

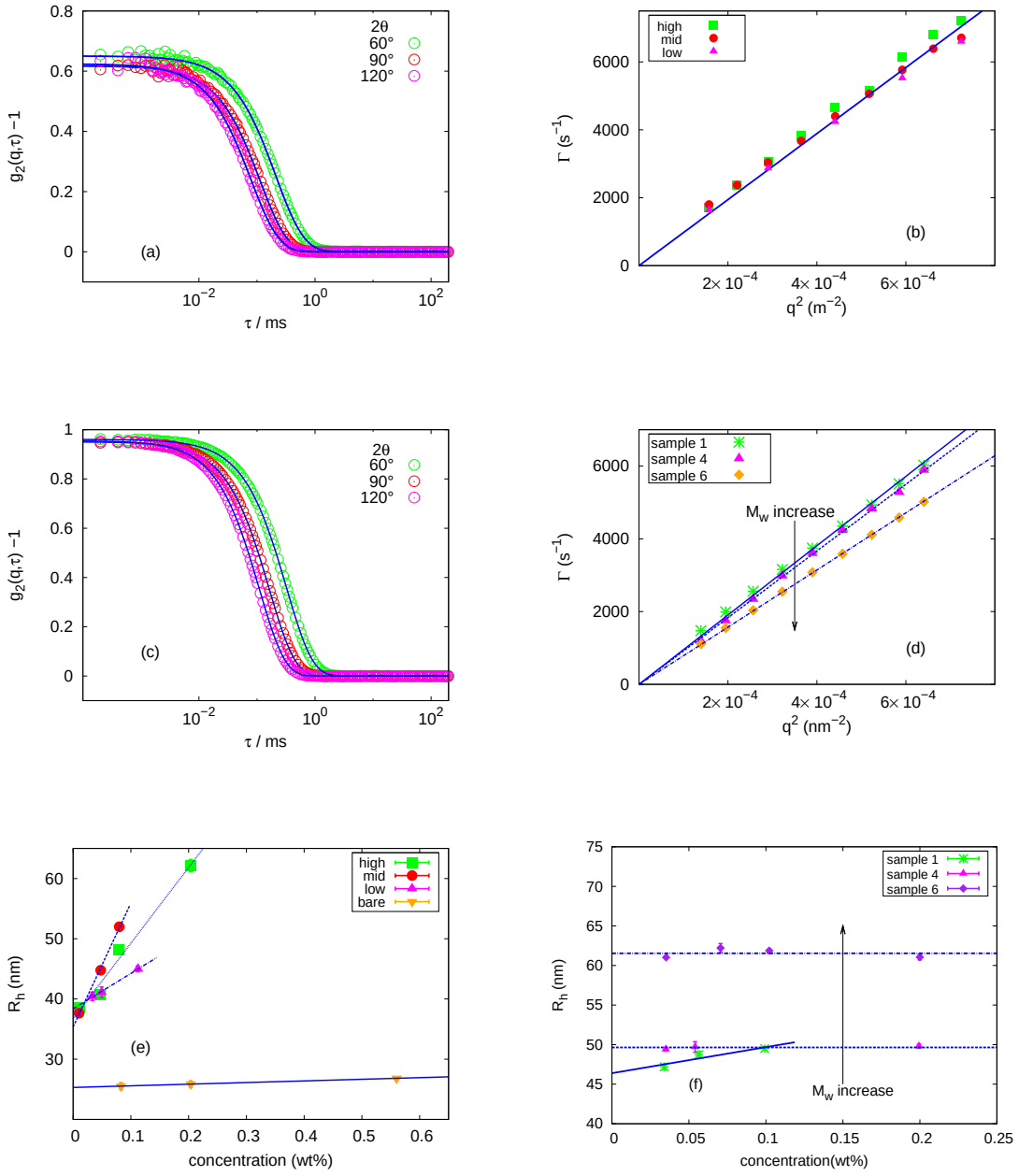


**Figure 5.11.:** Compilation of DLS results from bare, surface-modified and PS grafted d-PS nanoparticles. (a): Intensity autocorrelation function of surface-modified d-PS particles of intermediate initiator density in toluene as an example (c=0.01 wt%) (b): $q^2$ dependence of Γ to determine the diffusion coefficients of the surface-modified particles (c=0.01 wt% for high and mid, c=0.03 wt% for low initiator density of the particles). (c): Correlation curves for PS grafted d-PS particles (sample 6) in 0.03 wt% THF as an example. (d): $q^2$ dependence of Γ to determine the diffusion coefficient for selected examples. Sample notations are defined in Table 5.5. Solid lines in (a) and (c) present fits using the cumulant analysis and solid lines in (b) and (d) linear fits to obtain D of the samples denoted in the legends. (e): Concentration dependence of the bare and surface modified particles (f): Concentration dependence of the grafted particles for selective examples. Strong concentration dependence is exhibited in (e) for surface-modified particles, indicating that the interaction between particles is strong even at a low concentration, c=0.1 wt%. In contrast, the bare particles show the stable dispersion state at concentrations below c=0.6 wt% but a gradual decrease in the hydrodynamic radius toward lower concentrations demonstrates that an attractive interaction between the particles is present. Sample notations of the grafted particles are defined in Table 5.6.

and those of three sets of the surface modified particles in toluene were ∼36nm. The deviation of the size between the bare and surface-modified particles may be attributed to the swelling of the core due to the solvent quality or a thin initiator shell existing on the surface modified particles. The mean sizes of the surface modified particles obtained by DLS are significantly larger than those by SANS. As shown in Table 5.5, a relatively large polydispersity index by DLS can explain this deviation (up to 16%) since the DLS signal is affected by larger particles. The conversion of the core sizes can be made with application of eq. 2.65 where an additional heuristics for each PDI, PDI/2.071, was applied. The DLS results for the bare and surface-modified particles, including sizes using the conversion formula, are also listed in Table 5.5. The core radii of d-PS particles of high and mid initiator density, converted from DLS data, show good agreement with those from SANS and SAXS results. However, the deviation between the converted and static radius seen for the particles of low initiator density demonstrates that the division of PDI by 2.071, applied for the particles of low initiator density having a low PDI value $< 0.1$ (see Table 5.5) may be overestimated. We note that, for a low PDI index, the division of PDI by 2.071 may not be necessary, as division of the PDI value by 2.071 would result in a large mean size of $R_{\mathrm{conv}}$ compared to the case where the division is not done. However, it is noteworthy that the two results, converted and static $R_c$, are comparable, and this further indicates that the conversion formula presented in eq. 2.65 can "approximate" the mean size obtained by static scattering data from the DLS results, at least for a spherical core (see Figure 5.10), since eq. 2.65 is designed to be applied for spherical geometry.

Similarly to the SANS data analysis, the core radius obtained from the surface modified particles in toluene was used to extract the size of the grafted chains. The viscosity [101] and the refractive index [102] of toluene and of water were taken from the literature [103, 104]. The viscosity of toluene at 20 °C is 0.5867 cP and its refractive index for $\lambda$=632.8 nm is 1.495612 at 20 °C, respectively. The values for water at 20 °C are 1.002 cP and 1.33211 for $\lambda$=632.8 nm. Figure 5.11 (e) demonstrates that the radii of the surface modified particles in toluene depend strongly on the concentration. This strong concentration dependence may originate from the surface structure of the particles. As shown in Figure 5.9, bromide is located on top of the surface and has a strong polarity in comparison with a non-polar molecule of toluene. Therefore, the difference in polarity between the molecule on the surface and the toluene molecule may result in a slower diffusion and thus a larger value of $R_h$ at a higher concentration. This is reflected as a strong attractive interparticle interaction in Figure 5.11 (e). We note that the surface modified particles were measured just after sonication for two hours to avoid the aggregation of the particles.

PS grafted particles were dispersed in THF, and the values for the viscosity and the refractive index of THF were the same as in the case of silica particles. Here, the difference between before and after grafting was taken as a measure of the hydrodynamic thickness of the grafted chains, named $D_h$. It was previously stated that the converted radius $R_{\mathrm{conv}}$ from the DLS result might merely approximate the number-averaged static radius so $R_{\mathrm{conv}}$ was not used for the thickness of the PS layer instead of $D_h$.

The molecular weights were obtained from the freely grown PS using a sacrificial initiator which is expected to be well suited to obtain a value close to the grafted molecular weight for the organic core. The variation of the initiator density is expected to contribute to varying grafting density. As shown in Table 5.7, the hydrodynamic thickness, $D_h$, corroborates the growth of the grafted chains as the molecular weight increases (note that an increase in the sample number represents an increase in molecular weights).

The SLDs used for the SANS data fit are schematically represented in Figure 5.12. In the case of the d-THF solvent, due to the small difference in the SLDs between the core and the solvent, the scattering curves mainly show the form factor of the polymeric shell rather than that of the core, namely shell contrast. For d-toluene, on the other hand, the scattering from both the core and the shell contribute to the data, namely core-shell contrast.

Figure 5.13 shows the experimental scattering curves and fits of the grafted particles of different molecular weights in d-toluene (a) and d-THF (b). The solid lines are fits of the total intensity shown in eq. 5.12. The linear density profile with the Debye term implemented to fit the SANS data described

the data reasonably well. The curves from the particles in d-toluene converge to a constant amplitude toward $q \rightarrow 0$, indicating good dispersion of the particles in solution. On the other hand, the curves from the particles in d-THF show a strong upturn toward low $q$ values, indicating that the particles were aggregated. We note that, for dispersing particles in solution, only magnetic stirring was applied, which could not effectively disperse the particles. This aggregation at a low $q$ led to the use of the term $Cq^{-\alpha}$ shown in eq. 5.11, as previously done for the bare and surface modified particles. The overall fit parameters were the volume fraction $\phi$, the thickness $\Delta$, the SLD of the shell, G to determine the scale of the fluctuation term of $I_{\text{fluct}}$, shown in eq. 4.48, and $\xi$, also from $I_{\text{fluct}}$. For those in d-THF, the constants C and $\alpha$ were additionally required to perform the fit while keeping the polydispersity fixed at the values for d-toluene to obtain reliable fits.
The resulting fit parameters from the particles in d-toluene and d-THF are compiled in Table 5.6 and 5.7, respectively. The radius of the surface modified particles was fixed to the respective values for the surface modified particles. The thickness, $\Delta$, obtained by SANS, again corroborates chain growth by increasing the length of the grafted chains, as verified by DLS measurements of the same grafted particles in THF.

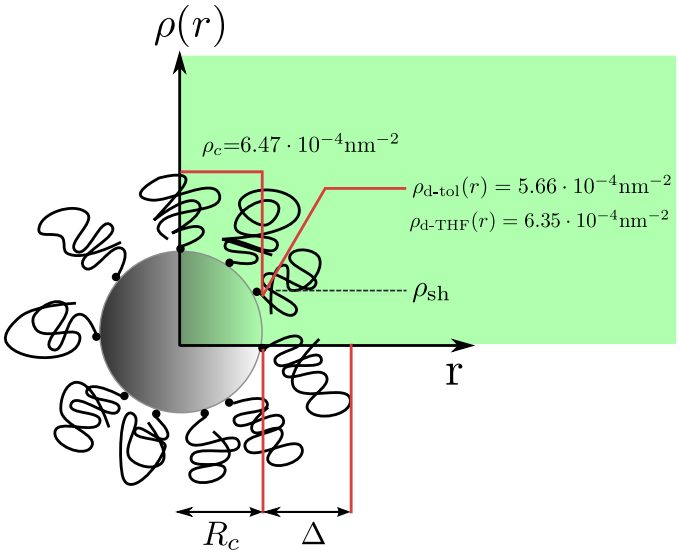


**Figure 5.12.:** Schematic representation of a spherical d-PS nanoparticle grafted with PS chains to show the SLD contrast situation. The red line is the radial SLD distribution with certain values. $\rho_c$ is the SLD of the d-PS core, which is a constant. The SLDs of the solvent are either $\rho_{\text{d-tol}}$ or $\rho_{\text{d-THF}}$ for d-toluene or d-THF, respectively. These values are constants. The radial distribution of the volume fraction of PS segments leads to a linear distribution, with $\rho_{sh}$ being the initial SLD of PS on the d-PS surface. The important structural parameters are the d-PS particle radius $R_c$ and the grafted PS layer thickness $\Delta$.

As examples of the quality of the data fit, the components of the fit function to analyze the data from d-PS particles grafted with 46 kg/mol PS dispersed in d-toluene and d-THF, are displayed in Figure 5.14 (a) and (b). Figure 5.14 shows that the fit function indeed provides a good description of the experimental data.
For a comparison of the fit function to analyze the data using the core-linear shell model added to the Debye function, the data set of the d-PS particles with a PS shell in d-toluene was analyzed by the core-shell-chain model for the box-Gaussian profile of a shell, named model 2 and included in the core-shell-chain models in section 4.3.1. In order to illustrate the fit quality provided by the core-shell-chain model, Figure 5.15 shows selected examples of the data from d-PS particles grafted with low molecular weights of PS (sample 1 to 3). A significant deviation of the calculation from the experimental data is found, especially at high $q$ ranges, even though the resulting fit parameters were comparable to those obtained by the core-linear shell model superimposed on the Debye function shown in Table 5.6. According to Table 5.6, the parameter $\xi$ for these samples was small, less than ∼1 nm. For those small

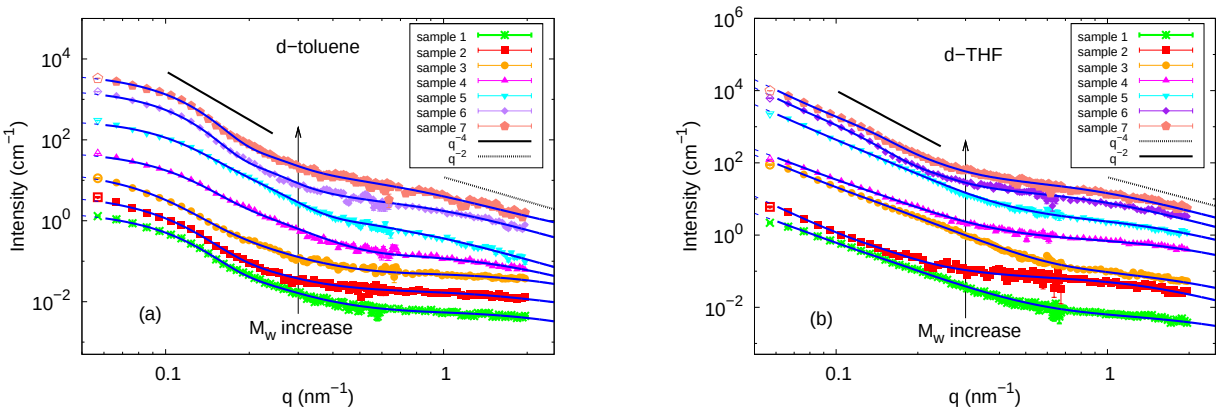


**Figure 5.13.:** (a): SANS data for PS grafted d-PS dissolved in d-toluene (c=0.2 wt%) with curve fits. (b): SANS data for the same particles with the same concentration in d-THF. The linear density profile and Debye function were used to fit the SANS data. For the data for the particles in d-THF, the phenomenological term $Cq^{-\alpha}$ in eq. 4.11, was additionally used to describe the scattering from the aggregates. Sample notations are as given by Table 5.6. Trend lines, $q^{-2}$ for high $q$ regimes and $q^{-4}$ for low $q$ regimes. The incoherent experimental background was subtracted from the intensity, and the curves were vertically shifted for clarity. Open symbols were not considered in analyzing the data. Arrow indicates an increase in molecular weights.

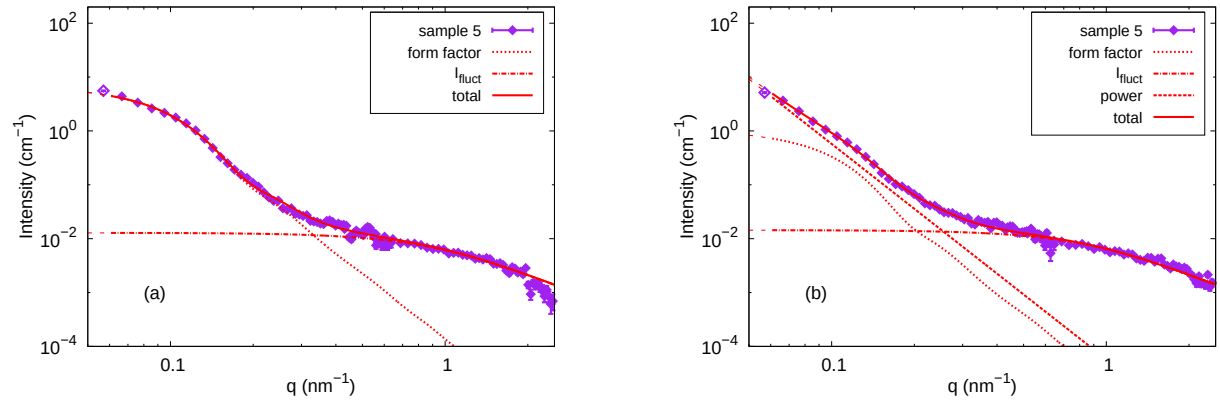


**Figure 5.14.:** (a): Components of the fit function of the core-linear shell model superimposed on the Debye term for the d-PS particles grafted with 46 kg/mol PS in c=0.2 wt% d-toluene. (b): Components for the same particles in c=0.2 wt% d-THF. In (b) due to the strong upturn toward low $q$ ranges, for the data analysis, the additional term of $Cq^{-\alpha}$ from eq. 4.11 was required to fit the data for low $q$ regimes. For (a) and (b), $I_{\text{fluct}}$ denotes Debye function, form factor denotes core-linear shell form factor, power power law contribution namely $Cq^{-\alpha}$, and total total fit function, respectively.

values of $\xi$, the core-shell-chain model appears to be inadequate for the data description of the polymer coated nanoparticles. On the other hand, for the particles with sparsely grafted PS chains or the largest molecular weight (sample 7), the core-shell-chain model provided a good description with a comparable fit quality from the core-linear shell plus the Debye function. However, the parameter obtained from this fit was unphysical. For example, the thickness obtained by this fit function was significantly smaller than $R_g$ of the free PS chain in the same solvent, d-toluene. We can therefore surmise that, for the

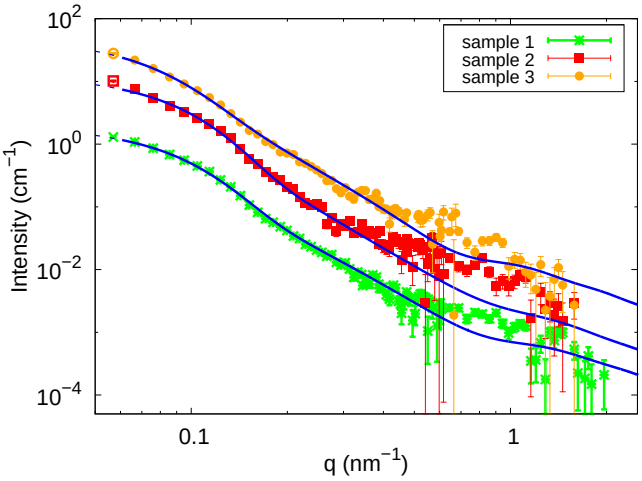


**Figure 5.15.:** Selected examples of scattering curves analyzed by the core-shell-chain model for the box-Gaussian density profile of a shell, named model 2 and included in the core-shell-chain models in section 4.3.1 (sample 1 to 3). The calculation explicitly deviates from the experimental data at a high $q$, indicating that the description of the inter- or intra-chain correlation is not appropriate.

particles with low molecular weight or low grafting density, this model is not adequate to describe the experimental data. In the following section, moreover, these two model descriptions will be further compared to render an explicit answer, in order to allow the selection of the most appropriate fitting model.

### 5.2.4 Determination of the conformation of PS chains

| | | | SANS | | | | | |
|---|---|---|---|---|---|---|---|---|
| label | $M_w$ (g/mol) | $PDI_{SEC}$ | $R_c$ (nm) | $\Delta$ (nm) | SLD ($10^{-4} nm^{-2}$) | $\sigma$ (chains /nm$^2$) | $\sigma_x$ | $\xi$ (nm) |
| sample 1 | 6,700 | 1.19 | 20.8 | 7.9 ± 0.1 | 5.1 ± 0.1 | 0.06 ± 0.002 | 0.27 | 0.7 ± 0.03 |
| sample 2 | 7,300 | 1.24 | 19.6 | 8.4 ± 0.2 | 5.4 ± 0.1 | 0.03 ± 0.003 | 0.3 | 0.8 ± 0.04 |
| sample 3 | 7,800 | 1.24 | 20.8 | 9.3 ± 0.1 | 5.2 ± 0.1 | 0.06 ± 0.002 | 0.35 | 0.7 ± 0.04 |
| sample 4 | 12,100 | 1.28 | 20.8 | 11.2 ± 0.1 | 5.2 ± 0.1 | 0.048 ± 0.001 | 0.31 | 1 ± 0.04 |
| sample 5 | 28,500 | 1.17 | 20.8 | 17.8 ± 0.2 | 5.3 ± 0.1 | 0.027 ± 0.001 | 0.33 | 2.2 ± 0.08 |
| sample 6 | 46,000 | 1.23 | 20.8 | 19.6 ± 0.1 | 5.6 ± 0.1 | 0.004 ± 0.0002 | 0.24 | 1.6 ± 0.06 |
| sample 7 | 62,200 | 1.46 | 19.6 | 19.3 ± 0.1 | 5.6 ± 0.1 | 0.002 ± 0.0002 | 0.25 | 2.1 ± 0.08 |

**Table 5.6.: Structural parameters derived by SANS data from PS@d-PS in d-toluene**

$M_w$: weight averaged molecular weight
$PDI_{SEC}$: polydispersity index of polymers determined by SEC measurement
SLD: scattering length density of the shell at interface, r=$R_c$
$R_c$ was set at the same values as in Table 5.5.

The results from SANS and DLS will be shown to reveal the conformation feature of grafted PS chains. The grafting density was determined from the results of the SANS data fit using the volume fraction profile, $\Phi(r)$, calculated from the linear SLD profile of the shell. The calculation of the grafting density was based on the methods introduced in section 5.1.3 using eq. 5.4 to eq. 5.9. They were determined for a series of samples and listed in Table 5.6 and 5.7. We note that, since the molecular weights of freely

| | SANS | | | | | | DLS | |
|---|---|---|---|---|---|---|---|---|
| label | $\Delta$ (nm) | SLD ($10^{-4} nm^{-2}$) | $\sigma$ (chains /nm$^2$) | $\sigma_x$ | $\xi$ (nm) | $\alpha$ | $D_h$ (nm) | PDI |
| sample 1 | 9.3 ± 0.4 | 5.8 ± 0.1 | 0.065 ± 0.004 | 0.27 | 0.6 ± 0.04 | 2.7 ±0.03 | 11 ± 1 | 0.06 |
| sample 2 | 8 ± 0.8 | 6.0 ± 0.1 | 0.03 ± 0.004 | 0.3 | 1.1 ± 0.03 | 3.5 ±0.05 | 8.8 ± 0.8 | 0.06 |
| sample 3 | 10.4 ± 0.1 | 5.7 ± 0.1 | 0.07 ± 0.001 | 0.35 | 0.8 ± 0.03 | 3.1 ±0.02 | 11 ± 1.3 | 0.05 |
| sample 4 | 13.2 ± 0.7 | 5.8 ± 0.1 | 0.054 ± 0.004 | 0.31 | 0.9 ± 0.01 | 2.9 ±0.04 | 14.3 ± 0.5 | 0.08 |
| sample 5 | 19.6 ± 1.8 | 5.9 ± 0.1 | 0.037 ± 0.004 | 0.33 | 1.4 ± 0.04 | 3.4 ±0.02 | 23.9 ± 1.3 | 0.03 |
| sample 6 | 19.6 ± 0.2 | 6.3 ± 0.1 | 0.001 ± 0.0001 | 0.24 | 1.7 ± 0.03 | 4 | 26.2 ± 0.6 | 0.06 |
| sample 7 | 23.1 ± 0.5 | 6.3 ± 0.1 | 0.001 ± 0.0001 | 0.25 | 1.9 ± 0.03 | 3.8 ± 0.03 | 17.6 ± 0.6 | 0.05 |

**Table 5.7.:** Structural parameters derived by SANS and DLS data from PS@d-PS in d-THF

$D_h$: Apparent hydrodynamic thickness of grafted PS
$R_c$s were set to be the same values with those in 5.6.Those were, therefore, not shown here.

| label | $R_h$ (nm) | $R_{\mathrm{conv}}{}^{a}$ (nm) | $D_{\mathrm{h}}{}^{\mathrm{conv}}$ (nm) |
|---|---|---|---|
| sample 1 | 46.4 ± 0.9 | 36.9 ± 1.9 | 16.2 ± 2.7 |
| sample 2 | 47.1 ± 0.8 | 37 ± 1.4 | 8.8 ± 2.1 |
| sample 3 | 47.7 ± 0.2 | 39.9 ± 3.2 | 20.2 ± 4.6 |
| sample 4 | 49.6 ± 0.1 | 36.4 ± 1.9 | 15.7 ± 2.6 |
| sample 5 | 60.6 ± 0.3 | 54.5 ± 0.5 | 34.8 ± 3.3 |
| sample 6 | 61.5 ± 0.3 | 49.2 ± 1.7 | 28.6 ± 2.5 |
| sample 7 | 56 ± 0.6 | 46.8 ± 2.1 | 18.7 ± 2.6 |

**Table 5.8.:** Conversion of intensity-weighted radii obtained by DLS to the number-weighted radii for the Schulz distribution function

$R_h$: hydrodynamic radii for given samples
$R_{\mathrm{conv}}$: converted radii from $R_h$
$D_{\mathrm{h}}{}^{\mathrm{conv}}$: thickness of grafted chain obtained by the difference in $R_{\mathrm{conv}}$ between surface-modified and grafted particles

grown PS chains were considered those of the grafted PS chains, these values may deviate from those of the grafted chains and usually show slightly smaller values than those of the grafted ones. It could lead to a small estimated grafting density as the segmental volume of PS can be overestimated. $\xi$ obtained from the Debye term in eq. 4.48 was found to be on the order of 1-2 nm. This quantity corresponds to the correlation length inside the polymeric layer. Similar values were reported for the polyelectrolyte grafted PS particles in good solvent, water [105]. The polydispersity indices of the samples from the SANS results lie between 0.2 and 0.3, and this indicates that the sizes of the samples investigated in our study are rather polydisperse, perhaps originating from the PS chain polydispersity shown in Table 5.6. As discussed in section 3.2, on a curved substrate, the polymer chains are known to adopt the “mushroom ” conformation at a low grafting density limit where the chains are well separated and do not interact. For the mushroom conformation, the thickness, here denoted as h, of the grafted layer of polymer scales with the radius of gyration $R_g$ and degree of polymerization N (see Figure 3.5),

$$h \sim N^{0.6} \approx 2R_g. \tag{5.13}$$

The radius of gyration $R_g$ of a free PS chain in toluene might be calculated by an approximation given by Huber et al. [93], as introduced previously in section 5.1.3:

$$2R_g = (0.025) \cdot \mathrm{M}_w{}^{0.595}(\mathrm{nm}) \tag{5.14}$$

The calculated values of $2R_g$ can then be compared with the fitted values of $\Delta$ from SANS and $D_h$ from DLS to judge whether the particles are in a dilute polymer regime, a semi dilute polymer brush regime (SDPB, semidilute polymer brush) or even a concentrated polymer brush regime (CPB). As in the previous section on the silica particles, $\Delta$ and $D_h$ will be assigned as the apparent thickness $d_{\text{app}}$ and compared with the values of $2R_g$ to reveal the conformation of the grafted PS layer.
Figure 5.16 shows the measured $d_{\text{app}}$ as a function of the molecular weight $M_w$ of the grafted PS chains obtained by SANS (a) and DLS (b). Both results demonstrate that values for $d_{\text{app}}$, except that for the largest $M_w$, are systematically larger than the $2R_g$ of the respective free PS chains calculated by Huber's formula. Thus, our grafted nanoparticles are in the SDPB or CPB regime except for the sample of the largest $M_w$. It is also observed, from the lowest to the highest $M_w$ the difference between $2R_g$ and $d_{\text{app}}$ decreases, reaching the limit of dilutely grafted nanoparticles, moreover, the values for $d_{\text{app}}$ approximately follow $\sim M_w^{0.6}$. We take this as a hint that our particles are grafted in the SDPB regime.
Note that, for SANS experiments, PS grafted d-PS particles were dissolved in d-toluene or d-THF, and for DLS, in THF. As mentioned in section 5.1.3, THF is a good solvent for PS if the Hansen solubility parameters for PS and THF are compared. Toluene can also be considered a good solvent, since the Hansen solubility parameter of toluene, 18.2 $\text{Mpa}^{0.5}$, is close to that of PS (22.7 $\text{Mpa}^{0.5}$). That of THF was 19.4$\text{Mpa}^{0.5}$; its value is closer than that of toluene to PS, but the values of the two solvents are not very different [89, 90]. Complete miscibility is expected if the solubility of the parameters of two materials are similar (see the appendix). The sizes of the grafted chains for THF were slightly larger than those for toluene, which corroborates aforementioned smaller difference in the solubility parameter between THF and PS than that between toluene and PS.

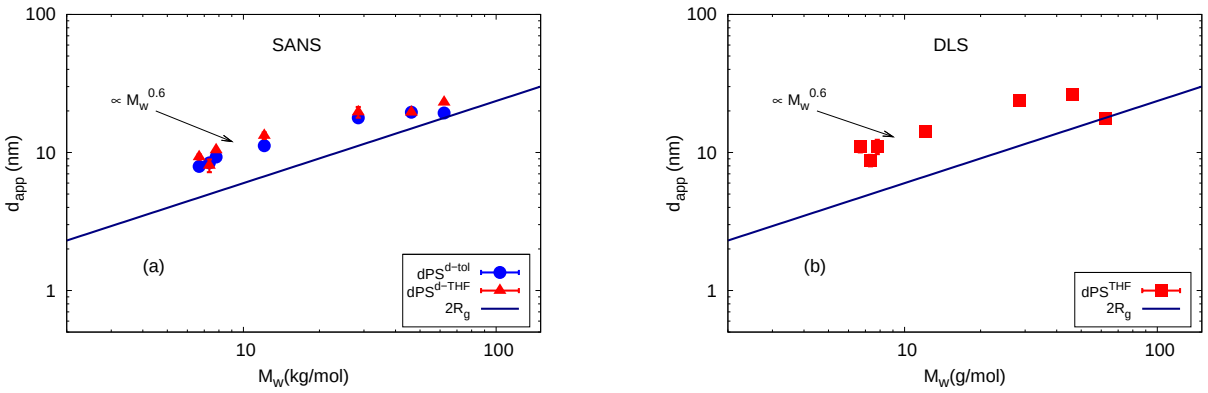


**Figure 5.16.:** Variation of the apparent thickness ($d_{app}$) of the grafted PS layer on the surface of d-PS particles in d-toluene and in d-THF obtained by SANS (a) and by DLS (b), as a function of $M_w$. Solid line shown in (a) is $2R_g$, as calculated for PS in toluene. Note that the plots are on logarithmic scales on both the horizontal and vertical axes.

It is shown in Table 5.7 that the values of $d_{\text{app}}$ obtained by DLS in the same solvent, THF, are slightly larger than the values obtained by SANS. Relatively small PDI values for given particle systems will clarify this small difference. Again, as done previously, the results from DLS measurements were converted to compare the quantities obtained by the two measurements and shown in Table 5.8. Thereby, converted radius was used to determine the thickness of grafted chains as the difference in the radius between surface modified and grafted particles. It is noteworthy that the results are at least on the same order of magnitude but they show a deviation. Therefore, a direct comparison between the two values appears to be difficult due to the fact that the heuristics applied to the PDI value (PDI/2.071), mentioned in section 2.3.1, was determined empirically. Then, the converted $D_{\text{h}}^{\text{conv}}$ shown in Table 5.8, was not used as a $d_{\text{app}}$.

In the SDPB regime where the thickness of the polymer layer is larger than $2R_g$, it is known that, besides the molecular weight the brush height, h, scales with the curvature or the radius of the particles and the grafting density, $\sigma$, of polymer chains (see Figure 3.5):

$$h \sim N^{0.6} \cdot {R_c}^{0.4} \cdot \sigma^{0.2}. \tag{5.15}$$

Here, $R_C$ denotes the size of the core radius and N denotes the degree of polymerization. This is a situation where the pairwise interaction between the grafted chains plays a main role in determining the conformation of the chains. At high grafting densities, $\sigma$, the exponents describing the scaling law become larger [8] (see also Figure 3.5):

$$h \sim N^x \sigma^{0.5x} \text{ with } (0.6 < x \leq 1). \tag{5.16}$$

In this case, the interaction between chains is not pairwise but rather of a higher order, so a more stretched layer is expected. Based on the grafting density obtained previously, as shown in Table 5.6 and 5.7, the grafting density for the sample of the highest $M_w$ is rather low, so we assume the grafted polymer layer to undergo a transition from the SDPB regime to the dilutely grafted regime supported by the measured thickness $d_{\text{app}}$ converging to $2R_g$.
As a final test and summary of our experimental results, we normalized all measured $d_{\text{app}}$ for the silica and d-PS nanoparticles, with respect to the corresponding radii ${R_c}^{0.4}$ and the molecular weight and radii (a) and (b), the grafting density $\sigma^{0.2}$ (c) and (d), in order to check whether the scaling concept for the SDPB regime shown in eq. 5.15 is valid. The result is shown in Figure 5.17, where all calculated normalized thicknesses are summarized, including the values of previous results on the silica particles from section 5.1. The normalized data from both SANS measurements in Figure 5.17 indeed follow the predicted power law with a dependency on ${M_w}^{0.6}$ , giving good agreement between our data and the scaling prediction except the aforementioned values for high $M_w$ or low $\sigma$ (sample 6 and sample 7). The grafting density scaling shown in Figure 5.17 also verifies this argument. The normalized data from DLS shown in Figure 5.17 results follow the power law prediction better than those from the neutron results. In Figure 5.16, the result from sample 6 remains with the power law prediction due to the fact that the DLS measurement is more sensitive to larger objects. The normalization of the data from DLS then leads to a slightly different behavior for high molecular weights, arising from the difference in the results from sample 6.
Here, we note that the different substrate material does not play an important role in the grafted PS chain conformation. It appears that the different character of the enthalpic interaction between the grafted PS chains and the substrate materials, silica and d-PS, has a negligible contribution to the change in the conformation feature of the grafted chains. Furthermore, it is clear that the application of eq. 5.16 allows for a direct comparison of the grafted chain conformation as long as the chains are in SDPB regimes.

### 5.2.5 Conclusion

We have investigated the conformation of a grafted polymer layer consisting of protonated PS on organic deuterated PS nanoparticles (d-PS). By varying the molecular weight of the grafted PS over a wide range, we complete our previous study on PS chains grafted on inorganic silica nanoparticles. By combining SANS and DLS, we produced a detailed structural picture of the grafted d-PS nanoparticles with varying deuterated solvents. As reported previously, we calculated grafting densities by analyzing the radial SLD distribution. The grafted PS layer thickness is larger than the $2R_g$ of the free PS chain in a good solvent, revealing a slightly stretched chain conformation, meaning that we find our PS grafted d-PS particles to be in a semi-dilute polymer brush regime (SDPB) rather than in a dilute situation. However, for high molecular weights, we find hints of a SDPB-to-dilute transition where the grafting density becomes small and the thickness of the layer converges to $2R_g$. We could consistently describe our data with power laws

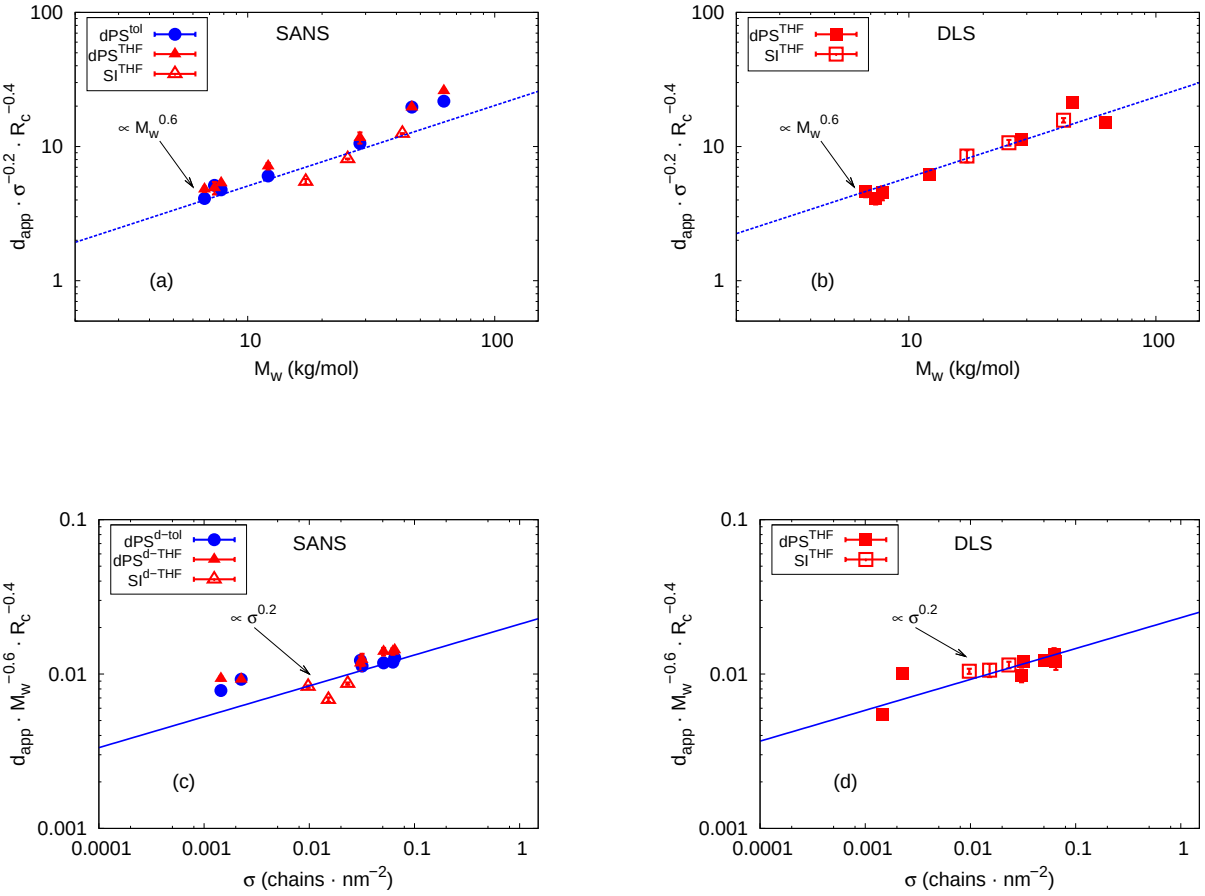


**Figure 5.17.:** Apparent grafted PS layer thickness $d_{app}$ on the surface of d-PS nanoparticles of radius $R_c$. (a), (b): Layer thickness by SANS and DLS, normalized with respect to grafting densities and particle radii to test molecular weight scaling. (c), (d): Layer thickness by SANS and DLS, normalized with respect to molecular weight and particle radii to test the grafting density scaling. Grafting densities ($\sigma$) used were the average values of the samples in d-toluene and d-THF listed in Table 5.6 and 5.7. Note that the plots are on logarithmic scales on both the horizontal and vertical axes.

accounting for the SDPB chain conformation. The results from the silica particles were combined with those from d-PS particles to investigate the influence of the substrate material of different hydrophobicities on the grafted chain conformation. The scaling concept applied for the SDPB regime for both sets of data revealed that the interaction between the grafted PS chains and the substrate material of different hydrophobicities does not play an important role in the grafted PS chain conformation.

## 5.3 PS grafted d-PS in a good solvent: "NMRP grafting from" method

This section describes the characterization of d-PS particles grafted with PS using the SI-NMRP method (surface initiated nitroxide mediated radical polymerization) [106]. The chemical details will be briefly described, and the main focus will be the characterization of the surface modified and PS grafted d-PS particles via DLS and SANS. The NMRP polymerization method is expected to gain a relatively high grafting density and the corresponding architecture of the grafted PS chains is expected to be different from that with sparsely grafted particles, which were described in sections 5.1 and 5.2. Insights into the scaling behavior and conformational features of surface-attached PS chains on deuterated PS nanoparticles are investigated by using DLS measurements in order to prove that polymer brushes are formed. Additionally, the d-PS particles with a surface-attached initiator are shown to be uniform spherical core-shell particles by SANS measurements.

### 5.3.1 Synthesis

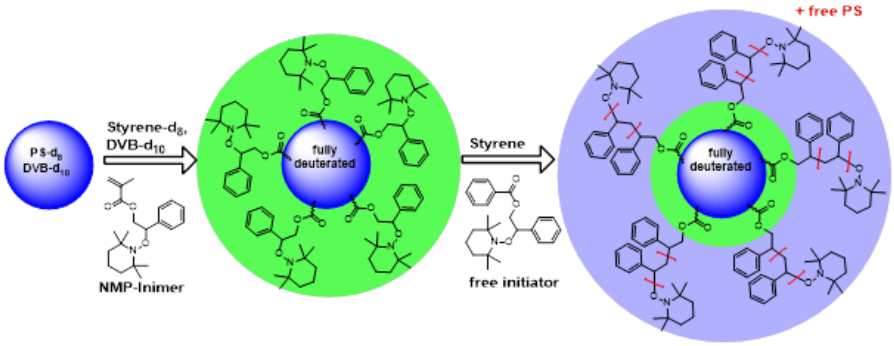


**Figure 5.18.:** Schematic illustration of SI-NMRP of styrene from the surface of fully deuterated PS nanoparticles [100]

Bare d-PS particles were synthesized by the same method as introduced in section 5.2. The bare particles retained an average diameter of d = 57±10 nm, as determined by TEM (Figure 5.19). In order to functionalize the NMRP initiator, styrene, divinylbenzene, and NMRP initiator were added to water (step 2). DLS gave a core size of the functionalized particles of $R_c \approx 43$ nm. For the SI-NMRP of styrene, a free initiator was added to the particles in anisole as a solvent. With the optimized conditions for controlled radical polymerization by adding a two-fold excess of free initiator with respect to the surface attached initiator, SI-NMRP was carried out from the surface of the particles. The molar masses obtained were up to 75,300 g/mol with low polydispersities (<1.22) for PS chains formed in solution (Table 5.9, step 3). Free PS chains were removed by repeatedly dispersing the particles in THF and ultracentrifugation at least eight times. The synthesis of the particles is summarized schematically in Figure 5.18. The scaling relation of the thickness of the grafted PS chains with the molar masses will be highlighted in the next sections using DLS measurements. We note that the details of the experimental method of DLS were described in section 2.3.2 and the details of the SEC and TEM experimental methods were described in section 5.1.2.

### 5.3.2 Results and discussion

#### DLS measurements

The structure of the surface-modified and PS grafted d-PS particles were investigated by DLS. The scaling behavior of the surface-attached PS with increasing molecular weights and the corresponding change in

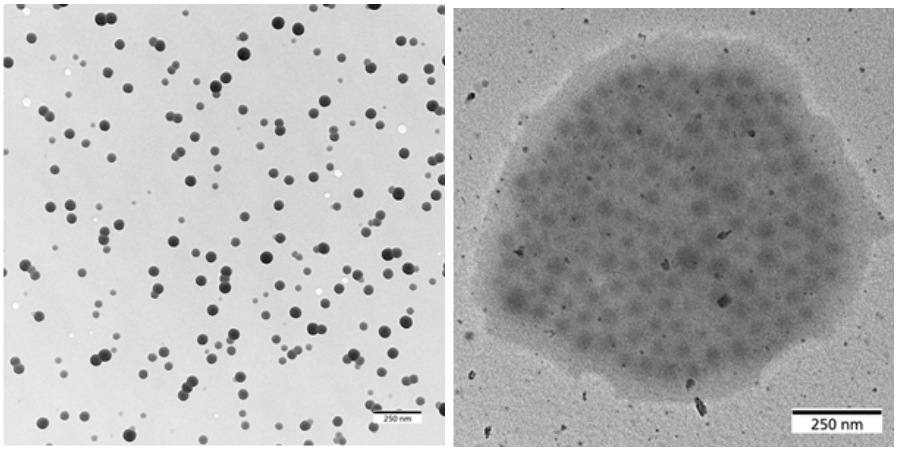


**Figure 5.19.:** TEM images representing the fully deuterated cross-linked PS particles (left) and the same particles after SI-NMRP of styrene (right). The samples were prepared via the drop-cast method of particle dispersion in water on carbon-coated copper grids.

**Table 5.9.:** Molar masses of freely formed PS on d-PS particles obtained by SEC measurements with PS standards and results for DLS measurements of aliquots of PS grafted fully deuterated particles.

| PS label | $M_w$ [a] (kg/mol) | $PDI_{SEC}$ [b] | $R_h$ [c] | $D_h$ [d] |
|---|---|---|---|---|
| Core particle | – | – | 43.3 ± 0.2 | – |
| 31k | 30.6 | 1.56 | 52.6 ± 0.2 | 9.2 ± 0.3 |
| 40k | 40.2 | 1.35 | 64.4 ± 0.4 | 21.1 ± 0.4 |
| 52k | 52.2 | 1.35 | 73.3 ± 0.9 | 30 ± 0.9 |
| 62k | 61.8 | 1.22 | 78.7 ± 0.2 | 35.3 ± 0.2 |
| 75k | 75.3 | 1.22 | 89.7 ± 0.2 | 46.4 ± 0.3 |

a: Molar masses were determined by SEC measurements for the freely formed PS chains by NMRP solution
b: PDI index of polymers determined by SEC measurements
c: Hydrodynamic radius of the given particle systems
d: Difference in $R_h$ between the surface-modified and grafted particles

the conformation of surface-attached PS were revealed using DLS measurements. Details of the DLS experimental setup were described previously in section 2.3.2. DLS measurements were carried out at 25 °C and a series of particle concentrations in THF were prepared to obtain the effective $R_h$. The effective $R_h$ for each concentration was extrapolated to obtain $R_h$. Ultrasonic treatment was applied for three hours for the grafted particles and six hours for the surface-modified particles to yield stable dispersions. After the sonication, the experimentally obtained value of the hydrodynamic radius $R_h$ was constant over time. Figure 5.20 shows the representative intensity autocorrelation functions of 75 kg/mol of PS grafted particles in THF at a high dilution (0.01 wt%) and the variation of $\Gamma$ with $q^2$ for each example. In all cases, the intensity autocorrelation functions were very close to single exponential. No indication of polydispersity was found. The linear variation of $\Gamma$ with $q^2$ was nicely fulfilled by our data representing the diffusive motion of the particles. Also shown in Figure 5.20 is the extrapolation into zero concentration to obtain the hydrodynamic radius. For the determination of the PS shell thickness, named $D_h$, we used $R_h$ for the surface-modified particle and the grafted particle and took the difference as the shell thickness. All results are compiled in Table 5.9. The results plotted in Figure 5.21 show that there is a good linear relationship between the shell thickness and the molecular weight of the grafted PS chains. Here, we do not attempt to convert the intensity-weighted $R_h$ from DLS measurements to number-averaged $R_{conv}$, since no indication of polydispersity was found, indicating the conversion

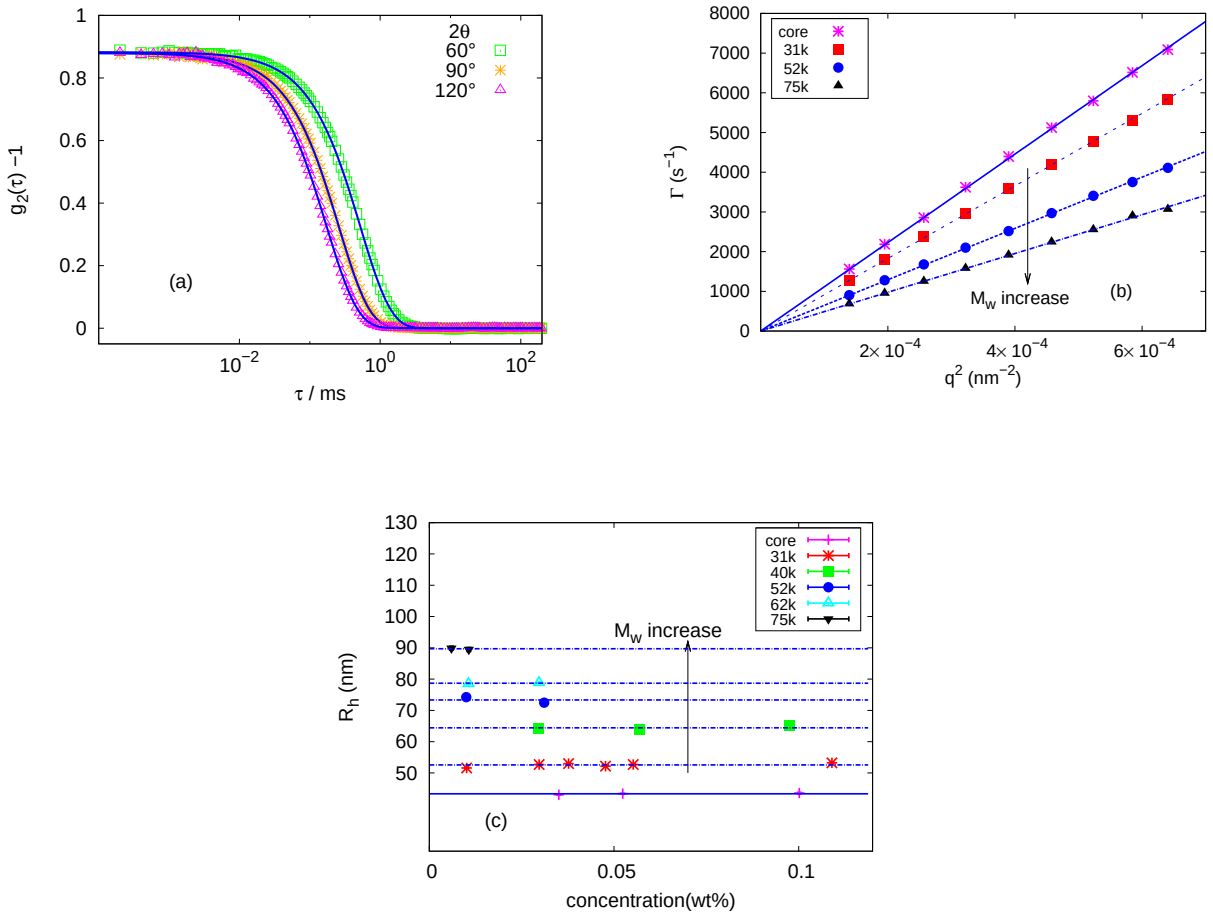


**Figure 5.20.:** (a): Intensity autocorrelation functions of 75 kg/mol of PS grafted d-PS particles in c=0.01 wt% THF at selected angles. (b) Γ as a function of $q^2$ for the samples of surface-modified and PS grafted d-PS particles in high dilution. The linear dependence of Γ with $q^2$ indicates the diffusive motion of the particles, the decrease of the gradients of the curves for increasing $M_w$, and the increase of the $R_h$ for given concentration. Sample notations are defined in Table 5.9, and "core" denotes a surface-modified particle. (c): Variation of $R_h$ as a function of concentration (wt%) for the surface-modified and grafted d-PS particles. The constant variation of $R_h$ for the samples in the plot shows a stable dispersion state at a high dilution limit. Average values were taken for $R_h$. Arrow in (c) and (d) indicates the increase in $M_w$.

provides almost identical sizes.

The deviation obtained for the sample with the lowest molecular weights shown in Figure 5.21 may be attributed to the overestimated molecular weight. It was previously noted that molecular weights used for the grafted PS chains on d-PS particles were taken from the freely grown chains and that the NMRP of styrene under the applied conditions seemed to be less controlled in the incipient part of the reaction, as also reflected in the larger values for the polydispersities. However, in the posterior state of the controlled radical polymerization, polydispersities decreased significantly, and the corresponding deviation in the molecular weight between the grafted and free chains seems to be smaller, as the resulting hydrodynamic thickness in Figure 5.21 tends to follow the trend line.

We now focus on the scaling relationship found for our results, shown in Figure 5.21. The results from d-PS particles shown in Figure 5.21 display a linear dependence of the shell thickness for the d-PS particles on the molecular weights. As discussed in section 3.2, the linear relationship shown in Figure 5.21 may

indicate that the conformation of the grafted polymer layer is that of the concentrated polymer brush regime (CPB), as in the results of Savin et al. [6] and Ohno et al. [7].

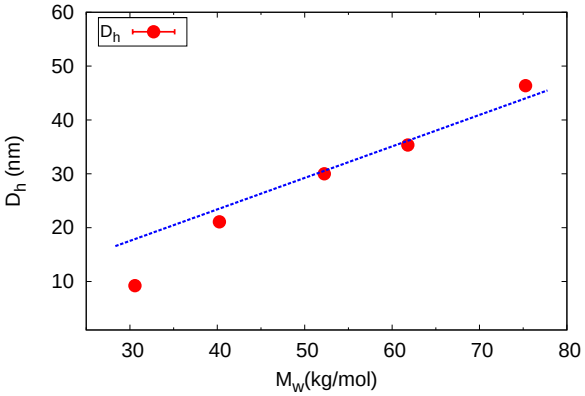


**Figure 5.21.:** Scaling behavior of the PS chains at the surface of d-PS particles obtained by DLS measurements. The dashed line is a linear fit of the experimental data from d-PS particles. $D_h$ denotes a difference in $R_h$ between the surface-modified and grafted particles, namely the hydrodynamic brush thickness.

The linear scaling law found in our experiments was very similar to that of polymer brushes on a flat substrate [56, 107]. This demonstrates that polymers with sufficiently high grafting densities can exhibit a highly stretched conformation, similar to the behavior of polymer brushes on a planar substrate.
We note that the complete scenario of the scaling behavior between the thickness of the brush and the molecular weight should contain the grafting density. However, we did not attempt to include the effect of the grafting density on the scaling relationship, as the grafting density was not obtainable for the given particle systems. Nevertheless, the linear relationship between the shell thickness and the molecular weight shown in Figure 5.21 will enable us to assert that the grafting density variation is not significant.

### SANS measurements

Finally, the structure property of the surface-modified d-PS particle was investigated by SANS. The respective scattering from the particles is shown in Figure 5.22. The particles were dissolved in d-toluene at a low concentration (c=0.1 wt%). This allowed us to determine the single particle scattering without interference from interparticle scattering. The measurement was done at the KWS-1 beam line at FRM-2 in Munich. Figure 5.22 shows the results obtained using two detector distances as described in section 2.2.2. Details of the data correction process are described in section 2.2.2. Here, the large $q$ values using the closest detector distance are not included in the data presentation to highlight the intermediate $q$ behavior of the scattering curve. The relatively large error bars shown in the intermediate $q$ are caused by the low intensity of the sample scattering after correction for the background, that is, empty cell correction, as shown in section 2.2.2. The data were well described with a form factor from a spherical core-shell particle, as shown in the full line in Figure 5.22. The fit was obtained using the SLD of the core of d-PS of 6.47 $\times 10^{-4}$ nm$^{-2}$ and that of the solvent of d-toluene of 5.66 $\times 10^{-4}$ nm$^{-2}$. It should be noted, however, that the concentration entered an intensity carried a significant error due to the marginal solubility of the particles. The resulting volume fraction ($\phi$=0.02%) was smaller than expected ($\phi$=0.08%).
The fit resulted in a core radius of 32.5 nm with low polydispersity (19%). This was in accordance with the observation made from the TEM results shown in Figure 5.19. The shell corresponded to a layer

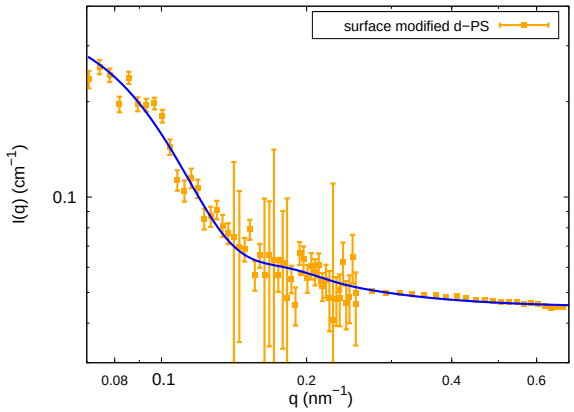


**Figure 5.22.:** SANS data of surface-modified d-PS particles dissolved in c=0.1 wt% d-toluene. Solid line is a fit with a core-step like shell form factor.

of 3.5 nm, which was again in accordance with the expectation for the thickness of the NMRP initiator layer.
We note that organic d-PS nanoparticles grafted with protonated PS brushes will have an excellent contrast in SANS experiments to gain further insights into the grafted PS chain conformation, as described in section 5.1 and 5.2. These studies will be the focus of a future work.

### 5.3.3 Conclusion

Previously, chain conformation on silica and d-PS nanoparticles with rather low grafting densities was investigated experimentally by combining scattering methods, DLS, SAXS, and SANS. Here, polymer chain conformation has been investigated as an extension of the previous results on the d-PS nanoparticle systems with rather low grafting densities, where the polymer chain conformation was found to be that of a semi-dilute polymer brush (SDPB). Hereby, the grafting density was intended to be increased compared to the previous case with a different chemical synthesis method. Grafted chain conformation was investigated for a wide range of the molecular weights, similar to the previous case.
The SI-NMRP (surface initiated nitroxide mediated radical polymerization) of styrene was successfully applied on almost fully deuterated PS-nanoparticles ($R_c = 43$ nm) to synthesize PS grafted d-PS particles, and the scaling behavior of the PS shell on the d-PS particles was studied by DLS. DLS measurements of surface-grafted d-PS particles confirmed the existence of PS brushes, resulting in a linear relationship of the shell thickness with increasing molecular weights. The conformation of the grafted PS chains on the given particle systems showed a more stretched conformation than on silica and d-PS nanoparticles made by the ATRP method, which indicates that the conformation of the polymer brush here is that of the concentrated polymer brush (CPB) rather than SDPB. Therefore, larger grafting density could be expected compared to the previous cases.
SANS investigation showed that the surface-modified particles were spherical core-shell particles with a deuterated core and a thin layer of the NMRP initiator. The surface- modified particles will be used as a base particle for a future work for SANS measurements, to investigate the grafted PS chain conformation where enhanced contrast between the protonated PS layer and the deuterated solvent is expected.

## 5.4 Conclusion

Polystyrene (PS) was grafted from the surface of inorganic silica nanoparticles ($R_c \sim 26$ nm), and organic d-PS nanoparticles ($R_c \sim 21$ and 33 nm) using different synthesis methods. For silica, the surface initiated anionic polymerization method (SIAP) was applied, for d-PS, atomic transfer radical polymerization (ATRP) for small particles and nitroxide mediated radical polymerization (NMRP) for large particles, respectively. The NMRP method for the d-PS particles was applied to yield a higher grafting density than the ATRP method. The resulting particles had a variety of grafting densities and molecular weights of the grafted chains on cores with comparable sizes, which were named the internal parameters expected to influence the conformation of the grafted chains in good solvents.

SAXS, SANS, and DLS were combined to reveal the conformation feature of the grafted chains on three sets of the particles in good solvents, either toluene or THF. The use of protonated grafted PS chains in deuterated solvents, d-THF or d-toluene, enabled us to probe the grafted chain conformation explicitly by means of SANS. SAXS could be used as a complementary method to obtain the size of the core, especially for the case of silica particles due to the large electron density contrast between the core and the solvent. Finally, DLS was used to obtain the hydrodynamic thickness of the grafted PS layer to support the complete picture of the grafted chain conformation. For the DLS measurements, normal solvents of toluene or THF were used instead of deuterated solvents. It was crucial to determine the grafting density of our samples accurately to probe the conformation features of the grafted chains. This was done with the information gained from the SANS data analysis. The silica particles and small d-PS particles grafted with PS were investigated by SANS. In the analysis of the SANS data, the core-linear shell model and the Debye function were used. The use of the core-linear shell model was found to be appropriate to describe the SANS data due to the low scattering length density contrast between the solvent and the corona shell. The Debye function was used due to the characteristic $q^{-2}$ scattering at high $q$ ranges. The grafting density could be obtained by the use of the linear density profile of the corona shell, and for the silica particles, the results from SANS could be directly compared with those form TGA (thermo gravimetry analysis). For the case of d-PS particles, the results from SANS data fits have been also applied to obtain the grafting density.

As discussed in sections 5.1, 5.2, and 5.3, for the silica and small d-PS nanoparticles, SANS and DLS were used to obtain the thickness of the grafted PS layer for the molecular weights over a wide range. For the large d-PS particles, only DLS was used. For the silica and the small d-PS nanoparticles, the thickness overall scaled with ${M_w}^{0.6}$ with a size larger than $2R_g$ of the free PS chains in the same good solvents, demonstrating that the grafted chain conformation is that of the semi-dilute polymer brush rather than dilute polymer. The scaling prediction for the SDPB regime shown in eq. 5.15 was applied to the data from both particle systems, and the validity of eq. 5.15 for the data supported the SDPB conformation of the grafted chains on the silica and small d-PS nanoparticles. For the largest molecular weights of the grafted PS on d-PS with a small core, we found hints of an SDPB-to-dilute transition where the grafting density was determined to be small compared to others and the thickness converged to $2R_g$. In addition, the conformation of the grafted chains was barely affected by substrate materials of different hydrophobicity, illustrating that the interaction between the grafted chains and the substrate does not play an important role in the change in conformation.

For d-PS particles with a large core, we found different scaling of the thickness compared to the previous cases. DLS results demonstrated that the thickness scaled linearly with the molecular weights, verifying that the grafted chains are in the concentrated polymer brush (CPB) regime rather than in the SDPB or dilute polymer regime. Therefore, a large grafting density for the given particle systems could be expected. It is noteworthy that, for this particle system, the NMRP method was applied to synthesize and grow PS on the particle surfaces. For the organic d-PS nanoparticles, the NMRP method has been found to yield a high grafting density compared to other methods of SIAP or ATRP.

In the next chapter, the main issue will be the phase behavior of the nanoparticles in a polymer matrix which is chemically identical to the grafted polymer. To that end, d-PS and p-PS will be used as a matrix

polymer and a grafted polymer, respectively. Representative samples from three sets of the samples in chapter 5 will be selected to observe the change in the conformation of the grafted chain and the dispersion state of the grafted particles, in dependence on the variation in the molecular weights of d-PS matrices.

# 6 Polymer grafted nanoparticle in the same polymer matrix

In section 3.2.2, the change in the conformation of the grafted polymer on nanoparticles dispersed in a chemically identical polymer matrix (wetting-dewetting transition) and the corresponding change in the particle dispersion were described based on recent results from simulations and experiments. The direct observation of the size of the grafted chains and the change in the dispersion state with respect to the change in molecular weights of the free matrix chains, however, remained an open question.

Here, we present our results concerning the structural characterization of a polymer nanoparticle composite (PNC) made of spherical nanoparticles (silica and deuterated PS, d-PS) grafted with protonated PS (p-PS) and d-PS matrices. These systems were measured by SANS and SAXS. For the purpose of SANS measurements, d-PS was used as a matrix and p-PS was used as a grafted chain in order to achieve a large SLD contrast between the grafted p-PS layer and the matrix d-PS. Especially for the SANS experiments of the d-PS particles, the shell contrast could be achieved by using p-PS as grafted chains and d-PS as a core and a matrix. For the silica particles, the core and shell both contributed to the contrast, leading to core-shell contrast.

One set of inorganic silica nanoparticles ($R_c \approx 26$ nm by SAXS) and two sets of organic d-PS nanoparticles ($R_c \approx 21$ nm and $\approx 32.5$ nm by SANS) were used for the investigation. PS was grafted on silica nanoparticles using the surface initiated anionic polymerization method and on d-PS nanoparticles using ATRP (atomic transfer radical polymerization method) for smaller particles and NMRP (nitroxide mediated radical polymerization) for larger particles. The NMRP method was used to yield a higher grafting density than the ATRP method. The chemical details of the polymerization methods for each set of the nanoparticles are briefly described in sections 5.1, 5.2 and 5.3. The grafting density for the silica particle was determined to be ≈0.02 or 0.035 chains/nm$^2$ (the former obtained by SANS and the latter by TGA), and that for the small d-PS particle ≈0.032 chains/nm$^2$ (obtained by SANS). The conformation of both particle systems under a good solvent condition were revealed to be SDPB, semi-dilute polymer brush, which shows a slightly stretched conformation compared to the random coil conformation in the bulk state [74], as previously discussed in sections 5.1 and 5.2. The grafting density for the large d-PS particle was, however, unknown but found to be in CPB regime, as discussed in section 5.3.

The primary objective of this chapter is to investigate the variation in the thickness of the grafted PS layer for the given systems as a function of the molecular weight of d-PS matrices, which may permit direct observation of the change in the conformation of the grafted PS layer in response to the variation in the molecular weight of d-PS matrices. Its change corresponds to that of the wetting of the matrix polymer chains on the grafted chains, namely the wetting-dewetting transition. The thickness obtained for each set of particle systems will be compared to see the influence of the various parameters, such as the grafting density, the molecular weight ratio between the free and grafted matrix chains, namely the molecular weight ratio $\kappa$, and the curvature, $D/R_g$, on the phase transition. SANS will be used as the primary tool to evaluate the thickness and conformation of the grafted PS polymer on the spherical substrates. SAXS will be used as a complementary tool to extract the core radius of the given systems. Note that, in order to track the change in the conformation depending on the length of the matrix polymer, the length of the grafted polymer, could also be varied. However, this was not done for this work due to the difficulty of creating a series of different grafted chains compared to those of different matrix chains with the same grafting density.

The second objective is to relate the change in the conformation of the grafted PS with the dispersion of the particles. The thickness obtained from the SANS results will be compared with the parameter for

the dispersion, the correlation length from the Debye-Bueche term, $\xi_{DB}$, which is also obtained from SANS results. It is indeed clear that, via comparison of the two parameters of thickness and $\xi_{DB}$, the link between the dispersion and the change in the conformation will be revealed. Finally, recent results for the same or similar PNC systems will be compared with our results for a better understanding of how the parameters of the grafting density and molecular weight ratio as well as the curvature parameter affect the wetting-dewetting transition.

## 6.1 Sample preparation

In order to make the polymer-nanoparticle composite (PNC), the particles were first dissolved with d-PS matrices in THF and sonicated for one hour. In order to completely evaporate THF, the mixture was dried in air for one day and further annealed in a vacuum oven at 135°C for one day. The annealing process was then applied to prepare the film samples in order to completely evaporate the solvent, avoid voids arising from air bubbles, and effectively disperse the particles in the matrices. The annealing temperature was set above the glass transition temperature (about 100 °C for PS) of PS, to effectively disperse the particles. As we thought that the temperatures and duration of application of annealing may play a role in the dispersion of the particles, various sets of annealing temperatures and durations were attempted to obtain at least a mechanically stable film, which may correspond to a good dispersion of the particles. The optimized temperature and duration of annealing were 135°C and one day. However, we have not attempted to investigate the effect of these parameters on the change in the microscopic structure by means of SANS.
The effect of the duration of annealing was investigated by Akcora et al. [52]. They reported that, for particle systems of PS grafted silica with a diameter of 14 nm, when they were annealed at 150 °C, the size of the aggregates increases with annealing time, especially for the particles in larger molecular weights of matrix PS than that of grafted PS chain, and the domain formation of aggregates becomes slower for the particles in large molecular weights of PS matrices. Slow domain formation is intuitively understandable since large molecular weight polymers become more viscous and less mobile compared to low molecular weight polymers.

**Table 6.1.:** Properties of d-PS matrix polymers used for grafted silica and smaller d-PS particles, and composites

| PS label | $PDI_{SEC}$ [a] | $M_w$ [b] (kg/mol) | molecular weight ratio of SI - $\kappa = N_f/N_g$ [c] | molecular weight ratio of d-PS - $\kappa = N_f/N_g$ [d] |
|---|---|---|---|---|
| 7k[e] | 1.05 | 7.2 | – | 0.3 |
| 16k[f] | 1.05 | 16.4 | 0.6 | 0.6 |
| 22k[f] | 1.07 | 21.6 | 0.9 | 0.8 |
| 32k[f] | 1.06 | 32.4 | 1.3 | 1.1 |
| 41k[f] | 1.09 | 40.9 | 1.6 | 1.4 |
| 118k[f] | 1.15 | 118.2 | 4.7 | 4.2 |

a: PDI index of polymers determined by SEC
b: Weight-averaged molecular weight of d-PS matrix polymers
c: $N_f$ is the polymerization index of the matrix PS and $N_g$ is that of the grafted PS. $\kappa$ is the molecular weight ratio of the free matrix to the grafted PS. Calculation based on the molecular weight of grafted PS on silica particles (25.4 kg/mol)
d: Calculation based on the molecular weight of grafted PS on d-PS particles (28.5 kg/mol)
e: Matrix polymers used for dispersing d-PS particles
f: Matrix polymers used for dispersing silica and d-PS particles

**Table 6.2.:** Properties of d-PS matrix polymers used for grafted d-PS particles of a large core, and composites

| PS label | $PDI_{SEC}$ | $M_w$ [a] (kg/mol) | molecular weight ratio - $\kappa = N_f/N_g$ [b] |
|---|---|---|---|
| 17k | 1.06 | 17.3 | 0.2 |
| 30k | 1.03 | 30.2 | 0.4 |
| 49k | 1.02 | 49.4 | 0.7 |
| 81k | 1.02 | 80.8 | 1.1 |
| 120k | 1.06 | 120.3 | 1.6 |
| 174k | 1.19 | 174 | 2.3 |
| 361k | 1.42 | 361 | 4.8 |

a: Weight-averaged molecular weight of d-PS matrix polymers
b: Calculation based on the molecular weight of grafted d-PS (75.3 kg/mol)

The concentration of the particles in the composite was set low (c=1 wt%) to minimize the interaction of the particles. Finally, the film was made with a hydraulic press (Weber Pressen), where the temperature and the pressure on the plate can be modulated. Thereby, the pressure could be varied from 0 to 3,183 kN/m$^2$ and the temperature from 0 to 400 °C. A powder consisting of particles and matrix polymer was put onto the plate of the press and afterwards the temperature and pressure were applied to create the film samples. The initial temperature was set at 120 ° C for the samples containing low molecular weights of d-PS matrix (7 to 30 kg/mol) and 135 °C for large molecular weights. After the temperature was initiated, a moderate pressure of ∼80 kN/m$^2$ was applied, and the sample was cooled slowly. The cooling rate of the samples of low molecular weights of d-PS matrices (7 to 30 kg/mol) was approximately 2 K/min and for the other samples, 3 K/min. The films obtained from the samples for the measurement, had a thickness of ∼0.1 mm to optimize the transmission from the samples for both scattering experiments, SAXS and SANS. The thickness was measured using a Mitutoyo Micrometer Screw with a tolerance of error of 0.01 mm. For the measurements of SANS and SAXS, the samples were directly attached onto the sample holder by a transparent tape, which does not influence the scattering since it was attached to the outer boundary of the sample holder.
The parameters expected to affect the change of the wetting property of the free matrix polymer on the grafted polymer on the spherical interface are the molecular weight ratio $\kappa$, the ratio of the molecular weight of the matrix to the grafted PS, $\sigma$, the grafting density, and the ratio of the particle diameter (D $= 2R_c$) to the length of the grafted polymer ($R_g$), the curvature parameter $D/R_g$. $\kappa$ was denoted as the ratio of the degree of polymerization of the free matrix polymer ($N_f$) to the grafted polymer ($N_g$), as defined previously in section 3.2.2. $R_g$ was taken from the well-known relation for the bulk PS in a theta solvent, $R_g = 0.0275 \times {M_w}^{1/2}$ (nm) [10, 108]. The $M_w$ of the grafted chains for each system was taken into account in calculating $R_g$. The molecular weight of grafted PS used in this study was 25 kg/mol for the silica particles, 29 kg/mol for the small d-PS particles, and 75 kg/mol for the large d-PS particles, while that of the matrix PS was varied from ≈7 kg/mol to 361 kg/mol. The molecular weights of the grafted PS for the organic core, d-PS, were obtained from the freely grown PS using a sacrificial initiator, which is expected to be a well-suited method to obtain a value close to the grafted molecular weight for the organic core. That of the silica particles was, on the other hand, that of the grafted chains, which was obtained by detaching the grafted PS by etching the silica core with hydrofluoric acid (HF). The deuterated PS polymer was synthesized by a conventional anionic polymerization method in house. One set of d-PS polymers, shown in Table 6.1, was prepared for the measurements at D11 at ILL, and the other set of d-PS polymers shown in Table 6.2 was prepared for the measurements at KWS-1 at FRM 2. The molecular weight ratio, $\kappa$, was then tuned from ≈0.4 to 4.8 at constant grafting densities for each particle system, and it was expected to cover a wide range of $\kappa$ to observe the wetting-dewetting

transition. The details of the sample specifications are listed in Table 6.1 for the measurement at ILL and 6.2 for the measurements at KWS-1. The curvature parameters $D/R_g$, were 11.9 for the silica particles, 9.3 for the smaller d-PS particles and 7.6 for the larger d-PS particles.

## 6.2 Description of experimental data

As described in section 4.3, the experimental SANS data is analyzed by the following calculation of intensity:

$$I(q) = \phi \frac{\left\langle |F(q,R)|^2 \right\rangle}{\left\langle V_p \right\rangle} + I_{DB} + I_b. \tag{6.1}$$

$\phi$ is the volume fraction of particles suspended in solution, $F(q,R)$ is a form factor, $I_b$ is an experimental background, and $I_{\mathrm{DB}}$ is a Debye-Bueche function which was introduced and discussed in eq. 4.12 in section 4.1. As discussed in section 4.3, the bracket representation of $V_p$ and $F(q,R)$ indicates that those quantities have been averaged with respect to the core size distribution function, in our case a Schulz function. This can be done with integration of the given quantities with the distribution function in spherical coordinate. Due to the presence of aggregates, a strong upturn toward a low $q$ in a small angle scattering curve appears, and the Debye-Bueche contribution $I_{\mathrm{DB}}$ was then implemented to describe the low $q$ scattering arising from aggregates, as discussed in section 4.1. In this section, the Debye-Bueche function was used since the data was extended to low $q$ values to cover the whole profile of the scattering curves from the aggregates: a plateau at a lower $q$ and a decay followed by the plateau.
In the analysis of the SANS data of systems of silica and d-PS nanoparticles with a relatively low grafting density, a form factor, $F(q,R)$, of the spherical core-step-like shell model was used to analyze the experimental SANS scattering curves, and that of a spherical core was used for the SAXS data analysis. The core-step-like shell model is given by

$$F_{\mathrm{cs}}(q) = (\rho_c - \rho_{sh}) \cdot V_c \cdot F_{\mathrm{sphere}}(q,R_c) + (\rho_{sh} - \rho_m) \cdot V_{\mathrm{cs}} \cdot F_{\mathrm{sphere}}(q,R_c + \Delta). \tag{6.2}$$

$\rho_c$, $\rho_{sh}$, and $\rho_m$ are the scattering length density (SLD) of the core, shell and dispersion matrix. $R_c$ is a core radius and $\Delta$ is the thickness of the shell. $V_c$ is the volume of a core and $V_{cs}$ is that of a core-shell particle. The above expression assumes that both the core and shell have a uniform SLD profile. $F_{\mathrm{sphere}}(q,R)$ is amplitude of a solid sphere form factor introduced in eq. 4.24.
For the analysis of the SANS curves from PS grafted silica and smaller d-PS particles, application of a core-diffusive shell such as a core-linear shell and a core-exponential shell did not lead to a better fit of the experimental data compared to a simple core-step-like shell model. Additionally, the parameters obtained from each fit using different profiles were comparable. Therefore, the latter model of the core-step-like shell was used to analyze the experimental SANS scattering curves. We note that the SAXS data were not in absolute scale, so $\phi$ simply represented a scale factor. We assumed that the core has a spherical shape for considering model functions to evaluate the data for the particle systems investigated in our study. The use of the spherical core is evidenced by the TEM pictures introduced in sections of 5.1, 5.2, and 5.3.
On the other hand, for d-PS particles with a high grafting density, we used the core-shell-chain model introduced by Pedersen or the core-linear shell model with a fluctuation term. The former model function was described in section 4.3.1 and the latter in section 4.3.2. We note that the existence of $q^{-2}$ behavior of the scattering curves at a high $q$ for the d-PS particles with a high grafting density required the use of a more advanced model: either the core-shell model with an additional fluctuation term or the core-shell-chain model introduced by Pedersen. The scattering function from Pedersen was assumed to have a spherical core and a corona shell with a half-Gaussian profile and a fluctuation term describing $q^{-2}$ behavior at a high $q$ was intrinsically included in the function as a form of the Debye term (model 2 in

the category of core-shell-chain models defined in section 4.3.1). Two model descriptions will then be applied to analyze the SANS data for the d-PS particles with a high grafting density, and one of them will be selected based on the fit quality and the parameters which physically makes sense.
As the first approach, a form factor, $F_{cs}(q,R)$, of a core-linear shell was used in a form of eq. 4.42 using a linear profile for the corona shell on the spherical core, shown in eq.4.43. For calculation of the total intensity, the fluctuation term $I_{\text{fluct}}(q)$ in eq. 4.48 was superimposed on the intensity $I(q)$, shown in eq. 6.1 as given by

$$I_{\text{total}}(q) = I(q) + I_{\text{fluct}}(q) \tag{6.3}$$

As the second approach, the form factor was based on Pedersen's approach, where the core is surrounded by a diffused shell with a half-Gaussian profile and an additional Debye term included (model 2 included in the core-shell-chain models as defined in section 4.3.1). A squared form factor $P(q)$ was introduced in eq. 4.28. Components of the scattering function were introduced in section 4.3.1.
For the shell contrast situation, where the SLD of a core is matched with that of a dispersion medium, both the core and matrix PS were deuterated. In this case, $P(q)$ in eq. 4.28 reduces to

$$P(q) = N_c {V_{\text{chain}}}^2 \Delta{\rho_{\text{chain}}}^2 \cdot \left[P_{\text{chain}}(q,R_g) + (N_c - 1)S_{\text{chain-chain}}(q)\right]. \tag{6.4}$$

$N_c$ is the number of grafted chains per particle, $V_{\text{chain}}$ is the volume of a single chain, $P_{\text{chain}}(q,R_g)$ is the Debye function shown in eq. 4.25, and $S_{\text{chain-chain}}(q)$ is given in eq. 4.37 using eq. 4.38. $V_{\text{chain}}$ is calculated from $N_x \cdot V_{\text{monomer}}$, where $N_x$ is the degree of polymerization of x polymer and $V_{\text{monomer}}$ is the volume of a monomer of a given x polymer. Considering eq. 6.1, the calculation of the total intensity for the core-shell-chain form factor is given by

$$I(q) = \frac{\phi}{\langle V_p \rangle} \cdot \langle P(q) \rangle + I_{\text{DB}} + I_b \tag{6.5}$$

$V_p$ is the volume of a particle containing a core and $N_c$ grafted chains, given in eq. 4.31.

**Table 6.3.:** Scattering length densities and electron densities used for data fitting [16, 109]

| compound | scattering length density($10^{-4}$ nm$^{-2}$) | electron density (nm$^{-3}$) |
|---|---|---|
| $SiO_2$ | 2.92 | 556 |
| p-PS | 1.41 | 340 |
| d-PS | 6.47 | 340 |

The scattering length densities and electron densities of constituents of PS grafted silica and d-PS particles in d-PS matrices are listed in Table 6.3 and schematically illustrated in Figure 6.1. As the grafted and free matrix polymers are chemically identical, SAXS is appropriate to characterize the core for the case of silica particles. SANS is, on the other hand, sensitive to the chain conformation due to the large difference in the SLD of the protonated PS shell (p-PS) and the d-PS matrix. Therefore, for the silica case, SAXS was used to determine the core radius, $R_c$, and this radius was used and fixed for fits of the SANS data to obtain other parameters more reliably. For d-PS particles, only SANS was used for the characterization due to the large contrast between the shell and, the matrix and the core, originating from deuterium labeling of the core and matrix polymer. SAXS was not implemented for a characterization tool due to missing contrasts of the constituents of the investigated system (zero contrast among the core, shell, and matrix). For SANS "shell contrast" was achieved due to the almost identical SLD of

the core and the matrix. Note that the d-PS core consists of 90 wt% of d-PS and 10 wt% of deuterated divinyl benzene (d-dVB) as a cross linker which has a chemically similar structure with PS. Therefore, the SLD of the core could be approximated to that of the d-PS since the difference in the SLD between the core containing d-PS and d-dVB, and d-PS would be negligible.

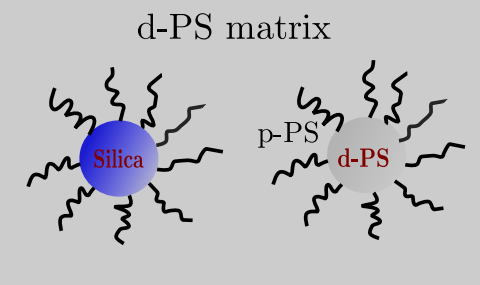


**Figure 6.1.:** Schematic picture of the SLD contrast of silica and d-PS nanoparticles in a d-PS matrix from SANS.

## 6.3 Results and discussion

SANS experiments were performed on the D11 instrument at ILL in Grenoble for silica particles and d-PS particles with a small core size and low grafting density. Another series of SANS measurements was made on the KWS-1 instrument at FRM 2 for d-PS particles with a large core and high grafting density. Complementary SAXS experiments were performed in house. All SAXS and SANS measurements were performed at room temperature and the samples had the form of a solid thin film with a thickness of ∼0.1 mm. The samples were directly attached to the sample holder. The experimental details for each experiment were previously described in section 2.2.2.

### 6.3.1 Results of PS grafted silica and small d-PS particles in d-PS matrices

We begin with a description of the data from PS grafted- silica and d-PS with a small core size in d-PS matrices. Figure 6.2 shows the experimental SANS and SAXS scattering curves of PS grafted silica nanoparticles in d-PS matrices and curve fits using eq. 6.1 in terms of the core-step like shell form factor and the Debye-Bueche function.
As is shown in Figure 6.2 (a), the core-step-like shell model and the Debye-Bueche function describes the experimental SANS data from the given particle systems reasonably well. Since the core-shell form factor decays as $q^{-4}$, it is clear that there is no indication of $q^{-2}$ behavior at a high $q$ range. Therefore, more advanced models such as the core-diffusive shell plus a fluctuation term or the core-shell-chain model, would not be adequate to analyze the data due to the existence of the Debye function phenomenologically included in the fit functions.
For the SANS data fit of the systems of PS grafted silica and d-PS nanoparticles in d-PS matrices, the core-step-like shell model and Debye-Bueche contribution were applied, and for the SAXS fit of the systems of PS grafted silica nanoparticles, the form factor of a solid sphere was applied. For the SAXS data fit, the Debye-Bueche contribution was not used, as $q$ was not extended to a relatively low $q$ range compared to the SANS experiment. The information on the dispersion of the particles is to be shown at a lower $q$ range than the $q$ limit of the SAXS experiment, and the $q$ range of the SAXS data did not allow us to obtain adequate information on the dispersion of the particles. Therefore, only the form factor was used to obtain the information on single particle. Moreover, domains of aggregates may be formed with a rather large size, and they may not be distributed homogenously. Note that a SANS beam (1 × 1 cm of rectangular shape in our case) is significantly larger than a SAXS beam (diameter of 200 $\mu$m and a circular shape in our case). Correspondingly the large beam size from SANS scattering methods may be

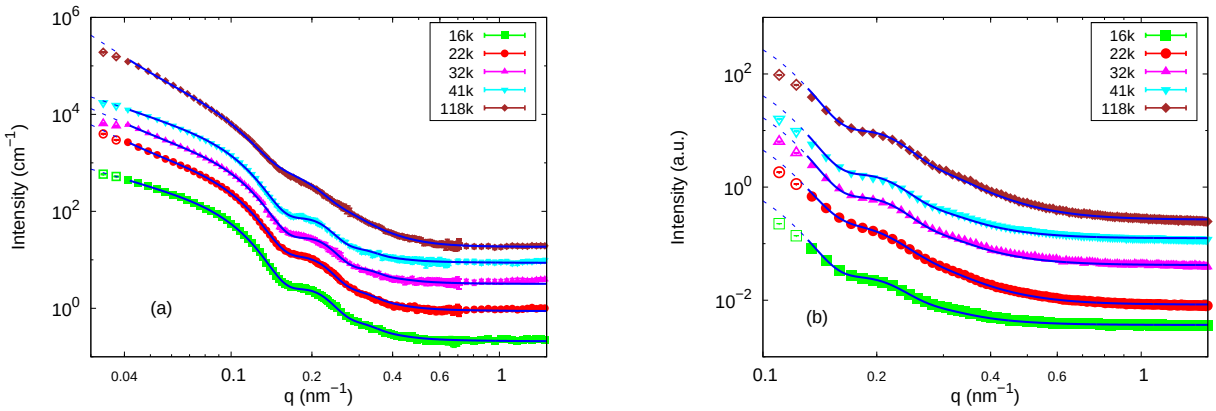


**Figure 6.2.:** (a): SANS scattering curves of PS grafted silica in 1 wt% d-PS matrices of $M_w$ of 16 kg/mol to 118 kg/mol with curve fits. (b): SAXS scattering curves for the same particle systems with fits. Solid lines are fits according to eq. 6.1. For (a) core-shell form factor shown in eq. 6.2 and Debye-Bueche term in eq. 4.12 were implemented and for (b) sphere form factor in eq. 4.13 was implemented. The data were vertically shifted for clarity, and sample notations are defined in Table 6.1. The open symbols were not taken into account in analyzing the data.

able to capture and detect larger size scales than the SAXS method. Therefore, SANS may detect more precisely the domains of the aggregates than SAXS.

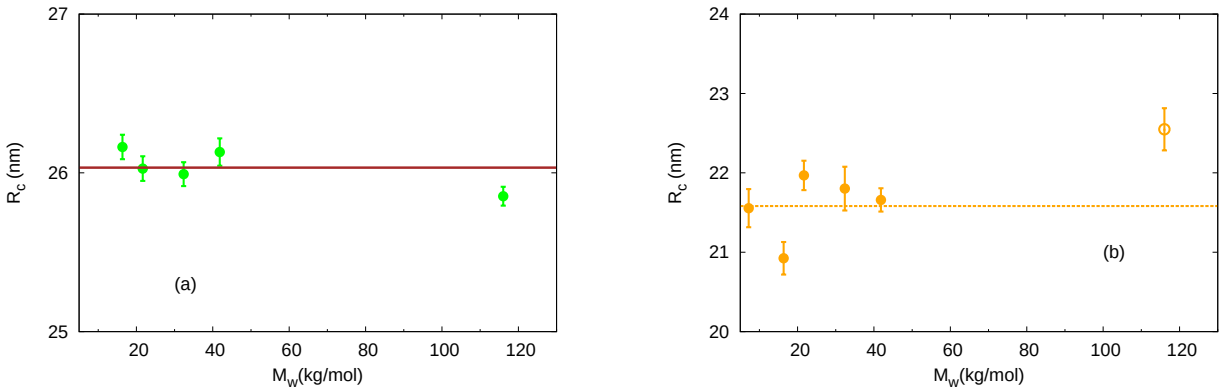


**Figure 6.3.:** (a): The mean core radius ($R_c$) was determined by taking an average value over all investigated samples of PS grafted silica particles in d-PS matrices. The core radius for each molecular weight was determined by SAXS data fits for the given samples using the solid sphere form factor. (b): $R_c$ was determined by taking an average value over the samples of PS grafted d-PS particles in d-PS matrices. The core radius for each molecular weight was determined by SANS data fits with other parameters varied as well, and for further fit processes, the average core radius was held constant to obtain reasonable fit parameters. Note that, for determination of an averaged radius in the case of (b) 5 samples of low $M_w$s were considered since the sample of largest $M_w$ deviated from the values from other samples.

For silica particles, SAXS data has been used to obtain the core radius $R_c$ by taking an average value over all samples investigated, as shown in Figure 6.3. $R_c$ was then determined to be ≈26 nm to be consistent with that of the surface-modified particle as reported in section 5.1. This radius was set as the core size in

the SANS data analysis to reduce the fit parameters and correspondingly extract other parameters from the fits more reasonably. The variable parameters for the SANS data fit of silica particle systems were the volume fraction $\phi$, the polydispersity of the core, the thickness and the SLD of the polymeric shell, the prefactor A, and the correlation length $\xi$ for the Debye-Bueche contribution. The SLD of the core and matrix were set at the values from Table 6.3 and not varied during the fit process. For SANS data from the d-PS particle systems, the variable parameters were the same as in the case of silica particle systems except the SLD of the shell. The SLD of the shell for that case was not varied because, in a shell contrast situation, the SLD of the shell and the volume fraction $\phi$ are coupled to act in scaling the intensity. Therefore, the SLD of the shell was fixed at that of bulk PS, as shown in Table 6.3. The core-shell model and the Debye-Bueche contribution described the experimental data reasonably well. The components of the model function used for the SANS data fit are additionally displayed in Figure 6.5.
As shown in Figure 6.2 (a), SANS scattering curves from PS grafted silica in matrices of 16 to 41 kg/mol have almost similar features throughout whole $q$ ranges but a curve from PS grafted silica in a matrix of 118 kg/mol presents explicitly different scattering behavior. A gradual increase in the intensity toward lower $q$ values is observed for the samples of matrices of 16 to 41 kg/mol, while the sample of a matrix of 118 kg/mol is distinguished by a steeper increase in the intensity. The steeper increase in the intensity at a low $q$ range ($q < 0.1$ nm$^{-1}$) observed for the latter case is indicative of the formation of the larger objects. As for the high $q$ scattering behavior (0.1 nm$^{-1}$ $< q <$ 0.6 nm$^{-1}$) a similar oscillation pattern of the scattering curves is shown for the samples of lower molecular weights of d-PS (16 to 41 kg/mol) while the smeared oscillation is observed for the sample of the largest molecular weight of d-PS matrix. The change in the scattering pattern for the variation in the molecular weight of the matrix PS was reflected in the resulting fit parameters and these are plotted in Figure 6.6.

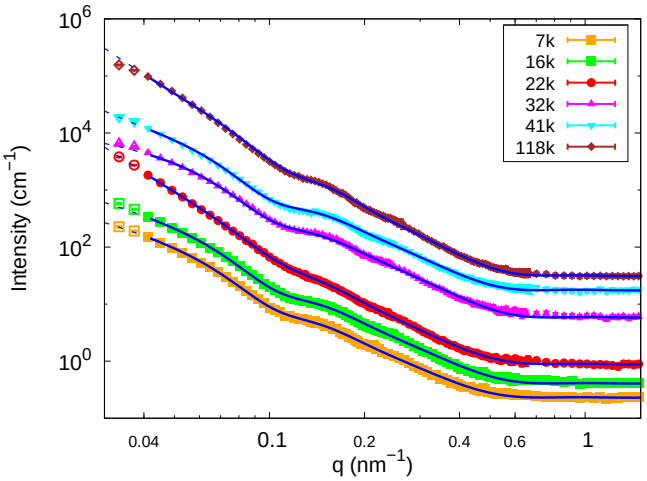


**Figure 6.4.:** SANS scattering curves of PS grafted d-PS in 1 wt% d-PS matrices of $M_w$ of 7 kg/mol to 118 kg/mol with curve fits. The fit function implemented was eq. 6.1 based on core-step-like shell form factor shown in eq. 6.2. The data were vertically shifted for clarity, and sample notations are as given in Table 6.1. The open symbols were not taken into account in analyzing the data.

Figure 6.4 displays the experimental scattering curves and fits of the PS grafted d-PS particles with a small core in d-PS matrices. The core-step-like shell model and the Debye-Bueche contribution in the form of eq. 4.12 was used as before. The SAXS experiment could not give information on the structure of the given particle systems due to missing contrasts among the core, shell, and matrix. The core radius was then obtained by taking an average value of the core radii obtained by the fits of the SANS data from the particles in d-PS matrices of $M_w$ of 7 kg/mol to 41 kg/mol, excluding the sample of the largest $M_w$

of d-PS matrices, because the value obtained for the sample of the largest $M_w$ of a d-PS matrix deviated from those for the samples of smaller $M_w$ of d-PS matrices. We note that the resulting mean core size was ∼21.5 nm, which agrees well with that in d-toluene obtained by SANS, 21 nm. This verifies that the given particles are not swollen with respect to the different solvent quality, indicating that the core is formed with dense networks. This slight difference may, on the other hand, originate from the difference in resolution of the two instruments (present particle was measured by the D11 instrument and the surface-modified particles by the KWS-2 instrument). It is noteworthy that the deviation in the mean size found by the two instruments are however negligible. The mean core size, ∼21.5 nm, is therefore to be used for that of the present system to characterize other parameters.
This core radius was then held constant for the next fitting iteration. Again, the fit function of the core-step-like shell model and Debye-Bueche contribution, provides a nice description of the experimental data. Herein, all scattering curves show almost identical scattering patterns at a high $q$ range ($0.1\ \mathrm{nm}^{-1} < q < 0.6\ \mathrm{nm}^{-1}$), indicating that the microscopic structures of the samples are almost identical. The intensity gradient at a low $q$ range is altered for each sample, and this implies no systematical variation in the formation of large objects. The resulting fit parameters are plotted in Figure 6.7. In Figure 6.5, the components of the fit function for the data for PS grafted silica in a matrix of $M_w$ of 41 kg/mol and for the data for PS grafted d-PS in a matrix of 7.2 kg/mol, are displayed as examples. The contribution of each component from the fit function is displayed in the plots below.

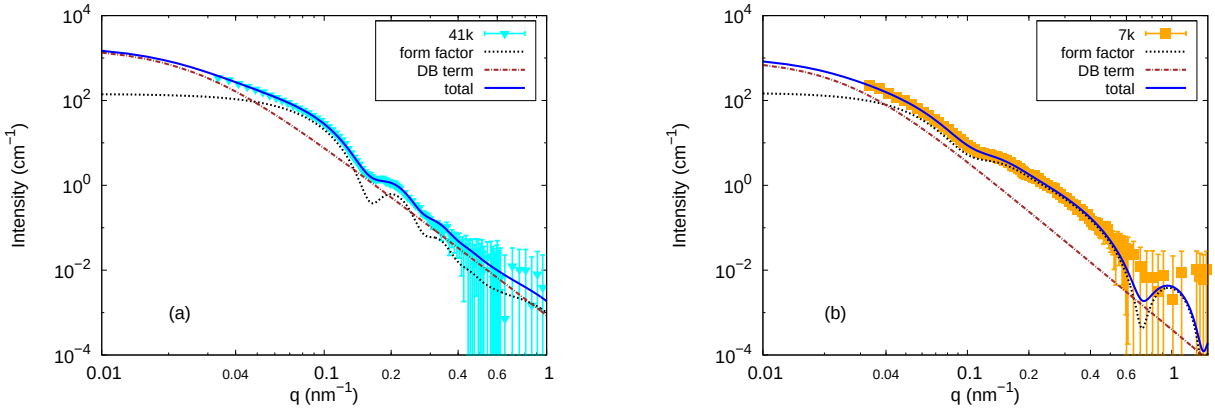


**Figure 6.5.:** (a): Constituent parts of the model function to describe the data from PS grafted silica in a matrix of $M_w$ of 41 kg/mol (b): Constituent parts from PS grafted d-PS in a matrix of $M_w$ of 7.2 kg/mol. For data fits, the fit function of the core-step like shell was superimposed on that of the Debye Bueche term to describe the low $q$ behavior. For both data presentations, the experimental incoherent background was subtracted from the intensity. The theoretically expected incoherent background for PS grafted SI and d-PS in a d-PS matrix is ∼ 0.01 cm$^{-1}$ for both cases, if the equation $I_b{}^{\mathrm{theo}} = \left(\frac{d\Sigma}{d\Omega}\right)_{inc} = \frac{1}{v_m}\sum_{j=1}^{n}\left(\Delta b_j{}^2\right)$ and the volume fraction of the particles for both systems are considered. $I_b{}^{\mathrm{theo}}$ is a theoretical background, $v_m$ is the molecular volume and $\Delta b_j$ is the incoherent scattering length of a component in a molecule (see section 2.1.5 for details). However, the experimental incoherent background $I_b$ is larger by more than an order of magnitude. Note that the reason for this large deviation between the theoretical and experimental incoherent background may be due to the scattering from voids within the sample, the parasitic scattering from air or experimental environments, or possible protonated components contained in a d-PS matrix and d-PS core.

Explicitly shown is that the Debye-Bueche term describes scattering at a low $q$ and core-step-like shell form factor, that at an intermediate $q$.
In Figure 6.6 and Figure 6.7, the variation in the thickness and the correlation length of the grafted

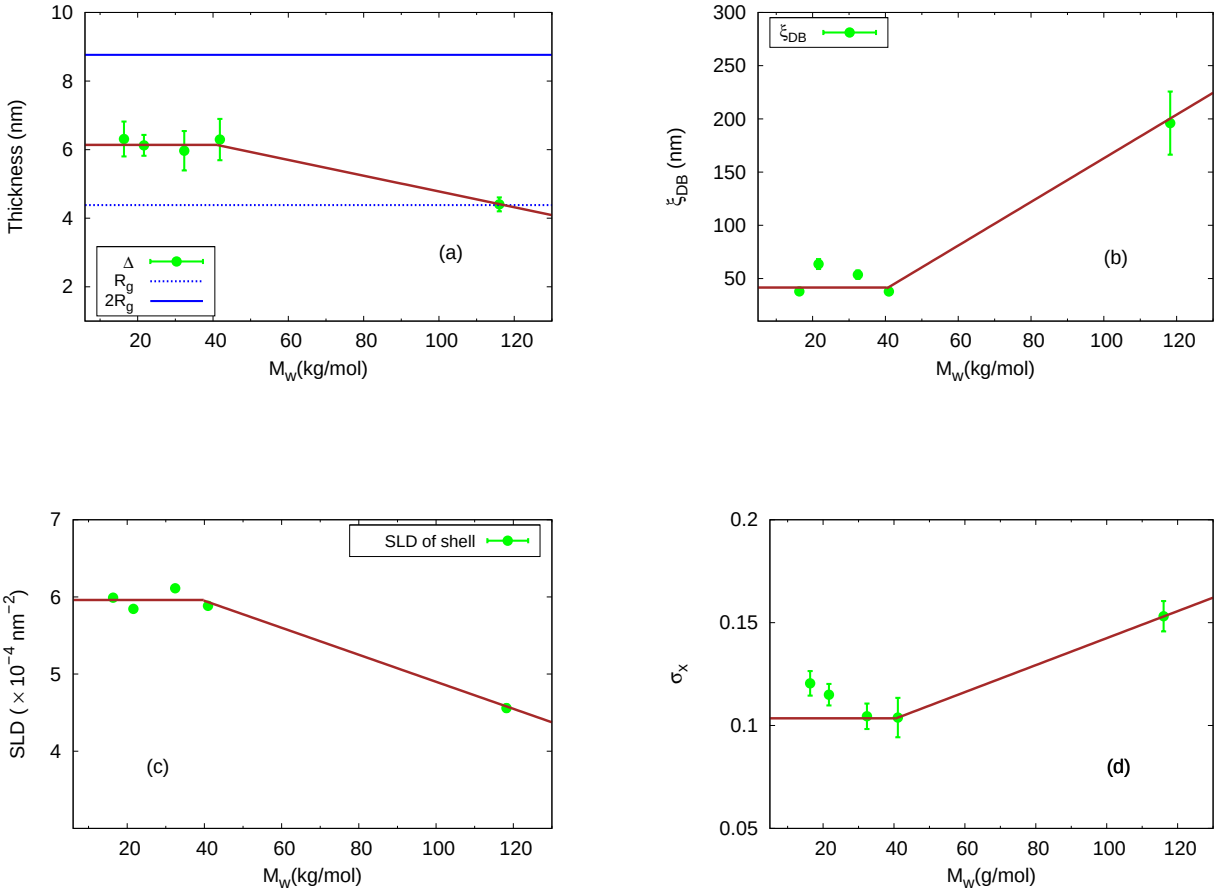


**Figure 6.6.:** (a): Variation in the thickness of the grafted PS layers on silica particles with $M_w$ of d-PS matrices. (b): Correlation length from the Debye-Bueche contribution in eq. 4.12 for the silica particles as a function of $M_w$ of d-PS matrices (c): SLD of the corona shell as a function of $M_w$ of d-PS matrices (d): Polydispersity index (denoted as $\sigma_x$ in the label) variation for given particle systems with $M_w$ of d-PS matrices. Autophobic dewetting is clearly observed in (a), (b) and (c). All parameters shown above were obtained by SANS data fits for given particle systems. All plots here are in linear-linear scales.

PS layer for both systems are plotted as a function of the molecular weight of d-PS matrices. Here, we begin with a discussion on the results from the silica particles shown in Figure 6.6. For the silica particle systems, decreased thickness for the sample of the largest $M_w$ of matrix d-PS is clearly seen, while these values remained constant at lower molecular weights, which is a clear indication of the change in the conformation induced by a change in the length of the matrix polymer. Along with variation in the thickness, variation in the correlation length is also observed as a function of $M_w$ of d-PS matrices. The increase in the correlation length at the largest $M_w$ may indicate the formation of large objects and appears to accompany a drop in the thickness. Large objects may be either aggregates or voids which might be formed during the film preparation process. This point will be clarified in detail with a comparison of the results from the d-PS particles with a small core. It is noteworthy, however, that this coupling may indicate that the change in the conformation of the grafted layer is related to that of the interaction between the particles in the d-PS matrix. It is theoretically expected that the dispersion state of the particles is influenced by the interaction between the grafted and free polymer chains, where a reduction in the mixing-demixing entropy driven by a large matrix polymer chain induces the collapse of the grafted polymer chain to balance the resulting free energy. As stated in section 3.2.2, the free energy

consists of the elastic chain stretching and the mixing-demixing term. The total free energy is balanced by the weighting of both terms. A large length of the free matrix chains reduces the mixing term for the total free energy and results in a decrease in the chain stretching term, a collapse of the grafted chains. As shown in Figure 6.6, the transition for the silica particles in d-PS matrices occurs between the molecular weight of d-PS matrix of 41 kg/mol and 118 kg/mol, corresponding to the molecular weight ratio $1.6 < \kappa < 4.7$ (see Table 6.1). The phenomenon of the wetting-dewetting transition is also reflected in the variation in the SLD of the shell with the molecular weight of the d-PS matrix, as shown in Figure 6.6. The reduction of the interpenetration of the grafted and free chains is proved by the decrease in the SLD of the shell because a decrease in the SLD value of the shell represents a decrease in the number of free matrix d-PS chains between the grafted sites.
The results from d-PS particles in Figure 6.7 show a different behavior compared to those from silica particles.

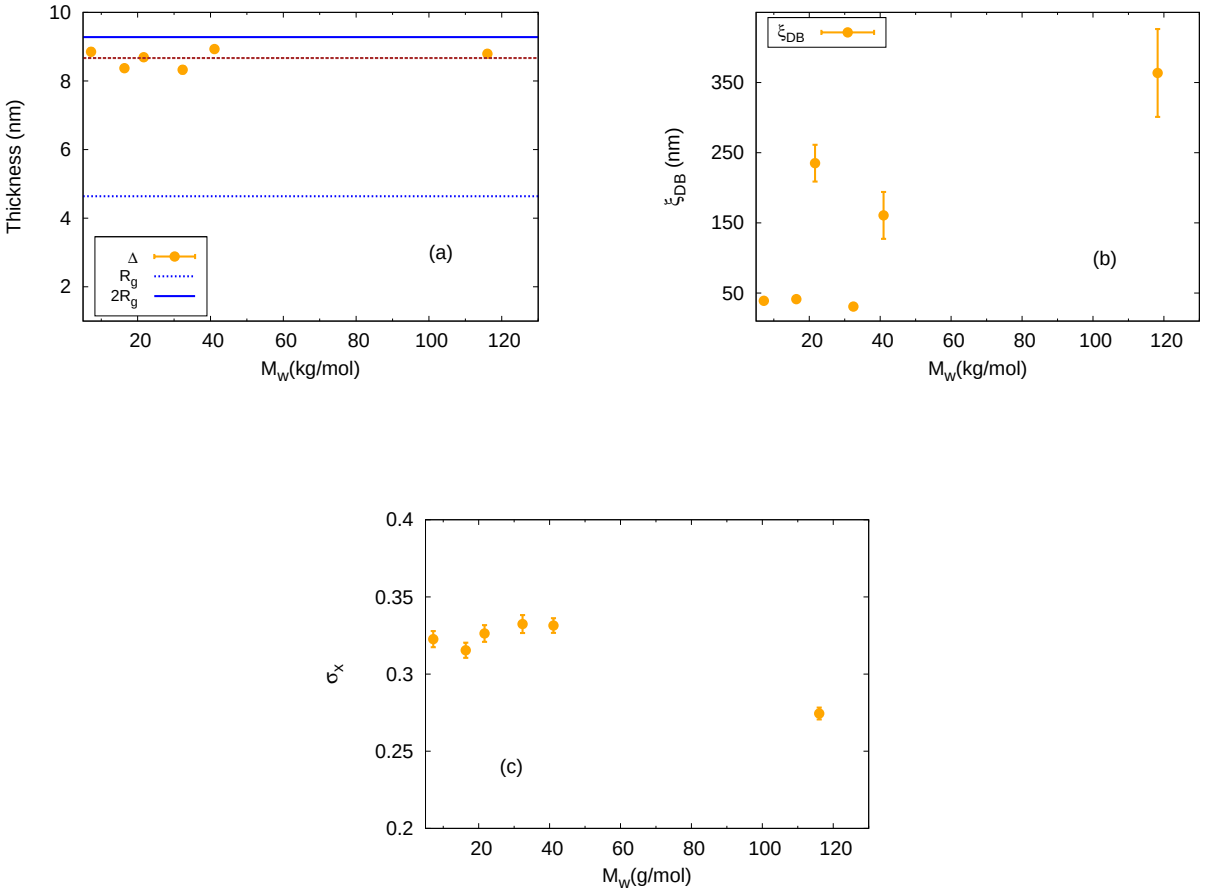


**Figure 6.7.:** (a): Variation in the thickness of the grafted PS layer on d-PS with a small core with $M_w$ of d-PS matrices. (b): Correlation length from the Debye-Bueche contribution as a function of $M_w$ of d-PS matrices. (c): Polydispersity of the core size for the given systems as a function of $M_w$ of d-PS matrices. No indication of the wetting-dewetting transition was observed for the given particle systems since the thickness remained constant over variation of $M_w$ of d-PS matrices. The correlation length does not vary systematically, indicating that there is no systematic tendency for the formation of large objects (see text for details). All parameters shown above were obtained by SANS data fits of given particle systems with a fixed core radius. All plots here are in linear-linear scales.

As shown in the plot, the thickness remains constant over the variation in $M_w$ of d-PS matrices, and the correlation length from the Debye-Bueche contribution is not varied systematically. The constant values of the thickness throughout the variation of the $M_w$ of d-PS matrices demonstrate that the conformation of the grafted PS chains did not change in d-PS matrices of varying $M_w$. Non-systematic variation in the correlation length may be caused by aggregation or voids formed during the film preparation process, and their contributions are presented in the scattering curves, as shown in Figure 6.7 (b), as a consequence of low $q$ scattering patterns for the given samples. Note that the voids might be formed by the infiltration of air bubbles during the film preparation process, most probably during the pressing process to fabricate the thin film. Constant variation in the thickness of the grafted PS layer indeed demonstrates that the wetting-dewetting transition of the d-PS particles did not occur for the range of $M_w$ of d-PS matrices used in our study. The polydispersity of the core shown in Figure 6.7 (c) remained almost constant over variation of $M_w$ of d-PS matrices of 6 kg/mol to 41 kg/mol and decreased slightly for the largest $M_w$ of d-PS matrix. This decrease in the polydispersity shows the opposite trend from that of the silica particles. The difference in the tendency of the polydispersity between the silica and d-PS particles in the largest $M_w$ of d-PS matrix may originate from the difference in the interaction character between two particle systems. Since, for the silica particles, the free matrix chains dewetted and for the d-PS particles still wetted to the grafted chains, an attractive interaction for the silica particles is expected, while the repulsive interaction is expected for the d-PS particles. The difference in the interaction, therefore, seems to be reflected in the difference in the tendency of the polydispersity for the silica and d-PS particle systems, which demonstrates that the dispersion state described by the Debye-Bueche term in the analysis of the data, is a rather simplified description.

The difference in the dispersion of the two particle systems can be checked by different behaviors in the parameter of $\xi_{\mathrm{DB}}$. Note that the $\xi_{\mathrm{DB}}$ of both particle systems at the same large molecular weight (118 kg/mol) was comparatively large. A sudden increase in $\xi_{\mathrm{DB}}$ should be correlated with the formation of large objects. Moreover, the large objects would be either large voids or aggregates, and the scattering from voids or aggregates is expected to make the same contribution to the scattering curves at low $q$ ranges. It is not easy to distinguish the difference between the two contributions. However, according to the above theoretical prediction between the change in the wetting property of the free chains and the dispersion state of the particles, the silica particles are likely to be agglomerated and the d-PS particles are not.

Note that the wetting-dewetting transition did not occur for d-PS particles in the largest $M_w$ of d-PS matrix but did for silica particles. The corresponding different transition behavior of the two particle systems illustrates that the behavior of interpenetration of the free matrix chains to the grafted chains for the same $M_w$ of d-PS matrix differs significantly. It is then expected that the difference in the parameters for the two particle systems will clarify the difference in the wetting-behavior of the free matrix chains. As noted before, for both particle systems, internal parameters such as the grafting density and the molecular weights are comparable, while the core size is slightly different. A slightly smaller core size was found for the d-PS particles ($R_c$=21.5 nm) compared to that of the silica ($R_c$=26 nm). This will be a clue to the different phase behavior at the largest $M_w$ of the d-PS matrix polymer, and this will be discussed later.

### 6.3.2 Results of PS grafted, large d-PS particles in d-PS matrices

We now turn to describe the scattering patterns of PS grafted d-PS nanoparticles with a large core ($R_c$ = 28.5 nm from TEM) and a large grafting density (see section 5.3). The presence of $q^{-2}$ behavior in the scattering curves at a high $q$ for d-PS particles with a high grafting density required the use of a more advanced model: either the core-shell model with an additional fluctuation term or a core-shell-chain model for the box-Gaussian profile of a shell, defined as model 2 included in the category of the core-shell-chain models in section 4.3.1. For the purpose of obtaining $R_c$ and $N_c$ for both cases, the scattering curves from the particles in d-PS matrices of 30 kg/mol to 361 kg/mol, were considered, where the

distinct oscillation feature is present at an intermediate $q$ range ($0.1\text{nm}^{-1} < q < 0.3\text{nm}^{-1}$). The data from the particles in a d-PS matrix of 17 kg/mol was not used due to a smeared oscillation pattern at an intermediate $q$ range, which leads to difficulty in obtaining the size of the particles. Then, in the next iteration of the fit process, the given mean core size, $R_c$, and $N_c$ were fixed to fit other parameters to obtain reasonable results. As an example of the quality of the data fit, Figure 6.8 shows a comparison of the fits of the same data for PS grafted d-PS in a d-PS matrix of $M_w$ of 17 kg/mol analyzed by two different fit functions. In the plot, the half-Gaussian represents the fit function based on the core-shell-chain model for half-Gaussian SLD profile of a shell (defined as model 2 included in the category of the core-shell-chain models in section 4.3.1) and linear-debye represents the fit function based on core-linear shell with the Debye function. For both cases, the Debye-Bueche function was implemented to describe low $q$ scattering behavior. It is clearly shown in the plot that the core-linear shell model can not properly describe the smeared oscillation pattern shown at the intermediate $q$ range with an exceptionally large value of the polydispersity, ∼0.7 but the core-shell-chain model could serve with a moderate polydispersity value of ∼0.23. Therefore, it is clear that the given system is not physically described by the core-linear shell model but by the core-shell-chain model.
We additionally note that the mean core size obtained by the core-linear shell model ($R_c \sim 25$nm) deviates from that in solution by SANS ($R_c \sim 32.5$ nm) or that in dried state by TEM ($R_c \sim 28.5$ nm) as shown in section 5.3. Therefore, we decided to use the fit function from the core-shell-chain model based on the aforementioned considerations.

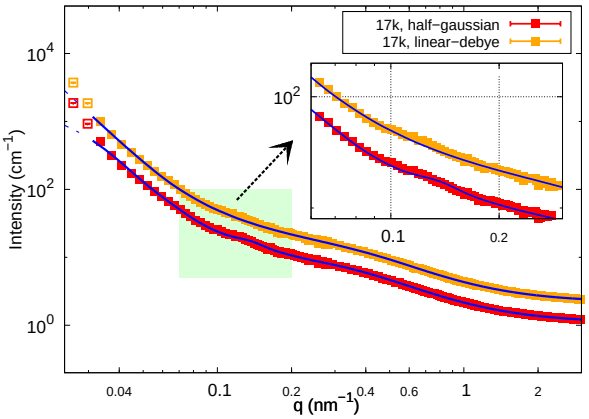


**Figure 6.8.:** Comparison of the fit by the core-shell-chain model for a box-Gaussian profile of a shell (model 2 included in the category of the core-shell-chain models in section 4.3.1) with that by the core-linear shell model plus Debye function. To fit the low $q$ ranges, the Debye-Bueche function was implemented. The data represented here is from the d-PS particles in a matrix of $M_w$ of 17 kg/mol and denoted as 17k in the plot. It is clear that the core-linear shell model fails to describe the smeared oscillation present at intermediate $q$ range ($0.1\ \text{nm}^{-1} < q < 0.3\ \text{nm}^{-1}$).

Figure 6.9 presents the scattering curves from d-PS nanoparticles with curve fits. In Figure 6.9 (b), the incoherent experimental background was subtracted to present $q^{-4}$ behavior at a low $q$ and $q^{-2}$ behavior at a high $q$. The former behavior originates from the scattering from the core-shell architecture and the latter from the Gaussian chain behavior or the density fluctuation of the polymer chains within the corona shell, as discussed previously. In Figure 6.9 (c), the fit function based on the core-shell-chain model was decomposed to show the contribution of each component.
The fits of the experimental data were performed by the fit function based on the core-shell-chain model for the half-Gaussian SLD profile of a corona shell with a Debye Bueche term as introduced previously. The fit parameters were the volume fraction $\phi$, the core radius $R_c$, the number of grafted chains $N_c$,

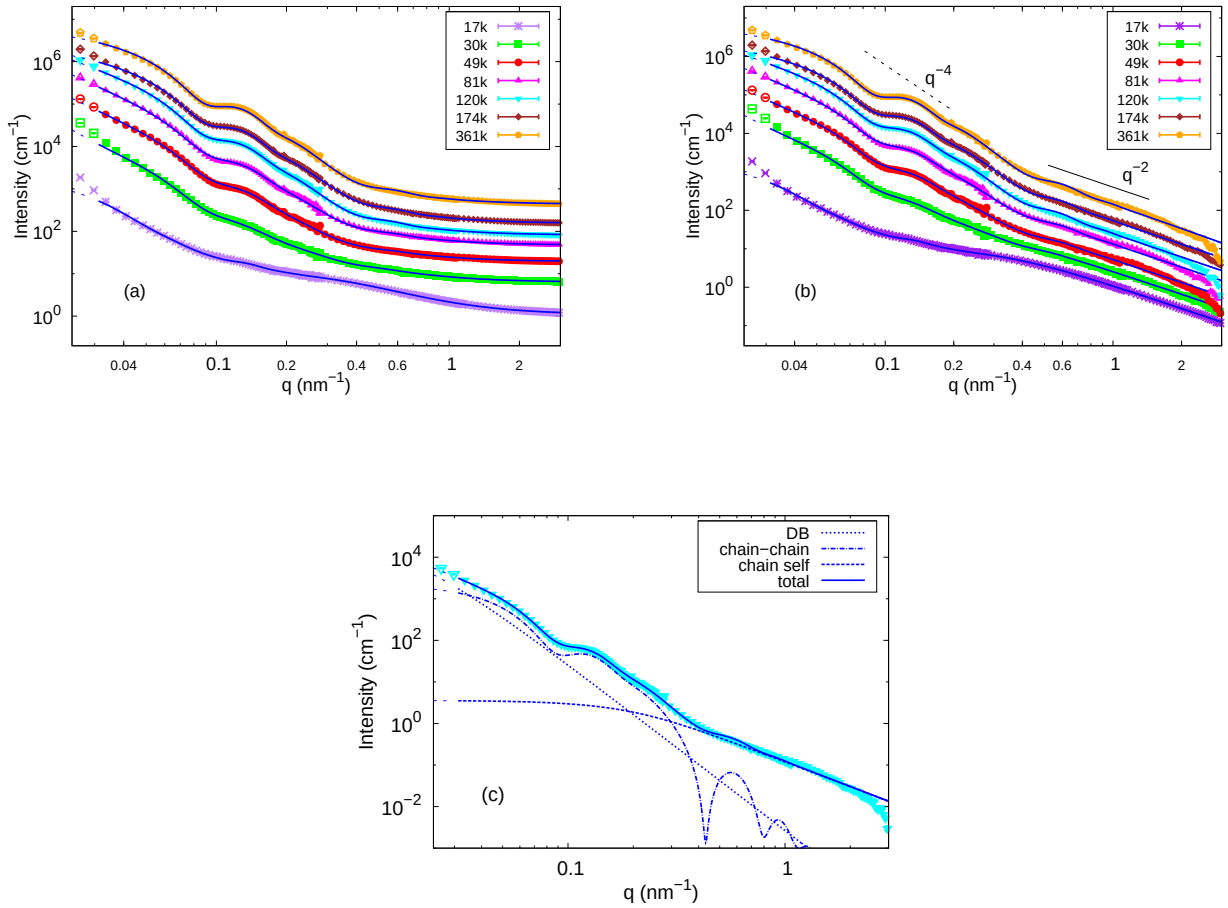


**Figure 6.9.:** (a): SANS scattering curves of PS grafted d-PS with a large core and large grafting density in c=1 wt% d-PS matrices of $M_w$ of 17 kg/mol to 361 kg/mol with curve fits. (b): The same curves with the incoherent experimental background subtracted. (c): Components of the fit function based on the core-shell-chain model for the half-Gaussian SLD profile of a shell (model 2 within the category of the core-shell-chain models in section 4.3.1) as an example with the data. The data is from PS grafted d-PS particles in 120 kg/mol of d-PS matrix. DB denotes the Debye-Bueche term, chain-chain denotes the chain-chain correlation term, chain-self, the Debye-function, included in the core-shell-chain model. Total means the total fit function shown in eq. 4.28. The fit function implemented was a superposition of the core-shell-chain model for a half-Gaussian SLD profile of a shell and Debye-Bueche term in the form of eq. 6.5. The data were vertically shifted for clarity. The open symbols were not taken into account in analyzing the data and sample notations in the plots are given in Table 6.2. $q^{-4}$ behavior at low $q$ ranges and $q^{-2}$ behavior at high $q$ ranges are also displayed in the plot in (b) (see text).

the thickness of the grafted PS layer, the polydispersity of the core size, $R_g$, the background $I_b$, the correlation length $\xi_{\mathrm{DB}}$ and the prefactor $A$ from the Debye-Bueche contribution. The SLD of the core, shell, and matrix were set at that of bulk d-PS for the core and matrix, and that of bulk p-PS for the shell, as shown in Table 6.3. Note that the SLD of the shell is not to be varied in the core-shell-chain model, as its SLD profile is assigned to be that of the grafted chains, not that of the whole corona shell, usually treated as a mixture of the grafted chains and dispersion medium in the core-shell approach. The contribution of the corona shell is then obtained by weighting the chain form factor with the number of chains, $N_c$, as shown in eq. 4.28. The chain volume, named $V_{\mathrm{chain}}$, is a fixed parameter calculated by taking the $M_w$ of the grafted PS chains into account (see section 6.2). For the calculation, a volume of a styrene monomer $V_{\mathrm{monomer}}$, 166.1 Å$^3$ [69], was considered. The degree of polymerization $N_{\mathrm{PS}}$ was taken

by considering the weight-averaged $M_w$ of the grafted PS obtained by the SEC measurement of freely grown chains. This was determined to be ∼75 kg/mol, and it was used to obtain $N_{PS}$. The volume of the chain then represents the volume occupied by the polymer segments. In order to fit the data, the core size and the number of chains were first determined with the aforementioned parameters all varied. For the next fit iteration, the parameters of $R_c$ and $N_c$, were held constant, while the parameters except two fixed parameters were varied. The latter process was intended to obtain the resulting parameters more reasonably since variation in the core size and the number of chains would lead to unphysical results. In order to obtain $R_c$ and $N_c$, six scattering curves of $M_w$ of d-PS matrices of 30 kg/mol to 361 kg/mol were taken into account since the scattering curve of the lowest $M_w$ of d-PS matrix did not have a pronounced oscillation feature at the intermediate $q$ range (0.1 $nm^{-1} < q < 0.3$ $nm^{-1}$), which may be caused by missing the well-defined interface between the particle and the matrix. This data will be described in more detail below. After taking six curves into consideration, $R_c$ and $N_c$ were obtained as shown in Figure 6.10.

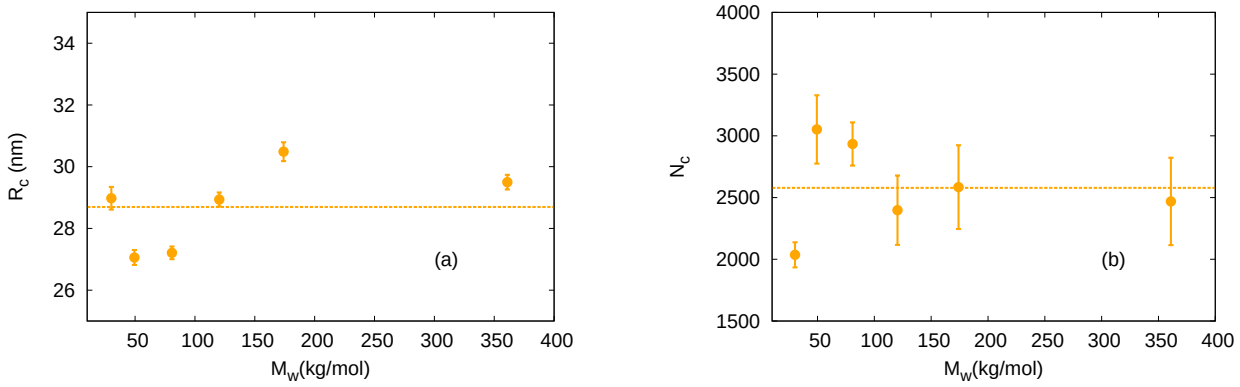


**Figure 6.10.:** (a): The mean core radius ($R_c$) was determined by taking an average value over samples of PS grafted d-PS particles in d-PS matrices of 30 kg/mol to 361 kg/mol. The data from the particles in the lowest $M_w$ of d-PS matrix was not used due to smearing of the oscillation of the scattering curve at the intermediate $q$ range. (b): The number of chains, $N_c$, was determined by taking an average value over samples of the particles in the same range of $M_w$ of d-PS matrices. Both parameters for each molecular weight were determined by SANS data fits with other parameters varied as well and for the further fit process, the mean values of the core size and the number of chains were fixed throughout the next fit iteration to obtain reasonable fit parameters.

The scattering curves from the samples of $M_w$ of 30 kg/mol to 361 kg/mol show an almost similar oscillation pattern at an intermediate $q$ range (0.1 $nm^{-1} < q < 0.3$ $nm^{-1}$) but the curve from the sample of 17 kg/mol is distinguished by the smearing of the oscillation pattern and pronounced $q^{-2}$ behavior. The curve from the sample of the lowest $M_w$ of d-PS matrix indeed shows “chain-like behavior”, as the $q^{-2}$ behavior is extended to low $q$ ranges, and this $q^{-2}$ behavior appears to be a dominating term compared to other curves. It may represent the swelling of the grafted PS chains due to the penetration of small free matrix chains to the grafted chains, thus leading to the expansion of the grafted chains and the absence of a well-defined interface, where increased mixing-demixing entropy is in that case balanced by the expansion of the grafted chains. This could be checked by the results from the fit, indeed showing the pronounced swelling of the corona shell compared to others.
As for the low $q$ scattering behavior, the Debye-Bueche contribution describes the experimental data from the samples of $M_w$ of 17 kg/mol and 30 kg/mol only approximately at the lowest $q$ limit. At this $q$ range, the scattering curves show an additional scattering which slightly deviates from the theoretical power law dependence from the Debye-Bueche contribution. This may indicate the structural feature of

the aggregates or the loss of the resolution for the large aggregates. Therefore, for the samples in d-PS matrices of $M_w$ of 17 kg/mol and 30 kg/mol, the information on the size of the aggregates from the Debye-Bueche contribution could carry a large systematic error and be only approximations. The Debye-Bueche contribution can then describe only the Porod regime for the aggregates, the surface scattering of the aggregates. However, for the remaining samples of $M_w$ of 49 kg/mol to 361 kg/mol, the Debye-Bueche contribution provides a good description of the low $q$ scattering behavior of the given curves. In Figure 6.11 (b), we then show the results of the correlation length, $\xi_{\mathrm{DB}}$ as a measure of the aggregates for the samples of $M_w$ of 49 kg/mol to 361 kg/mol and for the other samples of small $M_w$ of 17 and 30 kg/mol as an approximation. Therefore, the results from the samples of small $M_w$s are represented by open symbols while those from large $M_w$s from 49kg/mol to 361kg/mol, were represented by filled symbols in the plot. The correlation length, $\xi_{\mathrm{DB}}$, obtained by data fits are also plotted in Figure 6.11, and the sample of $M_w$ of 30 kg/mol is distinguished by a sudden increase in $\xi_{\mathrm{DB}}$, while $\xi_{\mathrm{DB}}$ for other samples is comparatively small. For that sample, strong aggregation seemed to occur which might have been formed during the film preparation process. We note that the force on the plate of the press machine could not be homogeneously applied on the powder when the amounts of powder were small compared to the large size of the plate of the press. This might have induced the aggregation for the given sample. $R_c$ was found to be ∼29nm, comparable to but slightly smaller than ∼32.5 nm, the previously reported value for the surface-modified particles in d-toluene obtained by SANS in section 5.3. Note that the different solvent quality would create the difference in the mean sizes on the d-PS cores. D-toluene is a good solvent and can penetrate the d-PS cores. This can lead to swelling of the cores. However, penetration of the matrix polymer is not expected due to the presence of the divinyl benzene cross-linker (10 wt% in a particle), then the core size will tend to decrease compared to the result determined in solution. The slight decrease in the mean core size of d-PS particles can therefore be corroborated. This mean core size can be compared with the results from TEM for the same surface-modified particles measured in a dried state. It was found to be ∼29 nm, consistent with the current value found by SANS for the same particles in the polymer matrix. The number of chains obtained by fit was ∼2,555 and this quantity corresponds to a grafting density, $\sigma \approx 0.25$ chains/nm$^2$. This is indeed a large grafting density compared to the previous cases for silica ($\sigma \approx 0.02$ chains/nm$^2$) and the d-PS with a small core size ($\sigma \approx 0.032$ chains/nm$^2$). Note that the previous results in sections 5.1, 5.2, and 5.3, demonstrated that, under a good solvent condition, the grafted chains on the large d-PS particles adopt the concentrated polymer brush (CPB) while those on silica and d-PS with a small core adopt the semi-dilute polymer brush (SDPB) regime. Additionally, the parameter $\phi$ from the SANS data fit of large d-PS particles remained constant over the range of $M_w$ of d-PS matrix of 30 kg/mol to 361 kg/mol, at $\sim 0.015$. This value agrees well with the expectation from the sample preparation ( $\phi \sim 0.011$), for which the volume of the chain from the half-Gaussian profile has been considered to obtain the volume fraction of the chains in the whole particle architecture. However $\phi$ for the smallest $M_w$, 17 kg/mol, was found to be ∼0.045. Note that the parameter of chain volume, $V_{\mathrm{chain}}$, was fixed at ∼120 nm$^3$ for the fit process, the derivation is given in section 6.2. According to eq. 6.4 and eq. 6.5, in order to obtain a value of $\phi$ for this sample that is comparable with others, the volume of the chain should be increased by a factor of 2. This increase is another verification of the swelling of the grafted PS chains.

The change in the wetting property can be directly checked by the variation of the thickness of the corona shell with $M_w$ of d-PS matrices. The swelling of the grafted PS layer is observed for the smallest free matrix chains (17 k) and it is maintained for the next $M_w$ (30 k). The constant thickness persisted over the rest of the samples, which is a clear indication of the wetting-dewetting transition. As shown in Figure 6.11, the transition occurs between $M_w$ of 30 kg/mol to 49 kg/mol and the corresponding molecular weight ratio, $0.4 < \kappa < 0.7$. It is recognized that the wetting-dewetting transition for the given particle systems occurred at a smaller $\kappa$ than for the silica particle systems. Both particle systems have differences in the grafting density and the core size, as well as different hydrophobicity. The difference in these three parameters may have an influence on the wetting-dewetting behavior of the free matrix chains. We previously stated in section 5.2 that the different hydrophobicity of the substrate

materials, either silica or d-PS, does not influence the grafted chain conformation under a good solvent condition. It is expected that the different hydrophobicity of the substrates will not influence the grafted chain conformation on the particles in a melt as well.

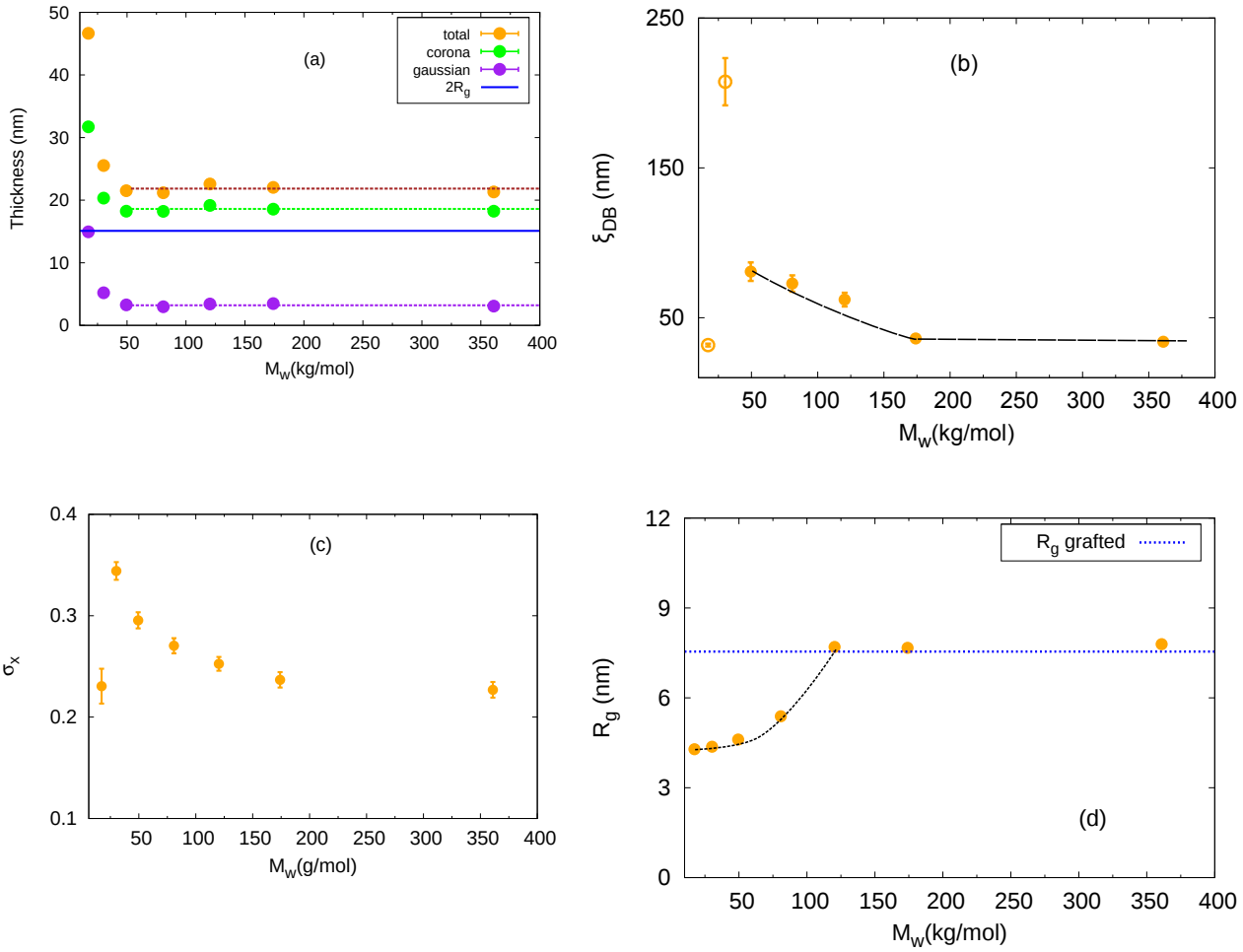


**Figure 6.11.:** Graphical representation of SANS fit results for d-PS nanoparticles with a large core. (a): Variation in the thickness of the grafted PS layer with $M_w$ of d-PS matrix. Corona denotes the thickness of the part of the flat profile in the half-Gaussian profile of the shell, Gaussian that of the part of the Gaussian profile, and total that of the combined one. (b): Variation in the correlation length with $M_w$ of d-PS matrix. (c): Variation in the polydispersity of the core size. (d): Variation in the radius of gyration to describe the high $q$ scattering behavior and to explain further the variation in the correlation length of the mixture of the grafted and free matrix chains within the corona shell on the particles. Parameters were obtained by fits of the experimental data by the core-shell-chain model for a half-Gaussian SLD profile of the shell superimposed with the Debye-Bueche function. All plots are linear scaled in the horizontal and the vertical axis. The trend line shown in (a) is a linear fit of the results ranging from $M_w$ of 30 kg/mol to 361 kg/mol to show a constant variation in the thickness. The results for low $M_w$s, shown in (b) are presented with open symbols since these results could carry large systematic errors (see text for details). Dashed lines in (b) and (d) are guide lines to show the tendency of the results. Dotted line in (d) is an $R_g$ of the grafted chains in a theta solvent.

As for the determination of the correlation length, $\xi_{DB}$, for the samples of $M_w$ of 17 kg/mol and 30 kg/mol, due to the deviation of the scattering curves with the theoretical expectation from the Debye-Bueche function, the discussion will be limited to the case of the samples in the range of 49 kg/mol to 361 kg/mol. This range of samples was assigned to the dewetted state. $\xi_{DB}$, decreased gradually over the variation of the $M_w$ in that range, verifying that the size of the aggregates decreases slightly with $M_w$

of d-PS matrix as well. Here, it is noteworthy that the coupling of the variation between the correlation length and conformation of the grafted PS chains was not observed. For the sample of $M_w$ of 49 kg/mol, where the wetting-dewetting transition occurred, a sudden increase in $\xi_{\mathrm{DB}}$ was not observed, unlike in the case of silica particles.
Small values of $\xi_{\mathrm{DB}}$ indicates that the aggregates are rather compact, not a large dimension. Rather small values of $\xi_{\mathrm{DB}}$ may be attributed to the steric stabilization from the densely grafted polymer layer, as also reported by Srivastava et al. [53] for the particles at high grafting densities. Therefore, at a rather high grafting density of the particles investigated here, the spatial distribution of the particles is not severely affected by the interaction between the free and the grafted chains, which means that, as long as the chains are densely grafted to show the CPB conformation, the wetting-dewetting transition is not coupled with the change in the dispersion state.
As a last result, $R_g$ from SANS data fits are shown in Figure 6.11 (d). $R_g$ increases gradually and remains constant as $M_w$ increases. The dotted line drawn in the plot is the calculated $R_g$ of the grafted PS chain, considering $M_w$=75 kg/mol. The well-known relation for the bulk PS in a theta solvent, $R_g = 0.0275 \times {M_w}^{1/2}$ (nm), was applied [10, 108]. This behavior may contain the contribution of the mixture or blend of the grafted and free chains within the corona shell according to random phase approximation (RPA). However, we did not attempt to conduct a quantitative analysis on this point but briefly describe the behavior. The scattering function $S(q)$ derived by RPA, for a mixture of A polymer and B polymer is given by [16, 66, 110]:

$$\frac{1}{S(q)} = \frac{1}{\phi\, \upsilon_A S_{\mathrm{A}}(q)} + \frac{1}{(1-\phi)\upsilon_B S_{\mathrm{B}}(q)} - \frac{2\chi}{\upsilon_u} \tag{6.6}$$

Here, $S_{\mathrm{A}}(q)$ and $S_{\mathrm{B}}(q)$ are the Debye function for the polymer A and B, as described in eq. 4.25, and $\phi$ is the volume fraction of the A polymer. $\upsilon_A$, $\upsilon_B$, and $\upsilon_u$ are the volume of the segments of polymer A, B, and both polymer A and B, respectively. $\chi$ is a Flory Huggins interaction parameter. It is dimensionless and determined in an empirical manner in the local free energy per reference unit. For example, for an ideal mixture of Gaussian chains, $\chi = 0$, and as the interaction between chains increases, it increases. The Debye function included in our fit function in eq. 4.28 can be replaced by eq. 6.6 to describe the behavior of the blend rather than that of the single chains. The above expression in eq. 6.6 represents, in our situation, if A and B polymer are assigned to be grafted and free polymer within the grafted PS layer, more penetration of the free chains to grafted chains makes it become that of the Debye function for the free chains, leading to an effective coil size to be that of the free chains. On the other hand, the reduction of the intrusion of the free chains will lead to eq. 6.6 to become the Debye function for the grafted chains. This trend might be included in the variation of the parameter $R_g$. However, the variation in $R_g$ does not follow precisely the expected wetting behavior extracted from that of the thickness of the corona, and this implies that the interaction parameter $\chi$ and the segmental volume of both polymer A and B, $\upsilon_u$, may play an additional role in the description of a high $q$ scattering behavior. Moreover, the above expression in eq. 6.6 can be written in a Lorentzian form [16],

$$\frac{1}{S(q)} = \frac{1}{S(0)}(1 + q^2\xi^2) \tag{6.7}$$

where

$$\frac{1}{S(0)} = \frac{1}{\upsilon_A \phi} + \frac{1}{\upsilon_B(1-\phi)} - \frac{2\chi}{\upsilon_u} \tag{6.8}$$

and

$$\xi^2 = \frac{S(0)}{2}\left(\frac{{R_{g,A}}^2}{\upsilon_A \phi} + \frac{{R_{g,B}}^2}{\upsilon_A(1-\phi)}\right) \tag{6.9}$$

$R_{g,A}$ and $R_{g,B}$ are the radii of gyration of polymers A and B, respectively. It was stated in section 4.3.2 that the Debye function can be approximated well by the Lorentzian function as shown in eq. 4.49, so the Debye function used in the fit function based on the core-shell-chain model shown in eq. 4.28 can be replaced by an RPA approximation in eq. 6.6. However, for the sake of simplicity, we did not attempt to replace the Debye function by eq. 6.6.

## 6.4 Comparison of the results from different PNC systems

In order to gain insight into the theoretical expectation on the wetting-dewetting transition, we take into account the phase diagram developed by Green et al. [50, 57, 58] as introduced in section 3.2.2. Currently, the phase diagram introduced by Leibler et al. [55] will not be considered, as its description is just an approximation of the scaling of the thickness with other parameters, and interactions between the grafted particles were not considered, which will also induce the dewetting state [111]. However, some of the scaling expectation of the thickness will be discussed briefly to describe its behavior rather quantitatively.

The phase diagram of the nanoparticles grafted with a polymer in a chemically identical polymer matrix is illustrated in Figure 3.6. This diagram was made for a polymer brush on a planar substrate and the phase behavior of the polymer chains on the nanoparticles in a polymer matrix was assumed to be similar to that on a planar substrate in a polymer matrix. The wetting of the free chains was characterized as a function of the molecular weight ratio, $\kappa$, $N_f/N_g$ in the horizontal axis and the grafting density $\sigma$, chains/nm$^2$, in the vertical axis. $N_f$ is the degree of polymerization of the free chain, and $N_g$ is that of the grafted chain. The wetting regime is intersected by the line drawn by $\sigma_1$ as the lower boundary and $\sigma_2$ as the upper boundary. The diagram explicitly shows that the wetting or the penetration of the free chains to the grafted chains leads to a uniform dispersion of the particles, while the dewetting or the expulsion of the free chain from the grafted chains leads to the aggregation of the particles, characterized by “allophobic dewetting” or “autophobic dewetting”. Allophobic dewetting occurs at low grafting density when the matrix prevents the brush stretching; that is, the van der Waals interaction between the particles becomes stronger than the interaction between the grafted and the free chains [48, 50]. This region in the phase diagram is located below the lower boundary line $\sigma_1$. Above the upper boundary of the wetting region, $\sigma_2$ in the diagram, autophobic dewetting occurs at rather high grafting density when the free matrix chains are expelled from the grafted chains as a consequence of the balance of the free energy, as discussed previously. When the free chain becomes larger, the grafted chains adopt the collapsed conformation to balance the free energy reduction mediated by the decrease in the mixing-demixing term in the total free energy.

We previously reported that the grafted PS chains on the silica particles used in our study retained a slightly stretched conformation in a good solvent, namely SDPB conformation. As the chains in our study are sufficiently grafted onto the silica particles in this study, to overcome the particle aggregation purely driven by the particular interaction, it can be concluded that the wetting-dewetting transition observed here is driven by the chain autophobicity, not allophobic dewetting, driven by the van der Waals interaction.

A similar experimental observation using SANS was reported for silica particles ($R_c$=13 nm) grafted with PS with a grafting density ($\sigma$=0.2 chains/nm$^2$) [112]. Their results illustrated that the conformation of the grafted PS chains are stretched in a theta solvent ($\Delta$ = 12 nm), behaving like a small free chain and becomes Gaussian chain-like ($\Delta$ = 6 nm) in a large matrix PS. It is noted that their experimental findings indicate the wetting-dewetting transition, but the effect of the variation in the length of the matrix

polymer could not be revealed in their study since they merely compared the conformation difference between the chains in a theta solvent and in a matrix polymer.
For similar PNC systems in a chemically identical polymer matrix, numerous studies have shown that the critical molecular weight ratio, $\kappa_c$, where the transition occurred, was in the range from 1 to 6 depending on the curvature and the grafting density [14, 15, 50, 53]. However, direct comparison of their results with our experimental data could not be made due to the large grafting densities used for most of the studies. For similar grafting densities, Akcora et al. [52] observed the evolution of the aggregates of small PS grafted silica particles ($R_c$ = 7 nm) as a function of the molecular weights of PS matrices. Their observation was, however, limited to the change in the particle dispersion state, not the change in the conformation of the grafted PS chains. Our results demonstrated that the thickness of the grafted PS layer on silica particles varies from ≈6.2nm for short matrix chains to ≈4nm for the largest matrix chains. The values for the short chains are slightly stretched compared the bulk $R_g$, and those for the largest chains merge to the bulk dimension, similar to $R_g$. Here, we do not attempt to obtain the quantitative expectation of the thickness value in light of a theoretical approach, as most of the theoretical studies have focused on the scaling of the thickness on the planar geometry, not the spherical geometry [54, 55].
It was previously mentioned that the wetting-dewetting transition is influenced by various parameters, such as grafting density, molecular weight ratio $\kappa$, and curvature. Note that the grafting density and $\kappa$ of the systems of the silica and small d-PS particles are almost similar in values and the grafting density of the systems of the large d-PS particles differs significantly.
First we compare the phase behavior of the systems of the silica and small d-PS particles due to their proximity of the parameters. As discussed previously, the conformation of the grafted PS chains on the d-PS particles remained constant over the variation of $M_w$ of d-PS matrices, while that on the silica particles varied for the largest $M_w$ of d-PS matrix. The maintained conformation of the grafted PS chains for d-PS particles can be attributed to a large curvature compared to the silica particles. It was previously noted that the conformational freedom of the grafted chains rises as the curvature increases. Therefore, the large curvature induces more intermixing of the grafted and free matrix chains, and the change of the conformation of the grafted chains tends to appear for a large molecular weight ratio, $\kappa$, for a large curvature. This intuition can lead to a first remark on our experimental results for both particle systems. The different behaviors of the variation in the conformation of the grafted PS layers observed for both particle systems might then be influenced by the different core size, namely the curvature parameter. Note that the previously determined curvature parameter, $D/R_g$, was 11.9 for silica particles and 9.3 for d-PS particles with a small core and 7.6 for d-PS particles with a large core or large grafting density. The curvature parameter for the silica particles is slightly larger than that for d-PS particles with a small core, indicating that the silica particle has a low curvature for a single grafted chain. The effect of the curvature is illustrated in Figure 6.12 (b).
As for the thickness of the grafted PS chains on d-PS particles, the thickness values are larger than $R_g$ and close to $2R_g$. Those on the silica particles are slightly larger than $R_g$ by a factor of approximately 1.4 for the comparatively stretched conformation at low $M_w$s of d-PS matrices. We previously noted that the thickness of the grafted PS layer on the d-PS particles in a good solvent, d-toluene, was found to be ∼17.8 nm and that on the silica particles in d-THF was to be ∼13.4nm. In section 5.2, we compared both quantities using normalization by $\sigma$ and $R_c$, and they resulted in similar quantities, demonstrating that the conformation of the grafted chains is influenced by the grafting density and the curvature, while the influence of a substrate of different hydrophobicity is negligible. Here we find that the thickness of the grafted PS layer on the silica particle was found to be ∼6.2nm and that on the d-PS particle of a small core ($R_c$=21.5nm) in low molecular weights of d-PS matrices was found to be∼ 8.8 nm, both of which are diminished almost by a factor of two compared to those in good solvents. The decrease in the thickness by the same factor in both particle systems demonstrates that the relatively large thickness for d-PS particles may be attributed to a large grafting density and a small radius compared to those of the silica particles, as in the previous description for the same particles in good solvents.

The expansion in size of the grafted chains from the theta condition to the good solvent condition by a factor of 2 could be verified by the experimental results reported by Kaiser et al. [113]. They investigated the variation in the hydrodynamic radius of PS grafted iron oxide ($FeO_x$) nanoparticles in cyclohexane (theta solvent for PS) with the temperature by means of DLS and extracted the hydrodynamic brush thickness as the difference in the hydrodynamic radius between a surface-modified and a grafted particle, as we did previously. They observed the thickness ratio of ∼2 when the PS chains were transferred from the theta condition to the good solvent condition.
The difference in the thickness of the grafted PS layers with low molecular weights of d-PS matrices, 6.2 nm for the silica, and 8.8 nm for the d-PS of a small core could be explained by the difference in the van der Waals interaction between the free PS chains and the substrate material. An increase in the attractive van der Waals interaction will lead to a collapsed conformation of the grafted chains. In order to describe the van der Waals force, the free PS chain and the substrate material are assumed to have spherical shapes. The van der Waals force between two spheres is given by [114]:

$$F_{\mathrm{vdw}} = \frac{A_{12} r_{12}}{6 {z_0}^2}, \tag{6.10}$$

where $z_0$ is the contact distance and $r_{12}$ is the relative radius defined by [114]:

$$\frac{1}{r_{12}} = \frac{1}{r_1} + \frac{1}{r_2} \tag{6.11}$$

$A_{12}$ is the Hamaker constant which can be calculated using the approximate combination law [114]:

$$A_{12} = \sqrt{A_1 \cdot A_2} \tag{6.12}$$

The Hamaker constants of the PS and the silica are, respectively, $A_1 = 79 \cdot 10^{-21}$J and $A_2 = 65 \cdot 10^{-21}$J [114, 115]. With these Hamaker constants, the Hamaker constant of the two systems consisting of the silica and PS, and PS and PS, are determined with the approximate combination law, $A_{12} = 72 \cdot 10^{-21}$ J, for the silica and PS and $79 \cdot 10^{-21}$J for PS-PS systems, respectively. The Hamaker constants in both cases are similar, indicating that the van der Waals interactions of the free chains with the different substrates do not play a role in the change in the conformations. The change in the internal parameters characterizing the grafted particles, the grafting density and the core size, would, rather, play a main role in the change in the conformations.

**Table 6.4.:** Physical parameters obtained from SANS data fits of PNC systems investigated

| | Silica | d-PS$^{\mathrm{small}}$ | d-PS$^{\mathrm{large}}$ |
|---|---|---|---|
| ${R_c}^a$ (nm) | 26 ± 0.1 | 21.6±0.2 | 28.7 ± 0.5 |
| $\mathrm{D}/{R_g}^b$ | 11.9 ± 0.1 | 9.3±0.4 | 7.6 ± 1.1 |
| ${\kappa_c}^c$ | $1.6 < \kappa_c < 4.7$ | – | $0.4 < \kappa_c < 0.7$ |
| $\sigma$ (chains/nm$^2$) | $0.023 \pm 0.001^d$ | $0.032 \pm 0.005^d$ | $0.25 \pm 0.05^e$ |

a: Mean core size ($R_c$) obtained from, SAXS data fits for silica particles, and SANS data fits of the d-PS particles in melts (see sec. 6.3)
b: Calculation of $R_g$ based on the relation $R_g = 0.0275 \times {M_w}^{1/2}$ (nm) [10, 108] and D=2$R_c$.
c: Calculation of $\kappa$ shown in Table 6.1 and Table 6.2. $\kappa_c$ represents the value of $\kappa$ at which the wetting-dewetting transition occurs.
d: Value obtained from SANS data fits of the particles in solution (see sec. 5.1 and sec. 5.2)
e: Value obtained from SANS data fits of the particles in a melt (see sec. 6.3)

We now turn to the results of the d-PS nanoparticle with a large core and a large grafting density. It was verified that the grafted PS chains for that particle system, in a good solvent, have the conformation of the concentrated polymer brush, CPB, rather than semi-dilute polymer brush, SDPB. This indicates that the PS chains are densely grafted on the given particle systems showing rather high stretched conformation compared to other particle systems in our study, the silica and d-PS with a small core. SANS data fits of this particle in the PS matrix revealed that ($\sigma \sim 0.25$ chains/nm$^2$) was high compared to others ($\sigma \sim 0.02$ chains/nm$^2$ for silica and 0.032 chains/nm$^2$ for d-PS with a small core). The effect of the grafting density on the wetting property of the free matrix chains is illustrated in Figure 6.12 (a). Besides the grafting density difference between the d-PS particles with a large core and the silica particles, the curvature parameter for both particle systems was not significantly different in values, as previously noted. However, the observed critical molecular weight ratio for the d-PS with a large core ($0.4 < \kappa < 0.7$) is significantly smaller than that for the silica particles ($1.6 < \kappa < 4.7$). Therefore, "acceleration" of the wetting-dewetting transition is mainly attributed to the difference in the grafting density of the two particle systems. Intuitively, the wetting-dewetting transition occurs at lower molecular weight ratio, as the grafting density increases due to the fact that the penetration of the free chains to grafted chains needs higher free energy cost for the elastic chain stretching term. It is then apparent that the acceleration of the transition for the given particle systems, shows an effect of the grafting density on that transition rather than that of the curvature. The results from three sets of PNC systems are summarized in Table 6.4.

The thickness of the grafted PS layer on the large d-PS nanoparticles was found to be ~47 nm for the smallest $M_w$ of d-PS matrix and ~22 nm for the rest $M_w$ of d-PS matrices. A large thickness for the smallest $M_w$ would be due to the large grafting density, as in the case of the good solvent, so the grafted chains scaled as $h \propto M_w$ rather than $h \propto {M_w}^{0.6}$. Such a linear relation of the thickness of the grafted chains with the molecular weight and grafting density was expected in the results of Leibler et al. [55] for the stretched wet brush, which may correspond to our results. However, we did not attempt to make a quantitative comparison between the theory and our experimental results since the results of Leibler et al. were just an approximation and exhibit only the scaling of the thickness with the parameters of grafting density and molecular weight.

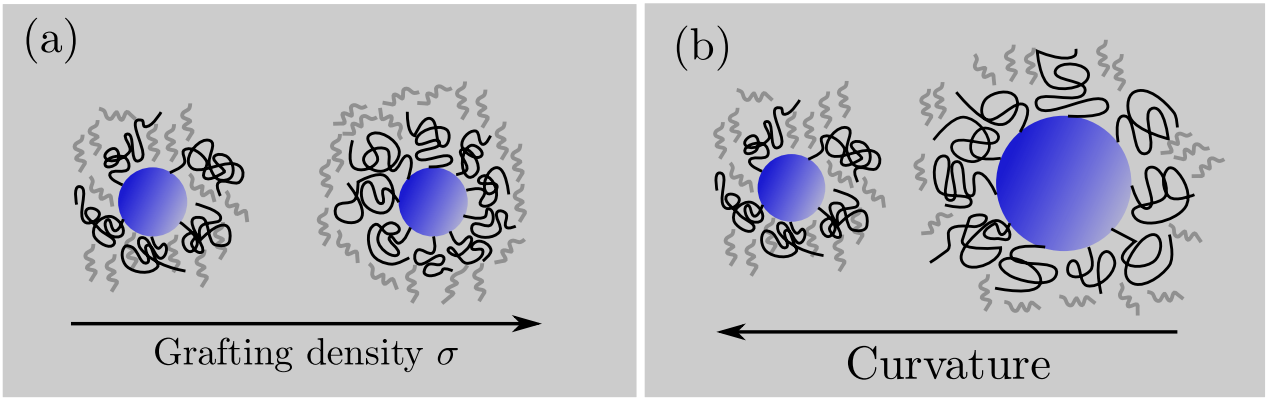


**Figure 6.12.:** Schematic picture to illustrate the effect of grafting density [111] (a) and curvature [116] (b) on the wetting-dewetting transition. In (a), at a low grafting density, free matrix chains can wet grafted chains due to the conformational freedom of the free ends of the grafted polymers. At a high grafting density, however, free matrix chains of the same length dewet due to high stretching of the grafted polymers. In (b), an increase in curvature provides relaxation of the stretching of the grafted chains, and this influences the wetting-dewetting behavior of the free matrix chains on the grafted chains. It is illustrated in (b), that, at a small curvature for the same length of free chains, the free chains dewet the grafted chains, and at a large curvature, they wet the grafted chains. Arrows in (a) and (b) indicate an increase of the grafting density (a) and the curvature (b).

## 6.5 Conclusion

We have presented the phase behavior of nanoparticles grafted with p-PS chains in d-PS homopolymer matrices using particles made by different chemistries. One silica particle system and two d-PS particle systems were prepared for the core particles, and they were all grafted with PS chains of different molecular weights. "Grafting from" method has been utilized for all particle systems, for which the grafting methods are, however, all different: anionic polymerization method for silica, ATRP for d-PS with a small core, and NMRP for d-PS with a large core. Both silica and d-PS nanoparticles with a small core had comparable internal parameters of the grafting density and molecular weight, while these parameters for the d-PS with a large core were different. SANS experiments were conducted for these particle systems to investigate the change in the grafted PS chain conformations with a variation in $M_w$ of d-PS matrix in order to see the effect of the parameter of the length ratio between the matrix and the grafted chains, defined by $\kappa = N_f/N_g$. Along with the variation in the length ratio of the free matrix to the grafted chains, the influence of other grafting density and curvature parameters on the change in the conformation was probed by SANS experiments as well. In the case of the silica particles, complementary SAXS experiments were performed to extract the core size, but in the case of the d-PS particles, SAXS could not be used due to missing contrasts among the core, corona shell, and d-PS matrix. The change in the grafted PS chain conformation was directly observed in the variation of the thickness of the grafted PS layer using SANS, which was able to provide information on the signature of the wetting-dewetting transition.

Our results showed that the wetting-dewetting transition occurred for the silica particles and the d-PS particles with a large core and large grafting density, and this could be corroborated by the variation in the thickness with $M_w$ of d-PS matrices. The critical molecular weight ratio, defined by $\kappa_c$, where the transition occurs for the silica system, was found to be $1.6 < \kappa_c < 4.7$, and for the d-PS particle system with a large core, it was found to be $0.4 < \kappa_c < 0.7$. This difference in the critical molecular weight ratio between the two particle systems demonstrates that the transition is mainly affected by the difference in the grafting density rather than that in the core size or the curvature parameter since the curvature parameter for the two particle systems is comparable but the grafting densities are significantly different. Note that the wetting-dewetting transition accelerates as the grafting density increases due to the fact that the penetration of the free matrix chains requires a higher free energy cost for the elastic chain stretching of the grafted chains. The transition did not occur for the d-PS particles with a small core even though the grafting density and the length of the grafted PS chains were comparable to those of the silica particles. This might be due to the smaller core size than that of the silica particles, for which more conformational freedom near the free ends of the grafted chains is expected for the smaller core size and correspondingly permits more penetration of the free chains into the grafted chains.

It is noteworthy that, for the d-PS particles with a large core and silica particles, it could be concluded that the wetting-dewetting transition has occurred by the chain autophobicity rather than allophobic interaction between particles. Sunday et al. [50] reported that the chain autophobicity occurs at a relatively large grafting density to screen the interparticle interaction, and in our situation since the particles used in our study are sufficiently grafted to overcome the inter-particle interaction (SDPB or CPB conformation), the wetting-dewetting transition was verified to be driven by the chain autophobicity rather than an allophobic interaction.

The relation between the change in the conformation of the grafted chains and the dispersion state of the particles was another main issue in this chapter. It was apparent for the silica particle that the wetting-dewetting transition is closely linked to the change in the dispersion state and the dewetting of the free chain induces the aggregation of the particles. On the other hand, for the d-PS particles with a large core, such a close relation could not be observed, possibly due to the steric stabilization achieved by densely attached polymers on the particle surface. Different behavior between the two particle systems is therefore caused by the difference in the grafting density.

# 7 Summary

The main focus of this work is the experimental observation of the static structure of grafted chain conformation in a good solvent condition or in a melt condition. Therefore, the structural properties of the grafted chains in the given conditions were investigated by SANS, SAXS, DLS, and TEM to gain insight into the conformation features of grafted chains on a spherical substrate, which was clearly discernible from that of bulk chains in the same condition.

Polystyrene (PS) was grafted from the surface of silica nanoparticles ($R_c \sim 26$ nm) and d-PS nanoparticles ($R_c \sim 21$ and 33 nm) using different synthesis methods. For the silica, the surface-initiated anionic polymerization method (SIAP) was applied, while for the d-PS, atomic transfer radical polymerization (ATRP) was used for the small particles and nitroxide-mediated radical polymerization (NMRP) for the large particles. The NMRP method for d-PS particles was applied to yield a higher grafting density than the ATRP method. The resulting particles exhibited variation in the grafting density and molecular weights of the grafted chains on the cores with comparable sizes, which were named the internal parameters expected to influence the conformation of the grafted chains either in a good solvent or in a polymer matrix.

SANS, SAXS, and DLS were combined to reveal the conformation features of the grafted PS chains on three sets of the particles in good solvents, either toluene or THF. It was advantageous to use SANS to probe the grafted chain conformations due to selective deuterium labeling of the system. The use of a deuterated solvent, d-THF or d-toluene, enabled us to investigate the conformation of the grafted "protonated PS" layer explicitly by means of SANS. SAXS was utilized to obtain complementary information about the size of the cores, especially in the case of the silica particle, due to its high scattering contrast between the core and the solvent. Finally, the results from DLS supported the complete picture of the conformation of the grafted PS layer to make use of normal solvents, THF or toluene, rather than deuterated ones. It was crucial to determine the grafting density of the samples accurately to probe the conformation features of the grafted chains. This was done with information gained from the SANS data analysis. In order to analyze the SANS data of the silica and d-PS nanoparticles with a small core size ($R_c$ = 21 nm) grafted with PS in good solvents, we implemented the core-linear shell model superimposed with the Debye function. The use of the core-linear shell model was adequate to describe the SANS data of the silica and small d-PS nanoparticles, and the use of the Debye function was due to the existence of characteristic chain scattering, $q^{-2}$ behavior at high $q$ ranges. Overall, the use of the combination of two model functions was effective in describing our SANS data. The grafting density could be obtained by the use of the linear radial density profile of the corona shell, and the corresponding result was comparable with TGA (thermo gravimetry analysis) for the case of the silica particles. The same method was applied to obtain the grafting density for the case of d-PS particles with a small core, and the resulting grafting densities could be used to compare the size of the grafted chains with the scaling prediction valid for semi-dilute-polymer brush (SDPB).

Under good solvent conditions, three regimes of the conformation of the grafted chains on the spherical substrates were expected: a dilute polymer regime, a semi-dilute polymer brush regime (SDPB), and a concentrated polymer brush regime (CPB). For the dilute polymer brush regime, the grafted chains adopt a random coil conformation, as in the case of the bulk polymer.

$$h \sim {M_w}^{0.6} \approx 2R_g \tag{7.1}$$

Here, h is the thickness of the grafted chain, $M_w$ is the molecular weight, and $R_g$ is the radius of gyration of the same polymer in the bulk state in the same good solvent. Here, the size of the grafted chains

becomes similar to $2R_g$ in the same solvent. For the SDPB regime, the grafted chains become more swollen than $2R_g$, as the chains are densely grafted on the surface of the spherical substrate. Then, the thickness is affected by the grafting density, $\sigma$, and size of the cores, $R_c$.

$$h \sim {M_w}^{0.6} {R_c}^{0.4} \sigma^{0.2} \tag{7.2}$$

For the concentrated brush regime (CPB), the chains are more densely grafted on the surface, and the interaction between chains not only becomes pairwise but a higher-ordered and more stretched layer is also expected. This behavior is reflected in the exponents to describe the scaling law of the grafting density and the molecular weight with larger amplitudes.

$$h \sim {M_w}^{x} \sigma^{0.5x} \ (0.6 < x \leq 1) \tag{7.3}$$

Our results demonstrated that the grafted PS layer on the silica and d-PS particle with a small core size retained the conformation of semi-dilute polymer brush rather than that of a dilute polymer, that is, the random coil conformation observed in the bulk state. This was evidenced by the experimental observation that the thickness of the grafted PS layer on the given particle systems over the range of the molecular weights investigated was larger than the $2R_g$ of the free PS chain in good solvents, and the scaling prediction applied to the data shown in eq. 7.2 was deemed valid. It is noteworthy that, for large molecular weights of grafted PS on d-PS with a small core, we found hints of a SDPB-to-dilute transition where the grafting density was determined to be small compared to others and the thickness converges to $2R_g$. As for the effect of the substrate material on the conformation feature, the results demonstrated that the grafted chain conformation is barely affected by the different characters of the interaction between the grafted chains and the substrate material. The results were highlighted in chaper 5.

For the d-PS particles with a large core, we found different scaling of the thickness compared to the previous cases. The thickness scaled linearly with the molecular weights, verifying that the grafted chains are in the CPB regime rather than in the SDPB or dilute polymer regime. It is again noteworthy that different methods were applied to synthesize and grow the chains on the surface of the nanoparticles. For the organic particle systems, the NMRP method yielded a high grafting density compared to the SIAP or ATRP methods. However, the discussion about the synthesis of the grafted chains is limited in this work and requires an excursion into the realm of "polymer chemistry" far beyond the scope of this work [117, 118].

The conformation of the grafted chains in a polymer matrix has been extensively investigated throughout this work. Representative samples from three sets of grafted particle systems, silica and d-PS with different core sizes, as mentioned before, were selected to observe the change in the conformation in dependence on the variation of the molecular weights of the matrix polymer. The samples were dispersed in d-PS matrices which were chemically identical to the grafted chains. The use of matrix polymers of various molecular weights was intended to tune the length ratio of the free chains to the grafted chains (defined by $\kappa$), while the molecular weight of the grafted chains was 25 kg/mol for the silica, 29 kg/mol for the d-PS with a small core size, and 75 kg/mol for the d-PS with a large core size. The internal parameters of the grafting density, the molecular weight and the curvature of the given particle systems were also expected to contribute to the change in the conformation of the grafted chains. As for the curvature parameter, we have introduced the parameter $D/R_g$, where D denotes the diameter of the core and $R_g$ the radius of gyration of the grafted chains, calculated based on the bulk geometry in a theta solvent. This indicates a measure of curvature for a single polymer chain on the surface of the nanoparticles. Those values were 11.9 for silica, 9.3 for d-PS with a small core, and 7.6 for d-PS with a large core.

The phase behavior of the polymer nanoparticle composite (PNC) constituted by the grafted particles and the polymer matrix was expected to change with respect to the internal parameters as well as $\kappa$.

The phase transition from wetting to dewetting was expected mostly due to the change in $\kappa$ driven by the entropic interaction between the free and grafted chains. In terms of the free energy description of the entropy of the free and grafted chains, the small free chains tend to penetrate the grafted chains, and this behavior leads to the swelling of the grafted chains. On the other hand, the large free chains tend to be expelled from the grafted chains, and this behavior leads to the collapse of the grafted chains. It was then aimed to investigate this phenomenology, driven by the length ratio $\kappa$ by experiments. SANS experiments were an effective and appropriate tool in that the change in the thickness or that of the conformation could be directly observed by the enhanced contrast achieved by the use of the deuterated PS matrix and protonated grafted PS chains.

Experiments were conducted separately for the silica and d-PS nanoparticles with a small core at D-11 at ILL and at KWS-1 at FRM-2, for the d-PS nanoparticles with a large core and large grafting density. The range of $\kappa$ for the former experiments was $0.3 < \kappa < 4.7$, and for the latter experiments $0.2 < \kappa < 4.8$. With this range of $\kappa$, the phase behavior of the given nanoparticle systems in d-PS matrices could be revealed by means of the analysis of SANS data. Complementary SAXS measurements were made in house for the silica particles and enabled us to extract the mean core size due to a large electron density contrast between the core and the matrix. For d-PS particles, however, SAXS measurements were not made due to missing contrasts among the core, the shell and the matrix since they were chemically identical.

In order to analyze the SANS data for the particles of silica and d-PS particles with rather sparsely grafted chains, the core-shell form factor plus the Debye-Bueche function were applied. For the d-PS particles with densely grafted chains, the form factor of the core-shell-chain model for the half-Gaussian profile of a shell, superimposed with the Debye-Bueche function, were implemented. The former term described the intermediate and high $q$ range behavior of the scattering curves and the latter the low $q$ scattering, mainly driven by the aggregated structure. The fit functions for both cases provided a nice description of the experimental SANS data. The use of the different fit approaches was due to the high $q$ scattering behavior of the scattering curves. We note that, for particles with sparsely grafted PS chains, no indication of the $q^{-2}$ behavior was found, while for those with densely grafted chains, a clear indication of the $q^{-2}$ behavior was found.

Our results showed that the wetting-dewetting transition occurred for the silica particles and the d-PS particles with a large core and large grafting density, and this could be corroborated by the variation in the thickness with $M_w$ of d-PS matrices. The critical molecular weight ratio, defined by $\kappa_c$, where the transition occurs for the silica system was $1.6 < \kappa_c < 4.7$, and for the d-PS particle system with a large core, it was $0.4 < \kappa_c < 0.7$. This difference in the critical molecular weight ratio between two particle systems demonstrates that the transition is mainly affected by the difference in the grafting density rather than in the core size or the curvature parameter since the curvature parameter for the two particle systems is comparable but the grafting densities are significantly different. Note that the wetting-dewetting transition occurs at a smaller value of $\kappa_c$ as the grafting density increases because the penetration of the free matrix chains requires a higher free energy cost for the elastic chain stretching of the grafted chains. The transition did not occur for the d-PS particles with a small core even though the grafting density and the length of the grafted PS chains were comparable to those of the silica particles. This might be due to the smaller core size than that of the silica particles, for which more conformational freedom near the free ends of the grafted chains is expected for the smaller core size and correspondingly permits more penetration of the free chains into the grafted chains. For the d-PS particles with a large core and the silica particles, it is noteworthy that the wetting transition occurred due to chain autophobicity, not due to the allophobic interaction between the particles.

The relation between the change in the conformation of the grafted chains and the dispersion state of the particles was another main issue in this chapter. It was apparent for the silica particles that the wetting-dewetting transition is closely linked to the change in the dispersion state and dewetting of the free chain induces the aggregation of the particles. On the other hand, for the d-PS particles with a large core, such a close relation could not be observed, possibly due to the steric stabilization achieved by

densely attached polymers on the particle surface. Different behaviors between the two particle systems may therefore originate from the difference in the grafting density.

As a future perspective, we propose to measure the dynamics of the grafted chains in bulk PNCs, as the wetting-dewetting transition occurs as $\kappa$ is changed. Quasi-elastic neutron scattering (QENS) is a promising technique to measure the dynamics of the grafted chains by selective deuterium labeling, where the grafted chains are selectively visible in the neutron scattering by achieving "shell contrast". The study of Akcora et al. [119] revealed that the segmental mobility of the grafted PMMA chains on silica nanoparticles ($R_c$= 10 nm and $\sigma$ = 0.12 chains/nm$^2$) decreased as the nanoparticles were aggregated. The dispersion state of the nanoparticles was observed by TEM measurements, and the measure of the segmental mobility was the mean square displacement $< u^2 >$ obtained by the data fit of the elastic intensity from QENS. The slow dynamics observed by their experiments was, however, due to the increased annealing time, not due to the variation in the length ratio, $\kappa$, unlike our experimental results.

Up to now, direct observation of the relation between chain autophobicity, change in the local dynamics of the grafted chains, and the macroscopic dynamics of the PNC system are still lacking and remain unresolved. Therefore, measurements of the local dynamics of the grafted chains will be central to understanding the dynamical response to the change in the wetting property of the free chains.

# 8 Acknowledgement

I would like to express my deepest appreciation to Prof. Stühn, who gave me an opportunity to be involved in this project and sincerely guided my Ph.D work. I can not forget his kindness in discussing scientific topics and sometimes private problems relevant to my life here.

I would like to thank my chemistry colleagues, Markus Mazurowski and Katrin Sondergeld, who synthesized and provided samples for the measurements. The discussion about our Ph.D works has been fruitful and meaningful, and the measurements with them have given me a lot of good memories.

I would like to thank my local contacts at FRM 2 and ILL, Henrich Frielinghaus and Isabelle Grillo, for helping us to perform the SANS experiments.

I would like to thank Tinka Spehr and Martin Kraska for fruitful discussions about my Ph.D works and some of the publications we created together.

I would like to thank Harald Hartig, who prepared the film sample without “giving up” on the neutron scattering experiments.

I would like to thank my office mate, Marina Khaneft, who has always been ready to talk with me about scientific and non-scientific topics and guided me the right direction to get the right answer.

I would like to thank my colleagues at AG Stühn to always giving me a great deal of help, discussion and shared memories.

I would like to thank my wife and my father, my mother and my sister for their mental support during my Ph.D work. Their mental support was endless and priceless in motivating my work.

I additionally thank my church family in Frankfurt, including Priest Chung You Jin, who supported me mentally and guided me a right direction during my Ph.D studies.

# A Hansen solubility parameter

Hansen solubility parameters were used to predict the solubility of polystyrene (PS) in good solvents in chapter 5. Hansen introduced the solubility parameter to predict whether one material would dissolve in another material [89, 90]. It is practical to use this parameter to predict the solubility of a polymer in a solvent. It is assumed that the solubility parameter can be described by three parameters, dispersion, polar, and hydrogen bonding parameters, each of which is derived experimentally. They are related by the following equation.

$$\delta_t{}^2 = \delta_d{}^2 + \delta_p{}^2 + \delta_h{}^2 \tag{A.1}$$

Here, $\delta_t$ is Hansen's total solubility parameter, $\delta_d$ the dispersive term, $\delta_p$ the polar term, and $\delta_h$ the hydrogen-bonding term. The respective terms could be determined by direct measurements, correlations with other physical parameters, or calculations. The three component parameters can be plotted on a set of three mutually perpendicular axes. Complete miscibility is expected to occur if the solubility parameters of two materials ($\delta_t$), such as the polymer and the solvent, are similar. Here, we do not describe the details of the parameters or how to determine the parameters for each material but provide the results available in the literature. The parameters for the solvents and polymers of usual interest used throughout this work are presented. We note that the Hansen parameters shown in chapter 5 are $\delta_t$ from the Table below.

**Table A.1.:** Hansen solubility parameters of the materials [89, 90]

| | | Solubility parameter $[(\mathrm{MPa})^{1/2}{}^a]$ | | | |
|---|---|---|---|---|---|
| Solvent | V ($\mathrm{cm}^3/\mathrm{mol}^b$) | $\delta_d$ | $\delta_p$ | $\delta_h$ | $\delta_t$ |
| Acetone | 74.0 | 15.5 | 10.4 | 7.0 | 20.1 |
| Benzene | 89.4 | 18.4 | 0.0 | 2.0 | 18.6 |
| Chloroform | 80.7 | 17.8 | 3.1 | 5.7 | 19.0 |
| Carbon disulfide | 60.0 | 20.5 | 0.0 | 0.6 | 20.5 |
| Methanol | 40.7 | 15.1 | 12.3 | 22.3 | 29.7 |
| Tehtrahydrofuran | 81.7 | 16.8 | 5.7 | 8.0 | 19.4 |
| Toluene | 106.8 | 18.0 | 1.4 | 2.0 | 18.2 |
| Water | 18.0 | 15.5 | 16.0 | 42.4 | 47.9 |
| Styrene | 115.6 | 18.6 | 1.0 | 4.1 | 19.0 |
| Polystyrene | – | 18.64 | 10.52 | 7.51 | 22.69 |

a: $\mathrm{MPa}^{1/2} = 2.0455 \times \mathrm{cal}^{1/2}\ \mathrm{cm}^{-2/3}$

b: molar volume of the substances

# B Analytical calculations of core-linear and core-exponential form factor

Here, explicit expressions for the form factor of the core-linear shell model and core-exponential shell model will be given. First, the analytical calculation of the form factor of the core-linear shell $F_{\mathrm{cs}}(q,R_c)^{\mathrm{lin}}$ is obtained by solving the integration given in eq. 4.42. This is given by,

$$\begin{aligned} F_{\mathrm{cs}}(q,R_c)^{\mathrm{lin}} = (\rho_{\mathrm{sh}}-\rho_{\mathrm{sol}})\cdot\frac{4\pi}{q^4\cdot\Delta}\Big[&-2\cdot\cos(q(R_c+\Delta))-q\cdot(R_c+\Delta)\cdot\sin(q(R_c+\Delta)) \\ &+\cos(qR_c)\cdot(q^2\cdot\Delta R_c+2)+\sin(qR_c)\cdot(q\cdot R_c-q\Delta)\Big] \\ &+(\rho_c-\rho_{\mathrm{sol}})\cdot(4\pi/3)\cdot {R_c}^3\cdot 3\frac{\sin(qR_c)-qR_c\cos(qR_c)}{(qR_c)^3} \end{aligned} \tag{B.1}$$

Here, subscript cs, c, and sol represent core-shell, core and solvent. $\rho_{\mathrm{sh}}$ is the initial SLD of the particle surface. $R_c$ is the core radius and $\Delta$ is a thickness of the corona shell. The last term shown in the above equation is the form factor of a solid sphere with a homogeneous SLD within the core, as shown in eq. 4.13.
Next, the form factor calculation of the core-exponential shell $F_{\mathrm{cs}}(q,R_c)^{\mathrm{exp}}$ is given by,

$$\begin{aligned} F_{\mathrm{cs}}(q,R_c)^{\mathrm{exp}} = \frac{(\rho_{\mathrm{sh}}-\rho_{\mathrm{sol}})}{q}\cdot\frac{4\pi\lambda_c}{({\lambda_c}^2q^2+1)^2}\cdot\Big[&({\lambda_c}^3q^3R_c+2{\lambda_c}^2q+R_c\lambda_cq)\cdot\cos(qR_c) \\ &+(-{\lambda_c}^3q^2+{\lambda_c}^2q^2R_c+\lambda_c+R_c)\cdot\sin(qR_c)\Big] \\ &+(\rho_c-\rho_{\mathrm{sol}})\cdot(4\pi/3)\cdot {R_c}^3\cdot 3\frac{\sin(qR_c)-qR_c\cos(qR_c)}{(qR_c)^3} \end{aligned} \tag{B.2}$$

where $\lambda_c$ is a characteristic length as defined in section 4.3.2.

# Bibliography

[1] A. Naji, C. Seidel and R. R. Netz (2006) Theoretical Approaches to Neutral and Charged Polymer Brushes, Adv. Polym. Sci., 198, 149–183

[2] K. Binder and A. Milchev (2012) Polymer Brushes on Flat and Curved Surfaces: How Computer Simulations Can Help to Test Theories and to Interpret Experiments, J. Polym. Sci. Part B: Polym. Phys., 50, 1515–1565

[3] O. Azzaroni (2012) Polymer Brushes Here, There, and Everywhere: Recent Advances in Their Practical Applications and Emerging Opportunities in Multiple Research Fields, J. Polym. Sci. Part A: Polym. Chem., 50, 3225–3258

[4] M. A. C. Stuart, W. T. S. Huck, J. Genzer, M. Müller, C. Ober, M. Stamm, G. B. Sukhorukov, I. Szleifer, V. V. Tsukruk, M. Urban, F. Winnk, S. Zauscher, I. Luzinov and S. Minko (2010) Emerging applications of stimuli-responsive polymer materials, Nat.Mat., 9, 101–113

[5] P. F. Green (2011) The structure of chain end-grafted nanooparticle/homopolymer nanocomposites, Soft Matter, 7, 7914

[6] A. Savin, J. Pyun, D. Patterson, T. Kowalewski, T. Matyjaszewski (2002) Synthesis and characterization of silica-graft-polystyrene hybrid nanoparticles: effect of constraint on the glass-transition temperature of spherical polymer brushes, J. Polym. Sci. Part B: Polym. Phys., 40, 2667–2676

[7] O. Kohji, M. Takashi, T. Satoshi, T. Yoshinobu, and F. Takeshi (2007) Suspensions of Silica Particles Grafted with Concentrated Polymer Brush: Effects of Graft Chain Length on Brush Layer Thickness and Colloidal Crystallization, Macromolecules, 40, 9143–9150

[8] D. Dukes, L. Yu, L. Sarah, B. Benicewicz, L. Schadler, and S. Kumar (2010) Conformational Transitions of Spherical Polymer Brushes: Synthesis,Characterization, and Theory, Macromolecules, 43, 1564–1570

[9] E. Huebner, J. Allgaier, M. Meyer, J. Stellbrink, W. Pyckhout-Hintzen, D. Richter (2010) Synthesis of polymer/silica hybrid nanoparticles using anionic polymerization techniques, Macromolecules, 43, 856–867

[10] C. Chevigny, D. Gigmes, D. Bertin, J. Jestin and F. Boue (2009) Polystyrene grafting from silica nanoparticles via nitroxide-mediated polymerization (NMP): Synthesis and SANS analysis with the contrast variation method, Soft Matter, 5, 3741–3753

[11] H. Jia, I. Grillo, S. Titmuss (2010) Small angle neutron study of polyelectrolyte brushes grafted to well-defined gold nanoparticle interfaces, Langmuir, 26(10), 7482–7488

[12] G. Carrot, A. El Harrak, J. Oberdisse, J. Jestin, F. Boue (2006) Polymer grafting from 10nm individual particles: proving control by neutron scattering, Soft Matter, 2, 1043–1047

[13] G. Carrot, F. Gal, C. Cremona, J. Vinas, H. Perez (2009) Polymer grafted-platinum nanoparticles: from three-dimensional small angle neutron scattering study to tunable two-dimensional array formation, Langmuir, 25, 471–478

[14] S. Kumar, N. Jonault, B. Benicewicz and T. Neely (2013) Nanocomposites with Polymer Grafted Nanoparticles, Macromolecules, 46(9), 3199–3214

[15] C. Chevigny, F. Dalmas, E. Di Cola, D. Gigmes, D. Bertin, F. Boue, and J. Jestin (2011) Polymer-Grafted-Nanoparticles Nanocomposites: Dispersion, Grafted Chain Conformation, and Rheological Behavior, Macromolecules, 44, 122-133

[16] R. Ryong Joon (2000) Methods of X-ray and Neutron Scattering in Polymer Science, 1st ed., Oxford, New York

[17] D. S. Sivia (2011) Elementary Scattering Theory, Oxford, New York

[18] A. J. C. Wilson and V. Geist (2006) International Tables for Crystallography, Mathematical, Physical and Chemical Tables, C, Kluwer Academic Publishers, London

[19] I. Grillo (2008) Small-Angle Neutron Scattering and Applications in Soft Condensed Matter, Springer-Verlag Berlin Heidelberg

[20] S. Weber (2010) Temperaturabhängige Röntgenkleinwinkelstreuung an Silica-Nanopartikeln, Bachelor Thesis, TU Darmstadt

[21] NMI3 homepage, `http://nmi3.eu/neutron-research/techniques-for-/structural-research/large-scale-structures.html`

[22] B. Berne and R. Pecora (2000) Dynamic Light Scattering, Dover, New York

[23] P. Linder et al. (2002) Neutrons, X-Rays and Light: Scattering Methods Applied to Soft Condensed Matter, Elsevier, Amsterdam

[24] B. Chu (1991) Laser Light Scattering: Basic Principles and Practice, 2nd ed., Academic Press, San Diego

[25] A. Einstein (1905) Über die von der molekularkinetischen Theorie der Wärme geforderte Bewegung von in ruhenden Flüssigkeiten suspendierten Teilchen, Annalen der Physik, 17, 549–560

[26] G. Williams and D. C. Watts (1970) Non-symmetrical Dielectric Relaxation Behavior Arising from a simple Empirical Decay Function, Trans. Farad. Soc., 66, 80

[27] M. Berberan-Santos, E. N. Bodunov, and B. Valeur (2008) History of the Kohlrausch (stretched exponential) function: Pioneering work in luminescence, Ann. Phys. (Berlin), 7, 460–461

[28] D. E. Koppel (1972) Analysis of macromolecular polydispersity in intensity correlation spectroscopy: the method of cumulants, J. Chem. Phys., 57, 4814–4820

[29] H. Bogaert, P. Douglas and P. Van der Meeren (1992) Improved Methods for the Analysis of Dispersed Kinetics in Heterogeneous Systems, J. Chem. Soc. Faraday Trans., 88(23), 3467–3474

[30] B. J. Frisken (2001) Revisiting the method of cumulants for the analysis of dynamic light-scattering data, Applied Optics, 40, 24, 4087–4091

[31] J. C. Thomas. (1987) J. Colloid Interface Sci. 117, 187–192

[32] L. H. Hanus and H. J. Ploehn (1999) Conversion of Intensity-Averaged Photon Correlation Spectroscopy Measurements to Number-Averaged Particle Size Distribution. 1. Theoretical Development, Langmuir, 15, 3091–3100

[33] C. Juretzka (2010) Dynamische Lichtstreuung - Temperaturabhängige Messungen an polystyrene grafted silica, Bachelor Thesis, TU Darmstadt

[34] Wacker Chemie AG, Wacker Silikonöl AK

[35] Heraeus Quarzglas GmbH & Co. KG. Quarz Glass for optics (2010) - Data and Properties. Technical report, Heraeus

[36] M. Rubinstein and R. H. Colby (2003) Polymer Physics, Oxford, New York

[37] S. T. Milner (1991) Polymer Brushes, Science, 251, 905–914

[38] W. J. Britain and S. Minko (2007) A Structural Definition of Polymer Brushes, J. Polym. Sci. Part A: Polym. Chem., 45, 3505-3512

[39] T. Wu, K. Efimenko, J. Genzer (2002) Combinational study of the mushroom-to-brush crossover in surface anchored polyacrylamide, J. Am. Chem. Soc., 124(32), 9394–9395

[40] T. Wu, K. Efimenko, P. Vlcek, V. Subr, J. Genzer (2003) Formation and properties of anchored polymers with a gradual variation of grafting densities on flat substrates, Macromolecules, 36, 2448–2453

[41] C. Devaux, F. Cousin, E. Beyou, and J. P. Chapel (2005) Low Swelling Capacity of Highly stretched Polystyrene Brushes, Macromolecules, 38, 4296–4300

[42] M. Daoud and J. P. Cotton (1982) Star shaped polymers: a model for the conformation and its concentration dependence, J. Physique, 43, 531-538

[43] S. Förster, E. Wenz, and P. Linder (1996) Density profile of Spherical Polymer Brushes, PRL, 77, 95–97

[44] J. S. Pedersen and P. Schurtenberger (1999) Static properties of polystyrene in semidilute solutions: A comparison of Monte Carlo simulation and small-angle neutron scattering results, EPL, 45, 666

[45] C. M. Wijmans and E. B. Zhulina (1993) Polymer brushes at Curved Surfaces, Macromolecules, 26, 7214–7224

[46] A. Brulet, F. Boue and J. P. Cotton (1996) About the Experimental Determination of the Persistence Length of Wormlike Chains of Polystyrene, J. Physique. France, 6, 885–891

[47] F. Lo Verso, S. A. Egorov, A. Milchev and K. Binder (2010) Spherical Polymer Brush Under Good Solvent Conditions: Molecular Dynamics Results Compared to Density Functional Theory, J. Chem. Phys. 133, 184901

[48] R. Hasegawa, Y. Aoki, and M. Doi (1996) Optimum Graft Density for Dispersing Particles in Polymer Melts, Macromolecules, 29, 6656–6662

[49] A. Robbes, F. Cousin, F. Meneau, F. Dalmas, R. Schweins, D. Gigmes, and J. Jestin (2012) Polymer-Grafted Magnetic Nanoparticles in Nanocoposites: Curvature Effects, Conformation of Grafted Chain, and Bimodal Nanotriggering of Filler Organization by Combination of Chain Grafting and Magnetic Field, Macromolecules, 45, 9220–9231

[50] D. Sunday, J. Ilavsky, and D. Green (2012) A Phase Diagram for Polymer-Grafted Nanoparticles in Homopolymer Matrices, Macromolecules, 45, 4007–4011

[51] D. Maillard, S. Kumar, B. Fragneaud, J. W. Kysar, A. Rungta, B. C. Benicewicz, H. Deng, L. C. Brinson, and J. F. Douglas (2012) Mechanical Properties of Thin glassy Polymer Films Filled with Spherical Polymer-Grafted Nanoparticles, Nano Lett., 12, 3909–3914

[52] P. Akcora, H. Liu, S. K. Kumar, J. Moll, Y. Li, B. C. Benicewicz, L. S. Schadler, D. Acehan, A. Z. Panagiotopoulos, V. Pryamitsyn, V. Ganesan, J. Ilavsky, P. Thiyagarajan, R. H. Colby and J. F. Douglas (2009) Anisotropic self-assembly of spherical polymer-grafted nanoparticles, Nat. Mat., 8, 354–358

[53] S. S. P. Agarwal, and L. A. Archer (2012) Tethered Nanoparticle-Polymer Composites: Phase Stability and Curvature, Langmuir, 28, 6276–6281

[54] M. Aubouy, G. H. Fredrickson, P. Pincus, and E. Raphael (1995) End-Tethered Chains in Polymeric Matrices, Macromolecules, 28, 2979–2981

[55] I. Borukhov and L. Leibler (2002) Enthalpic Stabilization of Brush-Coated Partcles in a Polymer melt, Macromolecules, 35, 5171–5182

[56] P. G. de Gennes (1980) Conformations of Polymer Attached to an Interface, Macromolecules, 13, 1069–1075

[57] D. Green and J. Mewis (2006) Connecting the Wetting and Rheological Behaviors of Poly(dimethylsiloxane)-Grafted Silica Spheres in Poly(dimethylsiloxane) Melts, Langmuir, 22, 9546–9553

[58] J. H. Maas, G. J. Fleer, F. A. M. Leermakers, and M. A. C. Stuart (2002) Wetting of a Polymer Brush by a Chemically Identical Polymer Melt: Phase Diagram and Film Stability, Langmuir, 18, 8871–8880

[59] D. Trombly and V. Ganesan (2010) Curvature effects upon interactions of polymer-grafted nanoparticles in chemically identical polymer matrices, J. Chem. Phys. 133, 154904

[60] M. Kotlarchyk and S. H. Chen (1983) Analysis of small angle neutron scattering spectra from polydisperse interacting colloids, J. Chem. Phys. 79(5), 2461–2469

[61] D. J. Kinning and E. L. Thomas (1984) Hard-Sphere Interactions between Spherical Domains in Diblock Copolymers, Macromolecules, 17, 1712–1718

[62] S. Sen, Y. Xie, S. Kumar, H. Yang, A. Bansal, D. Ho, L. Hall, J. B. Hooper, and K. Schweizer (2007) Chain Conformations and Bound-Layer Correlations in Polymer Nanocomposites, PRL, 98, 128302

[63] P. Debye and A. M. Bueche (1949) Scattering by an Inhomogeneous Solid, J. Appl. Phys. 20, 518–525

[64] J. S. Pedersen and M. C. Gerstenberg (1996) Scattering Form Factor of Block Copolymer Micelles, Macromolecules, 29, 1363–1365

[65] J. S. Pedersen (2001) Structure factors effects in small-angle scattering from block copolymer micelles and star polymers, J. Chem. Phys., 114, 2839–2846

[66] A. C. Genix, M. Tatou, A. Imaz, J. Forcada, R. Scheweins, I. Grillo, and J. Oberdisse (2012) Modeling of Intermediated Structures and Chain Conformation in Silica-Latex Nanocomposites Observed by SANS During Annealing, Macromolecules, 45, 1663–1675

[67] A. S. Robbes, F. Cousin, F. Meneau, C. Chevigny, D. Gigmes, J. Fresnais, R. Scheweins and J. Jestin (2012) Controlled grafted brushes of polystyrene on magnetic $\gamma - Fe_2O_3$ nanoparticles via nitroxide-mediated polymerization, Soft Matter, 8, 3407–3418

[68] F. C. Giacomelli, I. C. Riegel, P. Stepanek, C. L. Petzhod, M. D. Nimago, A. J. Satii, A. E. Ciolino, M. A. Villar, V. Schmidt, and C. Giacomelli (2010) Structure of Micelles Formed by Highly Asymetric Polystyrene-b-Polydimethylsiloxane and Polystyrene-b-poly[5-(N,N-diethylamino)isoprene] Diblock Copolymers, Langmuir, 26, 14494–14501

[69] J. S. Pedersen, C. Svaneborg, K. Almdal, I. W. Hamley, and R. N. Young (2003) A Small-Angle Neutron and X-Ray Contrast Variation Scattering Study of the Structure of Block Copolymer Micelles: Corona Shape and Excluded Voluem Interactions, Macromolecules, 36, 416–433

[70] J. S. Pedersen and P. Schurtenberger (1996) Scattering Functions of Semiflexible Polymers with and without Excluded volume Effects, Macromolecules, 29, 7602–7612

[71] V. Carstelletto, W. Hamley and J. S. Pedersen (2002) A small-angle neutron scattering investigation of the structure of highly swollen block copolymer micelles, J. Chem. Phys. 117, 8124–8129

[72] W. H. Press, B. P. Flannery, S. A. Teukolsky, W. T. Vetterling (1989) Numerical Recipies. Cambridge University Press, Cambridge, England

[73] S. I. Yun, R. Briber, R. Kee and M. Gauthier (2003) Polymer, 44, 6579–6587

[74] C. J. Kim, K. Sondergeld, M. Mazurowski, M. Gallei, T. Spehr, H. Frielinghaus, M. Rehahn and B. Stühn (2013) Synthesis and characterization of polystyrene chains on the surface of silica nanoparticles, Colloid. poly. sci., 291, 2087–2099

[75] P. G. de Gennes (1979) Scaling Concept in Polymer Physics; Cornell University Press, Ithaca, New York.

[76] P. Auroy, L. Auvray, L. Leger (1991) Structures of end-grafted polymer layers: a small-angle neutron scattering study, Macromolecules, 24, 2523–2528

[77] T. Cosgrove, T. G. Heath, K. Ryan (1994) Terminally attached polystyrene chains on modified silicas, Langmuir, 10, 3500–3506

[78] K. Sondergeld, Private communication

[79] B. Gonzalez, N. Calvar, E. Gomez and A. Dominguez (2007) Density, dynamic viscosity, and derived properties of binary mixtures of methanol or ethanol with water, ethyl acetate, and methyl acetate at T=(293.15, 298.15, and 303.15)K, J. Chem. Thermodynamics, 39, 1577-1588

[80] R. J. Jimenez Rioboo, M. Philipp, M. A. Ramos and O. K. Krueger (2009) Concentration and temperature dependence of the refractive index of ethanol-water mixtures: Influence of intermolecular interaction, Eur.Phys.J.E., 30, 19-26

[81] D. R. Lide (2005) CRC Handbook of Chemistry and Physics, Internet version

[82] J. P. Longtin and C. H. Fan (1998) Precision Laser Based Concentration and Refractive index Measurement of Liquids, Microscale Thermophysical Engineering, 2, 261-272

[83] T. Vad, W. F. C. Sager, J. Zhang, J. Buitenhuis, A. Radulescu (2010) Experimental determination of resolution function parameters from small angle neutron scattering data of a colloidal $SiO_2$ dispersion. J. Appl. Cryst., 43, 686-692

[84] Q. Zhou, S. Wang, X. Fan, R. Advincula (2002) Living anionic surface-initiated polymerization of a polymer on silica nanoparticles, Langmuir, 18, 3324–3331

[85] O. Prucker and J. Rühe (1998) Mechanism of radical chain polymerizations initiated by Azo compounds covalently bound to the surface of spherical particles. Macromolecules, 31, 602

[86] O. Prucker and J. Rühe (1998) Synthesis of poly(styrene) monolayers attached to high surface area silica gels through self-assembled monolayers of Azo initiators. Macromolecules, 31, 592

[87] H. Böttcher, M. L. Hallensleben, S. Nuss, H. Wurm (2000) ATRP grafting from silica surface to create first and second generation of grafts, Polym. Bull., 44 , 223

[88] D. Green, J. S. Lin, Y. F. Lam, M. Z. C. Hu, D. W. Schaefer and M. T. Harris (2003) J.Colloid Interface Sci., 266, 346–358

[89] J. Mark (2007) Physical properties of polymer handbook, Chapter 16, 2nd edn. Springer Science, New York; P 289

[90] E. J. Brandrup, E. Immergut, E. Grulke (1999) Polymer handbook, Chapter 7, vol 4. Wiley, New York, p 675

[91] S. Förster, C. Burger (1998) Scattering functions of polymeric core-shell structures and excluded volume chains, Macromolecules, 31, 879–891

[92] Y. Y. Won, H. T. Davis, F. S. Bates, M. Agamalian, G. D. Wignall (2000) Segment distribution of the micellar brushes of poly(ethylene oxide) via small-angle neutron scattering, J. Phys. Chem. B., 104, 7134–7143

[93] K. Huber, S. Bantle, P. Lutz, B. Walther (1985) Hydrodynamic and thermodynamic behavior of short-chain polystyrene in toluene and cyclohexane at 34.5°C, Macromolecules, 18, 1461–1467

[94] D. H. S. Ramkumar and A. P. Kudchadter (1989) Mixture Properties of the water + $\gamma$-Butylrolactone + Tetrahydrofuran System. 2. Viscosities and Surface Tensions of $\gamma$-Butyrolactone + water at 303.15 - 343.15K and $\gamma$-Butylrolactone + water at 298.15K, J. Chem. Eng. Data, 1989, 34, 463-465

[95] A. Van Asten, H. F. M. Boelens, W. T. Kok, H. Poppe, P. S. Williams, and J. C. Gidding (1994) Temperature Dependence of Solvent Viscosity, Solvent Thermal Conductivity, and Soret Coefficient in Thermal Field-Flow Fractionation, Separation Science and Technology, 29:4, 513–533

[96] A. K. Nain (2008) Refractive index of Binary Mixtures of Tetrahydrofuran with Aromatic Hydrocarbon at Temperatures from (288.15K to 318.15K), J. Chem. Eng. Data, 53, 850–853

[97] Wohlfarth, Ch. (2008) Refractive index of tetrahydrofuran. Lechner, M.D. Springer Materials - The Landolt-Börstein Database. Springer-Verlag Berlin-Heidelberg.

[98] T. Blochowicz, C. Gogelein, T. Spehr, M. Müller, B. Stühn (2007) Polymer-induced transient networks in water-in-oil microemulsions studied by small-angle x-ray and dynamic light scattering, Phys. Rev. E., 76, 041505

[99] Y. Q. Shen, S. P. Zhu, F. Q. Zeng, R. Pelton (2000) Vesatile Initiators for Macromonomer Syntheses of Accrylates, Methacrylates, and Styrene by Atom Transfer Radical Polymerization, Macromolecules, 33, 5399–5404

[100] M. Mazurowski, Private communication

[101] F. J. V. Santos, C. K. Dalaouti, M. J. Assael, A. Nakashima (2006) Standard Reference Data for the viscosity of Toluene, J. Phys. Chem. Ref. Data, 35,1

[102] Wohlfarth, Ch. (2008) Refractive index of toluene. Lechner, M.D. Springer Materials - The Landolt-Börstein Database. Springer-Verlag Berlin-Heidelberg.

[103] A. N. Bashkatov and E. A. Genina (2003) Water refractive index in dependence on temperature and wavelength: a simple approximation, Proceedings of SPIE, 5068, 393–395

[104] J. Kestin, M. Sokolov and W. A. Wakeham (1978) Viscosity of Liquid water in the Range -8°C to 150°C, J. Phys. Chem. Ref. Data, 7, 941–948

[105] Q. De Robillard, X. Guo, M. Ballauf, T. Narayanan (2000) Spatial Correlation of Spherical Polyelectrolyte Brushes in Salt-Free Solution As Observed by Small-Angle-X-Ray Scattering, Macromolecules, 33, 9109–9114

[106] M. Mazurowski, K. Sondergeld, J. Elbert, C. J. Kim, J. Li, H. Frielinghaus, M. Gallei, B. Stühn and M. Rehahn (2013) Polystyrene Brushes on Fully Deuterated Organic Nanoparticles by Surface-Initiated Nitroxide-Mediated Radical Polymerization, Macromol. Chem. Phys., 214, 1094–1106

[107] J. R. Ell, D. E. Mulder, R. Faller, T. E. Patten and T. L. Kuhl (2009) Structural Determination of High Density, ATRP Grown Polystyrene Brushes by Neutron Reflectivity, Macromolecules, 42, 9523

[108] H. Benoit, J. P. Cotton, D. Decker, B. Farnoux, J. S. Higgins, G. Jannink, R. Ober and C. Picot (1974) Dimensions of molecular chains in the bulk and solutions, J. Appl. Cryst., 7, 188

[109] G. D. Wignall (1996) Physical Properties of Polymers Handbook, Mark,J.E., Ed., American Institute of Physics, New York

[110] G. Strobl (2006) The Physics of Polymers, Springer, 3rd Edition, Berlin

[111] J. Kalb, D. Dukes, S. K. Kumar, R. S. Hoy and G. S. Grest (2011) End grafted polymer nanoparticles in a polymeric matrix: Effect of coverage and curvature, Soft Matter, 7, 1418–1425

[112] C. Chevigny, J. Jestin, D. Gigmes, R. Schweins, E. Di-Cola, F. Dalmas, D. Bertin, and F. Boue (2010) "Wet-to-Dry" Conformational Transition of Polymer Layers Grafted to Nanoparticles in Nanocomposite, Macromolecules, 43, 4833–4837

[113] A. Kaiser and A. M. Schmidt (2008) Phase Behavior of Polystyrene-Brush-Coated Nanoparticles in Cyclohexane, J. Phys. Chem. B, 112, 1894–1898

[114] J. Dejeu, M. Bechelany, L. Philippe, P. Rougeot, J. Michler and M. Gauthier (2010) Reducing the adhesion between surfaces using surface structuring with PS latex particle, Applied Materials and Interfaces, 2, 6, 1630–1636

[115] A. Parsegian (2005) van der Waals forces: a handbook for biologists, chemists, engineers, and Physicists, Cambridge University Press, New York, USA

[116] E. S. Harton, S. Kumar (2008) Mean-field theoretical analysis of brush-coated nanoparticles dispersion in polymer matrices, J. Polym. Sci. Part B: Polym. Phys. 46, 351–358

[117] K. Sondergeld (2014) Ph.D.Thesis, TU Darmstadt

[118] M. Mazurowski (2014) Ph.D.Thesis, TU Darmstadt

[119] P. Akcora, S. Kumar, V. G. Sakai, Y. Li, B. C. Benicewicz and L. S. Schadler (2010) Segmental Dynamics in PMMA-Grafted Nanoparticle Composites, Macromolecules, 43, 8275–8281

# List of Publications

1. C. J. Kim, K. Sondergeld, M. Mazurowski, M. Gallei, T. Spehr, H. Frielinghaus, M. Rehahn and B. Stühn (2013) Synthesis and characterization of polystyrene chains on the surface of silica nanoparticles, Colloid.poly.sci., 291, 2087–2099
2. M. Mazurowski, K. Sondergeld, J. Elbert, C. J. Kim, J. Li, H. Frielinghaus, M. Gallei, B. Stühn and M. Rehahn (2013) Polystyrene Brushes on Fully Deuterated Organic Nanoparticles by Surface-Initiated Nitroxide-Mediated Radical Polymerization, Macromol.Chem.Phys., 214, 1094–1106

# Curriculum vitae

## Chang Jong Kim

Robert-Bosch-Str.10
64293
Darmstadt, Hessen Germany

Email: changjongkim@yahoo.com
Born: December 23, 1975, Seoul, Korea
Nationality: Korean
Marital status: Married

### Areas of specialization

Physics; Polymer physics.

### Education

2008 – 2014 : Ph.D at Darmstadt University of Techonology / Darmstadt
2004 – 2008 : Master of Science at University of Stuttgart / Stuttgart
1996 – 2003 : Bachelor of Science at Seoul National University / Seoul, Korea
1990 – 1993 : General Education School / Seoul, Korea

### Publications

1. C. J. Kim, K. Sondergeld, M. Mazurowski, M. Gallei, T. Spehr, H. Frielinghaus, M. Rehahn and B. Stühn (2013) Synthesis and characterization of polystyrene chains on the surface of silica nanoparticles, Colloid.poly.sci. 291, 2087–2099
2. M. Mazurowski, K. Sondergeld, J. Elbert, C. J. Kim, J. Li, H. Frielinghaus, M. Gallei, B. Stühn and M. Rehahn (2013) Polystyrene Brushes on Fully Deuterated Organic Nanoparticles by Surface-Initiated Nitroxide-Mediated Radical Polymerization, Macromol.Chem.Phys. 214, 1094–1106

### Teaching

2000: School observation in high School attached to Seoul National University
2001: Teaching Practicum in high School attached to Seoul National University
2008–2009: Teaching Assistant for the lecture of “condensed matter physics”
2010–2012: Teaching Practicum at TU Darmstadt